Dissecting the host galaxies of Active Galactic Nulcei at high angular resolution

INAUGURAL-DISSERTATION

zur
Erlangung des Doktorgrades
der Mathematisch-Naturwissenschaftlichen Fakultät
der Universität zu Köln

vorgelegt von

Jens Zuther
aus Hannover

Köln 2007

Berichterstatter:	Prof. Dr. Andreas Eckart
	Prof. Dr. Johann Anton Zensus

Tag der letzten mündlichen Prüfung: 31.10.2007

Dissecting the host galaxies of Active Galactic Nulcei at high angular resolution

Zusammenfassung

Die hier vorgestellte Arbeit steht im Zusammenhang mit Fragen, die sich mit dem Wechselspiel zwischen der Struktur von Galaxien und dem Phänomen der Akkretion auf supermassive schwarze Löcher beschäftigen (d.h. aktive galaktische Kerne). Es existieren statistische Anhaltspunkte dafür, dass sich die supermassiven schwarzes Löcher und ihre assoziierten zentralen galaktischen Verdickungen (bulges) Hand in Hand entwickeln. Jedoch ist die genaue Kenntnis über die damit verbundenen physikalischen Vorgänge immer noch weitgehend unvollständig. Um theoretische Modelle, die sich mit dieser Problematik beschäftigen, zu testen und zu verbessern, sind räumlich hochauflösende Beobachtungen der umgebenden Galaxie und den in ihnen enthaltenen schwarzen Löchern notwendig. Abbildende und spektroskopische Untersuchungen der innersten Region von aktiven Galaxien erlauben es die chemische Zusammensetzung und die Dynamik von Sternen und Gas unter dem Einfluss des schwarzen Lochs detailliert zu studieren. Damit können die energetischen Signaturen der Sternentstehung und Akkretion voneinander getrennt und daraufhin in Beziehung gesetzt werden. Solche Beobachtungen, werden sie auf Galaxien mit immer größeren Rotverschiebungen angewandt, erlauben es, entwicklungsbedingte Eigenschaften der zuvor genannten Wechselwirkungen zu untersuchen. Mit Entwicklung der adaptiven Optik (AO) sind solche Arten von Beobachtungen Realität geworden. AO Systeme ermöglichen es, den negativen Einfluss der turbulenten irdischen Atmosphäre auf das Auflösungsvermögen von großen Teleskopen zu überwinden.

Der erste Teil dieser Arbeit beschreibt die Methoden, mit denen man Stichproben von Galaxien bestimmen kann, die für AO unterstützte Beobachtungen geeignet sind. Diese Stichproben basieren auf Daten von großflächigen Himmelsdurchmusterungen in verschiedenen Wellenlängenbereichen. Nur mit solchen panchromatischen Daten können Stichproben von interessanten Objekten, für detaillierte Folgebeobachtungen, homogen selektiert werden. Das Hauptaugenmerk liegt dabei auf dem im Optischen arbeitenden Sloan Digital Sky Survey und den Röntgenkatalogen des ROSAT All Sky Surveys. Im Rahmen des (German) Virtual Observatory können diese großen Kataloge effizient durchsucht werden.

Im zweiten Teil werden Ergebnisse räumlich aufeglöster nah-infrarot Spektroskopie einer aktiven Galaxie mittels SINFONI am Very Large Telescope der europäischen Südstenwarte präsentiert. Diese Galaxie stammt aus einer Stichprobe, die, wie im ersten Teil beschrieben, hergeleitet wurde. Eines der wichtigen Resultate dieser Beobachtung ist die Erkenntnis der Präsenz von nuklearen Ausflüssen und ihres Einflusses auf das umgebende interstellare Medium. Solche Eigenschaften sind in den vorigen, gröberen Vermessungen unentdeckt gewesen.

Komplementär zu den Ergebnissen des zweiten Teils werden im dritten Teil nah-infrarot Beobachtungen einer hoch rotverschobenen (als das Universum nur ein Viertel seines jetzigen Alters hatte) aktiven Galaxie. Diese erscheint als ein Beispiel der Klasse von Galaxien, die als Vorgänger der heutigen massiven elliptischen Galaxien geführt werden. Damit wird auch eine evolutionäre Brücke zwischen aktiven Galaxien und massiven passiven Galaxien geschlagen.

Abstract

The work presented here is concerned with issues related to the interplay of galaxy structure and the accretion phenomenon onto supermassive black holes (SMBH), i.e. active galactic nuclei (AGN). There is statistical evidence for a coevolution of SMBHs and the galaxy bulges they reside in. The detailed knowledge of the involved physical processes, however, is still far from being satisfactory. In order to test and improve theoretical models of how this coevolution is arising, high angular resolution observations of the host galaxies of AGN are necessary. Imaging and spectroscopy of the innermost region of galaxies have the power to reveal information on the structure, the chemical composition, and the dynamics of stars and gas in the presence of an SMBH, and allow us to separate energetic signatures related either to star formation or to the accretion onto the SMBH. Considering such observations over cosmological distances (redshifts) – i.e. looking into the past because of the finite light-travel time – we are also able to assess evolutionary effects on the beforementioned properties. Such types of observations have now become possible with the advent of adaptive optics (AO) systems, which overcome the limitations of angular resolution imposed by the Earth's turbulent atmosphere.

The first part of this thesis presents methods to derive samples of galaxies, suitable for high angular resolution studies. These samples are based on large area sky surveys at different wavelengths, since only panchromatic information allows us to select samples homogeneously for detailed follow-up observations. The main focus lies on visible (Sloan Digital Sky Survey) and X-ray (ROSAT All Sky Survey) wavelengths. Within the framework of the (German Astrophysical) Virtual Observatory [(GA)VO], such large databases can be mined efficiently. From a sample of X-ray bright AGN, near-infrared, AO-assisted, spatially-resolved spectroscopy of an AGN with SINFONI at the Very Large Telescope (European Southern Observatory, ESO) will be presented. In particular, the results show the importance of star formation/SMBH feedback in terms of nuclear outflows that have been uncertain from previous coarse multiwavelength survey observations.

These observations of X-raying AGN will be complemented by the

near-infrared imaging study of a high redshift (when the Universe was only about one quarter of its present age) AGN with ISAAC at the ESO VLT. The host galaxy of this bright AGN appears to be an example of the class of objects, known to be the progenitors of the population of present-day most massive elliptical galaxies. This places nuclear activity and and massive galaxies in an evolutionary context.

Für meine Eltern

Riddles of the Universe
26/3/81

To think, even for a moment about the infinite regions of starry space, is to be struck with awe. The glittering majesty of the night sky in winter! And yet our frail human eyes can only see the barest scattering. Beyond are galaxies and star-systems of unapprehended grandeur and mysterious complexity. There are collapsed stars and exploding stars. There is the sinister phenomenon of the black hole, so dense that not even light can escape its gravity.

To think that earth-dwellers might be existing entirely alone in the universe is such a chilling thought - like a mouse or a spider lonely forever in the Empire State Building or the Palace of Versailles - that we cannot bring ourselves to credit it. [...] Other mysteries crowd in. The galaxies are receding from each other at ever-increasing speeds. Therefore, it is argued, in the beginning there was an enormous explosion of primordial matter. But where, in the first place, did the dense original stuff come from? There are many riddles to be answered. Sitting lonely, late at night [...] - as one shuts off the TV and, beyond the window, the innumerable star-systems wheel - one realises that one is not lonely at all. However isolated, in a croft above the seashore or on a hillside, we are involved with *homo sapiens*, we live on a teeming ant-hill of a planet, between skulls and seeds.

-George MacKay Brown, in Rockpools & Daffodils

Contents

CHAPTER 0

Executive summary

There is growing evidence that every galaxy harbors a *supermassive black hole* (SMBH) in its very center (Kormendy & Richstone 1995; Gebhardt et al. 2000; Tremaine et al. 2002; Yu & Tremaine 2002). In some objects the existence of these SMBH manifests itself as a bright, unresolved nucleus, often outshining (by up to a factor of ~100) the underlying host galaxy. Historically, these objects are called quasi stellar objects (QSOs), since they appear as unresolved point sources in optical imaging studies (e.g. Schmidt & Green 1983). The emission is thought to originate in matter heated by viscous friction while being accreted onto the SMBH (e.g. Soltan 1982). This activity in so called *active galactic nuclei* (AGN) is observed at different levels of intensity, ranging from quasi-stellar-objects (QSOs) at the high end down to Seyferts and low-ionization nuclear emission-line region (LINERs) at the low end. The dominant present-day galaxy population, however, shows no signs of activity (Ho et al. 1997; Heckman et al. 2004), and there has been a longstanding debate as to whether activity occurs only in a subset of galaxies or whether all galaxies harbor an AGN for a short time. Recently, measurements of the integrated motion of stars in the bulges of quiescent galaxies indicate that a central dark mass comparable to that of SMBHs is present and therefore raise the question of an evolutionary link between active and inactive galaxies (e.g. Kormendy & Richstone 1995; Silk & Rees 1998).

Underlying this work are major issues (e.g., removing angular momentum of the infalling matter) concerning the fueling of the circumnuclear star formation and accretion onto the SMBH in AGN, and in turn concerning the impact of outflows and radiation (e.g., radiation pressure and ionizing radiation) from the nucleus onto the surrounding interstellar medium. These can only be tackled by sensitive studies at high angular resolution, dissecting the circumnuclear environment on the ~ 100 pc scale.

On the following pages, each of the three main chapters will be presented briefly.

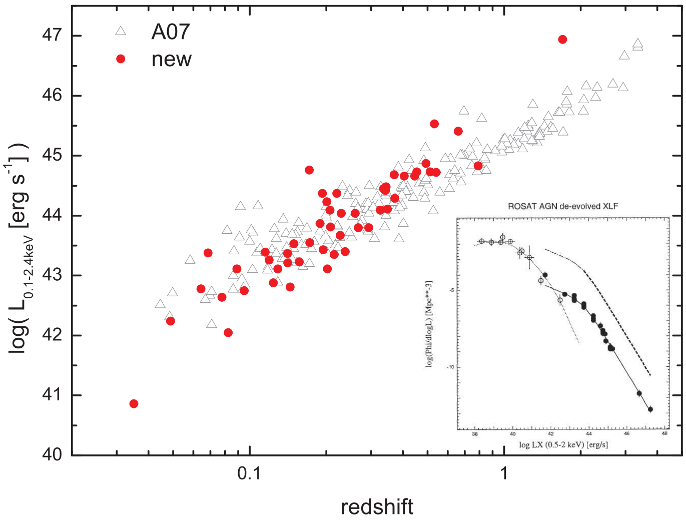

0.2-2.4 keV luminosity vs. spectroscopic redshift of the sample sources. The inset shows the X-ray luminosity functions (Hasinger 1998) of local normal galaxies (open circles), nearby AGN (filled circles) and $z \approx 2-3$ AGN (dashed line).

Chap. 2: X-raying AGN suitable for high angular resolution studies

X-ray selection has proven to be very efficient in finding AGN. Recent X-ray surveys have now resolved most of the cosmic X-ray background (CXRB) into discrete sources. While this represents a breakthrough in the understanding of the CXRB, the astrophysical nature of these sources still remains mysterious.

Only now, in the era of distributed computing over the World Wide Web (WWW) or the Grid – in astronomy this effort is termed *World Wide Telescope* or *Virtual Observatory* (VO) – it has become possible to efficiently digest the large amounts of data, coming from current multiwavelength sky surveys, as well as from the archives of past missions and telescopes. Examples are the Sloan Digital Sky Survey (SDSS) and the ROSAT All Sky Survey (RASS) that are used here to search for X-ray bright AGN, which are suitable for adaptive-optics (AO) assisted follow-up observations in the near-infrared (NIR). In order to reach the diffraction limit of ground-based large telescopes, AO systems have to compensate the wave-front distortions imposed by the turbulent atmosphere on the incoming galaxy light. The compensation is achieved by assessing the wave-front distortions by observing a point-source reference close to the science target and subsequent adjustment of a deformable mirror.

The X-ray/optical data allow us to characterize sources reliably. However, light at visible wavelengths is subject to scattering and absorption by interstellar dust. In contrast, NIR emission is significantly less influenced by these effects and on can probe deeper into the dust-enshrouded nuclear regions of AGN. In some cases, NIR observations can alter the classification of galaxies. This is also related to the question of the true number of obscured AGN, which would provide important constraints on evolutionary models.

The 241 X-ray AGN in the sample presented in this chapter have a nearby bright guide star (GS), and can therefore make use of AO systems. In every aspect, the presented AGN have X-ray properties similar to those of other studies and can be regarded as representative for the whole X-ray AGN population accessible with RASS and SDSS. However, the sample cannot be called complete, because of the small numbers of objects per subclass and redshift bin. The sample allows, nevertheless, the host galaxy properties to be studied in detail, in terms of case studies. One of these case studies is presented in the following chapter.

Chap. 3: SINFONI observation of Mrk 609

In this chapter results of NIR *J* and $H + K$ ESO-SINFONI integral field spectroscopy of the composite starburst/Seyfert 1.8 galaxy Mrk 609 are presented. The data were taken during the science verification period of SINFONI. As outlined above, this study aims to investigate the morphology and excitation conditions within the central 2 kpc. Additional Nobeyama 45 m CO(1-0) data are presented, which are used to estimate the molecular gas mass. Mrk 609 was selected from a previous version of the sample of SDSS/ROSAT-based, X-ray bright AGN presented in the previous chapter.

Integral field spectroscopy with SINFONI delivers simultaneous spatial and spectral coverage of the circumnuclear environment. In addition to the NIR light being less influenced by dust extinction than by optical light, it is sensitive to the mass- dominating stellar populations. Furthermore, several NIR emission lines allow the emission to be disentangled into Seyfert and starburst components. The presented NIR data reveal a complex emission-line morphology that is possibly associated with a nuclear bar seen in the reconstructed continuum images. The detections of [Si VI] and a broad Paα component are clear indicators of the presence of an accreting SMBH at the

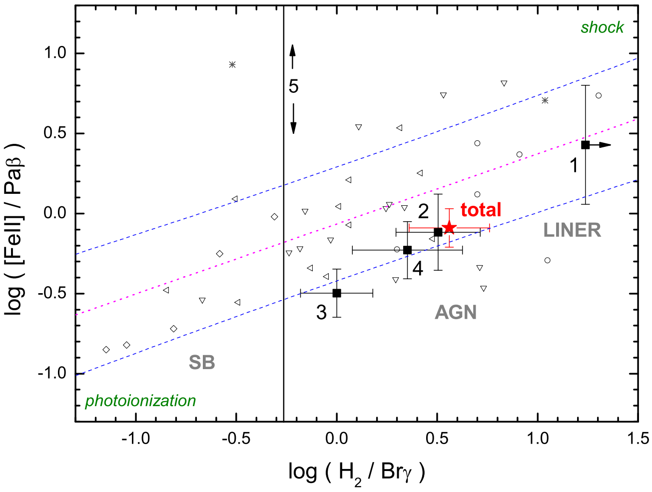

Line ratios of [Fe II] 1.257μm/Paβ and 1-0S(1) 2.121μm/Brγ. Activity types (starburst, AGN, LINER) are indicated. The dominant excitation mechanism changes from pure photoionization of starburst galaxies over a mixture of photoionization and shock driven excitation of AGN to pure shock-driven excitation of LINERs.

center of Mrk 609. In agreement with previous observations, it is found that the circumnuclear emission is not significantly extincted. Analysis of the high angular-resolution, molecular hydrogen emission, and [Fe II] emission reveals the LINER[1] character of the nucleus. The large H_2 gas mass deduced from the CO(1-0) observation provides the fuel needed to feed the starburst and Seyfert activity in Mrk 609. High angular resolution imaging spectroscopy provides an ideal tool for resolving the nuclear and starburst contributions in active galaxies. It could be shown that Mrk 609 exhibits LINER features that appear to be hidden in visible/NIR spectra with larger apertures.

---

[1] Low-ionization nuclear emission-line regions (LINERs) represent a very low nuclear-luminosity class of AGN, which spectroscopically resemble Seyfert 2 galaxies, except that low-ionization lines are particularly strong. The emission line excitation mechanisms appear to be related to nuclear outflows, shocking the circumjacent gas.

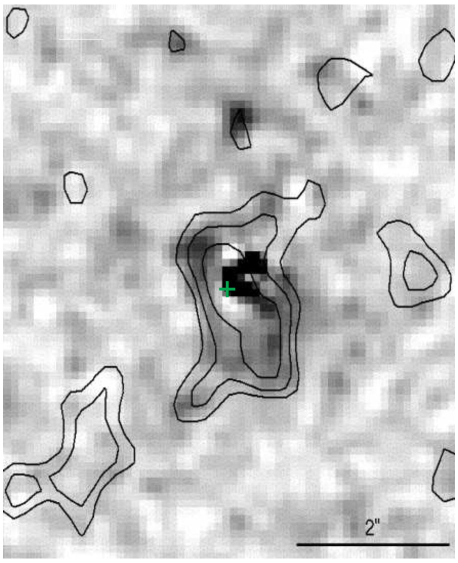

PSF-subtracted HST F814W image (rest-frame UV) overlaid with contours of the three-pixel-smoothed, PSF-subtracted *H* band image (rest-frame visible) of the BALQ 0134+3253. The lowest contour level corresponds to $1.5 \times \sigma$ of the sky noise. The green cross shows the position of the nucleus in the *H* band image. North is up and east is to the right.

Chap. 4: Broad absorption line quasars: Young AGN at high redshifts?

In this chapter, NIR imaging data of the host galaxy of the broad absorption line quasar (BALQ)[2] at $z = 2.169$, serendipitously found close to 3C 48 (Canalizo et al. 1998), are presented. The data were obtained with the ESO-VLT camera ISAAC during period 67. An extended, rest-frame optical emission around the BALQ is found after carefully subtracting a scaled stellar point spread function from the quasar nucleus in *J*, *H*, and *Ks*. The extended rest-frame optical emission can be interpreted as an approximately 2 Gyr old stellar population composing the host galaxy of the BALQ or a stellar population of similar age associated with an intermedi-

---

[2] BALQs form a rare class of QSO population at moderate to high redshifts ($z \approx 2 - 4$). The BAL phenomenon is related to outflows in quasars, which are metal absorption systems with large blueshifted velocities (several thousand km s^{-1}). Prominent P Cygny-type features are found at UV resonance transitions like C IV λ1548Å, Lyα λ1215Å, or Mg II λ2796 & 2803Å.

ate (z = 1.667) absorption system spectroscopically identified by Canalizo et al. (1998). The rest-frame-UV emission, on the other hand, is dominated by a young, $\sim$ 500 Myr old stellar population (Canalizo et al. 1998). The UV/optical colors resemble a mixture of the two populations. The young component accounts for roughly 80% of the total host emission. Assuming that the residual emission is located at the BALQ redshift, the host galaxy has a resolved flux of about 10% of the BALQ flux. The physical scale is quite compact, typical for radio quiet QSOs or Lyman break galaxies at these redshifts. These galaxies are believed to be the progenitors of todays massive elliptical galaxies, since they are already massive systems at $z = 2$ (i.e. $\sim$ 3 Gyr after the Big Bang) and are forming stars at high rates (up to 1000 $M_\odot\ \mathrm{yr}^{-1}$). This observation introduces an evolutionary context, in which BALQs are young AGN that have just started to remove the primeval gaseous cocoon via radiation pressure.

This evolutionary link leads back to questions posed in the beginning. Only sensitive, high angular resolution studies of sizable samples of AGN – most efficiently derived in the VO framework – are able to resolve the physical details, relating the nuclear activity and the star formation in the host.

CHAPTER 1

Active galactic nuclei and their host galaxies

Die Natur entspricht unserem Wissen, weil unser Wissen der Natur entspricht.
– Erwin Chargaff

The investigations presented in this thesis are concerned with questions of how the Seyfert phenomenon - i.e. the accretion of gas and dust onto supermassive black holes (SMBHs) at the centers of galaxies (Lynden-Bell 1969) - is related to the host galaxy, harboring the SMBH. Feedback might occur in the form of radiation pressure from the accretor, of outflows, and (circumnuclear) star formation (e.g. Begelman 1985; Shlosman et al. 1990). It has been demonstrated that the circumnuclear environment holds the key information on the possible links between the nuclear activity and star formation, and how they regulate each other. In this respect it is important to use observational techniques, which provide high angular resolution. In addition, high angular resolution is furthermore essential to access this information for galaxies over cosmological distances, as their apparent angular sizes decrease with redshift. Such observational studies allow us to investigate the evolution of SMBHs and their associated galaxies across time. The hierarchical framework, which explained quite successfully the build-up of galaxies and SMBHs from small to large units (Blumenthal et al. 1984), has been challenged to some extent in recent years (e.g. Glazebrook et al. 2004; Cimatti et al. 2004; Hasinger et al. 2005).

Stellar kinematical studies of nearby galaxies, furthermore, give reasons for speculating that every galaxy harbors a SMBH in its center (e.g. Kormendy & Richstone 1995; Gebhardt et al. 2000; Tremaine et al. 2002). Numerous studies of active galactic nuclei (AGN) and quiescent galaxies have furthermore revealed correlations between the SMBHs and the bulges hosting them (e.g. Magorrian et al. 1998; Page et al. 2001; Tremaine et al.

2002). These correlations indicate the existence of feedback mechanisms that regulate the coeval growth of SMBHs and their associated bulges.

1.1 Fueling of nuclear activity

The presence of the Seyfert phenomenon[1] is supposed to originate in the accretion of matter onto an SMBH in the centers of the galaxies (see Fig. 1.1). The fuel necessary for driving nuclear activity, which is composed of nuclear starbursts and Seyfert-like activity, has to be transported from galactic scales (∼10 kpc) down to nuclear scales (∼10 pc). We are still far from understanding the detailed processes that lead to the dissipation of angular momentum needed for the gas and stars to fall towards the nuclear region. However, considerable theoretical, as well as observational, effort has been made toward understanding these processes (e.g. Shlosman et al. 1990; Combes 1996; Knapen 2005). As concerned with triggers of the fueling process, external and internal ones can be distinguished.

External triggers: They are related to the environment of galaxies and gravitational interaction. Non-axisymmetries, which can lead to loss of angular momentum, can result from galaxy interactions. For ULIRGs, which show the most extreme case of infrared nuclear activity, there is intriguing evidence of a connection between galaxy interaction and nuclear activity (cf review by Knapen 2005, and references therein). Nevertheless, statistical studies show a significant fraction of nuclear active galaxies that are apparently free of any external trigger.

Internal triggers: For example, Shlosman et al. (1989) proposed a two-step process that is able to sweep the interstellar medium (ISM) via a stellar bar from large scales into a disk of several hundred pc in radius. In the second step, further instabilities (bar-within-bar) drive the material close to the nucleus until viscous processes take over the angular momentum transport.

While extensive nuclear star formation in quiescent[2] galaxies appears to be related to large-scale bars (Knapen 2005, and references therein), the ob-

---

[1] The Seyfert phenomenon relates to the presence of a strong, nonthermal nuclear continuum and a characteristic optical emission-line spectrum. The spectrum contains broad (FWHM $\sim 10^4$ km s^{-1}) and narrow (FWHM $< 10^3$ km s^{-1}) emission lines of allowed transitions (e.g., ionized hydrogen) and small emission lines of forbidden transitions (e.g., [Fe II], [N II]). Figure 1.1 demonstrates how these features can be unified in an orientation dependent scheme.

[2] *Quiescent* here refers to galaxies not showing Seyfert-like nuclei. Throughout the text the expressions *inactive* or *normal* galaxies will be used synonymously.

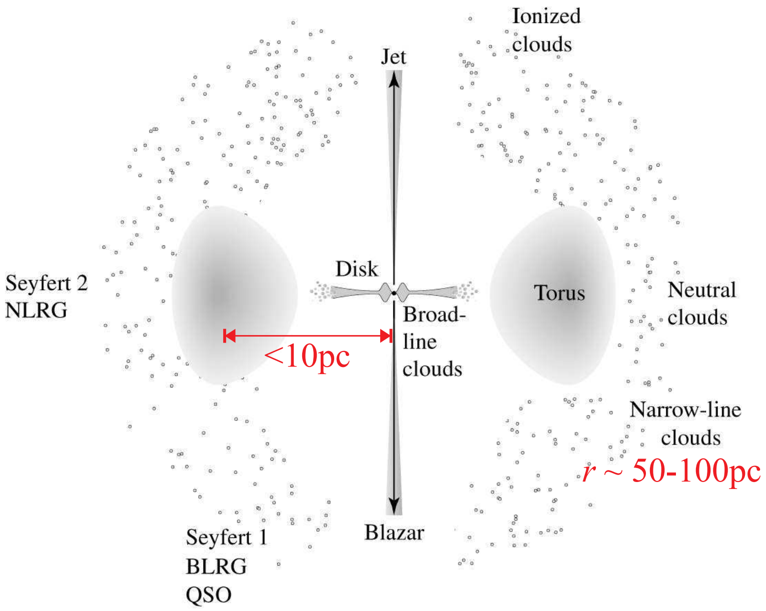

Figure 1.1: The unified scheme of AGN (Antonucci 1993). The observational characteristics of an AGN are a function of viewing angle. Broad (FWHM $\sim 10^4$ km s^{-1}) and narrow (FWHM $< 10^3$ km s^{-1}) lines are produced in clouds moving around the nucleus. An observer at small inclination will observe both broad and narrow emission lines (Seyfert 1 or type-1 AGN), whereas at large inclinations the dusty torus will block the direct view onto the broad-line region (Seyfert 2 or type-2 AGN). The dusty torus or a inhomogeneous distribution of clouds is believed to lie at a few pc distance from the nucleus (Elitzur & Shlosman 2006). Assuming that the cloud's motion is in virialized equilibrium, their velocity dispersions reflect the central gravitational potential and can be used to estimate the black hole mass (e.g., Shields et al. 2003). The jet component is generally oriented perpendicular to the accretion disk and the AGN appears as a BL Lac object when viewed along this line of sight. Adapted from Carroll & Ostlie (2006).

servational evidence of bar-related nuclear activity is not as clear for Seyfert galaxies. Laine et al. (2002) find a slight but significant increase in the galactic-bar fraction of active galaxies when compared to inactive galaxies. This does not appear to be the case for nuclear bars. On the other hand, there are a considerable number of AGN that show no signs of any bar or inactive galaxies that do possess bars. The overall lack of observational evidence of direct causal relationships between the presence of morphological asymmetries and the starburst/Seyfert activity might result from disregarding the correct spatial or time scales (Knapen 2005). To some extent the non-axisymmetries could occur on spatial scales that are currently not resolvable, or could be masked by dust or star formation (Laine et al. 2002). Considering lifetimes, the typical age for nearby spiral galaxies is 10^{10} yr. Only $\sim 10\%$ of nearby spirals display Seyfert activity (e.g. Ho et al. 1997). Sanders et al. (1988) propose an evolutionary scenario in which the Seyfert phenomenon is a transient phase. If all galaxies undergo this phase, the small fraction of active galaxies translates into an AGN lifetime of about 10^9 yr. But the non-stellar activity can also occur episodically on much shorter time scales (Martini 2004). The typical bar lifetime is 10^9 yr (Crenshaw et al. 2003), and the bar can trigger significant star formation within 10^8 yr (Hunt & Malkan 1999). Active circumnuclear star formation might, therefore, be related to the presence of a bar. But what happens with the bar when the Seyfert activity, under the assumption of bar-induced nuclear fueling, is episodic with a lifetime of about 10^4 yr? Further work has clearly to be done, primarily aimed at the kinematics and dynamics of the very central region of active and inactive galaxies.

The recent finding of a stellar surface mass density criterion for the separation of bulge-dominated and disk-dominated galaxies by Kauffmann et al. (2003) can shed some light on the problem. The authors find that bulges dominate in galaxies with stellar masses $\gtrsim 3\times10^{10} M_\odot$ corresponding to a mean stellar surface density of $\mu_\star \gtrsim 3 \times 10^8 M_\odot$ kpc^{-2}. Heckman et al. (2004) find that this stellar surface density is also the critical surface density for the onset of significant Seyfert activity. These results can be compared with the critical stellar surface density necessary for the onset of bar instability (Wyse 2004). It turns out that this surface density ($\mu > 1.7 \times 10^8 M_\odot$ kpc^{-2}) is very similar to the one found by Heckman et al. (2004) for nuclear activity. One expects that the stellar surface density increases once a bar is formed, since the subsequent gas infall towards the central regions will be accompanied by star formation. This is seen in both observations and in simulations and can explain the factor of about 2 below the observed stellar surface density for bulge dominance.

1.2 The hierarchical formation and evolution of galaxies

1.2.1 Cold dark matter and structure formation

It has been introduced in the previous section that the fueling of AGN is intimately related to the host galaxy. For understanding the evolution of SMBHs it is also important to study the formation and evolution of galaxies, which in fact provide the fuel for the accretion/growth phase. Our current understanding of the growth of structure in the Universe grounds on the *hierarchical (bottom-up) paradigm*[3]. Here, large structures form by the coalescence of smaller structures. This is a direct consequence of the *cold dark matter* (CDM) cosmology (cf Freedman & Turner 2003). Since the late 1970s there is growing evidence that most part of the matter in the Universe is not in stellar or gaseous (i.e. baryonic) form (see, e.g. Faber & Gallagher 1979). Only about 4% of the total mass energy is in the form of baryonic matter and about 30% acount for dark matter (DM). The rest exists in the form of some "mysterious" dark energy (Peebles & Ratra 2003), which is closely related to an accelerated Universe (Kamionkowski 2007, and references therein). The DM particles have neglegible thermal velocity with respect to the Hubble flow[4] and their non-gravitational interactions are much less pronounced than the weak interactions (Blumenthal et al. 1984). Hence, this matter is only recognizable by its gravitational action and it is therefore called *dark matter*. An example for the effects of DM shown by Zwicky (1933) in his study of Virgo cluster galaxies is that the cluster virial mass is much larger than the visible mass of the cluster members. Another example is the flatness of galaxy rotation-curves in their outer parts, which indicates that huge amounts of matter have to be located outside the visible part of galaxies (e.g., Rubin et al. 1980).

The CDM cosmology states that each visible galaxy is embedded in a much larger DM halo that detached from the expanding cosmic plasma at early times after the big bang. The dissipationless gravitational merging of these halos drives the growth of structure and the rate of cooling of hydrogen gas drawn into the merging halos governs the history of assembly and star formation in galaxies (Fig. 1.2). The assembly of the stellar (baryonic) content of galaxies is governed by much more complicated processes, often dissipative and nonlinear, which are generally poorly understood. Before the success of the CDM scenario, it was believed that at least some galaxies (presently quiescent ellipticals) form and evolve in a monolithic fashion at high redshift, i.e the gas turns into stars at the time of the initial

---

[3] Last year's Nobel Prize was awarded to J. Marther and G. Smoot for their discovery of the blackbody form and anisotropy of the cosmic microwave background. It is the anisotropy, which is believed to trace the primeval density fluctiations that are responsible for structure formation in the Universe.

[4] It is the general outward movement of galaxies and clusters of galaxies, resulting from the expansion of the universe. It occurs radially away from the observer and obeys the Hubble law. Galaxies can overcome this expansion on scales smaller than that of clusters of galaxies. The clusters, however, are being forever driven apart by the Hubble flow.

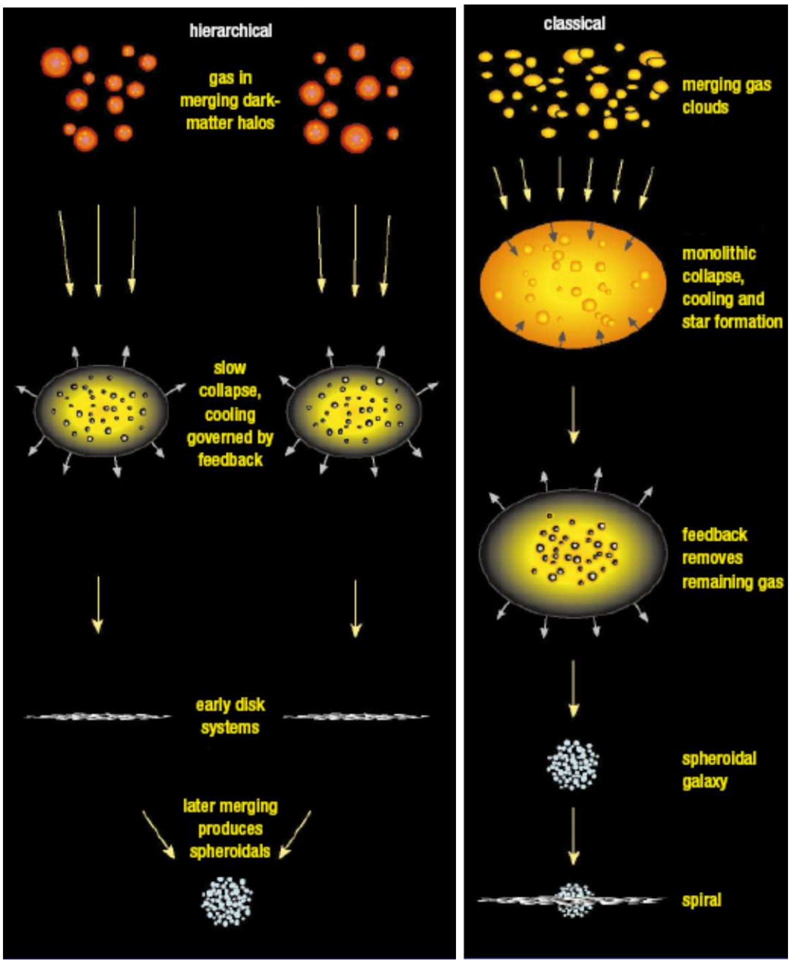

Figure 1.2: In the classical picture, galaxies evolve in isolation, retaining their morphologies from birth. The hierarchical picture supposes that galaxies assemble gradually within merging dark matter halos. Adapted from Ellis et al. (2000).

proto-galactic cloud collapse (e.g. Eggen et al. 1962; Kaviraj et al. 2005, and references therein). However, our present understanding of the participating physical processes in either of the evolutionary schemes is still far from satisfactory. This becomes clear when comparing observations with theoretical models and simulations.

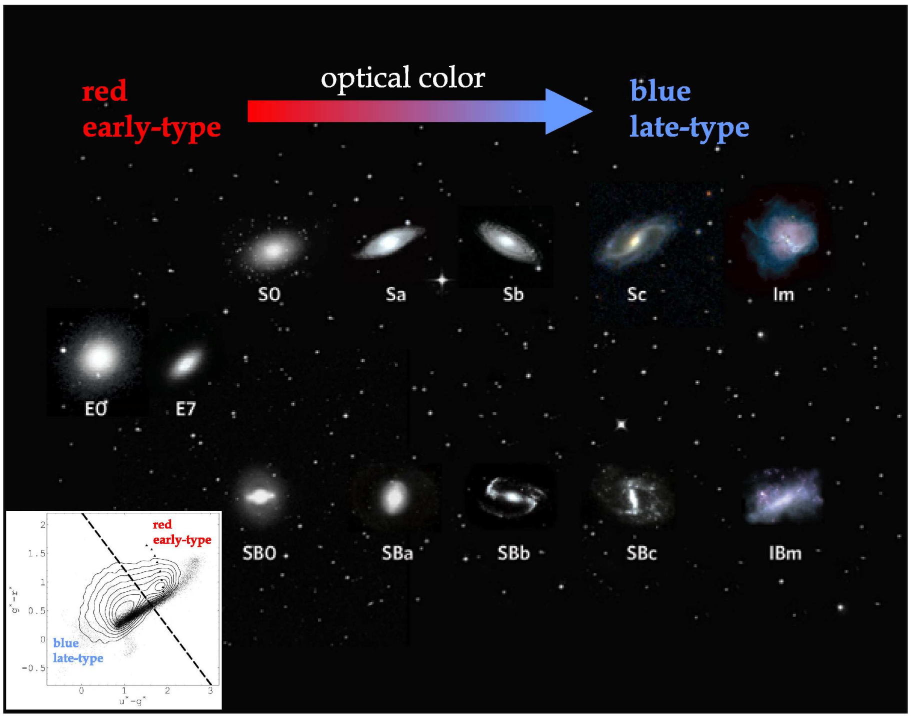

Figure 1.3: Bimodal galaxy morphology. *Early-type* galaxies show elliptical host structure whereas *late-type* galaxies show spiral arms and a flattened disk. Adapted from van den Bergh (2007). The lower left inset shows the optical 2-color diagram of SDSS normal galaxies. It is evident that the population shows two concentration of colors, a blue peak that can be associated with late-type galaxies and a red peak that can be associated with early-type galaxies. Black dots represent the colors of galactic stars. Adapted from Strateva et al. (2001).

1.2.2 Ly-break galaxies as probes of high redshift star formation

At redshifts $z < 1$ galaxies exhibit two morphological classes, early-type ellipticals and late-type spiral galaxies. The well-known classification scheme of Hubble is based on this observation (Fig. 1.3; Hubble 1926; van den Bergh 1998). Present-day star formation occurs in lower-mass galaxies and in the disks of late-type galaxies (Kauffmann et al. 2003; Heavens et al. 2004). These show blue optical colors. Elliptical galaxies have red colors and show no or little current star formation. This gives rise to the bimodal color distribution found in the Sloan Digital Sky Survey (Fig. 1.3 Strateva et al. 2001). Tracing star formation - e.g. using rest-frame UV and optical emission - with the Hubble Space Telescope revealed a strong increase in star formation towards $z \sim 2$, followed by a modest decline to even higher redshifts (Fig. 1.4; Giavalisco et al. 2004). The morphologies of high redshift ($z > 2$) Lyman-break galaxies (LBGs) are very compact and show faint, irregular shaped extended emission, far from resembling Hubble-sequence-like structures. These compact galaxies - with half-light radii typical of the sizes of present-day bulges - are massive and form stars intensely (Giavalisco et al. 1996). Accordingly, they are believed to be the progenitors of massive ellipticals and spirals at low redshifts. Because of the distinct UV-break of young stars around 912 Å, high-z LBGs can easily be found as U-band dropouts, as the rest-frame UV is shifted into the R-band. The corresponding $U - R$ colors show unambiguous traces of this fact (see Fig. 1.5). Nowadays, several thousand confirmed LBGs have been studied and provide a sound standing for statistical analyses of their collective properties (see review by Giavalisco 2002). Judging fromt the UV luminosity, LBGs account for over 50% of the unobscured cosmic star formation, and the star-formation rates (SFRs) are high ($\sim 10^{2-3} M_\odot$ yr^{-1}). The role of far-infrared luminous galaxies, observed as sub-mm galaxies at high redshifts, with respect to LBGs is still not clear. Dust reprocesses UV radiation into far-infrared (FIR) wavelengths and thereby is an important tracer of vigurous star formation. At small sub-mm fluxes(< 2 mJy), the LBG and sub-mm populations appear to share the same properties (e.g., Barger et al. 2000). But at higher sub-mm flux levels the sub-mm galaxies resemble local ULIRGs[5] that contain huge amounts of gas and dust. In this case, most of the UV emission is absorbed and one is unable to detect optical (LBG-like) counterparts with current telescope facilities. What needs to be established is how much star formation occurs at high redshifts in obscured systems (cf Fabian 1999). The $z \sim 3$ LBGs are already massive ($M \lesssim M^* = 10^{11} M_\odot$, 2 Gyr after the Big Bang), comparable to local massive spiral galaxies (e.g., Papovich et al. 2001). This supports the observation that the most massive galaxies are already in place by $z = 2$ (Cimatti et al. 2004; Glazebrook et al. 2004).

The spatial clustering of LBGs (Giavalisco 2002, and references therein) is an important observation that supports our fundamental ideas about galaxy formation, namely the association between individual virialized DM structures (halos) and the activity of star formation. The galaxies form first and more efficiently in denser and more massive parts of the mass-density field.

---

[5] Ultraluminous infrared galaxies have $L_{IR} \geq 10^{11} L_\odot$ and represent the most extreme starbursts. More than 75% of the ULRIG population is undergoing a merger event.

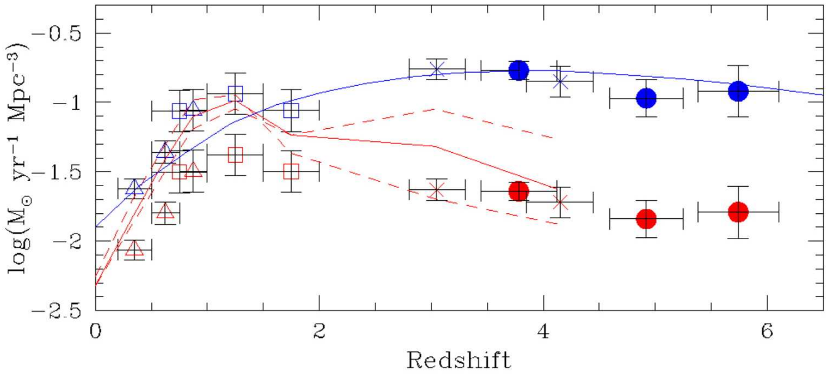

Figure 1.4: SFR density as a function of redshift. Circles represent GOODS (see Appendix B) *B*-, *V*-, and *i*-band dropout samples. Other symbols correspond to measurements from Lilly et al. (1996); Connolly et al. (1997); Steidel et al. (1999). The blue filled circles are as observed, whereas the red filled circles have been corrected for dust obscuration. The red curve and red dot-dashed lines are derived from the evolution of the HI mass density as traced by damped Lyα absorbers (Pei et al. 1999). The blue curve is from semi-analytical models of Somerville et al. (2001). In case of dust correction, a peak of the SFR density around $z \approx 1.4$ appears. Figure courtesy of Giavalisco et al. (2004).

Star formation then propagates to the less dense and massive halos during the case of evolution. This is referred to as *archaeological downsizing* and is a natural outcome of the merging of DM halos (Neistein et al. 2006). Another downsizing effect observed is that sites of active star formation shift from high-mass galaxies at early times to lower-mass systems at lower redshift (*downsizing in time;* Cowie et al. 1996). This kind of downsizing, however, cannot be explained with the merging of halos and feedback effects; shutting down star formation in more massive systems has to come into play (Neistein et al. 2006). We will return to this in the next section.

Although structure formation is believed to occur by merging of DM halos and subsequent cooling and accumulation of baryonic matter in the DM gravitational potential well, the implications of this process for the growth of galaxies via merging is not clear. At low redshifts mergers are rare, but when advancing to higher redshifts ($z > 0.7$) the number density of galaxies with disturbed morphologies or companions increases steeply (e.g., Conselice 2007; Bridge et al. 2007). Modelling of the merger rate shows that a massive galaxy ($M_* > 10^{11} M_\odot$), on average, undergoes one major merger from $z \sim 1.4$ to 0.4. The fraction of massive galaxies involved in major mergers is roughly 5-10% at $z \sim 1$. At redshifts $z > 2$

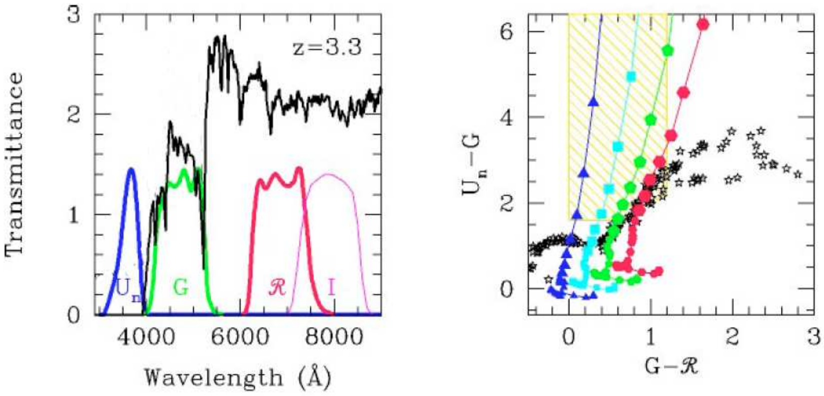

Figure 1.5: The principle of finding high redshift LBGs. In a suitable set of filters, star-forming galaxies can be identified by the colors in the spectral region around the 912 Å continuum discontinuity. Together with the filter transmission curves (U, G, R, I) redshifted synthetic model spectra of continuous star formation (Bruzual A. & Charlot 1993) are plotted. The two panels show dropouts at $z \sim 3$. The candidates are selected from their position in the 2-color space (right panel). The curves represent galaxies placed at progressively higher redshifts, starting at $z = 0.5$ with step $\Delta z = 0.1$. The four tracks correspond to different amounts of dust obscuration (triangles: no dust; squares: $E(B-V) = 0.15$; pentagons: $E(B-V) = 0.3$; hexagons: $E(B-V) = 0.45$). The shaded area in the right panel marks the region of $z \sim 3$ LBG candidates. Figure adapted from Giavalisco (2002).

massive galaxies appear peculiar, which can be attributed to the influence of merger processes. Conselice et al. (2003) estimated a merger fraction of 40-50% at $z > 2$. Although merging is being assumed to be the favorite way of mass assembly (cf Hopkins et al. 2006), the clustering results of LBGs indicate a dependence of SFR on their total mass, i.e. local gravity, rather than on external accidents such as interactions and merging. One has to keep in mind that the UV and optical light, however, only trace the sites of ongoing star formation and not necessarily of the underlying mass-dominating older stellar populations. This emission is furthermore susceptible to dust extinction. In early evolutionary stages, galaxies most likely contain large amounts of gas and dust and obscuration can contribute to the observed patchy morphology. The older stellar populations dominate the NIR and are shifted to the mid-IR at the redshifts of LBGs. Matters are further complicated by the cosmological surface-brightness dimming [SB $\propto (1+z)^{-4}$]. Current facilities do not have the angular resolution, as well as the sensitivity to study the rest-frame NIR properties of high-z (LB) galaxies. The peculiar morphology of LBGs might therefore mimic the presence of enhanced galaxy interaction.

1.2.3 Confronting theory with observations

While the basic hierarchical paradigm for the evolution of DM halos is widely accepted, our understanding of the rather more complex process of galaxy formation is still far from complete. The 'semi-analytical' approach taken is a compromise, which generally involves taking the DM halos from N-body CDM simulations and then adding basic prescriptions for gas physics, radiative cooling, complex processes of star formation, the output initial mass function, supernovae feedback, dust, enrichment, etc., attempting to reproduce the space density, luminosities, colors, and other properties of the observed galaxy populations (e.g., Almaini 2006, and references therein). Given the wide range of poorly understood phenomena, it is somewhat surprising that the models are quite successful (cf Marchesini & van Dokkum 2007). But there are important 'classic' problems with semi-analytical models (SAMs). SAMs have problems reproducing the faint and bright ends of the luminosity functions, e.g., far too many dwarfs are predicted than are observed in the local neighborhood (Kauffmann et al. 1993). Another problem is reproducing the knee in the galaxy luminosity function (LF)[6] above $L*$. What is the physical mechanism that appears to restrict the formation of the most massive galaxies? As mentioned in Sec. 1.1, the galaxy population is bimodal with respect to stellar mass and morphological type. Below the borderline of $M^* \sim 3 \times 10^{10} M_\odot$, local galaxies tend to be disk galaxies which have undergone recent episodes of star formation. Above M^*, local galaxies are dominated by old and red spheroidal systems. SAMs have great difficulties in producing such a bimodal distribution. In particular, a mechanism is needed for switching off star formation in the most massive galaxies at early times. Recent studies offer a possible solution: feedback by the AGN . Since SMBH and galaxy growth are related, as can be recognized by the black-hole mass / bulge velocity dispersion relation (Tremaine et al. 2002; Shields et al. 2003), it can be expected that nuclear outflows and radiation pressure will heat the surrounding host galaxy matter and thereby regulate the star formation and growth of the host (Scannapieco et al. 2005; Weinmann et al. 2006; Schawinski et al. 2006). These models constitute a step forward, but many problems still persist.

---

[6] The LF is the relative number of AGN at a given luminosity and the space density, which is the total number of sources per unit comoving volume over some luminosity range is the integral of the LF over its entire range. $L*$ is the characteristic luminositiy, for which the LF drops significantly towards higher luminosities.

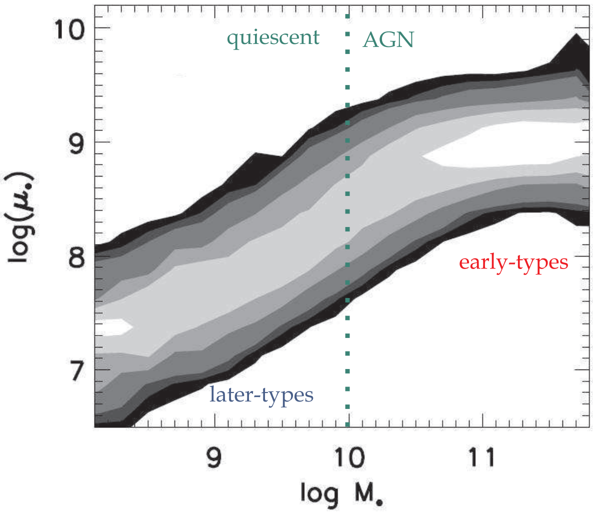

Figure 1.6: Surface mass density $\mu_\star$ distribution as a function of the stellar mass $M_\star$. A division into massive galaxies with high surface densities (earlier types) and less massive galaxies with low surface densities (later types) is evident. Kauffmann et al. (2003) find that AGN signatures are only found in the high stellar mass part of the diagram (indicated by the green dotted line). Normal galaxies, in which most of the present-day star formation occurs, populate the lower surface-density/low stellar mass regime. Adapted from Kauffmann et al. (2003).

Until now, the growth of SMBHs in the context of galaxy evolution has not been addressed. X-ray emission coming from AGN is believed to be related to the accretion process and this will be the topic of the following section.

1.3 The X-ray view of AGN

1.3.1 The origin of X-rays in AGN

During the last three decades, AGN have turned out to be strong X-ray emitters (e.g., Ku et al. 1980; Piccinotti et al. 1982; Bade et al. 1995; Giacconi et al. 2001). At higher flux levels they even dominate the source populations. The X-ray continuum is one of the main contributors to the bolometric luminosity, accounting for $\gtrsim 10\%$ of the observed energy. Furthermore, the X-ray band shows the largest amplitude and most rapid time variability of all continuum bands, indicating that it comes from the smallest regions (e.g., Mushotzky et al. 1993). The broad spectral coverage of current X-ray observatories like Einstein (0.2-20 keV), ROSAT (0.1-2.4 keV[7]), BeppoSAX (0.1-200 keV), Chandra, XMM-Newton (0.1-10 keV), or Suzaku (0.2-600 keV) allows us to use the deep penetrating power of X-rays to probe absorbing column densities of up to $N_H \sim 10^{25}$ cm^{-2}. Figure 1.7 presents the effects of photo-electric absorption of a photon spectrum, following an $\alpha = 1$ power law with varying column densities. The absorbing column densities in type-1 Seyferts are often consistent with absorption from the interstellar medium in our Galaxy. In type-2 AGN (edge-on view of the accretion disc) the column densities can reach up to 10^{25} cm^{-2}. When N_H exceeds 1.5×10^{24} cm^{-2}, which corresponds to the inverse of the Thomson scattering cross section σ_T, the Compton scattering optical depth equals unity and the source is denominated *Compton thick*. An extraordinary example of burried AGN is the very recent discovery of heavily obscured AGN, in which evidence for the presence of an SMBH stems only from X-rays (Ueda et al. 2007).

The origin of X-rays in AGN is still not fully understood. In many models, the X-ray emission is produced by inverse-Compton scattering of lower-energy photons by more energetic electrons, although the specific details vary greatly from model to model. The lower-energy photons are believed to originate from an accretion disk, which surrounds the SMBH, via viscous heating (Shields 1978). A look at the X-ray spectral energy distribution (SED) reveals several components that are characteristic of many AGN (Fig. 1.8):

- *UV bump:* a strong emission in the UV, generally interpreted as thermal emission of an accretion disk.
- A strong emission in the X-ray band, which can be generally fitted by a cut-off power law shape ($E^{-\Gamma} \times e^{-E/E_c}$) with a photon index $\Gamma = 1.9$ and cut-off energy E_c around 250 keV (Nandra & Pounds 1994; Perola et al. 2002).
- A neutral fluorescence $\mathrm{Fe}_{\mathrm{K}\alpha}$ near 6.4 keV.
- A bump peaking near 30 keV.
- *Warm absorber:* Atomic absorption edges below 1 keV.
- *Soft excess:* A soft component below 2 keV, in excess of the extrapolation of the high-energy power law.

---

[7] In order to relate eV to wavelength, calculate $\lambda[\mathrm{nm}] \times E[\mathrm{eV}] = 1239.842$.

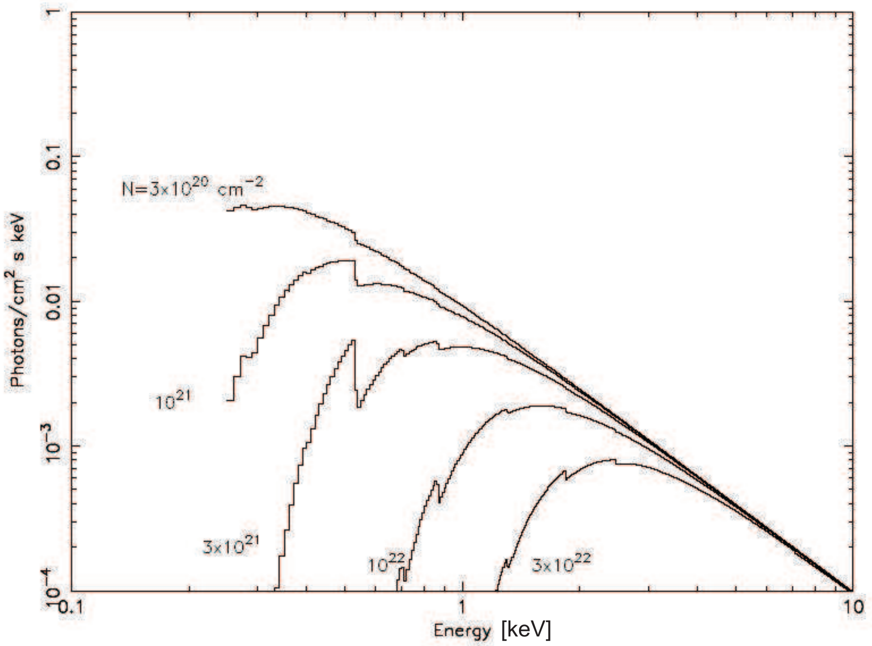

Figure 1.7: The observed photon spectrum of an $\alpha = 1$ power law model absorbed by rest-frame cold material of varying column density (0.03, 0.1, 0.3, 1, and 3×10^{22} cm^{-2}). Adapted from Mushotzky (1997).

A common model used to explain these spectral features is based on reprocessing and up-scattering (Fig. 1.9). Thermal emission should emerge from an optically thick disk, providing the bulk of photons with energies spanning the range from optical to soft X-rays. Subsequently, Comptonization of these seed photons occurs in a hot optically thin corona made of thermal, mildly relativistic electrons, which extends above the accretion disk. In the presence of relativistic electrons lower-energy photons can be up-scattered to higher energies. Therefore, the bulk of X-rays is produced by successive inverse-Compton scattering of softer disk photons (see Rybicki & Lightman 1986, for a treatise of inverse-Compton scattering). The key parameters in this type of models are the temperature and optical depth of the corona and the temperature of the accretion disk. The energy balance between the cold disk and the hot corona determines the values of these parameters and, in turn, the shape of the resulting X-ray spectrum (Haardt et al. 1994; Stern et al. 1995).

The effects of photoelectric absorption have already been mentioned at

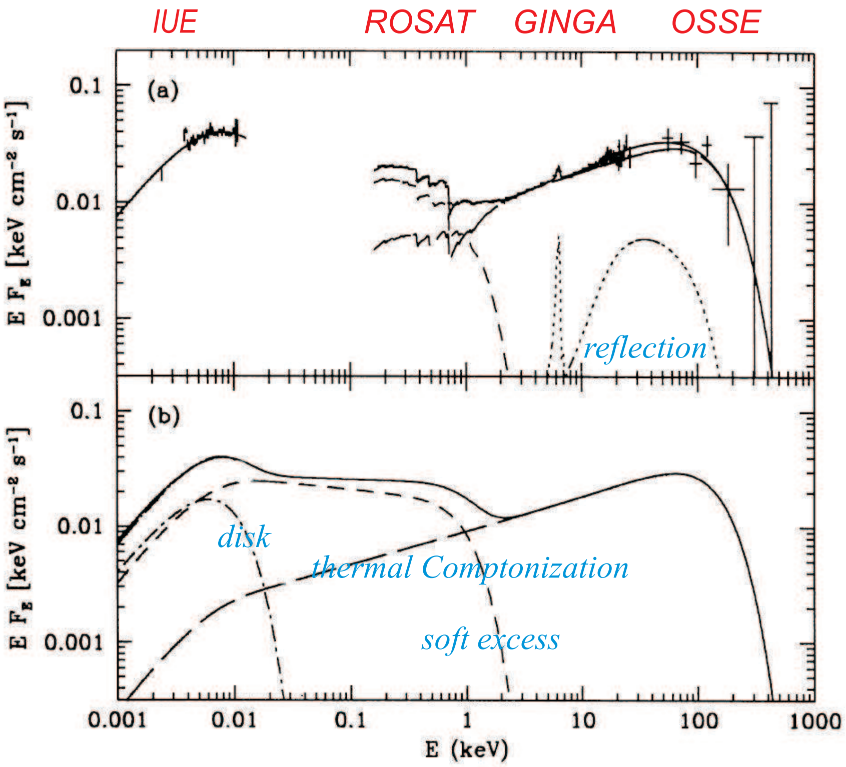

Figure 1.8: *Upper panel:* Typical UV/X-ray/γ-ray spectrum of the Seyfert galaxy NGC 5548. The space observatories which acquired the data are indicated. See Appendix B for explanations of the acronyms. *Lower panel:* Model fits to the observations. The dot-dashed and short-dashed curves show the disk and the soft-excess components, respectively. The soft-excess component comes from optically thick Comptonization and dominates the spectrum from the optical/UV up to 1 keV. The long-dashed and dotted curves show the thermal Comptonization X-/γ-ray continuum and the reflection component, respectively. Adapted from Magdziarz et al. (1998).

the beginning of this section. If the cold disk is irradiated by X-rays from the corona, photoelectric absorption is followed by fluorescent emission from several atomic species (C, O, and Fe). The most prominent among these lines is Fe Kα at 6.4 keV, which is quite common in type 1 AGN (Mushotzky et al. 1995). The structure of Fe Kα can be very complex. Its asymmetric, broad structure, as well as its short variability time-scale points towards an origin in regions of large relativistic effects (estimated distance to the central engine of $< 20R_S$, e.g., Mushotzky et al. 1995). Moreover, the contributions to Fe K emission are also expected from reflection onto

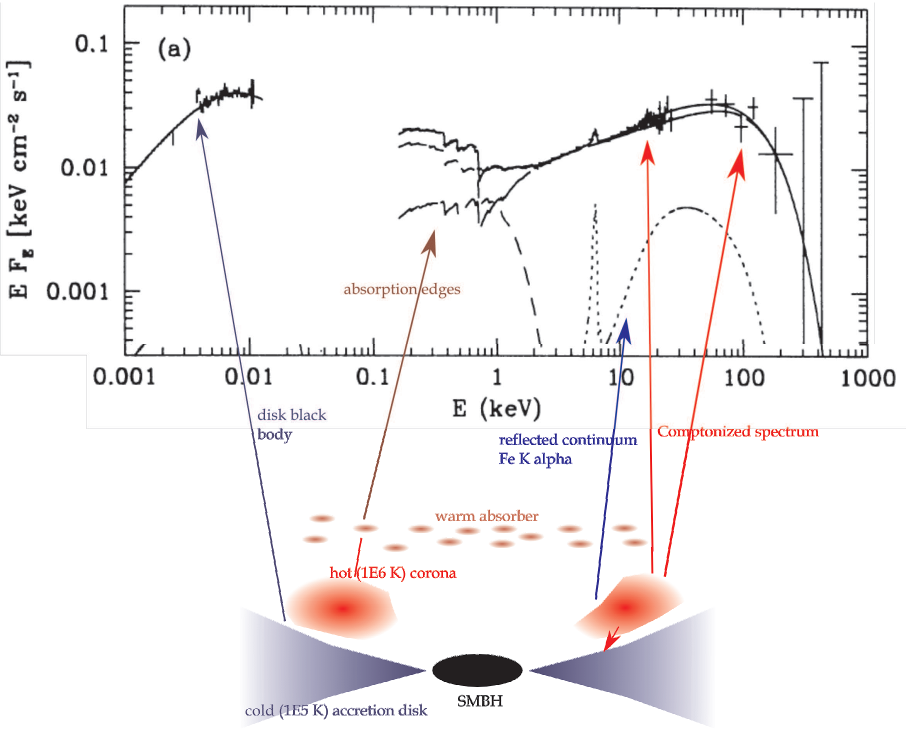

Figure 1.9: Depicting the regions generating the individual X-ray characteristics. The strength of these components varies, of course, from object to object on the basis of peculiarities and among different subclasses of AGN. The X-ray spectrum is the same as in Fig. 1.8. The lower part is a schematic representation of the geometrical configuration of the individual components of the nuclear environment.

the optically thick torus and onto BLR and NLR clouds. Hence, the final profile as well as the intensity of the line are both quite difficult to interpret.

The reflection component comes from the X-ray irradiated optically thick disk. Soft X-rays ($<$ 10 keV) are absorbed (see above), whereas harder photons ($>$30-40 keV) incident on the disk are backscattered via Compton scattering, transferring about 10% of their energy to the disk. This scattered emission results in a broad bump, peaking around 30 keV, beacause of the combination of Compton down-scattering at high energies and absorption at low energies (e.g., George & Fabian 1991). This bump has been observed with *Ginga* (Nandra & Pounds 1994) and BeppoSAX (Perola et al. 2002) thanks to their spectral coverage.

The high spectral resolution of Chandra and XMM-Newton allow us to study the physical properties of *warm absorbers*. These warm absorbers are related to absorption lines and some emission lines of H- or He-like ions. Line kinematics indicates that material is outflowing with velocities in the range $10 - 10^3$ km s^{-1} (McKernan et al. 2007). The column densities range from 10^{20} to 10^{23} cm^{-2}. From modelling, the most plausible location for this photoionized gas appears to be a stratified absorber with a range of ionization levels lying a few pc from the nucleus and extending possibly up to the NLR (Krolik & Kriss 2001). In some cases the outflow rates appear to exceed the accretion rate of the SMBH (McKernan et al. 2007), but it is currently not clear, whether the outflow knows about the accretion onto the SMBH or vice versa. Studies of warm absorbers can thereby provide constraints on parameters such as the geometry and the physical conditions of the innermost regions of AGN.

There are currently two interpretations of the *soft-excess*. On the one hand, it can just be the Comptonized hard tail of the Big Blue Bump (e.g., Gondhalekar et al. 1996), i.e. thermal radiation from the accretion disk. On the other hand, part of the soft-excess can result from down-scattering of hard X-ray photons in the inner parts of the accretion disk (Pounds & Reeves 2002). Probably it is a mixture of both.

The X-ray properties discussed so far are valid especially for type-1 AGN (Seyferts and QSOs). The situation is different when studying type-2 AGN. According to the unified scheme, these AGN are viewed edge on, i.e. along lines of sight through some sort of obscuring torus. These sources show hard X-ray spectra, with the soft part almost completely extinguished. It turns out that most AGN in the local Universe, in fact, are obscured in X-rays by large amounts of gas and dust. Since UV/visible[8] wavelengths are very susceptible to dust absorption, part of the X-ray obscured AGN are missed in traditional AGN selection schemes. This has profound implications on models of SMBH growth and galaxy evolution as will be discussed in the following paragraph.

1.3.2 The cosmic X-ray background

Since its discovery in 1962 in a rocket flight (Giacconi et al. 1962) the cosmic X-ray background (CXRB, Fig. 1.10) below energies of 30 keV has almost completely (~ 90%) been resolved into discrete sources, down to limiting fluxes of about 10^{-15} erg s^{-1} (0.5-10 keV) (see, e.g., the recent review by Brandt & Hasinger 2005). Deep X-ray surveys have been

---

[8] Throughout this work *visible* and *optical* refer to the visible wavelength regime of the electromagnetic spectrum and are used synonymously.

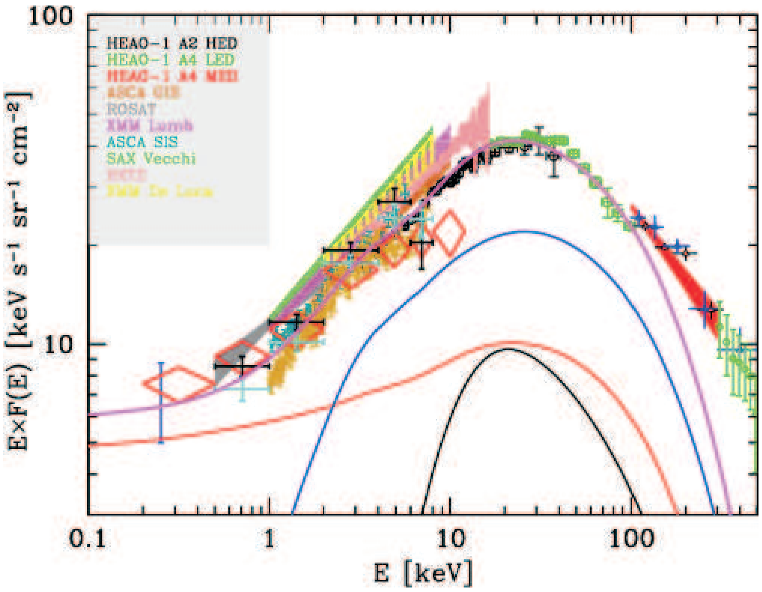

Figure 1.10: The spectrum of the CXRB measured by a number of missions, indicated in the legend. The contribution of unobscured AGN, compton-thin AGN, compton-thick AGN, and total AGN plus galaxy cluster are shown in red, blue, black, and magenta curves. From Gilli et al. (2007).

carried out with Chandra (Chandra deep field north/south, CDFN/S) and with XMM-Newton (Lockman hole). Extensive multi-wavelength follow-up work is under way or completed (e.g., Mushotzky et al. 2000; Hasinger et al. 2001; Barger et al. 2003; Bauer et al. 2004; Treister et al. 2004). The current missions have high positional accuracy (Chandra $< 1''$, XMM-Newton $< 3''$). This is a major improvement, concerning source matching and classification, compared to previous surveys like the ROSAT all sky survey (RASS), which resulted in source position uncertainties of $\lesssim 60''$ (see Chap. 2 for a discussion of RASS source matching).

Figure 1.11 shows counts of soft X-ray sources as function of soft X-ray flux. Most ($\gtrsim 70\%$) of the X-ray objects turn out to be AGN and only a minor fraction can be attributed to star-forming galaxies ($\sim 3\%$) (Bauer et al. 2004). Proceeding to higher energies (10 keV) the resolved fraction of the background drops to about 70% (Worsley et al. 2004). The spectral region between 10 and 100 keV, where most of the CXRB energy density is found, is only resolved on a few percent level (cf Brandt & Hasinger 2005) and only new space missions like Suzaku (Mitsuda et al. 2004) will be able

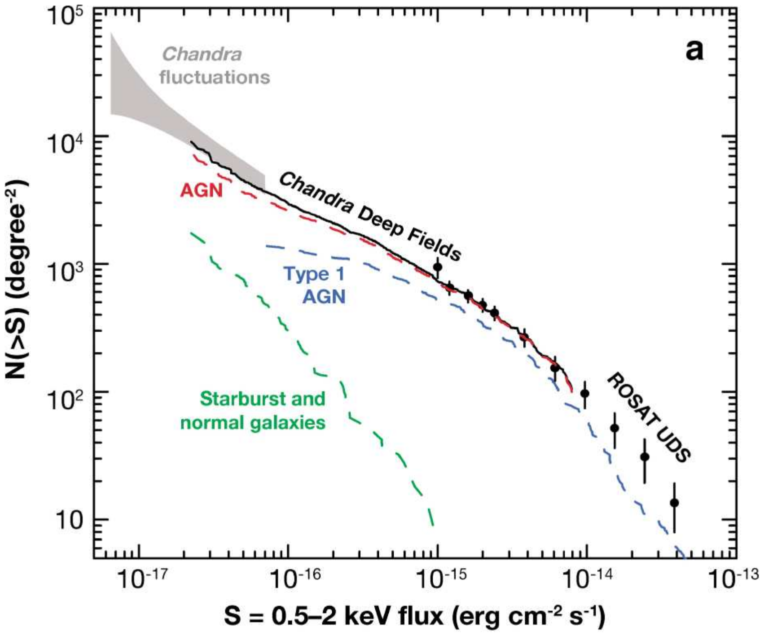

Figure 1.11: Number of sources, $N(> S)$, brighter than given flux, S, for the 0.5-2 keV band. The black circles are from ROSAT studies of the Lockman hole, the solid black curve is from deep Chandra deep fields study of Bauer et al. (2004), and the gray "fish" region shows the CDFN fluctuation analysis of Miyaji & Griffiths (2002). The dashed curves show number counts for AGN, type-1 AGN, and starburst/normal galaxies from Bauer et al. (2004) and Hasinger et al. (2005). From Brandt & Hasinger (2005).

to further resolve the very hard XRB. The sky density of X-ray detected AGN is remarkably large ($\approx$ 7200 deg^{-2}) and is a factor of 10-20 higher than that found in the deepest visible wavelengths surveys (e.g., Wolf et al. 2003). This observation stems from the effectiveness of finding AGN at X-ray wavelengths (reduced absorption bias and minimal dilution by host-galaxy light).

On the other hand, classification of X-ray sources by follow-up optical observations is challenging, since the counterparts are just too faint at visible wavelengths (e.g., Rigby et al. 2006). This fact gives rise to redshift completeness of only 50-70% of spectroscopic follow-up of deep X-ray surveys. Another complication concerning AGN classification, is the dilution of faint AGN signatures by host galaxy light contamination (Moran et al. 2002). But the results of multi-wavelength observations of X-ray AGN, furthermore, dispute the traditional unified AGN model, as not all X-ray obscured AGN have type-2 optical spectra and not all AGN with type-1 optical spectra are X-ray un-obscured (cf Matt 2002). Further observations and modelling of the central engine and its environment are needed. Five basic types of sources are found:

Unobscured AGN: Blue, broad-line AGN that do not show signs of obscuration at either X-ray or optical/UV wavelengths. They cover a broad range in redshifts ($z \approx 0 - 5$) and they comprise a significant fraction of the brightest X-ray sources (e.g., Szokoly et al. 2004). At redshifts higher than 1.5, un-obscured AGN make up a substantial fraction of all X-ray sources with spectroscopic identifications, which in part is due to their high luminosity.

Obscured AGN with clear optical/UV Seyfert signatures: Some objects show evidence for obscuration but still show Seyfert characteristics in their rest-frame optical/UV spectra. These sources can have both type-1 and type-2 optical/UV classifications (e.g. Matt 2002). Most of these objects have $z \lesssim 1.5$.

Optically faint X-ray sources: Optical magnitudes of the counterparts are typically $R \gtrsim 25$ and usually cannot be identified spectroscopically. Many, however, appear to be luminous, obscured AGN at $z \approx 1 - 4$, when considering their multiwavelength and spectroscopic properties (e.g., Treister et al. 2004; Mainieri et al. 2005; Rigby et al. 2006). Thus, part of these sources just belong to the previous class of objects, reaching higher redshifts and fainter fluxes. Though, some X-ray sources have no optical counterpart in the deepest images and are termed extreme X-ray/optical ratio sources (EXOs). Counterpart are often detected in NIR images (Koekemoer et al. 2004). EXOs can be explained as $z \approx 1.5 - 5$ obscured AGN in dusty or evolved hosts, although a minority may lie at $z > 7$ where the intergalactic medium absorbs essentially all of the observed-frame optical emission.

X-ray bright optically normal galaxies (XBONGs): XBONGs are observed to be early-type galaxies at $z < 1$ that have X-ray luminosities (10^{41-43} erg s^{-1}), X-ray spectral shapes, and X-ray-to-optical flux ratios, suggesting Seyfert activity of moderate strength (Comastri et al. 2002). Some XBONGs have X-ray spectra suggesting the presence of obscuration, whereas others do not (Severgnini et al. 2003). Therefore, their nature remains somewhat mysterious. Many, perhaps most may just be normal Seyferts where dilution by host-galaxy light prevents optical detection of the active nucleus (Georgantopoulos & Georgakakis 2005).A few of these objects appear to be true XBONGs and it may be that they are (a) AGN with inner radiatively inefficient accretion flows (Yuan & Narayan 2004), (b) AGN that suffer from heavy obscuration covering a larger solid angle, such that optical emission-line and ionizing radiation cannot escape the nuclear region (Matt 2002), or (c) BL Lac-like objects (Brusa et al. 2003).

The CXRB, of course, contains also non-AGN like objects:

Starburst and normal galaxies: At the faintest measured X-flux levels (0.5-2 keV, 5×10^{-16} erg s^{-1} cm^{-2}), a significant and rising fraction (30-40%) of the detected sources appears to be starburst and normal galaxies at $z \approx 0.1 - 1.5$ (e.g., Bauer et al. 2004, and see below).

Other sources are related to groups/clusters of galaxies, as well as stars in our Galaxy. But this will not be discussed here any further; instead please refer to the review by Brandt & Hasinger (2005).

Morphological studies show that X-ray selected AGN are generally hosted by galaxies with significant bulge components, and that they do not show evidence for enhanced interaction activity relative to normal field galaxies (e.g. Grogin et al. 2005; Pierce et al. 2007). The rest-frame optical colors of many of the non-broad-line[9] AGN are those of evolved, bulge-dominated galaxies, and there is little evolution of these colors from $z \approx 0 - 2$ (Szokoly et al. 2004). Additionally, most AGN in the deep X-ray surveys are radio quiet (Bauer et al. 2002).

1.3.3 Connecting the CXRB with evolutionary schemes of SMBHs and galaxies

From an optical perspective, numerous studies of Seyferts and QSOs across cosmic time have revealed a dramatic increase in the comoving space density of AGN until $z \approx 2$ and a subsequent decline towards higher redshifts (e.g., Fan et al. 2001; Wolf et al. 2003; Croom et al. 2004). There is some resemblance with the cosmic star-formation density, supporting the idea about an intimate link between galaxy evolution and SMBH feeding. During the epoch of maximum QSO activity also most of the star formation occurred, although it is not clear whether the SFRs are declining towards redshifts $z > 2$ (cf Sec. 1.2).

The LFs of these optically selected AGN can be plausibly explained by pure luminosity evolution (PLE)[10]. For X-ray selected AGN, which

---

[9] For type-2 AGN it can be assumed that the stellar dominates the non-stellar emission and therefore provides information on the host galaxy.

[10] In PLE the LF is kept constant, both in shape and numbers, but allows a shift of the luminosity coordinate as a function of redshift; $\Phi(M_B + L(z), z) = \Phi(M_B, z = 0)$. This applies to an assembly of objects of different luminosities that are all experiencing the same

probe the AGN LF further down at fainter fluxes, the situation is different. At high X-ray luminosities a strong positive evolution is seen from $z = 0 - 2$, whereas at lower luminosities the evolution is rather mild (cf Fig. 7 in Brandt & Hasinger 2005). Such evolution can only be explained by luminosity-dependent density evolution (LDDE; Barger et al. 2005; Hasinger et al. 2005, and references therein). The pure density evolution (PDE)[11] is furthermore dependent on the luminosity of the sources, i.e. a combination of PLE and PDE. The comoving space density of X-ray selected AGN exhibits different evolution for different X-ray luminosities. Figure 1.12 shows the evolution of the space densities of soft X-ray AGN. The AGN peak density moves to lower redshifts with decreasing luminosity and the rate of evolution from the local Universe to the peak redshift is slower for less-luminous AGN. It appears that SMBHs grow in an *anti-hierarchical* way. While $10^{7.5-9} M_\odot$ SMBHs in rare, luminous AGN could grow rapidly at $z \approx 1 - 3$, the $10^{6-7.5} M_\odot$ SMBHs in more common, less luminous AGN had to wait longer to grow ($z \lesssim 1.5$) (cf Fig. 12 of Hasinger et al. 2005).

One can use the X-ray LF as a direct measure of the accreted masses of remnant SMBHs in galaxy centers and thereby study the apparent anti-hierarchical growth. Soltan (1982) assumed that the AGN accumulate their mass during their lifetime T. Yet, the accretion process works with an efficiency κ. Then the accumulated mass calculates as

$$m = c^{-2} \kappa^{-1} L T, \tag{1.1}$$

where L is the luminosity of the AGN. Using a bolometric correction in order to translate band-pass-limited observations to total luminosity, the X-ray number counts can be related to the accreted mass density. Important to note at this point is that although X-rays are much less influenced by absorption, the obscured growth in Compton-thick AGN has to be taken into account. Best current estimates of the bolometric correction and of the fraction of missed obscured AGN leads to a SMBH mass density of $\rho_\bullet \approx 3.5\kappa^{-1} \times 10^5 M_\odot$ Mpc^{-3} (Marconi et al. 2004). The efficiency κ is estimated to lie in the range 0.054-0.36, depending on the nature of the SMBH. From the correlation of the bulge-stellar velocity dispersion with the mass of the central SMBH (see first paragraphs of this Chapter) a complementary estimate of the mass density can be made. Several authors find values consistent with the above stated value, if choosing a 10% mass-to-energy-

---

evolution $L(z)$ in their luminosities.

[11] In PDE the LF is only dependent on the density of sources at z; $\Phi(M_B, z) = \Phi(M_B, z = 0)\rho(z)$

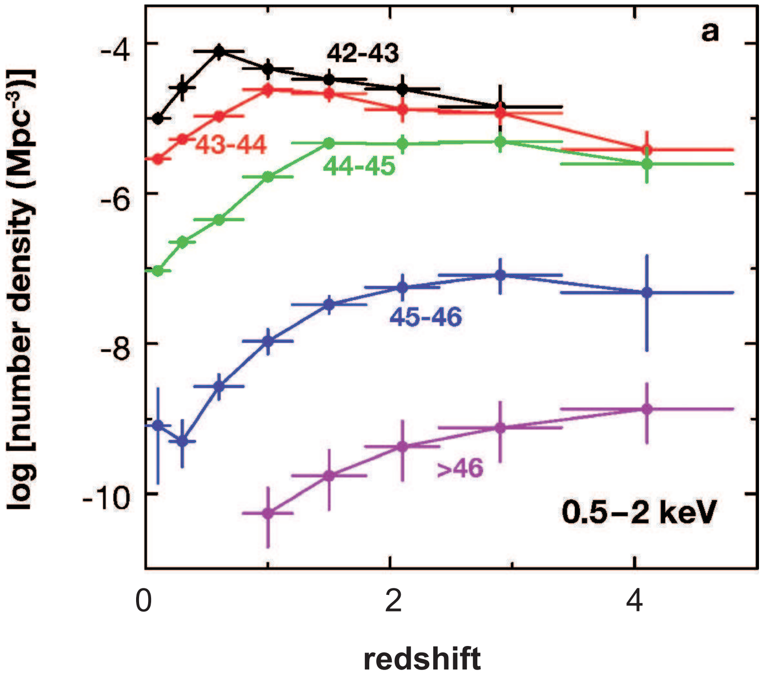

Figure 1.12: The comoving space density of AGN selected in the 0.5-2 keV band as a function of redshift. Results are shown for five luminosity ranges (their logarithmic values are indicated). Adapted from Brandt & Hasinger (2005).

conversion efficiency. The distribution function of local SMBHs (not neccessarily in an active state) has been demonstrated to be explainable with the observed accretion (Marconi et al. 2004).

The AGN found in X-ray surveys up to $z \sim 4$ are 10-30 times fainter than the QSOs found in optical surveys. Such moderate luminosity AGN are more numerous and thus more representative of the AGN population than the rare, highly luminous QSOs. Optical follow-up of high-z X-ray sources is very difficult, as already mentioned before. Still, the AGN sky density of X-ray selected sources is about 50-100 times as large as that of optically selected QSOs ($\rho = 0.12$ deg^{-2} for $z = 4.5.4$ selected SDSS QSOs; Schneider et al. 2003). Combining optical and X-ray observations shows that $z > 4$ AGN span a broad luminosity range and are accreting in basically the same mode as AGN in the local Universe.

In an effort to constrain even lower luminous $z > 4$ AGN, X-ray source-stacking techniques have been applied on $z > 4$ LBGs (Lehmer et al. 2005).

The results are that these sources are dominated by stellar processes. No AGN emission has clearly been detected. All these results indicate that the AGN contribution to the reionization phase[12] is rather low (Dijkstra et al. 2004). The deep X-ray surveys are also used to study the X-ray (and perhaps AGN) properties of distant infrared and sub-mm galaxies. In these galaxies much if not most of the cosmic star formation has taken place. At such wavelengths, AGN are expected to be an important contributor to the emission budget, owing to the reprocessing of their UV emission by the omnipresent gas and dust in these galaxies. As indicated above, however, the current knowledge points to a picture, in which massive star formation dominates over Seyfert activity. In the IR band for example, AGN contribute only 3-5% to the total background, the rest comes from starburst and normal galaxies (e.g., Silva et al. 2004). The situation has to be adjusted if a large number of obscured and hence IR-bright AGN is missed. But still after including Compton-thick AGN, active galaxies should represent only a minority of contributors to the IR background.

The sub-mm galaxies have redshifts between $z = 1.5$ and 3 and exhibit enormous SFRs of the order of $\sim 1000 M_\odot \, \mathrm{yr}^{-1}$ (e.g., Chapman et al. 2003). The optical counterparts are extremely faint, due to the large amounts of dust and gas. Thus, only X-ray observations can tell us about the AGN content in this class of objects. In the CDF-N about 15% of the sub-mm galaxies now have X-ray detections and the majority of the latter appear to contain obscured, moderate luminous AGN ($\sim$ 40% of the sub-mm population is expected to show Seyfert characteristics but only 10-20% of the bolometric luminosity can be attributed to the accretion process; Alexander et al. 2005). In sub-mm galaxies both, the SMBH and the stellar host are growing during the observed phase of intense star formation.

Despite the observational success, most of the sources in the CXRB have yet to be detected at optical/infrared wavelentgths. These are most probably distant starburts and normal galaxies. The processes of producing X-rays in these objects are X-ray binaries, supernova remnants, starburst-driven outflows, and hot gas. At the lowest X-ray fluxes these galaxies constitute a rising fraction (30-40%) and they will eventually dominate the source counts at soft X-ray flux levels around 10^{-18} erg $\mathrm{s}^{-1}\mathrm{cm}^{-2}$. X-rays from inactive galaxies can therefore be used as an independent method to trace the cosmic star formation history (e.g., Bauer et al. 2002). Derived SFRs agree quite well with those from optical, IR, and radio measurements.

---

[12] Reionization is the epoch after the Big Bang and the following Dark Ages, in which the first stars and AGN begin to ionize again the cooled neutral matter in the young Universe.

SFRs of distant X-ray galaxies are remarkably high $\approx 10 - 300\ M_\odot\ \mathrm{yr}^{-1}$ (Alexander et al. 2002). Therefore they are members of the strongly evolving, dusty starburst population responsible for creating much of the IR background.

We have seen that astronomers have learned quite a lot on the formation and evolution of galaxies and AGN. There are, however, several key issues that require further observational and theoretical studies. What are the physical reasons for the apparent downsizing in SMBH activity and mass, which obviously contradict the hierarchical scheme? A similar trend is observed in the assembly of inactive, i.e. normal galaxies (cf Sec. 1.2 and Cowie et al. 1996). Is there a connection between these two phenomena, as suggested by the bulge/SMBH correlation? Add to this the finding that high X-ray luminosities seem to favor BLAGN, whereas lower X-ray luminosities favor NLAGN (Steffen et al. 2003)[13]. Is the accretion efficiency changing over cosmic time? Only in the most recent models of coupled spheroid and SMBH growth the feedback from the active nucleus has been included in a rudimentary way (e.g., Scannapieco et al. 2005; Bower et al. 2006). Outflows and radiation pressure will have a profound impact on the circumnuclear star formation, like the quenching seen in the most massive QSOs, i.e. massive elliptical galaxies (Schawinski et al. 2006). However, these models await specific observations, especially at lower redshifts, since only there the resolved physical scales will allow to study the impact of star formation and nuclear outflows/radiation field on the circumnuclear environment in great detail. Adaptive-optics assisted, ground-based observations will allow us to study the circumnuclear environment at higher redshifts at high angular resolution and the steep gradients in comoving AGN space density and star formation history promise to find new insights in these important (evolutionary) questions. This will be discussed further in the following chapters.

---

[13] Sometimes referred to as *Steffen effect* (Barger et al. 2005).

CHAPTER 2

X-raying AGN suitable for adaptive optics follow up

Based on work about to be submitted to A&A and published in Zuther et al. (2004b, 2005a,b, 2006)

In this chapter, the need for high angular resolution studies of AGN host galaxy properties will be discussed, followed by an introduction to the technology (adaptive optics), with which high angular resolution can be achieved at ground-based telescopes. The basic equation, driving the need for larger telescopes, is the angular resolution, θ, of a circular aperture of diameter D, which is given by

$$\theta[\text{radian}] = 1.2\frac{\lambda}{D}. \tag{2.1}$$

Then, the methods to create a sample of AGN, suitable for such studies are presented. This sample is based on a cross-matching of the SDSS and the ROSAT All Sky Survey (RASS) databases. In the development process, search and visualization tools, provided by the Virtual Observatory (VO), are used. Subsequently, the sample and its detailed optical and X-ray properties are presented. Additional radio 21 cm and near-infrared data of some sample objects will be included to complement the former properties in order to get deeper insights into the physical nature of these objects.

2.1 On to the host galaxies of X-ray bright AGN

The previous chapter established a number of open astrophysical questions. Joining in, are observational challenges that are complicating efforts to resolve these questions. Since the apparent angular size of galaxies becomes smaller and at the same time the contrast between an AGN and its host becomes larger with redshift (Fig. 2.1), only space based (e.g., *Hubble Space Telescope*, HST) or adaptive optics (AO) assisted observations from

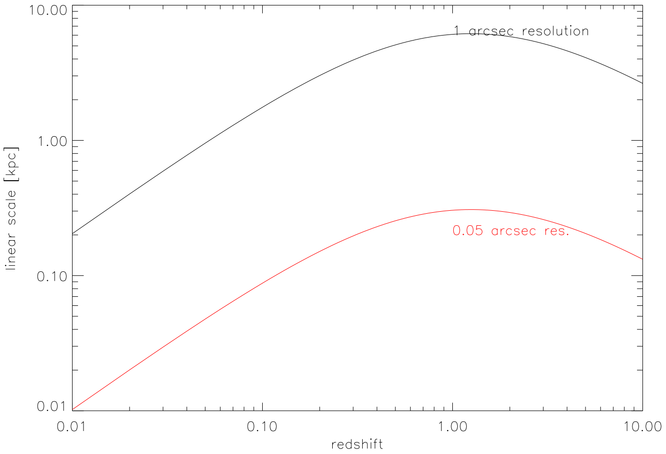

Figure 2.1: The angular diameter distance as a function of redshift, shown for two apparent angular measures. The black curve represents seeing-limited conditions and the red curve represents the diffraction limit of an 8 m class telescope at 2.2 μm. There is a significant gain in exploiting the diffraction limit of large telescopes as compared to the seeing-limited case.

the ground provide the levers to resolve the host galaxy structure across cosmological distances. Current seeing-limited studies (see Sec. 2.2 for an introduction to the terms AO and seeing)[1] are confined to galaxies in our backyard in order to exploit their effective resolving power. The major advantages of ground-based, AO-assisted observations compared to HST ones are the larger light collecting area (8-10 m instead of 2.4 m diameter) and the continuing replacement with state-of-the-art instrumentation. Current facilities offer AO-assisted integral field spectroscopy like SINFONI at the ESO-VLT, or OSIRIS at Keck and very recently the largest telescopes start to offer laser-guided AO. The latter technique overcomes the limitations of AO with natural guide stars (NGS) imposed by the small number of sufficiently bright NGS close to the object of scientific interest (see Sec. 2.2.3). NGS AO, however, has become standard observing mode in the meantime and the NGS can also be used as a tip-tilt star.

Systematic studies of the host galaxies of X-ray selected AGN are rare, one reason being the observational challenges mentioned above. Two recent studies address this topic. Schade et al. (2000) studied the optical

---

[1] The turbulent atmosphere reduces the possible angular resolution of large (> 5 m) telescopes effectively to that of a ~1 m telescope.

morphology of 76 low-redshift ($z < 0.15$), hard X-ray AGN with the HST. The primary result is that the observed AGN are hosted by earlier type galaxies than those of normal field galaxies. Based on the AEGIS[2] dataset, Pierce et al. (2007) come to a similar conclusion for 94 higher redshift ($0.2 < z < 1.2$) X-ray AGN. X-ray selected AGN reside in early-type galaxies in more than 50% of the cases. In contrast to this, in the case of infrared AGN selection, the hosts show no preference towards early types. The authors, furthermore, find that X-ray selected AGN hosts are found to be in close pairs more often than the field galaxy population by a factor of about 3. The morphologies, though, resemble those of undisturbed early-type galaxies. Thus, the activation mechanism for AGN activity remains unknown.

Sensitive, high angular resolution NIR studies can help resolving these obstacles. It follows a list of some starting points:

- **Obtain highest resolution images:** What is the detailed structure of the host galaxies? How dominant are the bulges? Do the nuclei stand out as compact objects to allow a clear separation from the central bulge? High resolution images, furthermore, allow a direct comparison of the structural and evolutionary properties of the more distant objects with those of closer ones (well-studied, seeing-limited) at the same spatial resolution.

- **NIR color information on the host galaxies:** The JHK host colors will allow the amount and distribution of extinction and the contribution of warm/hot dust to the NIR emission to be determined. NIR colors are more sensitive to higher amounts of extinction (by about a factor of 30 compared to visible wavelengths) and can be obtained at $\sim 0''.1$ resolution with 8 m-class telescopes. In these images one is able to identify dust lanes (along possible nuclear bars) and starburst rings, or asymmetric patchy distributions that might indicate disturbed systems. In addition, the colors provide important complementary information for stellar population synthesis. The NIR data on the hosts can also be efficiently combined with data from other wavelengths and thereby help improving the astrophysical characterization.

- **Nuclear excitation:** One goal is to study the effect of the intense

---

[2] All-wavelength Extended Growth strip International Survey is targeted on a special area of the sky, called the Extended Groth Strip that has been observed with the world's most powerful telescopes on the ground and in space, from X-rays to radio waves.

UV/X-ray radiation on the nuclear and bulge environment (cf Begelman 1985, 2004). For targets presented in the following sections, a variety of Brackett and Paschen series hydrogen recombination lines, [Fe II] lines, and the [SiVI] coronal line are available. Additionally, several thermally and/or fluorescently excited H_2(1-0) lines are in reach. Extended fluorescent H_2 line emission may arise if the nuclear radiation field impinges on the central molecular gas or if extended massive star formation is occurring. These effects have not yet been analyzed for the closest luminous X-ray AGN. An elaborate example can be found in Chap. 3.

- **Star formation:** The mass-dominating older stellar populations can be traced with absorption features like [SiI] λ1.589 μm, as well as, CO(6-3) λ1.63 μm and CO(2-0) λ2.29 μm (cf Origlia et al. 1993; Origlia & Oliva 2000; Fischer et al. 2006, and Sec. 3.4.3). Combined with information on hydrogen recombination lines and continuum colors, information on the stellar populations and implications for star formation in the circumnuclear environment can be discussed.

- **Kinematical information:** Spatially resolved spectroscopy (e.g., with SINFONI) allows for the study studies of the stellar and gaseous dynamics, which can be used to estimate host masses and possibly black hole masses (e.g., Davies et al. 2006). The velocity fields can also be used to investigate the transport of matter throughout the circumnuclear region (e.g., Kronberger et al. 2007). Are there traces of instabilities like bars or nuclear spirals (cf Sec. 1.1)?

After accomplishing the above goals, one will be in a position to derive and compare the circumnuclear host properties (morphology, kinematics, chemical composition) of bright X-ray AGN to those of optically or infrared selected QSOs (Bahcall et al. 1997; McLeod & McLeod 2001; Tacconi et al. 2002; Dunlop et al. 2003), ULIRGs (Tacconi et al. 2002), and ellipticals composing the fundamental plane (e.g., Kormendy & Djorgovski 1989). Then it might be possible to answer the question of whether nuclear bars and/or circumnuclear star forming rings are common in these objects or not of importance at all. With this work, one can contribute to the question of what the AGN parent population of X-ray bright AGN is: optically/UV-bright QSOs, low-z QSOs/radio galaxies or ULIRGs?

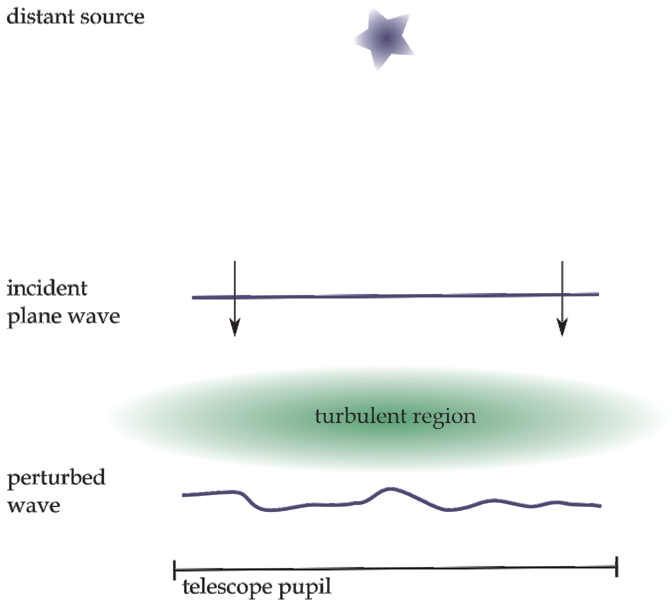

Figure 2.2: A schematic view of the influence of the turbulent atmosphere on a plane wavefront from an astronomical source. The plane wave incident onto the telescope pupil is distorted by the refractive index variations of the atmosphere..

2.2 Reaching high angular resolution at NIR wavelengths

In this section the principles of adaptive optics and hardware will be presented together with some remarks on recent implementations. In depth reviews are given by Beckers (1993), Roggemann et al. (1997), and Roddier (1999).

Significant advances have been made over the past two decades regarding the quality of the images and spectra recorded from the radiation of astronomical sources. During the passage of the light through the Earth's atmosphere, turbulence produce variations in the air refractive index that distort the incoming plane wave fronts from their straight propagation (usually referred to as *seeing*; see left panel of Fig. 2.2). The distortions blur out any structure in objects which have angular scales of less than about an arcsecond, which significantly affects the image quality of ground-based telescopes (see Fig. 2.2). This degradation can be counteracted by furnishing telescopes with *active optical elements* like deformable mirrors that

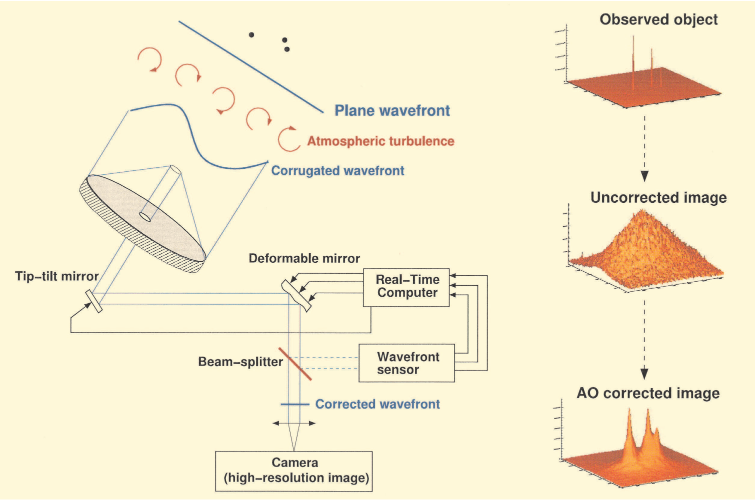

Figure 2.3: Principle of an AO system that compensates atmospheric distortions. Adopted from the ESO NACO user manual. The panels on the right show simulated images of a point source. The upper frame displays the speckle pattern (the light that strikes the mirror is in phase over only small regions of the pupil, causing the instantaneous image of a point source to appear as a series of speckles) of a short-time exposure, the middle frame shows the smeared PSF after a long exposure and the bottom right frame the diffraction limited PSF (without seeing or with AO correction).

compensate for the motions of the atmosphere and thereby reduce the distortions. Figure 2.3 displays a schematic representation of such a system. The shape of the wave fronts after passage through the atmosphere and reflection of the deformable mirror (DM) is measured by a *wave-front sensor* (WFS), which delivers the signals necessary to drive the correcting elements of the DM. Such systems, which provide a real-time compensation of the wave-front distortions, are called *adaptive optics* (AO) systems. The use of AO was first proposed by Babcock (1953).

From an engineering point-of-view an AO system can be defined as a multi-variable servo-loop. It is made of a sensor, the WFS, a control device, the real-time computer (RTC), and a compensating element, the DM. The goal of this servo is to compensate for an incoming, distorted optical wave front. It is designed to minimize the residual phase variance in the imaging path. The input and output of this servo are the wave front phase perturbations and the residual phase after correction, respectively.

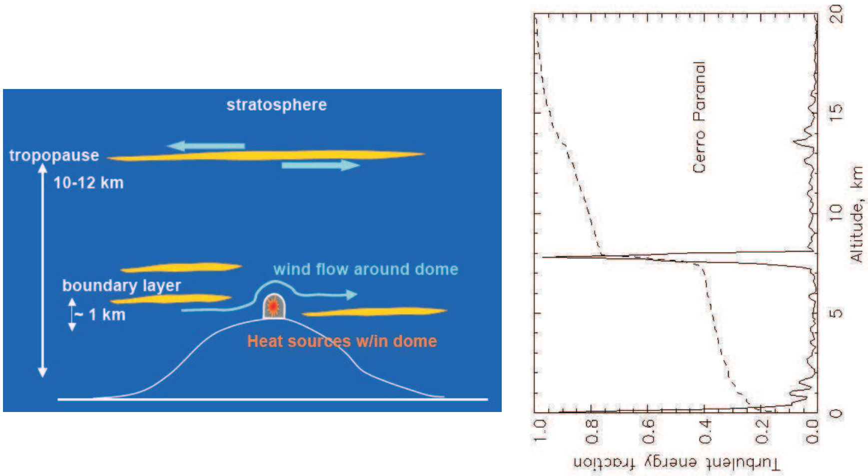

Figure 2.4: *Left panel:* Schematic representation of the whereabouts of sources of seeing. Courtesy of Claire Max (UC Santa Cruz). *Right panel:* The refractive index structure function C_n^2 as function of height above sea level (solid curve). Two maxima are apparent; one at the ground layer and one at a height of about 5 km. The dashed curve shows the cumulative fraction of the turbulence up to the height h. One can see that 50% of the total turbulence is created at altitudes below 8 km. Besides the two global sources for atmospheric turbulence one has to take local seeing into account, which can be generated, e.g., by the telescope dome. Courtesy of "Adaptive Optics Tutorial" by Andrei Tokovinin.

2.2.1 Atmospheric Turbulence and image formation

At optical wavelength, the angular resolution of all but the smallest telescopes is limited by the Earth's atmosphere, which gives rise to the blurring of images called *seeing*. Ideally, the image of a point-like source in the focal plane of a telescope should be a classical Airy diffraction pattern with a strong central peak and an angular width of about λ/D. In practice, the time-averaged image of such a source resembles a 2d Gaussian distribution. The full-width-half maximum (FWHM) of this distribution is usually taken as a measure of seeing quality. The quality of the produced image may also be described by its *Strehl ratio* (SR), which is the ratio of its intensity on axis to that which would be produced if there were no aberrations.

But what is causing the wave front errors? Electromagnetic waves are described by means of a complex number Ψ, called the complex amplitude. It is defined as

$$\Psi = A \exp(\mathrm{i}\varphi), \tag{2.2}$$

where A represents the amplitude and φ the phase of the field fluctuation. The surface over which φ takes the same value is called wave-front surface. Before entering the atmosphere, light from very distant astronomical sources forms plane waves. Inside the atmosphere, the speed of light will vary as the inverse of the index of refraction, and this will corrugate the wave-front surfaces. Refractive index variations arise from turbulence induced density variations in the air. This turbulence can be described in the framework laid out by Tatarski (1961), based on the work of Kolmogorov (cf Raichoudhuri 1998). In this theory kinetic energy is fed into the atmosphere at a large characteristic scale L_0, called the *outer scale* of turbulence. The energy is transported to smaller and smaller lossless eddies until finally the scale size is too small that eddy energy is converted into heat. The small scale is called the *inner scale* of turbulence. A statistical description results in the *refractive-index structure function* $D_n(\boldsymbol{\rho})$, which gives the variance in refractive index between two points a distant $\boldsymbol{\rho}$ apart:

$$D_n(|\boldsymbol{\rho}|) = C_n^2|\boldsymbol{\rho}|^{2/3}, \tag{2.3}$$

where C_n^2 is the *refractive-index structure constant.* It is assumed that in stratified, plane parallel atmospheric layers C_n^2 depends only on the height h above the ground. As mentioned above, the refractive index variations introduce phase and amplitude variations on the incoming wave fronts. A measure of the strength of the phase distortion of the wave front between two points, $\boldsymbol{\rho}$ and $\boldsymbol{\rho} + \boldsymbol{\xi}$, is the *phase structure function*

$$D_\varphi(\boldsymbol{\xi}) =< |\varphi(\boldsymbol{x}) - \varphi(\boldsymbol{x} + \boldsymbol{\xi})|^2| > \tag{2.4}$$

In terms of the index structure function (Eq. 2.3) and integration along the line of sight, Eq. 2.4 becomes

$$D_\varphi(\boldsymbol{\xi}) = 6.88(\xi/r_0)^{5/3}, \tag{2.5}$$

where

$$r_0 = \left[0.423k^2(\cos\gamma)^{-1}\int C_n^2(h)\mathrm{d}h\right]^{-3/5} \tag{2.6}$$

is a length called the *Fried parameter* (Fried 1965) and describes the seeing at a particular wavelength. k is the wave number and γ the Zenith angle. According to Eq. 2.6, $r_0 \propto \lambda^{6/5}$. An interesting property of r_0 is that the root mean square (rms) phase distortion over a circular area of diameter r_0 is about 1 radian, i.e. the signal is still correlated. The region of positively correlated phase thus increases with increasing λ.

Now, one wants to correct the atmosphere induced distortions, i.e. phase and amplitude, with a segmented, deformable mirror. This so called *zonal correction*[3] requires controlling at least three actuators (piston, tip, and tilt) per segment. Then, the number N of independently controlled parameters is about $N \approx (D/r_s)^2$, where r_s is the mean actuator spacing. The resulting fitting error is

$$\sigma^2_{fit} \propto \left(\frac{D}{r_0}\right)^{5/3} N^{-5/6}. \tag{2.7}$$

Controlling is therefore easier at longer wavelengths.

The next question is, how fast one has to correct for the distortions? The basic idea is that the seeing (turbulence) cells move with a constant average speed $\bar{v}$ across the telescope aperture. The related variance is

$$\sigma^2_{time}(\tau) = 6.88(\bar{v}\tau/r_0)^{5/3}, \tag{2.8}$$

where τ describes the time lag between measurement and correction.

The next step is concerned with the image formation; i.e. one has to relate the wave-front phase in the telescope entrance-aperture plane and the distribution of intensity in the telescope focal plane. This is a non-linear relationship. Above, we have seen that the rms phase distortions are equal to $\sim$1 radian over a circular area of diameter r_0. Hence, there is little need to correct wave-front distortions on smaller scales. A telescope with diameter D contains $(D/r_0)^2$ such areas. This gives the order of magnitude for the number of parameters one needs to control. Bringing the fitting error down below 1 radian requires the control of at least

$$N_0 = 0.27(D/r_0)^2 \tag{2.9}$$

actuators. The corresponding fitting error is (cf Eq. 2.7)

$$\sigma^2_{fit} = (N_0/N)^{5/6}. \tag{2.10}$$

From the above time-lag argument one can calculate the acceptable time delay τ_0 for the control loop. For the rms error to be less than 1 radian the delay must be less than

$$\tau_0 = (6.88)^{-3/5}\, r_0/\bar{v} = 0.314\, r_0/\bar{v}, \tag{2.11}$$

---

[3] In the zonal representation of wave fronts, one makes use of an expansion of the atmospheric wave front in a series of orthogonal functions. Usually this is done, using *Zernike modes* (see, e.g., Chap. 3.2 of Roddier 1999). The first four Zernike modes are the widely known piston, tip/tilt, defocus, and astigmatism. Note that zonal representation and segmented mirrors are just one possibility of correction.

which is call the *Greenwood frequency* and the associated error calculates as

$$\sigma_{time}(\tau) = (\tau/\tau_0)^{5/3} \tag{2.12}$$

One can imagine a full aperture as an array of N small subapertures, each producing a complex amplitude Ψ_k in the telescope focal plane. The resulting amplitude is

$$\Psi = \sum_{k=1}^{N} \Psi_k \tag{2.13}$$

and the resulting intensity is

$$I = |\Psi|^2 = \sum_{k=1}^{N} |\Psi_k|^2 + \sum_{k\neq j} \sum_{j} \Psi_k \Psi_j^* \tag{2.14}$$

The intensity in the image plane is the sum of the intensities produced by each subaperture plus the sum of the interference terms produced by each pair of subapertures. Each interference term describes a fringe pattern, i.e. a sinusodial term called *Fourier components* with spatial frequency $\boldsymbol{f}[\text{radians}^{-1}] = \xi/\lambda$.

The image formed on the detector can now be represented by an optical transfer function $G(\boldsymbol{f})$. This transfer function is the product of two terms, the telescope transfer function $T(\boldsymbol{f})$(or autocorrelation function of the aperture transmission) and the atmospheric transfer function $A(\boldsymbol{f})$ (representing the turbulent atmosphere introducing random additive phase errors).

$$G(\boldsymbol{f}) = T(\boldsymbol{f})A(\boldsymbol{f}) \tag{2.15}$$

These transfer functions represent the weights of the Fourier components described above (cf Eq. 2.14). The Fourier transform of the aperture autocorrelation function describes the image of a point source produced by a perfect diffraction-limited telescope, or Airy disk. Its angular width is about λ/D. The Fourier components of the image of a long exposure suffer from additional attenuation in the presence of a turbulent atmosphere.

Large aperture telescopes are essentially turbulence limited. The Fourier transform of $A(\boldsymbol{f})$ is a good approximation of a turbulence-degraded image. It is almost a Gaussian with an angular width about λ/r_0. Under partial AO correction

$$A(\boldsymbol{f}) = \exp\left[-\frac{1}{2}D_\varphi(\lambda\boldsymbol{f})\right], \tag{2.16}$$

but D_φ is no longer given by Eq. 2.5. AO systems mostly compensate large scale wave-front distortions, which have the largest amplitudes. This has

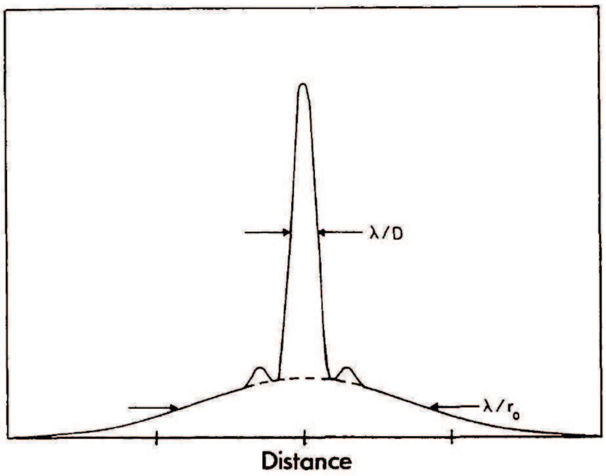

Figure 2.5: Structure of a partially corrected PSF. Courtesy of Beckers (1993). On top of the seeing-limited halo sits the diffraction-limited Airy.

the effect of leveling off the structure function at some level σ^2, where σ^2 is the variance of the remaining (uncorrelated) small scale wave-front distortions. The better the compensation, the smaller is σ^2. At low frequencies , $A(\boldsymbol{f})$ decreases as without compensation, converging to a constant

$$A(\infty) = \exp(-\sigma^2) \tag{2.17}$$

Therefore, $A(\boldsymbol{f})$ can be described as the sum of the above constant term plus a low frequency term. The point spread function (PSF), which is the Fourier transform of $G(\boldsymbol{f})$, is the sum of an Airy disk plus a halo due to light diffracted by the remaining small scale wave-front phase distortions (Fig. 2.5). Eq. 2.17 represents the fraction of light in the Airy disk. This is good measure of the quality of the compensation. The SR is the ratio of the maximum intensity in the point spread to that of in a theoretically perfect point source image. For large telescopes

$$R \approx \exp(-\sigma^2) \tag{2.18}$$

Thus, image quality degrades exponentially with the variance of the wave-front distortions. A variance of 1 radian corresponds to $R = 1/e = 0.37$. Image quality with higher SR is fairly good, whereas image quality for lower SR is poor, almost uncorrected. One can relate the SR to the number of correcting elements (Eq. 2.10)

$$R \approx \exp[-(N_0/N)^{5/6}] \tag{2.19}$$

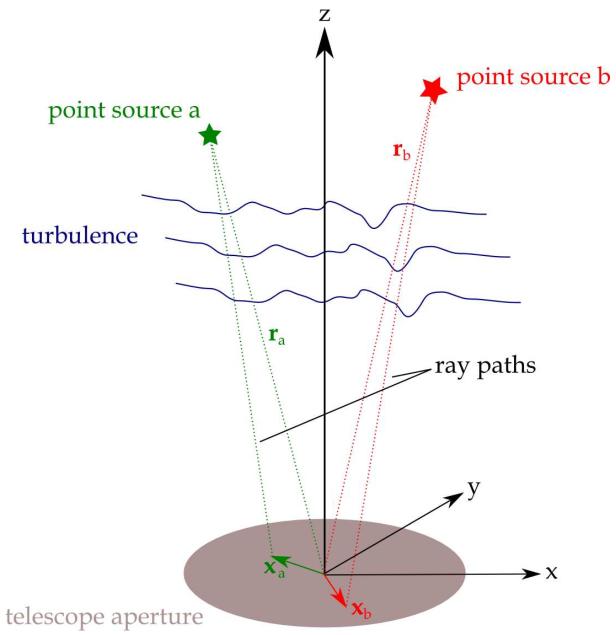

Figure 2.6: Geometry for deriving the anisoplanatic effects on the wave-front phase in the pupil of the imaging system. Ray paths are shown from the source points to two points in the pupil. In the case of AO imaging, one of the sources points models the guide star. The other source point the object being imaged. The question is, whether the two sources are close enough, so that the induced phase distortions on the wave fronts are still correlated.

and to the time delay in the servo loop

$$R \approx \exp[-(\tau/\tau_0)^{5/3}]. \tag{2.20}$$

Finally, one has to estimate the field of view over which the AO correction is acceptable. In this context it is important to note that the assessment of the wave-front distortions is usually done with a natural guide star (NGS), i.e. an external point-like object. Hence, the science target which is not on the optical axis of the NGS will not receive the best achieved AO correction. The reason for this is related to the height of turbulence layers. It occurs because of differences between wave fronts coming from different directions (Fig. 2.6). This effect is called *anisoplanicity*. As the angular distance θ between science target and NGS increases, image quality decreases. For a single turbulent layer at height $h/\cos\gamma$, the rms error σ^2_{aniso} on the wave front can be estimated from Eq. 2.5 by replacing ξ with $\theta h/\cos\gamma$. In practice, several turbulent layers contribute to image degradation. This motivates the approximation with a weighted average layer height $\bar{h}$ (Roddier & Roddier 1986). The anisoplanicity error can now be calculated as

$$\sigma^2_{aniso}(\theta) = 6.88 \left(\frac{\theta \bar{h}}{r_o \cos \gamma} \right)^{5/3} \tag{2.21}$$

What is the acceptable angular distance θ_0, for which the rms error is less than 1 radian?

$$\theta_0 = (6.88)^{-3/5} \frac{r_0 \cos \gamma}{\bar{h}} = 0.314 \frac{r_0 \cos \gamma}{\bar{h}} \tag{2.22}$$

This angular distance is called *isoplanatic angle*. The isoplanatic angle is proportional to $\lambda^{6/5}$, like the Fried parameter. Thus, the isoplanatic angle is larger for larger wavelengths. For example, assuming typical $r_0 = 20$ cm at $\lambda = 0.63\,\mu$m ($r_0 = 20(\lambda/0.63)^{6/5}$ cm), $\bar{h} = 1$ km, and observations at zenith ($\gamma = 0$), gives an isoplanatic angle of

$$\theta_0 = 22\overset{\prime\prime}{.}5 \left(\frac{\lambda}{\mu\mathrm{m}} \right)^{6/5} . \tag{2.23}$$

Thus $\theta_0 \approx 13''$ at R and $\approx 58''$ at K. The introduced error at θ_0 is

$$\sigma^2_{aniso} = (\theta/\theta_0)^{5/3} \tag{2.24}$$

θ_0 can also be related to the SR (Eq. 2.18)

$$R \propto \exp\left[-(\theta/\theta_0)^{5/3} \right] . \tag{2.25}$$

θ_0 is the angular distance from the guide star over which the Strehl ratio of a compensated image is divided by a factor e.

2.2.2 Assessing and correcting distorted wave fronts

Figure 2.3 shows a schematic representation of an AO system. The previous section already introduced the idea of wave-front sensing and correcting. In the following, some more details and possible realizations of such components are presented.

Wave-front sensing

The wave-front sensor is one of the most important components of any AO system. In order to assess the degree of wave-front phase and amplitude distortion measurements of the wave-front gradients (tilts) are used. Other

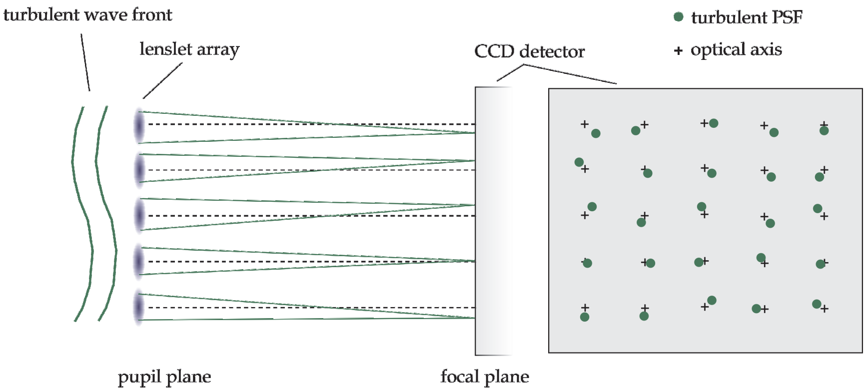

Figure 2.7: Schematics of the working principle of a Schack-Hartmann wavefront sensor.

methods use measurements of the curvature of the wavefronts (cf Beckers 1993, for further examples).

The simplicity of the *Shack-Hartmann* wave-front sensor has made it a popular choice (Fig. 2.7). An array of small lenslets is positioned in the image of the pupil. With this, an array of images of the guide star is produced whose positions are measured, in real time, to give the full wave-front tilt (in vector form) in the areas of the pupil covered by each lenslet. Without atmospheric turbulence, which corresponds to a flat wave front, the lenslets would focus the light of the guide star to an evenly spaced checkerboard array of spots on the camera. Turbulence introduces distortions on the flat wave front, such that the light is no longer focused to an evenly spaced array of spots, but to an irregular spacing. Due to the variability of turbulence the spots are "dancing" around on the CCD. By rapid measurement of the positions of the spots (see previous section for a discussion of the sampling frequency), the RTC can reconstruct the incident wave front and calculate the appropriate changes of the deformable mirror in order to compensate these distortions. The dimensions of the lenslets are often chosen to correspond approximately to r_0. For a perfect wavefront correction this results in a residual wavefront error leading to a Strehl ratio of about 90% as discussed above. Accounting for positioning uncertainties the final Strehl ratio for perfect compensation is of the order of 85%.

Usually, wave-front sensing is performed out at visible wavelengths, whereas the correction is carried out at NIR wavelengths.

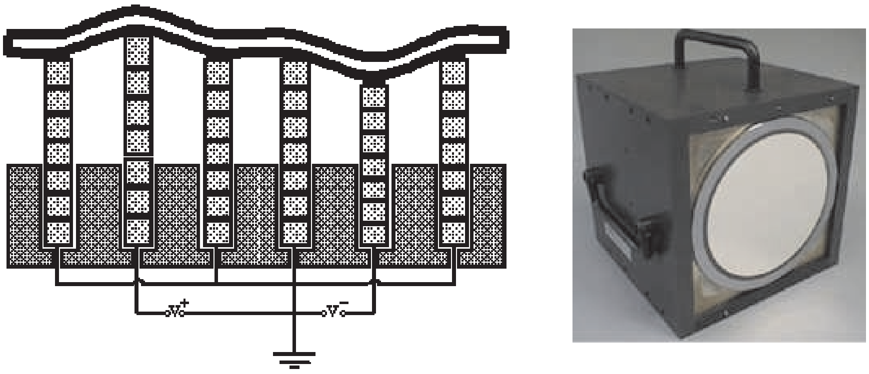

Figure 2.8: *Left panel:* Schematics of the working principle of a deformable mirror. *Right panel:* Example of a deformable mirror implemented in the AO system of ESO-NACO. Images courtesy of ONERA.

Active optical elements

In order to compensate the turbulence induced distortions active optical elements are needed. For this purpose, deformable mirrors are used (Fig. 2.8). They often are made of thin sheets of glass with a diameter of ~2 cm. Attached to their backs are actuators. These devices respond to an external Voltage signal by contracting or expanding. This leads to the deformation of the mirror.

The aim is to get a flat wave front, hence the wave front distortions are corrected by an inverse deformation of the mirror regarding the measured wave-front deformation. The number of required correcting elements and the required correcting speed have been discussed in the previous section.

2.2.3 Sky coverage and laser supported AO

As we have seen in the former two sections, the performance of the AO system is a function of the angular separation between science target and NGS, as well as the brightness of the NGS. The constraints imposed by current AO facilities on these two parameters can lead to serious limitations in sky coverage. Figure 2.9 shows the sky coverage as a function of NGS R-band magnitude and angular separation. Stellar number counts at 30° galactic latitude, i.e. close to galactic plane (higher stellar density), and at the galactic pole (lower stellar density) are considered (cf Roddier 1999). The red cross identifies nominal limits of ESO-NACO, which result in a

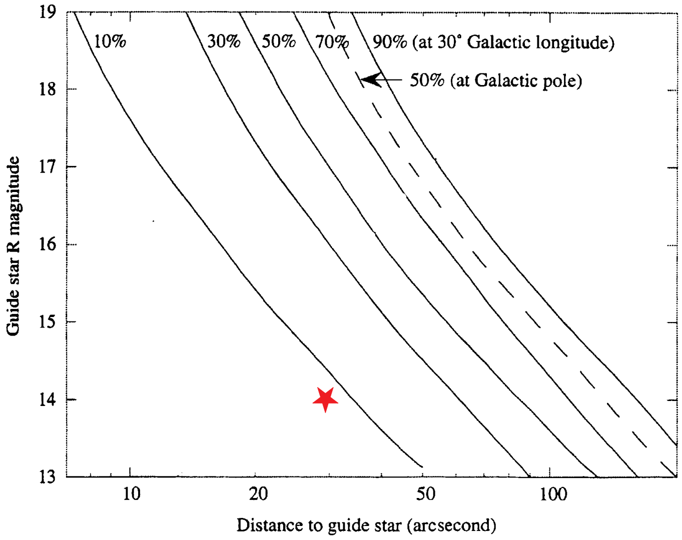

Figure 2.9: The sky coverage of an AO system as a function of guide star visual brightness and off-axis angle. The solid contours give the sky coverage at 30° Galactic longitude and the dashed contour gives the 50% sky coverage at the Galactic pole. Representative AO instrumentation like ESO-NACO (red star) has sky coverage well below 10%. Adapted from Roddier (1999).

sky coverage well below 10%.

Using NGSs results in very little sky coverage at visible wavelengths. The sky coverage increases rapidly towards longer wavelengths (since the size of the isoplanatic patch increases and since more stars are visible at NIR wavelengths), which, in conjunction with the reduced complexity (cf Sec. 2.2.1) and cost, is the reason why most current efforts focus on the 1-5 μm wavelength domain.

There is, furthermore, a possibility to reach almost 100% sky coverage. This can be achieved with the production of a synthetic guide star by a laser beacon; a so called *laser-guide star*. A laser excites a sodium layer at a height of about 90 km to resonance emission. This radiation is then used as the GS. But there are still problems, like the finite height of laser guide star. The LGS light is traveling within a light cone and not the whole isoplanatic patch is sampled. These problems somewhat diminish the effectiveness of LGS-AO compensation. Since the LGS light travels along a differnet path than that of the science target, another point-source reference is needed, in order to correct for this effect. Such additional point-source references are called *tip-tilt star* and they can be fainter than normal GSs, since their light is only needed to assess the lowest wave-front modes (cf Beckers 1993).

2.3 The Virtual Observatory in the context of AGN research

> *"The goal of the Virtual Observatory*
> *is enabling science not developing software."*

The Virtual Observatory (VO) is an international initiative with the aim to provide standards in data access and analysis methods to distributed observational and simulation data[4] (e.g., Brunner et al. 2001). Astronomical data is growing exponentially (a similar trend like in particle physics) as telescope area doubles every 25 years whereas CCD pixels double every two years (Szalay & Gray 2001). It becomes therefore necessary to cope with the vast amount of data efficiently. But not only the data management challenges the traditional ways of astronomical research (e.g., Szalay et al. 1999; Nieto-Santisteban et al. 2005). What is even more important is the interpretation of the data. The VO enables us to combine complementary information from many different sources (e.g., SDSS, 2MASS, FIRST, XMM, ESO archive, etc.) by virtue of standardized data formats and transmission protocols. Such large, multiwavelength data sets, for the first time, allow us to analyze the physical properties of astronomical objects on firm statistical ground and to discover new classes of objects (e.g. Bazell et al. 2006).

The VO consists of three layers (see Fig. 2.10; cf Szalay & Gray 2004):

- **Archives:** At the bottom layer the archives each store text, images, raw data, and their associated schematized data in relational databases. They provide data mining tools that allow easy search and subsetting of the data objects at each archive. They also contain metadata about their content, describing not only their physical units but also the provenance of the data.

- **Web Services:** The middle layer represents the interfaces to the information provided by the archives. This is usually achieved by Web services (WS; e.g., Monson-Haefel 2003). These offer on-demand

---

[4] See the International VO Alliance (IVOA) at `www.ivoa.net`

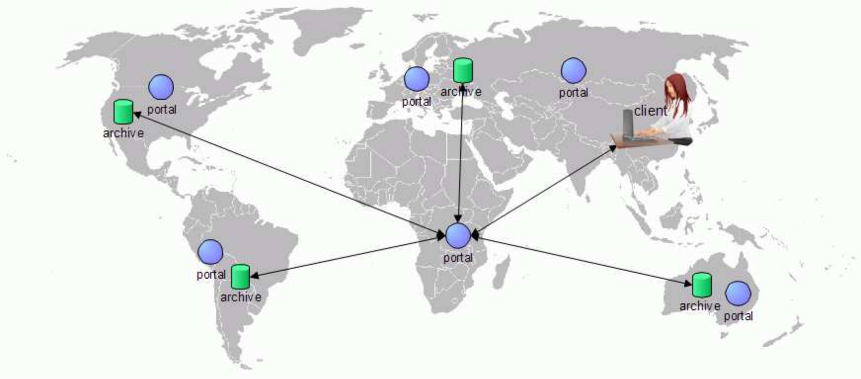

Figure 2.10: Conceptual visualization of the VO. The user/client can access one of the many world-wide portals that offer access to astronomical archives and further astronomy related Web services. The portals answer the user query by integrating data from many archives. The archives present their data as Web services.

queries and file-transfer service. All Web services support common core schemata that extend the VOTable data model[5]. The Simple Object Access Protocol (SOAP) and the Extensible Markup Language (XML) are the technical bases of WSs.

- **Portals:** The top layer which the client/user directly accesses consists of portals and registries. The registries store what kind of information each archive provides. They will be widely replicated. Portals handle the client requests and use the registries in order to answer the queries by integrating data from many archives.

An outstanding example of a survey that publishes its data and analysis tools in the VO environment is the international teamed Sloan Digital Sky Survey (SDSS, York et al. 2000). In its most recent 6th data release, more than 10 terabyte of imaging and spectroscopic data were made available to the public (Adelman-McCarthy & the SDSS Collaboration 2007). The SDSS, in its seventh year, is an optical survey of about 10,000 deg^2 of the northern hemisphere in five broad bands covering the visible part of the electromagnetic spectrum. Furthermore, high resolution spectroscopy in the same wavelength regime is carried out. The SDSS revolutionized optical astronomy in many aspects. Just to mention a few in the field of AGN research: the large homogeneous set of high quality/sensitivity data allowed

---

[5] See `www.ivoa.net/Documents/latest/VOT.html`

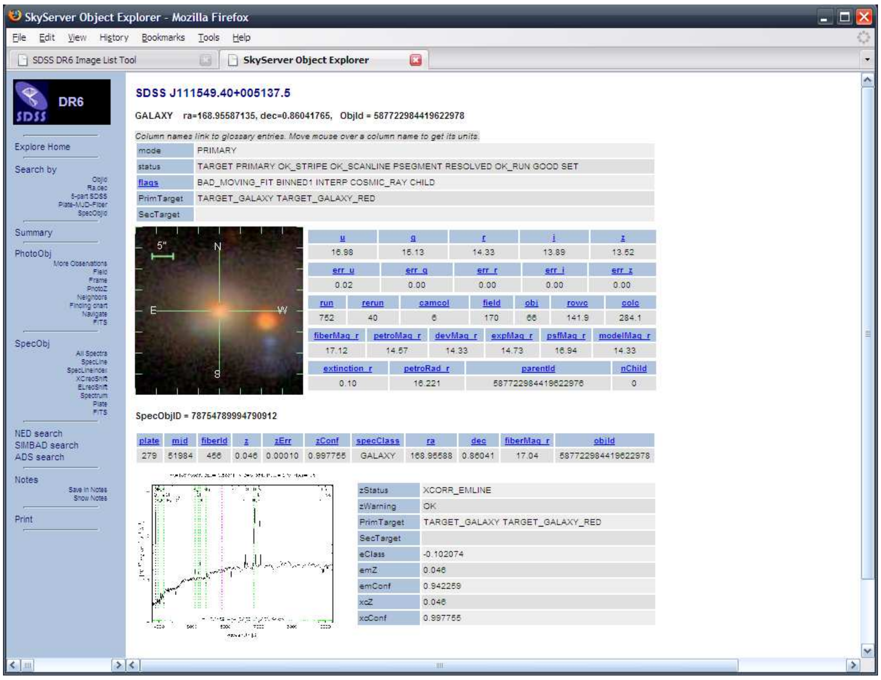

SDSS J111549.40+005137.5

GALAXY ra=168.95587135, dec=0.86041765, ObjId = 587722984419622978

Column names link to glossary entries. Move mouse over a column name to get its units.

mode	PRIMARY
status	TARGET PRIMARY OK_STRIPE OK_SCANLINE PSEGMENT RESOLVED OK_RUN GOOD SET
flags	BAD_MOVING_FIT BINNED1 INTERP COSMIC_RAY CHILD
PrimTarget	TARGET_GALAXY TARGET_GALAXY_RED
SecTarget	

u	g	r	i	z
16.98	15.13	14.33	13.89	13.52

err_u	err_g	err_r	err_i	err_z
0.02	0.00	0.00	0.00	0.00

run	rerun	camcol	field	obj	rowc	colc
752	40	6	170	66	141.9	284.1

fiberMag_r	petroMag_r	devMag_r	expMag_r	psfMag_r	modelMag_r
17.12	14.57	14.33	14.73	16.94	14.33

extinction_r	petroRad_r	parentId	nChild
0.10	16.221	587722984419622976	0

SpecObjID = 78754789994790912

plate	mjd	fiberId	z	zErr	zConf	specClass	ra	dec	fiberMag_r	objId
279	51984	456	0.046	0.00010	0.997755	GALAXY	168.95588	0.86041	17.04	587722984419622978

zStatus	XCORR_EMLINE
zWarning	OK
PrimTarget	TARGET_GALAXY TARGET_GALAXY_RED
SecTarget	
eClass	-0.102074
emZ	0.046
emConf	0.942259
xcZ	0.046
xcConf	0.997755

Figure 2.11: Exploration of an SDSS object via the SkyServer (`http://skyserver.sdss.org`). The main view presents key information on the selected astronomical object, like name, coordinates, magnitudes, radii, redshift, spectral type. In fact, all photometric, spectroscopic, and housekeeping data can be accessed from this view. In addition, external databases, like NED and SIMBAD, can be searched with the given object coordinates.

astronomers to find large samples ($> 10^4$ objects) of AGN subtypes, like quasars (Schneider et al. 2007), Seyfert 2 (Kauffmann et al. 2003), and X-raying AGN (Anderson et al. 2007). The 5-band photometric data, images, and spectra can be mined in a VO context, i.e. information retrieval via WSs like image or spectrum download, structured query language (SQL)[6] to query database content for object parameters (e.g. flux, size), etc. (see Figs. 2.11 and 2.12).

This chapter is concerned with the selection of a sample of AO-suitable AGN. The presented work made extensive use of VO tools, provided as part of the SDSS and the German Astrophysical Virtual Observatory (GAVO)[7]. The details will be addressed in the following sections, however, a few words on GAVO are in order. As part of the European Virtual Observatory

---

[6] `www.ivoa.net/twiki/bin/view/IVOA/IvoaVOQL`

[7] `www.g-vo.org`

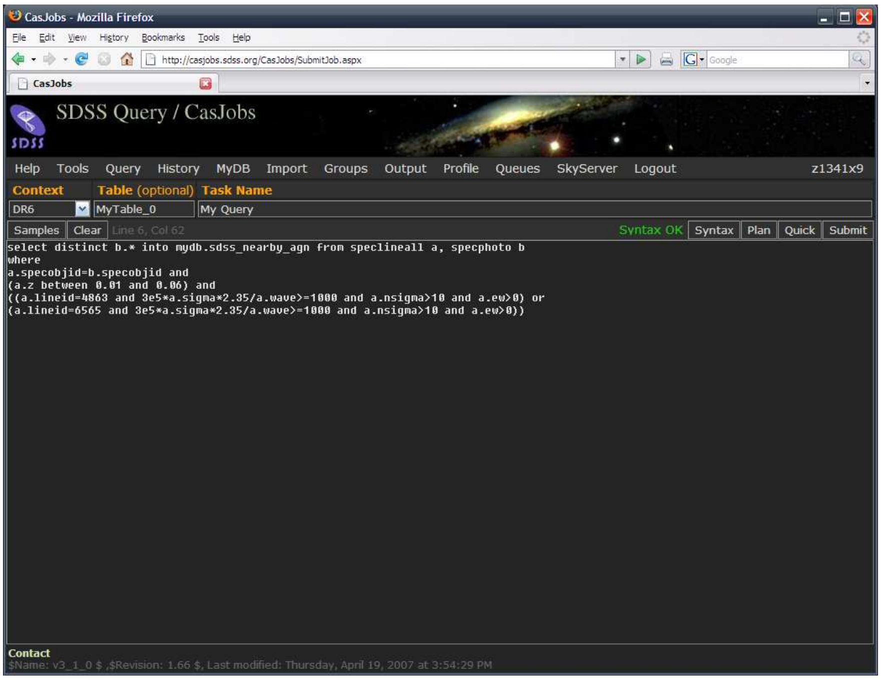

Context: DR6
Table (optional): MyTable_0
Task Name: My Query

```
select distinct b.* into mydb.sdss_nearby_agn from speclineall a, specphoto b
where
a.specobjid=b.specobjid and
(a.z between 0.01 and 0.06) and
((a.lineid=4863 and 3e5*a.sigma*2.35/a.wave>=1000 and a.nsigma>10 and a.ew>0) or
(a.lineid=6565 and 3e5*a.sigma*2.35/a.wave>=1000 and a.nsigma>10 and a.ew>0))
```

Figure 2.12: Example query in CasJobs (`http://casjobs.sdss.org/CasJobs`). CasJobs is an online workbench for large scientific catalogs. As a multi-server, multi-queue batch job submission and tracking system for the SDSS, the catalog archive server (CAS), it makes private workspace available to users and allows them to submit complex queries.

(EURO-VO)[8], GAVO is a national initiative, which contributes primarily in the field of X-ray data and Millenium-simulation data federation (e.g., Schuecker et al. 2004; Zuther et al. 2005a; Lemson & Virgo Consortium 2006). Within the cooperation with the Max-Planck-Institute for extraterrestrial physics (MPE), the ROSAT photon WS that allows one to study individual X-ray photons is used, as well as the *GAVO-matcher* with which several catalogs can be combined via probabilistic cross-matching (Adorf et al. 2006)[9].

The near infrared (NIR, $\lambda \approx 1 - 3\ \mu$m) is a sensitive tracer of the mass dominating (older) stellar populations in galaxies. At the same time the

---

[8] `http://www.euro-vo.org`; The EURO-VO project aims at deploying an operational VO in Europe. Its objectives are technology take-up and VO compliant resource provision, building the technical infrastructure and supporting its utilization by the scientific community.

[9] See Open SkyQuery at `http://www.openskyquery.org`

NIR is less affected by extinction, but still sensitive to the distribution and contribution of (warm) dust. Studying the detailed morphology, dynamics and composition of the sources described below is therefore ideally done in the NIR since especially the circumnuclear regions of the targets are expected to be extincted.

2.4 The AO sample

All-sky surveys conducted during the last decade produced an unprecedented richness of astronomical objects. These surveys allow us to study the evolution of individual classes of objects, their interrelationships, as well as to discover new classes of objects. Now more than ever, with the help of VO tools it is possible to tackle the problems mentioned in the previous sections in a efficient and panchromatic manner (e.g., Szalay & Gray 2001; Brunner et al. 2001).

The AO sample presented here is based on a cross-correlation of the fifth data release (DR5)[10] of the SDSS (Adelman-McCarthy et al. 2007) and the RASS Bright and Faint Source catalogs (BSC, FSC Voges et al. 1999).

The Sloan Digital Sky Survey

As already introduced in Sec. 2.3, the SDSS is an international collaboration, pursuing an optical sky survey of about one quarter of the northern hemisphere. The SDSS filter system covers the wavelength range from 3500 Å - 9000 Å in five broad filters (Tab. 2.1; Fukugita et al. 1996)[11]. A fiber-fed spectroscopy mode with a spectral resolution of $R \sim 1800$ complements the imaging. The DR5 covers about 8000 square degrees and contains 215 million unique objects, 1,048,960 of which have spectra (spectroscopic area 5740 square degree). The majority of spectroscopic objects are galaxies (~ 60%), about 10% are classified as AGN, and the rest are either stars, sky spectra for calibration purposes, or unknown objects. Due to sensitivity constraints, only galaxies with r-band magnitudes < 17.7 and AGN with i-band magnitudes < 19.1 receive spectroscopic observations. Each data release includes catalogs of photometric and spectroscopic data, as well as reduced and calibrated wide-field imaging and single-object spectroscopic data (see Stoughton et al. 2002, for a detailed description of the

---

[10] `http://www.sdss.org/dr5/`

[11] See App. A.2.1 for an introduction to the SDSS photometric system.

Table 2.1: SDSS filter system: designations, central wavelengths, and survey limiting magnitude for point sources.

Name	u	g	r	i	z
λ_{eff} [Å]	3551	4686	6165	7481	8931
limiting magnitude	22.0	22.2	22.2	21.3	20.5

data products). The median r-band PSF width is $1\farcs4$, which provides a fairly good basis for detecting extended structures and for studying galaxy morphologies.

The ROSAT All Sky Survey

The German/UK/US X-ray satellite mission ROSAT (*Röntgensatellit*) conducted an all-sky survey (RASS) in soft X-rays (0.1-2.4 keV, 100-5 Å) with the Position Sensitive Proportional Counter to a limiting sensitivity of about 10^{13} erg $\mathrm{s}^{-1}\mathrm{cm}^{-2}$. (Voges et al. 1999). The satellite was launched in 1990. The total survey exposure time amounts to 119.36 days. The basic survey strategy of ROSAT was to scan the sky in great circles, whose planes were oriented roughly perpendicular to the solar direction. This resulted in an exposure time varying between about 400 s and 40000 s at the ecliptic equator and poles respectively. X-ray photometry was carried out in 4 energy bands: A (0.1-0.4 keV), B (0.5-2 keV), C (0.5-0.9 keV), and D (0.9-2.0 keV). The gap between 0.4 and 0.5 keV arises due to carbon absorption, and hence this energy range is not used. The RASS database contains two distinct source catalogs. The main difference is the detection likelihood l ($l = -\ln(1 - P)$, P being the probability of a source detection) of X-ray sources from the photon statistics. The result is a bright source catalog (BSC, $l > 15$), containing 18,811 sources and a faint source catalog (FSC, $7 < l < 15$), containing 105,924 objects. The positional uncertainty is about $30''$, which presents a problem for the identification of optical counterparts (cf Sec. 2.4.2). Since X-ray data are often confronted with poor photon-number statistics, spectra are not always available. Instead, hardness ratios (HRs) measure the broad band spectral slope in the 0.1-2.4 keV band.

Besides the large sky coverage of the SDSS and RASS, their sensitivities are well matched. For characteristic X-ray-to-optical flux ratios (Tab. 1 in Stocke et al. 1991) one can expect to find an optical SDSS counterpart to all the RASS sources (cf discussion in Anderson et al. 2003). Here, the target selection algorithm presented in Anderson et al. (2003, 2007) is used for preselection of optical counterparts. SDSS primary objects are selected that are flagged as *TARGET_ROSAT_A* and *TARGET_ROSAT_B* (see Sec. 3 in Anderson et al. 2003, hereafter A03). X-rays from SDSS objects flagged in this way will have a high probability of originating from AGN or emission-line galaxies. In their study, in which they only used X-ray detections with $l \geq 10$, A03 find that previously confirmed QSOs/AGN are assigned in $> 90\%$ one or both of the above flags, during target selection. The resulting sample splits up into two subsamples: (i) objects that are reported in Anderson et al. (2007, hereafter A07) and (ii) a number of additional potential RASS counterparts based on SDSS and FIRST information. Subsequently, we cross-matched the sample with the 2MASS catalog, which is a much easier task, because of the similar positional accuracy and angular resolution of 2MASS and SDSS. For this purpose, we used the *GAVO-matcher* with a search radius of $2''$.

2.4.1 Adaptive optics selection criteria

Imaging through the atmosphere without correction significantly degrades the power of large aperture telescopes, since the coherence length of the atmospheric turbulence is comparably small ($r_0 \approx 60$ cm for $0\farcs75$ seeing at 2.2 μm and $r_0 \approx 13$ cm at 0.5 μm). As outlined in Sec. 2.2, AO helps to exploit the diffraction limit of large aperture telescopes (e.g., the diffraction-limited angular resolution of an 8 m telescope at 2.2 μm is about 50 mas). Because of the $\lambda^{6/5}$ dependence (Eq. 2.7), current AO implementations work in the NIR regime (cf Brandner & Kasper 2005, for an overview of current AO systems and first science results). A typical size of the isoplanatic patch at 1 μm is around $30''$ (e.g., Beckers 1993). Guiding on the reference point source is carried out at visual wavelengths with a limiting magnitude currently around $V \sim 13-14$. Therefore, we search for galaxies which are either self-referencing or which have a bright ($V < 14$) NGS at an angular separation of less than $40''$ (see Fig. 2.13). Note that this sample is also valuable for laser guided observations, because of the need for tip-tilt information provided by the NGSs presented here.

Figure 2.16 shows the distribution of angular separation between science target and NGS.

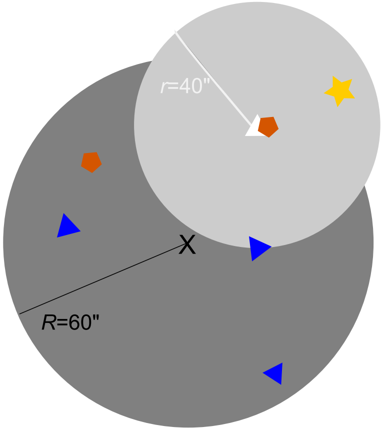

Figure 2.13: Schematic representation of the situation of an AO-suitable counterpart ([yellow] guide star within $r = 40''$ of the optical target white triangle and light grey circle, respectively) of a RASS source (black cross and dark grey circle, $R = 60''$). Blue triangles represent other optical counterparts and orange diamonds represent detections from other surveys (e.g., FIRST).

2.4.2 Matching X-ray objects with high density optical, radio, infrared catalogs

The 2σ ROSAT positional uncertainty is about $1'$ on average (e.g., A03). Reliable classification is, therefore, an issue (Fig. 2.13). With the large multiwavelength sky surveys like SDSS, ROSAT, 2MASS, FIRST and the development of the VO, new tools are available to address this problem (e.g., Anderson et al. 2003; Budavári et al. 2004; McGlynn et al. 2004; Padovani et al. 2004). From the DR5 database we selected[12] the 26207 objects flagged as *TARGET_ROSAT_A* or *TARGET_ROSAT_B*. In fact, these objects correspond to 2708 individual BSC and 9624 individual FSC sources. Note that only $l \geq 10$ X-ray sources are considered. On average each of these BSC (FSC) source has $\sim$ 1.8 ($\sim$ 2.2) *ROSAT_A*/*ROSAT_B*-flagged optical counterparts. In the next step we selected those possible optical counterparts which have an NGS ($r_{PSF} < 14$) within $40''$ of the optical position. $r_{\rm PSF}$ is the SDSS PSF magnitude. This search results in a set of 1550 optical counterpart/NGS pairs. Note that these pairs are not necessarily associated with the X-ray source. A further step is required, which selects from those X-ray sources with a galaxy/NGS pair the most proba-

---

[12] Using CasJobs (cf Fig. 2.12).

Table 2.2: Classification results.

Category	Frequency
QSO	8
GALAXY_FIRST	36
GALAXY_BLUE	4
GALAXY	1
AGN_COLOR	213
EXTENDED	98

ble optical counterpart. The following decision scheme is applied for all *TARGET_ROSAT_A*, *TARGET_ROSAT_B* flagged objects within the error cone of each BSC and FSC source. Spectroscopically identified objects receive the highest priorities (1-4). The remaining two categories rely on photometric information alone.

1. QSO: Spectroscopically identified as AGN (named QSO by the SDSS spectroscopic pipeline).
2. GALAXY_FIRST: Spectroscopically identified as a galaxy (passive or emission line galaxy) and coincident with a FIRST source.
3. GALAXY_BLUE: Spectroscopically identified as galaxy with blue color ($u_{\mathrm{PSF}} - g_{\mathrm{PSF}} < 0.6$). Blue colors are typical for AGN (e.g., Richards et al. 2002).
4. GALAXY: Spectroscopically identified as galaxy (no FIRST source and no blue colors).
5. AGN: No spectrum, but blue color ($u_{\mathrm{PSF}} - g_{\mathrm{PSF}} < 0.6$), typical of AGN.
6. EXTENDED: Extended optical emission (no spectrum, no blue color).

If there is more than one object in the highest priority class, we choose the one with the smallest angular separation to the X-ray position. This search results in 360 optical counterpart/NGS pairs (Tab. 2.2). Of these, only the first four categories have associated SDSS spectra and in the following only these 51 objects will be considered.

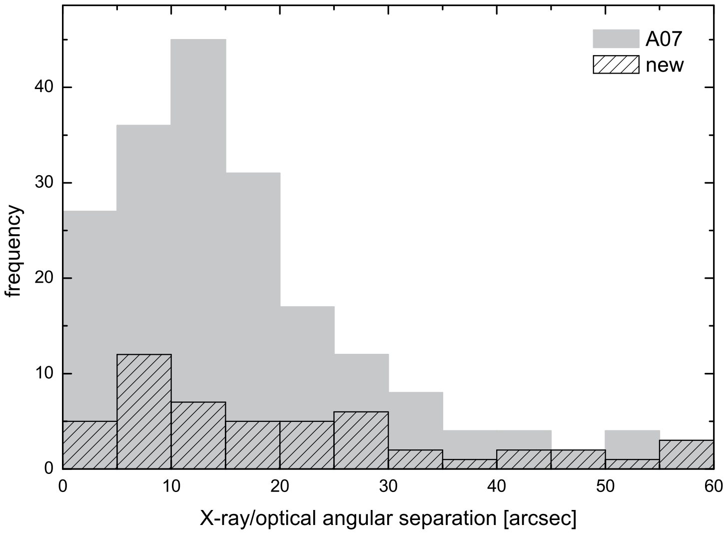

Figure 2.14: Angular separation between X-ray and optical positions. Grey bars correspond to sources identified in A07 and patterned bars to the additional targets identified in this work. Most of the optical counterparts are found within a distance of 30″ , which confirms the source correlation.

In addition, 191 of the in initial 1550 galaxy/NGS pairs are classified by A07 as broad-line AGN (BLAGN) or narrow-line AGN (NLAGN). This results in a total sample of 241 AO-suitable galaxies as optical counterparts to RASS sources. Figure 2.14 shows the distribution of angular separations of X-ray and optical positions. Most of the optical counterparts are found within 30″ of the X-ray position. Such a correlation is found in other ROSAT/optical identification work and confirms that coincidence by chance is small (e.g., Mickaelian et al. 2006; Suchkov et al. 2006; A07).

A caveat resulting from the AO selection procedure, however, is the presence of a bright star inside the ROSAT error circle in many cases. This star could contribute to the X-ray emission. In order to address this problem, GAVO is used to study the distribution of the individual X-ray photons around each source position. The distribution in some cases can give information on which is the more likely optical candidate. It is known that the source detection algorithm of the RASS catalogs is somewhat coarse, and some sources split up into multiple sources in different energy bands (W. Voges, priv. comm.). In the present case, a likely situation is the

Table 2.3: Distribution of angular separations of centroids in the lower three X-ray bands and the optical position of the galaxy and GS.

Difference type	Frequency	
	A07	new
$\forall d:\ d_{\mathrm{galaxy}} < d_{\mathrm{gs}}$	58	14
mixture[a]	123	29
$\forall d:\ d_{\mathrm{galaxy}} > d_{\mathrm{gs}}$	10	8

[a] For 28 (49) of which the soft components is closer to the GS (galaxy), whereas the hard components is closer to the galaxy (GS). For 28 (18), both the soft and hard components are closer to the galaxy (GS).

splitting into a soft stellar component, the GS, and a hard component, the galaxy/AGN. Therefore, the X-ray photon distributions in the three energy bands A, C, and D, within a radius of $7'$ have been investigated. For each energy band the centroid is calculated and compared to the optical positions. Angular distances, d, between the X-ray and optical positions are weighted by the variance of the photon centroid,

$$d[\mathrm{arcsec}] = 0.017 \frac{Hav_{xo}}{\sqrt{\sigma^2_{\mathrm{X-centroid}} + \sigma^2_{\mathrm{SDSS}}}}, \tag{2.26}$$

where Hav_{xo} is the angular distance in spherical coordinates, as defined in Eq. A.1 and σ are the uncertainties of photon centroid and SDSS optical position, respectively. Table 2.3 presents the results of this measurement. d_{galaxy} and d_{gs} correspond to the distances between the X-ray photon centroid in one of the three bands and the optical position of the galaxy or of the GS.

Only in about 15% (25%) of the A07 (new) cases the GS is closer to the photon centroids in all three X-ray bands, or at least the soft and hard bands. This provides confidence that the majority of X-ray sources is indeed associated with the galaxy. However, one has to keep in mind that often the number of detected photons is very small (<50, Fig. 2.18). Hence, centroid uncertainties grow with decreasing number of involved photons (see Fig. 2.15). For typical galaxy/GS separations of $30''$ (Fig. 2.16), there are several pairs, for which the centroid uncertainties are still smaller than the galaxy/GS angular separations.

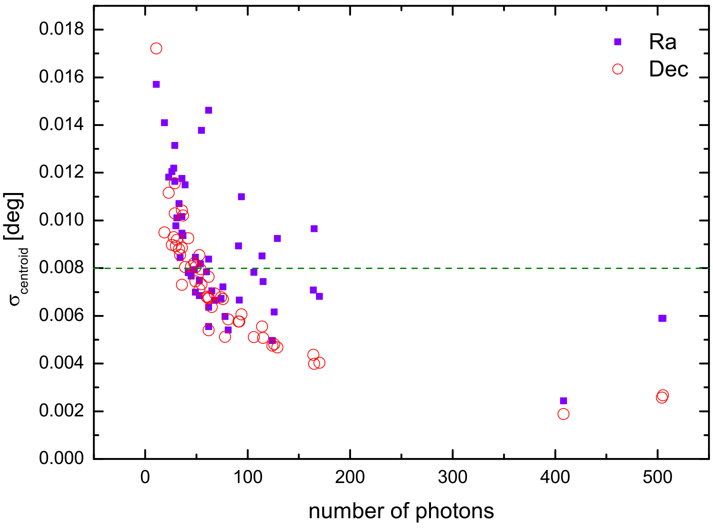

Figure 2.15: Dependence of the accuracy of the centroid position on the number of involved photons. The data points plotted represent soft photons. Precision increases with increasing number of photons. The dashed line corresponds to a typical galaxy/GS separation of 30″ .

Another way to study the relation between X-ray source and optical counterpart is to calculate the ratio of X-ray flux to optical flux, which is a coarse measure of the spectral slope. As outline in Stocke et al. (1991) and Maccacaro et al. (1988), each source population is characterized by a typical value of this ratio. Figure 2.17 presents $\log(F_x/F_o)$ vs. m_V (as defined in Maccacaro et al. 1988)[13]. X-ray fluxes have been computed by converting the X-ray counts to flux units using PIMMS[14] and assuming an absorbed power-law with an energy index $\alpha_X = 1.5$ (similar to Anderson et al. 2003)[15]. The absorbing column densities were determined from the H I map of Dickey & Lockman (1990). The visual magnitude V is computed from galactic extinction corrected SDSS PSF-magnitudes via $V = g - 0.55(g - r) - 0.03$ (Smith et al. 2002). The values distribute in a region typical for AGN ($\log(F_x/F_o) \sim 0$), galaxies ($\log(F_x/F_o) \sim -1$), and groups/clusters of galaxies ($\log(F_x/F_o) \sim -0.5$). Extended X-ray emission,

---

[13] $\log(f_X/f_V) = \log f_X + \frac{m_V}{2.5} + 5.37$

[14] Portable, Interactive Multi-Mission Simulator, Version 3.8a2

[15] Throughout this work we use $F_\nu \propto \nu^{-\alpha}$, $N(E) \propto E^{-\Gamma}$, and $\Gamma = \alpha + 1$.

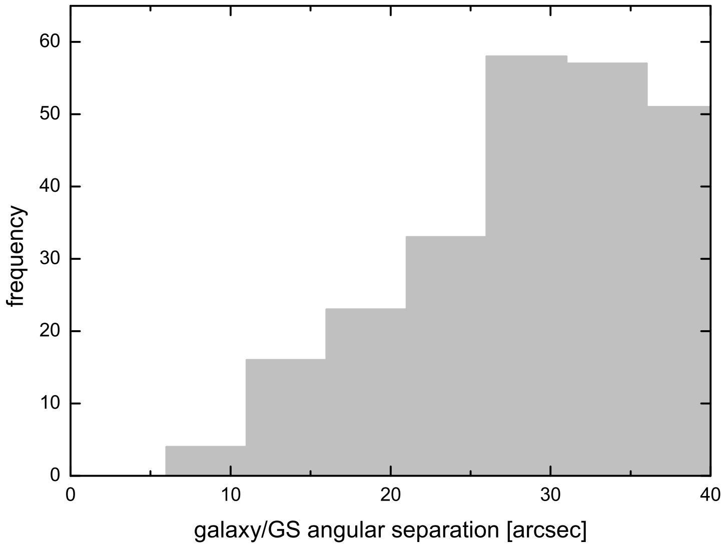

Figure 2.16: Galaxy/guide star angular separations of all AO targets.

like that from clusters of galaxies, are not the topic of this work. A certain fraction of the sample sources belong to clusters or groups and show signs of Seyfert activity. Recent studies show that the environment of galaxies indeed is important for some Seyfert activity (see online proceedings of the 10th Birmingham-Nottingham Extragalactic Workshop on Galaxy Interactions and Mergers[16]). Therefore, the galaxies identified to belong to groups/clusters are kept in the catalog.

2.4.3 X-ray and optical properties

The initial cross-matching provides X-ray and optical information. In the previous section, the ratio of X-ray flux to optical flux has been used to estimate the activity class of the X-ray sources. Similar to A07, spectroscopic redshifts are used to calculate X-ray luminosity, monochromatic rest-frame 2500Å , and 2 keV luminosity. The UV luminosity $L_{2500\text{Å}}$ is estimated from the g-band PSF magnitude, assuming an optical power-law index $\alpha_O = 0.5$ of AGN (Vanden Berk et al. 2001), and applying a K-correction (see App. A for more details). Figure 2.19 shows the X-ray

---

[16] `http://www.nottingham.ac.uk/~ppzcc1/meeting/programme.html`

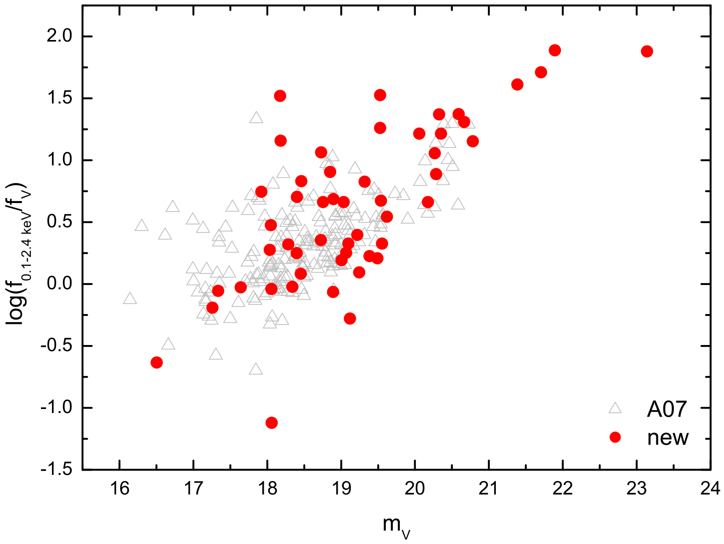

Figure 2.17: X-ray-to-visual flux ratio vs. visual magnitude for A07 objects (open triangles) and the new identifications (filled circles). The ratios are typical for those of AGN.

luminosity vs. redshift distribution of the sample. All X-ray objects have $L_{0.1-2.4\ \mathrm{keV}} \gtrsim 10^{41}$ erg s^{-1}. Such high X-ray luminosities are typical for AGN. The inset of Fig. 2.19 shows that luminous X-ray AGN can only be studied in sizable numbers at redshifts $z \gtrsim 0.1$ (cf Fig. 1.12), which is reflected by the present sample; only 23 sources have $z \lesssim 0.1$.

A large fraction of UV-excess and radio-selected AGN have been discovered to be strong X-ray emitters, with X-ray luminosities correlated with those measured in the rest-frame UV (e.g., Strateva et al. 2005, and references therein). This correlation is usually cast in the X-ray/UV spectral index,

$$\alpha_{ox} = -0.384 \log\left(\frac{L_X}{L_{2500\text{Å}}}\right). \tag{2.27}$$

Actually, this is just a parameterization of the relative UV/X-ray fluxes and not a real fit of the spectrum. The strong dependence of the X-ray luminosity on the UV luminosity ($\alpha_{ox} = -0.136 \log L_{UV} + 2.616$; Strateva et al. 2005) points towards a physical connection between the emission mechanisms (cf Sec. 1.3.1). There are, however, no specific theoretical studies of accretion disk plus hot corona to date, predicting the observed range of α_{ox}

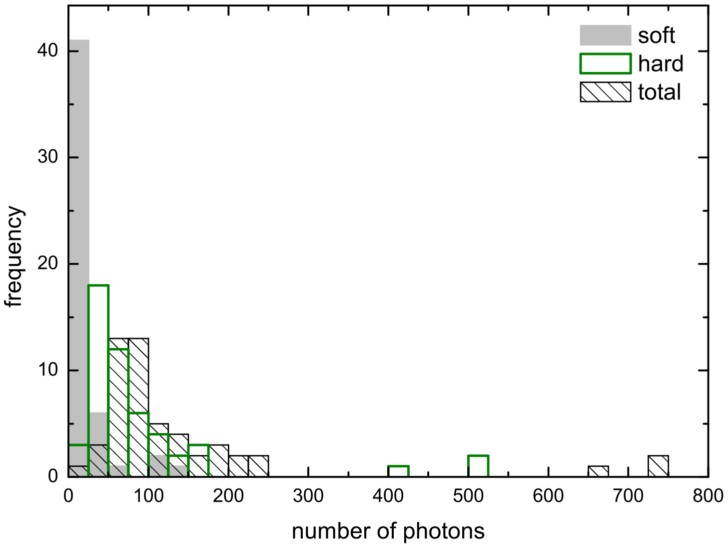

Figure 2.18: Number of detected photons around sources identified in this work. The photons are detected within a search radius of $7'$. Black, patterned bars correspond to the total sum, grey, filled bars to soft, and green bars to hard photons.

and its dependence on rest-frame X-ray/UV luminosity and/or redshift. It also appears that the dependence on UV luminosity outweighs that on redshift (e.g., Vignali et al. 2003). AGN redistribute their energy in the UV and X-ray bands depending on their overall luminosity. More luminous AGN are emitting fewer X-rays per unit UV luminosity than less luminous AGN. Turbulent magneto-hydrodynamic processes might possibly explain the observed anti-correlation (e.g., Balbus & Hawley 1998). Our sample displays a similar relation (Fig. 2.20). Note that the work of Strateva et al. (2005) is more elaborate, since the authors take intrinsic extinction effects, the influence of radio jets (beaming), and aperture effects into account. At the present stage, it is sufficient to realize that the AO sample exhibits similar properties to those of the other studies. Subsequent high angular resolution studies might shed new light onto the issue of energy redistribution close to the SMBH in AGN.

The RASS catalog, furthermore, provides some X-ray spectral information in the form of hardness ratios, which are a broad measure of the

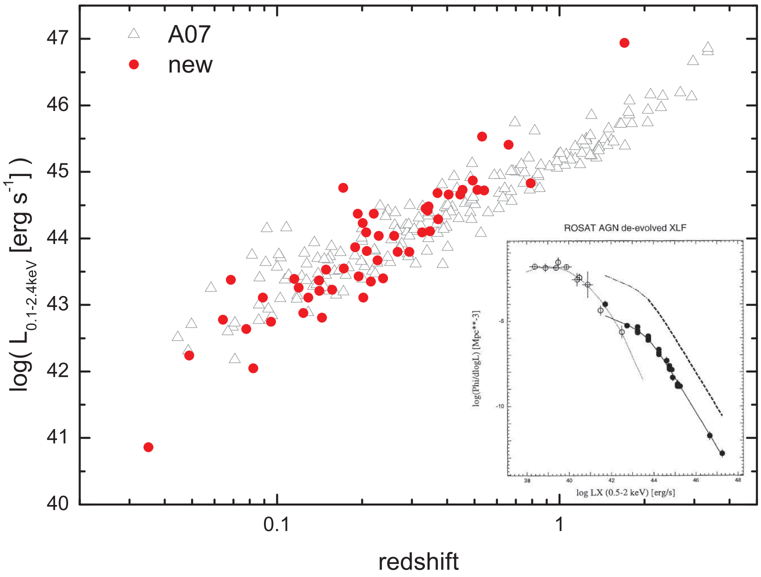

Figure 2.19: 0.2-2.4 keV luminosity vs. spectroscopic redshift of the sample sources. The inset shows the X-ray luminosity functions (Hasinger 1998) of local normal galaxies (open circles), nearby AGN (filled circles) and $z \approx 2-3$ AGN (dashed line). Luminous X-ray AGN can only be studied in sizable numbers at redshifts > 0.1.

X-ray spectral shape. The hardness ratios HR1 and HR2 are defined as

$$\begin{aligned} \mathrm{HR1} &= \frac{B-A}{B+A}, \\ \mathrm{HR2} &= \frac{D-C}{D+C}. \end{aligned} \tag{2.28}$$

HR1 is a measure of the softness of the X-ray emission. Values lie between -1 and 1. A negative value corresponds to a source, in which most of the photons are emitted below 1 keV. Hard X-ray sources have HR1 > 0.[17] HR2 only probes the 1-2 keV range. These hardness ratios or colors are used for extracting spectral properties of X-ray sources with poor photon statistics (cf Hong et al. 2004). Using simulations, it is possible to extract information like power-law index and intrinsic absorption (cf Sec. 1.3.1). As outlined in Carr et al. (2004), a grid of hardness ratios HR1 and HR2 is calculated for varying spectral index Γ and absorbing column density n_{H} (shown as cyan dashes in Fig. 2.21; see App. A.3.1), using PIMMS.

---

[17] One should not confuse hard soft X-rays, i.e. photon energies between 1 and 2 keV, with hard X-rays in the range 2-10 keV.

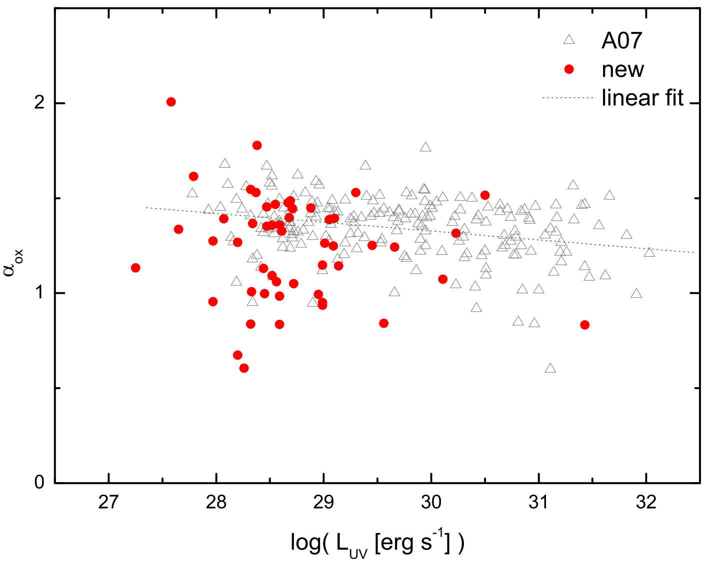

Figure 2.20: α_{ox} as a function of rest-frame UV emission. The dotted line represents a linear fit to the data. It is only intended to visualize the anti-correlation also found in other samples (e.g., Vignali et al. 2003; Strateva et al. 2005).

The scatter in the diagram is quite significant. Due to the small-number statistics for the RASS sources considered here, errors of hardness ratios of individual sources become large. That is why an average hardness ratio is used to give a first impression of the spectral index and absorption of the sample as a whole (Fig. 2.21). The average values of the two subsamples are given as large symbols in Fig. 2.21. The values lie close together and correspond to $\Gamma \approx 2.3 - 2.65$ and $n_H \approx 3 \times 10^{20}$ cm^{-2}. They are consistent with results of other studies of large samples of Seyfert 1 galaxies and quasars, which give an energy index $\Gamma \approx 2-3$ and absorption that is entirely the result of the cold Galactic gas (e.g., Gondhalekar et al. 1997).

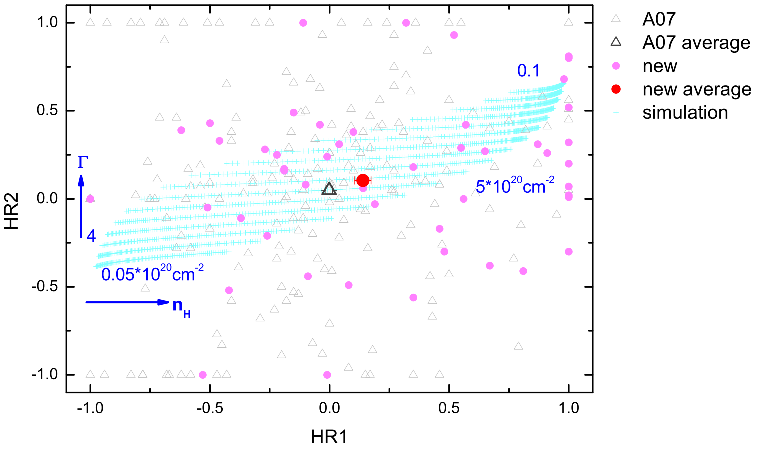

Figure 2.21: Hardness ratios HR2 vs HR1 of the sample sources. A simulated grid of hardness ratios is also shown (cf App. A.3.1). The energy index Γ increases from bottom ($\Gamma = 4$) to top ($\Gamma = 0.1$), whereas the absorbing column density increases from left ($n_H = 0.05 \times 10^{20}$ cm^{-2}) to right (5×10^{20} cm^{-2}). Average hardness ratios are shown as large symbols. A number of sources show HR= -1 or 1. These values are reached when on the involved energy bands contains no photons, or the background subtracted photon flux becomes negative.

2.4.4 Morphological and spectroscopic properties

Photometric data

The 5-band SDSS photometric data and images can be used to study the optical large-scale structural properties of the sample objects. As already mentioned at the beginning of this chapter, an important question is, how is morphology related to X-ray nuclear activity? The SDSS photometric pipeline measures fluxes within several apertures (cf Stoughton et al. 2002). PSF magnitudes, m_{PSF}, are measured in apertures that have been determined locally from the fitting of stellar point sources. Thus, they are ideal to retrieve total fluxes of point-like sources, like the nuclei of active galaxies. For extended objects, magnitudes, m, derived from model fits with exponential (late-type galaxies with $I(r) = I_0\ e^{-r/r_0}$) or de Vaucouleurs (early-type galaxies with $I(r) = I_0\ e^{-7.67[(r/r_0)^{1/4}-1]}$) profiles are the appropriate choice. A third method is to use Petrosian magnitudes, m_p. Invented to be a redshift independent measure of galaxy fluxes (Petrosian 1976), the Petrosian magnitude is the flux within an aperture with a radius, for which

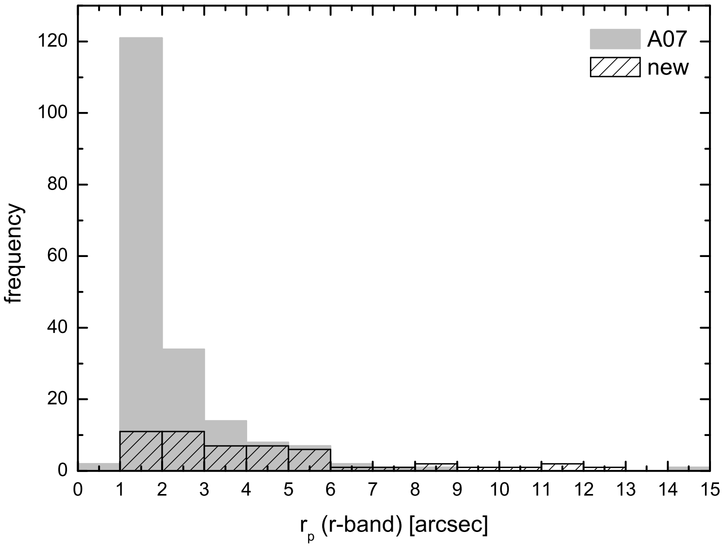

Figure 2.22: Distribution of r-band Petrosian radii. The large number of $R_p < 2''$ is a first indication that a large fraction ($\sim$ 65%) of sources is unresolved in SDSS optical images.

the ratio of the surface brightness within this radius and the surface brightness in a small annulus around this radius amounts approximately to 0.2. It can be shown that for objects that are extended significantly with respect to the seeing disk, the ratio is independent of redshift (see App. A.2)[18]. One can use the definition of the Petrosian magnitude and, hence, the Petrosian radius, r_p, to study the morphological type of galaxies. This can be done by calculating the *concentration index*, $C = r_{p90}/r_{p50}$. C is defined as the ratio of the radii containing 90% and 50% of the Petrosian r-band light (cf Strateva et al. 2001). Centrally concentrated ellipticals ($C \approx 5.5$) are expected to have larger concentration indices than spirals ($C \approx 2.3$). In addition to this value, the model fits mentioned above, provide a likelihood, *fracDeV*, for a galaxy having a late- (fracDeV=0) or early-type (fracDeV=1) light profile.

Figure 2.22 displays the distribution of characteristic galaxy sizes. Most ($\sim$ 65%) of the objects appear to have $r_p < 2''$. The effect of seeing on the Petrosian measures becomes important at such small values (cf Shimasaku et al. 2001). Nevertheless, the small Petrosian radii indicate that

---

[18] For faint and close to point-like objects this measure fails and PSF magnitudes are the better choice.

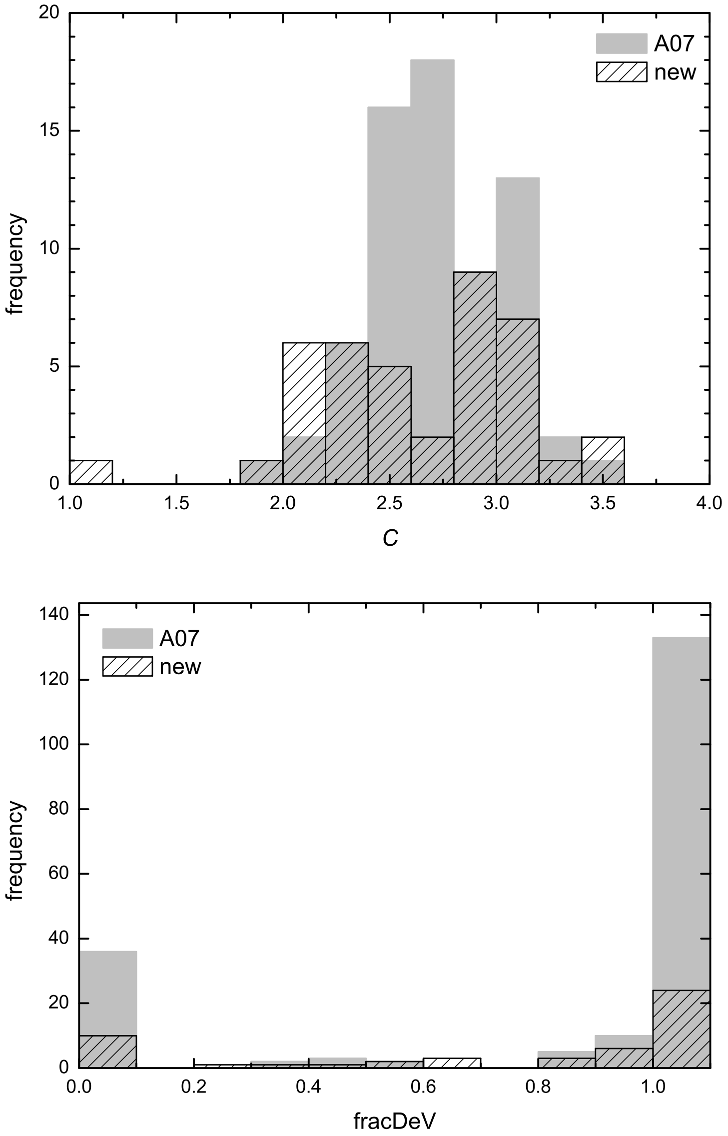

Figure 2.23: *Upper panel:* Distribution of the concentration index C for galaxies with $r_p > 2''$. Pure de Vaucouleurs profiles have $C \sim 2.3$, whereas pure exponential profiles have $C \sim 5.5$. *Lower panel:* fracDeV distribution of the sample. fracDeV= 1 corresponds to a highly concentrated profile. fracDeV= 0 corresponds to a purely exponential profile.

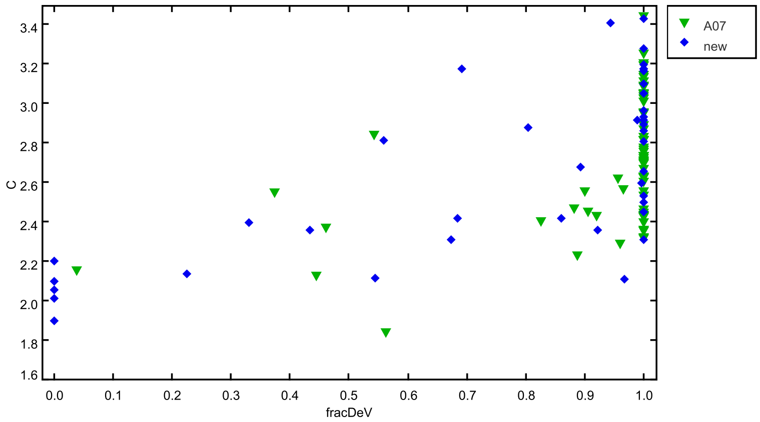

Figure 2.24: Comparison of concentration index, C, and fracDeV parameter for galaxies with $r_p > 2''$.

these ojects have a compact morphology. The concentration index, which is correlated with the morphological type, is distributed for sources with $r_p > 2''$ according to the upper panel of Fig. 2.23. C spans the range from typical exponential disks ($C \sim 2.3$) to $C \sim 3.5$. The latter value represents a mixture of exponential and de Vaucouleurs profiles, i.e. bulge plus disk components. The fracDeV parameter clearly shows two peaks at the extreme values (lower panel of Fig. 2.23). On has to exercise some caution, since, as Fig. 2.24 demonstrates, several galaxies with late-type fracDeV value have concentration indices characteristic of those of early-type galaxies. The major problem stems from the Petrosian measures of the small and faint structures. In such cases the solution for finding r_p is ambiguous and renders C impracticable. In this situation, visual inspection proves to be a valuable calibration (cf Fig. 2.25) and results in the sample containing ~66% of unresolved sources, ~16% of early-type (E/S0) galaxies, ~8% late-type of galaxies, and ~10% disturbed (possibly interacting) sources.

Since many sources are almost unresolved, the smearing due to seeing seems to play an important role if using measures like C or fracDeV for the morphological determination of shallow survey images. What is desperately needed, are deeper and higher angular resolution observations of these sources. The dominance of unresolved and early-type objects agrees with current sensitive studies of X-ray selected AGN in HST deep fields

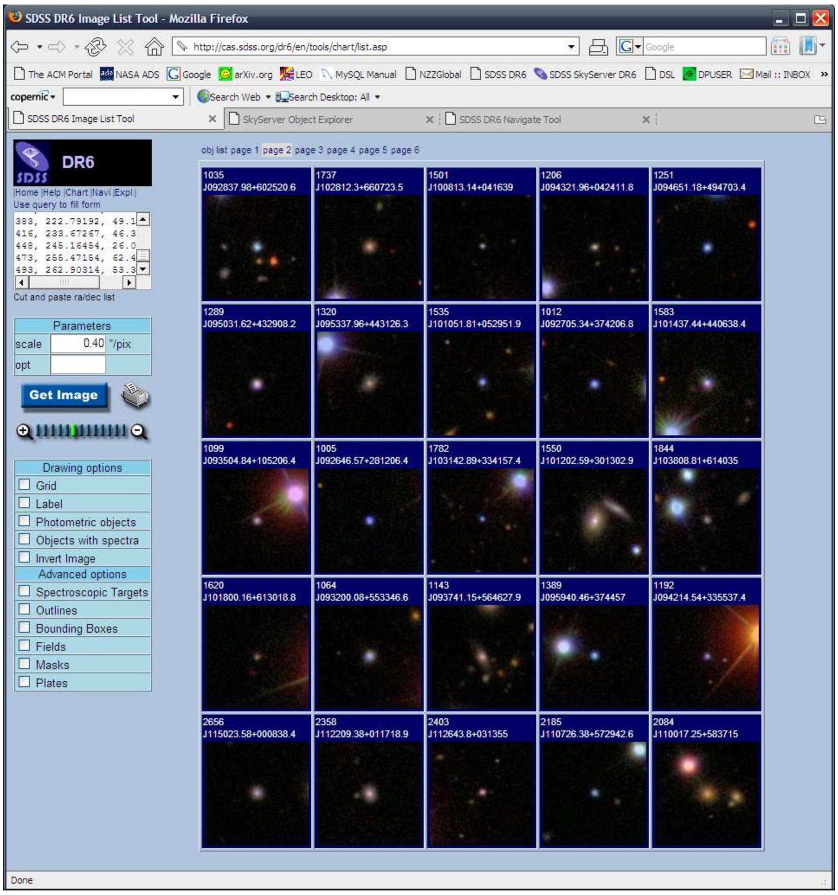

Figure 2.25: SDSS RGB images of some sample galaxies. This is a screenshot from the SDSS image server web site.

(Schade et al. 2000; Pierce et al. 2007). X-ray bright AGN appear to be present in massive, early-type systems, as suggested by Heckman et al. (2004) in their study of local SDSS selected AGN and QSOs. So far, photometric data cannot provide further information, but the global results are consistent with previous similar studies.

Spectroscopic properties

Spectroscopy can be used to further characterize the optical counterparts, in terms of dominant excitation mechanism. As found in previous studies (e.g., Hasinger et al. 2005), the majority of soft X-ray selected AGN are of

Seyfert-type 1. The 191 counterpart drawn from the A07 sample are already classified as NLAGN (22) or BLAGN (169). Table 2.4 lists the results of spectral classification according to the activity type.[19] The classification of the remaining 51 newly identified counterparts can also be found in the table. A large fraction of the latter exhibits an overall passive spectrum of an evolved stellar population. Almost all of these galaxies belong to groups and clusters.

Table 2.4: Spectral classification results.

Category	**Frequency**	
	new	A07
BLG	11	186
NLG	6	5
passive	31	–
unknown	3	–

The next step is to extract information, like emission line fluxes, widths, reddening, stellar host contribution, etc., from the spectra. In order to measure emission line properties, broad (FWHM > 1000 km s^{-1}) and narrow (FWHM < 1000 km s^{-1}) Gaussian profiles are fitted to the hydrogen-recombination lines Hα and Hβ. Forbidden narrow lines ([O III] λ5008Å, [N II] $\lambda\lambda$6550, 6585Å) are fitted with a single Gaussian component. In an attempt to separate host galaxy and nuclear emission, a linear combination (Eq. 2.29) of a power-law ($\alpha = 0.46$) describing the composite quasar spectrum (cf Fig. 3 in Vanden Berk et al. 2001) and an old 1.4 Gyr plus a young 250 Myr simple starburst from (Fig. 2.26 Bruzual & Charlot 2003, metallicity = 0.02) was fitted to the observed spectra,

$$\begin{aligned} g(\lambda) &= e^{-\tau_A(\lambda)} A \times \mathrm{AGN}(\lambda) \\ &+ e^{-\tau_B(\lambda)} \left\{ B \times \mathrm{HOST}_{\mathrm{young}}(\lambda) + C \times \mathrm{HOST}_{\mathrm{old}}(\lambda) \right\}. \end{aligned} \quad (2.29)$$

AGN(λ) is the QSO template spectrum, $\mathrm{HOST}_{\mathrm{young}}(\lambda)$, and $\mathrm{HOST}_{\mathrm{old}}(\lambda)$ are the 250 Myr and 1.4 Gyr starbursts, respectively. A, B, and C are the linear coefficients. Since all components are subject to extinction, the fluxes have

---

[19] The A07 spectral classification has been adapter according to the measurement procedure outlined below.

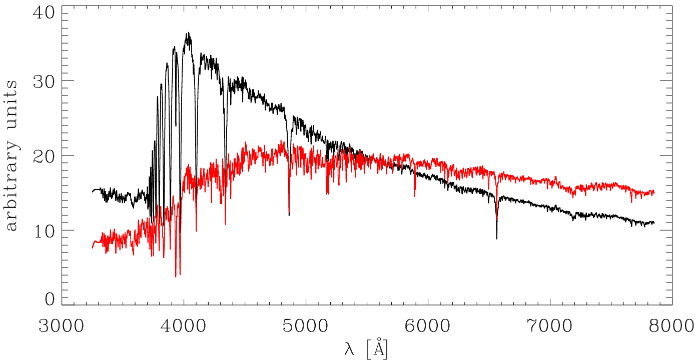

Figure 2.26: The two solar-metallicity stellar spectra fitted to our SDSS spectra. Both spectra are normalized to the wavelength region 5500-5700 Å. The red spectrum corresponds to a 290 Myr old stellar population and the black spectrum to a 1.4 Gyr old population. Spectral data were taken from Bruzual & Charlot (2003).

to be extinction corrected. Here it is assumed that young and old starburst are extincted by the same amount. A foreground screen and the Cardelli et al. (1989) extinction law are used.

This fitting scheme is carried out for all sample objects, with the limitation that spectra of galaxies at $z > 0.8$ are only fitted with a power-law component. As a result, broad H-recombination line components are found in 17 of the 22 NLAG of A07, which leaves only a minor fraction of narrow-line galaxies of about 5% (Tab. 2.4). Such a small fraction of narrow-line galaxies is also found in previous investigations of optical counterparts (Griffiths et al. 1996) at the X-ray flux levels of the RASS. The spectroscopically passive galaxies are all elliptical galaxies, most of which are found in groups or clusters. Their spectra are dominated by an evolved stellar population, i.e. the 1.4 Gyr spectrum dominates the fit. The remaining unknown objects have steep, featureless spectra. After matching the optical positions with NED[20], these galaxies turn out to be most likely Bl Lac objects, in which case the observer looks directly into the radio jet.

---

[20] NASA/IPAC extragalctic database, `http://nedwww.ipac.caltech.edu`

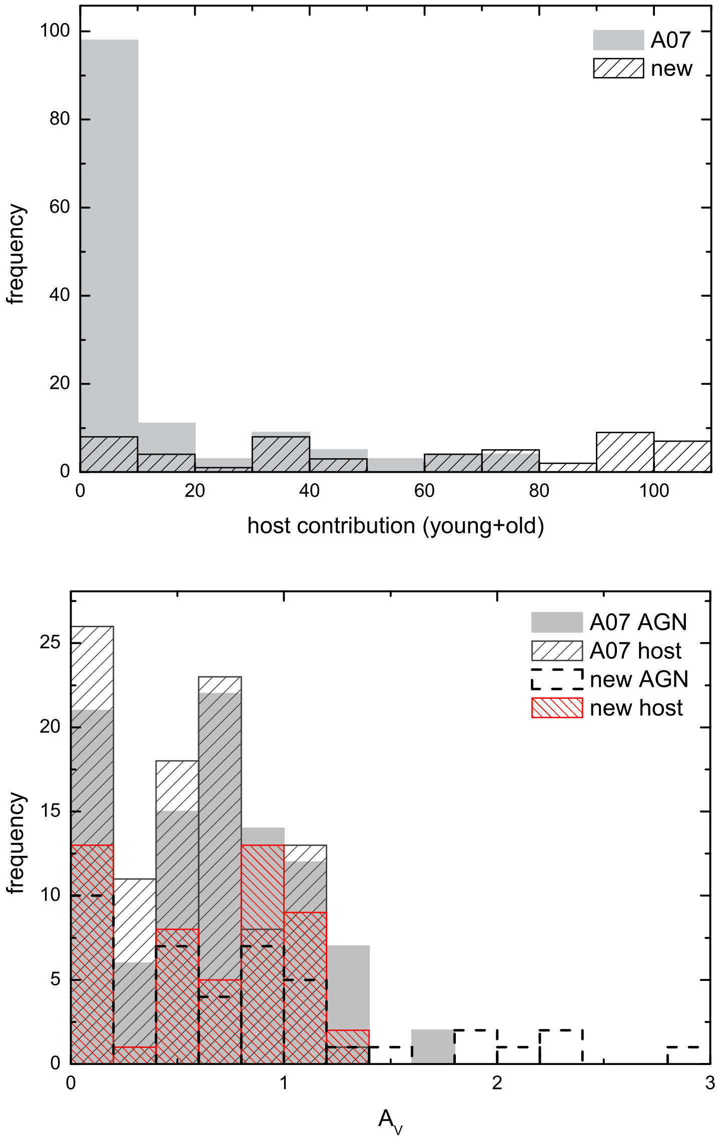

Figure 2.27: *Upper panel:* Host galaxy contribution (250 Myr plus 1.4 Gyr starburst) estimated form template fitting (Eq. 2.29). Note that only $z < 0.8$ are fitted with stellar templates. *Lower panel:* Reddening (due to a foreground screen) in visual magnitudes estimated from the template fitting procedure (Eq. 2.29). Shown are host and AGN components. A slight trend of the AGN emission being redder than the stellar one is evident.

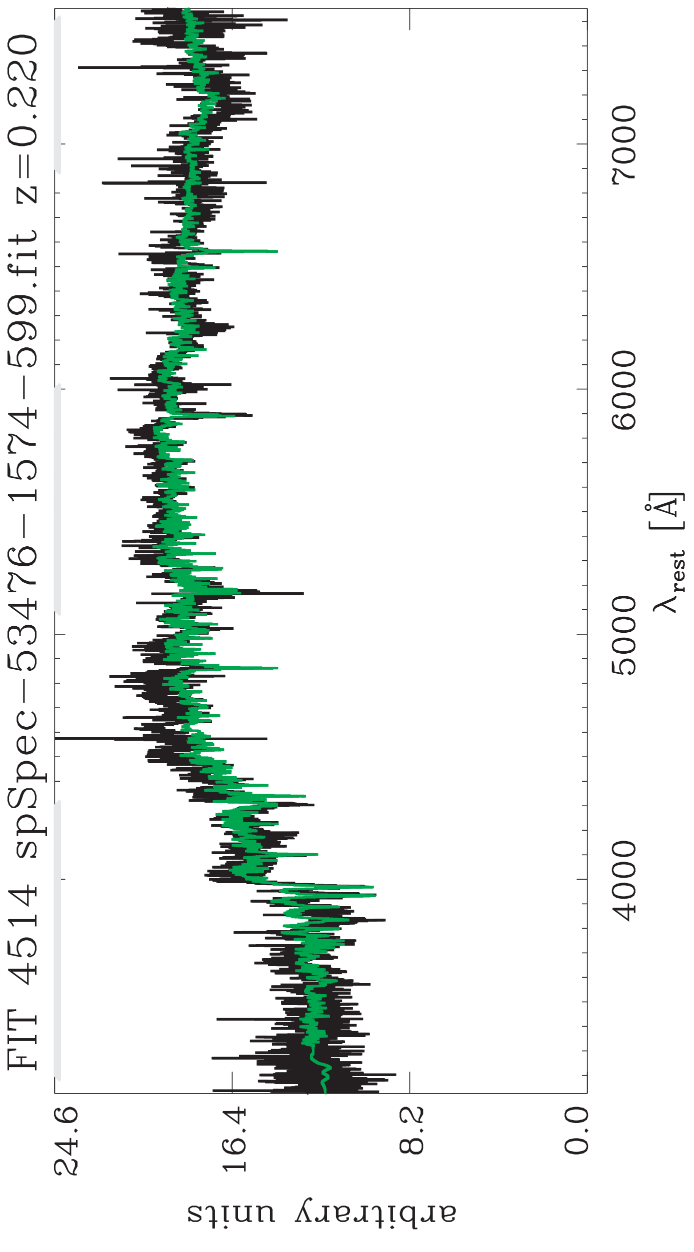

Figure 2.28: Example spectrum. Galaxy with evolved stellar population. The fitted green curve is dominated by the 1.4 Gyr starburst spectrum. *Middle panel:* Narrow emission-line galaxy with a significant host contribution (~ 40% 1.4 Gyr and ~ 10% 250 Myr starburst fraction) and a power-law fraction of ~ 50%.

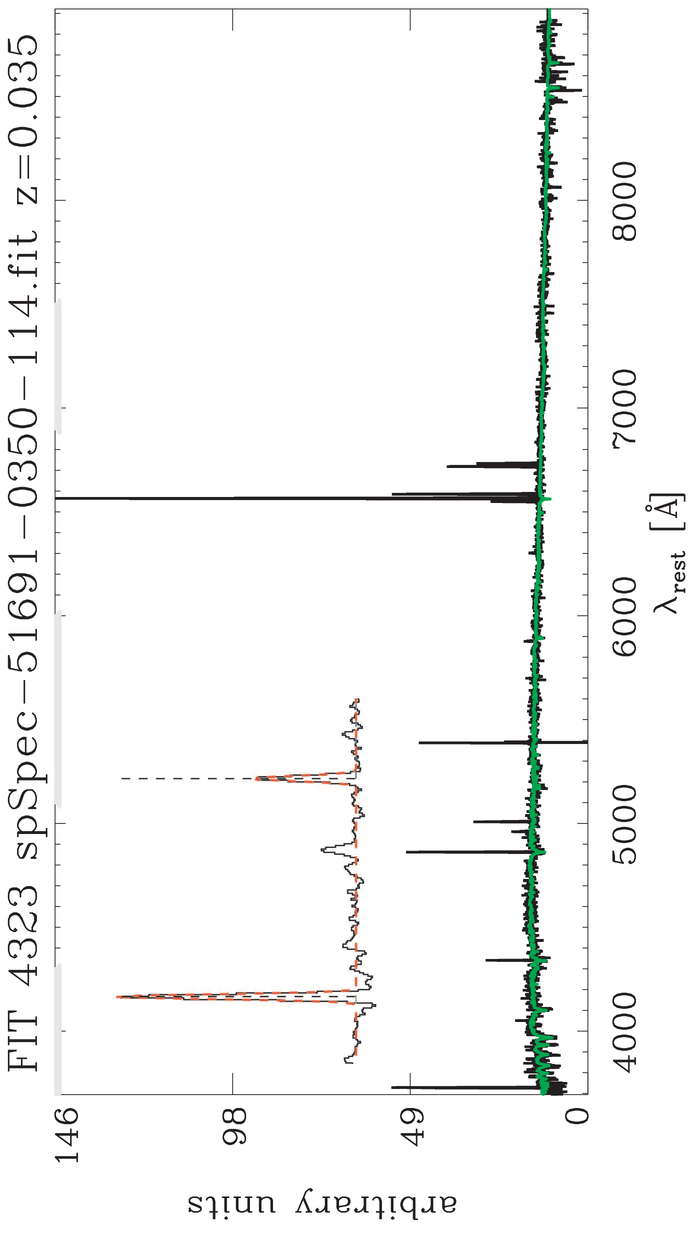

Figure 2.29: Example spectrum. Narrow emission-line galaxy with a significant host contribution ($\sim$ 40% 1.4 Gyr and $\sim$ 10% 250 Myr starburst fraction) and a power-law fraction of $\sim$ 50%. The inset shows fits the Hβ/[O III] complex. Here, Hβ is a composite of HII region emission and absorption from stellar atmospheres.

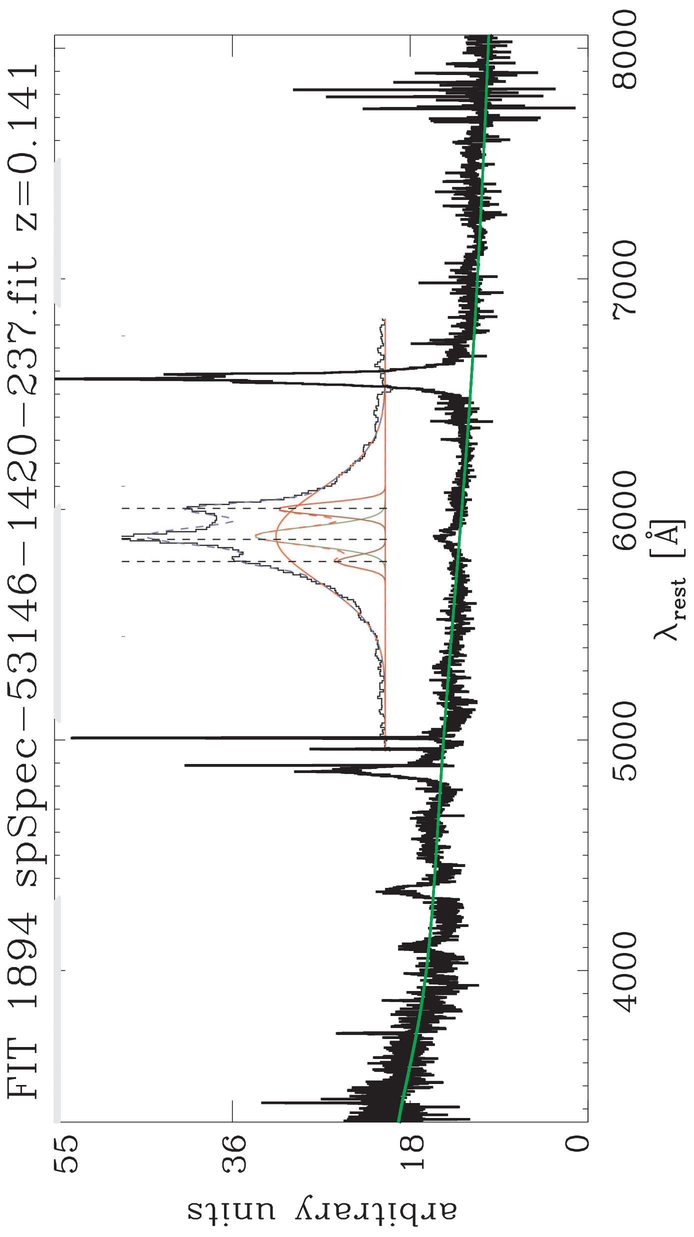

Figure 2.30: Example spectrum. Broad-line AGN with no discernible stellar component. The inset shows the multi-component fit to the Hα/[N II] complex.

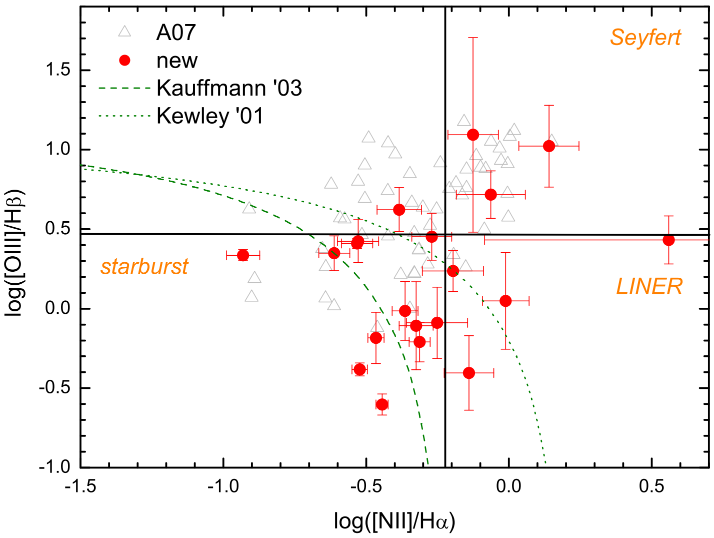

Figure 2.31: Diagnostics diagram for AGN of our sample for which all emission lines have been detected. Open triangles are targets also included in A07, and filled squares are our new additions. The dotted line corresponds to the starburst/AGN demarcation of Kewley et al. (2001). The dashed curve is the revised version of Kauffmann et al. (2003). The interjacent region represents starburst/Seyfert composite galaxies.

The fitting procedure returns two measures of extinction. The first is an estimate of the continuum reddening and the second one, the Balmer decrement ($H\alpha/H\beta$), an estimate of the differential reddening within the line-emitting regions. The latter one is commonly used to correct emission line fluxes. Baldwin et al. (1981) (hereafter BPT) and later revised by Veilleux & Osterbrock (1987), used line ratios of neighboring emission lines in order to distinguish between stellar and non-stellar excitation mechanisms. The flux ratios [O III] λ5008Å/Hβ and [N II] λ6585Å/Hα (the classical BPT diagram) have characteristic values for the cases of star-formation related UV excitation (in HII regions) and non-stellar excitation from the hard power-law of an active nucleus. Differential reddening can usually be neglected, because of the proximity of the involved emission lines. LINERs can be distinguished from Seyfert 2s by their low values of [O III] λ5008Å/Hβ relative to [N II] λ6585Å/Hα, and from the HII regions by their larger values of [N II] λ6585Å/Hα (cf Sec. 3.4.5).

The emission lines have been measured in the continuum- and stellar-contribution subtracted spectra and the BPT diagram of narrow-line ratios is shown in Fig. 2.31 for those galaxies, which have all the involved lines included and well detected in their rest-frame spectrum. Measurement error are shown only for some sources, but they are representative for all presented data point. The two green curves represent the division between star-formation driven and AGN driven emission. The dotted line has been derived from stellar photoionization simulations of Kewley et al. (2001), whereas the dashed line has been derived empirically from SDSS data by Kauffmann et al. (2003). The region in the BPT diagram between these lines is occupied by composite starburst/Seyfert galaxies (cf Sec. 3.1). Most data points of the present sample lie in the region occupied by Seyfert galaxies. A number of galaxies have line ratios typical of those of composite galaxies and only a few sources appear to be purely starburst driven. As will be outlined in Chap. 3, composite galaxy seem to be promising candidates to study the fueling processes of the nuclear starburst and Seyfert activity. As will also be discussed in Chap. 3, one has to take the SDSS spectroscopic fiber size into account. With a diameter of $3''$, the fibers cover a significant fraction of the host galaxy emission (Fig. 2.32). The probed physical sizes do additionally change with redshift. This complicates matters and this appears to be a serious problem regarding the identification of low-luminosity AGN. In these sources, Seyfert signatures can possibly be hidden by the strong host galaxy light (cf Moran et al. 2002). Aperture corrections for spectroscopy, however, are hard to come by (e.g., Kewley et al. 2005) and are, therefore, omitted at the moment.

2.4.5 FIRST, 2MASS data

In order to conclude this chapter, complementary information from the cross-match of the optical counterparts with the FIRST and 2MASS databases are presented.

Cross-matching with FIRST and 2MASS

As already discussed in Sec. 2.4.2, X-raying AGN are also often found to exhibit radio emission. Besides the X-ray/UV correlation discussed in Sec. 2.4.3, there is a positive correlation between X-ray luminosity and radio luminosity over 8 orders of magnitude (e.g., Brinkmann et al. 2000; Panessa et al. 2007). Again, such a correlation suggests that the emission mechanisms are physically linked. However, common belief is that radio emission originates from relativistic electrons in a jet, whereas the X-rays

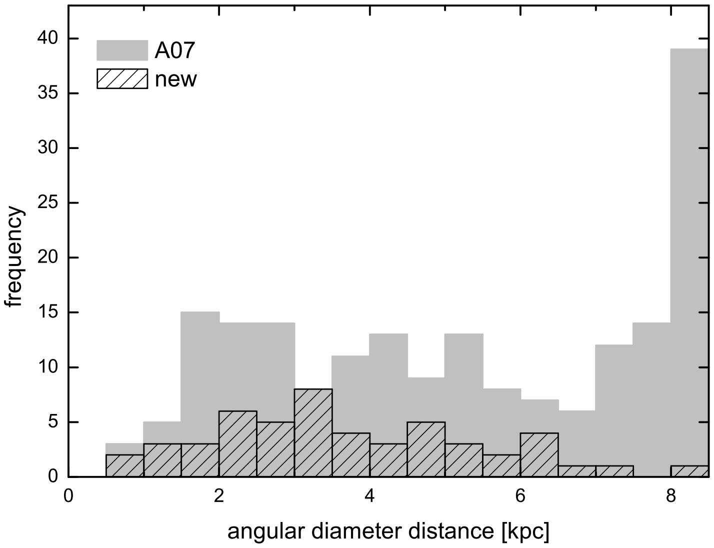

Figure 2.32: Distribution of angular diameter distances of the sample. The values have to be multiplied by 3 to yield the linear sizes covered by the 3″ diameter spectroscopic fibers.

originate from the hot accretion-disk corona. Therefore, it is not established yet, what the reason for this correlation is. One possible explanation is the inverse Compton up-scattering of radio photons in a relativistic electron plasma of a jet. Since no correlation is found between radio-loudness and X-ray luminosity (Panessa et al. 2007), this cannot be the only explanation.

A cross-match of the SDSS positions with the FIRST database resulted in a set of 51 radio detections (i.e. 21% of the sample). About 80% of the matches are unresolved[21] by FIRST. The remaining 20% are only slightly resolved and large scale radio jets have no influence on the results. Figure 2.33 displays the L_{radio}/L_X correlation, being similar to the studies mentioned above. The color-coding of the left panel illustrates the radio loudness of the objects. According to Ivezić et al. (2002b), the radio loudness is computed relative to the *i* band:

$$R_i = \log\left(\frac{F_{\text{radio}}}{F_{\text{optical}}}\right) = 0.4(m - t), \tag{2.30}$$

---

[21] A FIRST source is termed to be spatially resolved, if the square root of the ratio of integrated flux over peak flux is larger than 1; $\theta = \sqrt{F_{\text{int}}/F_{\text{peak}}} > 1$.

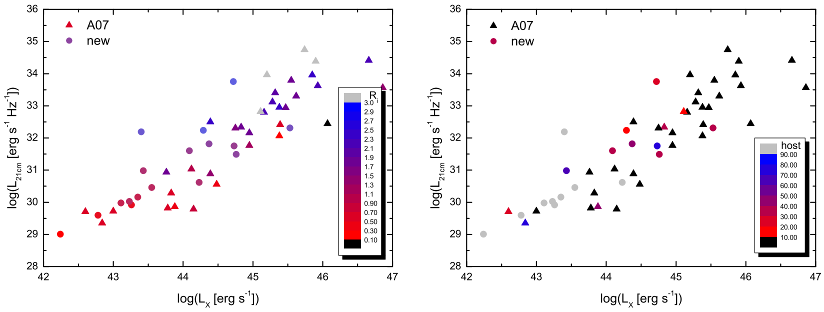

Figure 2.33: Correlation of X-ray and 21 cm radio luminosities. *Left panel:* The color coding shows the radio-loudness measure R_i relative to i_{PSF}. Radio loud objects typically have $R_i > 1$. A trend of more luminous objects being radio-louder is clearly visible. *Right panel:* The color coding shows the host galaxy contribution estimated from the spectral fitting. The more luminous the object, the smaller is the host galaxy contribution.

where

$$t = -2.5 \log \left(\frac{F_{int}}{3631 \text{ Jy}} \right) \tag{2.31}$$

is the AB[22] radio magnitude. In this equation, f_{int} is the integrated interferometric flux. Clearly, the more luminous the galaxy the more radio loud the galaxy is. A similar trend with radio/X-ray luminosity can be recognized for the host galaxy light contribution (Sec. 2.4.4). The AGN component dominates the more luminous objects.

Virtually all 2MASS objects have SDSS optical counterparts within 2″ of the NIR position (Ivezić et al. 2002a). A match of the SDSS position with the 2MASS database yields a set of 155 2MASS matches. As mentioned earlier, NIR radiation is less influenced by dust extinction and, furthermore, the QSO spectral energy distribution has a local minimum around 1 μm (cf Fig. 3.17). This reduces the contrast between the strong nucleus and the stellar host. The two-color diagram can be used to investigate the effects of dust extinction, and thermal or power-law origin of the emission (e.g., Alonso-Herrero et al. 1996). The J, H, and Ks fluxes are extracted manually from the 2MASS atlas frames in the following manner:

1. sky subtraction by using enclosed header information (SKYVAL),
2. determination of Gaussian FWHM at the position of the GS,

---

[22] Unlike the traditional calibration with the Vega spectrum, AB magnitudes are defined via a monochromatic spectrum source (e.g., Fukugita et al. 1996).

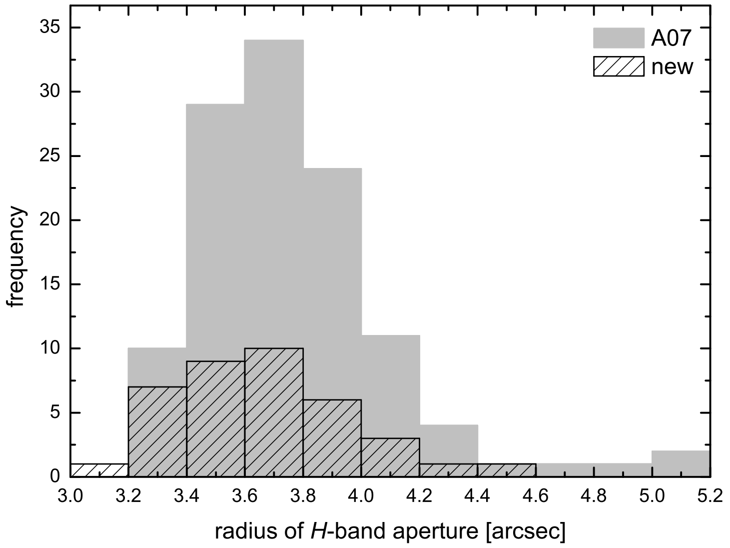

Figure 2.34: Size distribution of 2MASS apertures, as derived from the Gaussian FWHM of the GS.

3. centering the aperture with the size of the GS FWHM on the galaxy position,
4. count extraction and conversion to magnitudes via enclosed zero point.

The apertures have been chosen according to the FWHM of the seeing. The seeing has been determined from the GS (Fig. 2.34). In this way, the fluxes of all galaxies are measured within the seeing disk in each and therefore originate from comparable regions of the host galaxies. Figure 2.35 presents the results for the matched sources. In this figure, regions of typical colors of normal galaxies and of $z = 0$ QSOs are indicated. Most of the sources presented here populate the gap between these two regions. The location of objects can be explained by reddening due to warm and hot dust. Dust reddening occurs almost exclusively in the $H - Ks$ direction. This leads to the result that the red NIR colors of AGN are attributed to dust-reprocessed non-stellar emission (cf Glass & Moorwood 1985). The colors of the present sample can still be connected to the colors of normal galaxies. The effect of 1 mag of visual extinction is shown in the two-color diagram. Most colors, however, suggest a reddening due to dust heated most likely by

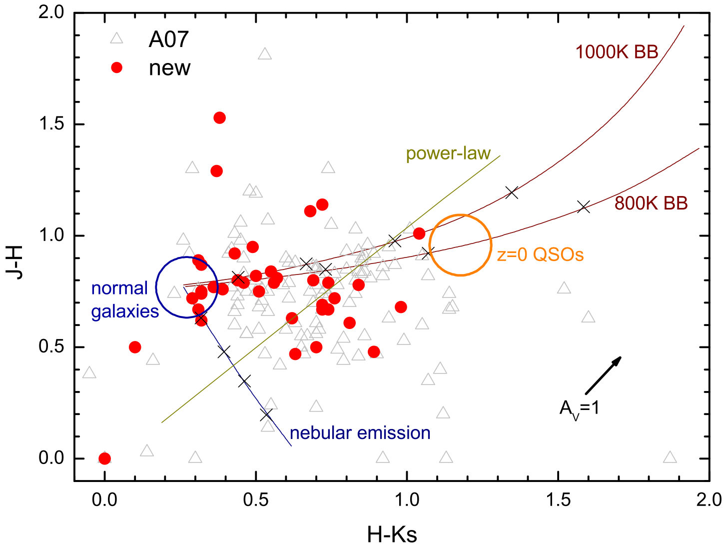

Figure 2.35: $J - H$ vs. $H - Ks$ two-color diagram. The average locations of normal galaxies and zero-redshift QSOs are shown. The effect of $A_V = 1$ is indicated by the arrow. Starting with stellar colors, mixing curves with different components are shown: pure blackbody emission with temperatures $T = 800$ K and $T = 1000$ K, and hydrogen nebular emission. The crosses on the curves indicate the fractions 0.2, 0.4, 0.6, and 0.8 due to non-stellar components in the Ks band. Pure power-law colors are also indicated.

an AGN – optical spectroscopy shows that $> 80\%$ are NLAGN or BLAGN (cf Tab. 2.4).

The results of the FIRST and 2MASS correlations are consistent to similar studies of X-ray selected AGN, and provide promising prospects for future source classification of the remaining ~ 1000 sources of the initial sample that do not have spectroscopic observations.

2.5 Conclusions

This chapter introduced the need for high angular resolution in order to tackle questions related to the fueling of nuclear activity in terms of SMBH accretion and star formation. Ground based observations have notoriously been hampered in the past by variable seeing conditions that did not allow the observer to exploit the diffraction limit of the telescope. Today, the wave-front distortions originating from Earth's turbulent atmosphere can be corrected with the help of AO systems. These systems require the acquisition of a point-source reference in order to assess the shape of the wave-front distortion. Usually, one chooses a natural GS close to the science target. The recently emerging framework of the VO in conjunction with large area sky surveys, can be used to come up with a sample of AO-suitable AGN efficiently. The panchromatic information (fluxes, colors, and spectra) can be consulted to carry out a global characterization and classification of these objects. X-rays prove to be very efficient in selecting AGN candidates, which can be further studied with optical, radio, and NIR data. In many cases, such multiwavelength information confirms the Seyfert character of the objects started with. In a next step, one can use the classification results of a sample of fully characterized sources and apply them to samples lacking part of the information (e.g., optical spectroscopy). AO-assisted NIR observations of samples selected in such ways represent a major new building block, since these observations will provide further clues on the connection between Seyfert activity and host galaxy evolution. The show case of Mrk 609 will be presented in the next chapter.

CHAPTER 3

SINFONI observations of Mrk 609

Based on work published in Zuther et al. (2007).

The starburst/Seyfert composite galaxy Mrk 609 was part of the initial sample as mentioned in Chap. 2 (Zuther et al. 2004b). Due to more stringent AO criteria, especiall the GS brightness, this galaxy is not part of the new sample (Chap. 2) anymore. The sucessful observation of Mrk 609 with the new integral field spectrometer (IFS) SINFONI[1] during its Science Verification, however, demonstrates that even under demanding observing conditions and partial correction, valuable host galaxy studies are possible. In the follwing sections an overview of the current knowledge of the starburst/Seyfert composite galaxies and of the observational setup will be given. Then follows a detailed analysis of the 3D spatial/spectral NIR data of Mrk 609 and an interpretation within the framework layed out in Chap. 1.

3.1 Starburst/Seyfert composite galaxies

A subgroup of AGN, the *starburst/Seyfert composite* galaxies (Moran et al. 1996), appears to be best suited to studying the starburst-AGN connection, since the AGN and starburst components present themselves at the same level of activity (Panessa et al. 2005). These objects can be characterized by optical spectra that are dominated by starburst features, while the X-ray luminosity and its variability are typical of Seyfert galaxies. The former property is based on the emission-line diagnostic diagrams by Veilleux & Osterbrock (1987). The latter argument stems from the light-travel-time argument, in which the size of the emitting region is given by the variability time scale times the speed of light. Close inspection of the optical spectra often reveals some weak Seyfert-like features, e.g. [O III] being

---

[1] Spectrograph for INtegral Field Observations in the Near Infrared @ ESO VLT, Chile

significantly broader than all other narrow lines or a weak broad Hα component. There is a resemblance to narrow-line X-ray galaxies (NLXG, e.g. Boyle et al. 1995), which also show spectra of a composite nature. Their soft X-ray spectra are hard, i.e. flat (Almaini et al. 1996), but it is still not clear how this strong and hard X-ray emission can be reconciled with the weak/absent optical Seyfert characteristics. The faintness of these objects in the X-ray, as well as in the optical domain, has not allowed us to study them in detail so far.

Near-infrared (NIR) imaging spectroscopy has considerable advantages over visible wavelengths: Besides the much smaller dust extinction, there are a number of NIR diagnostic lines (in emission and in absorption) to probe the excitation mechanisms and stellar content in galaxies. Among these are hydrogen recombination lines, rotational/vibrational transitions of H_2, stellar features like the CO(2-0) and CO(6-3) absorption band heads, and forbidden lines like [Fe II] and [Si VI] (Hill et al. 1999; Mouri 1994; Marconi et al. 1994).

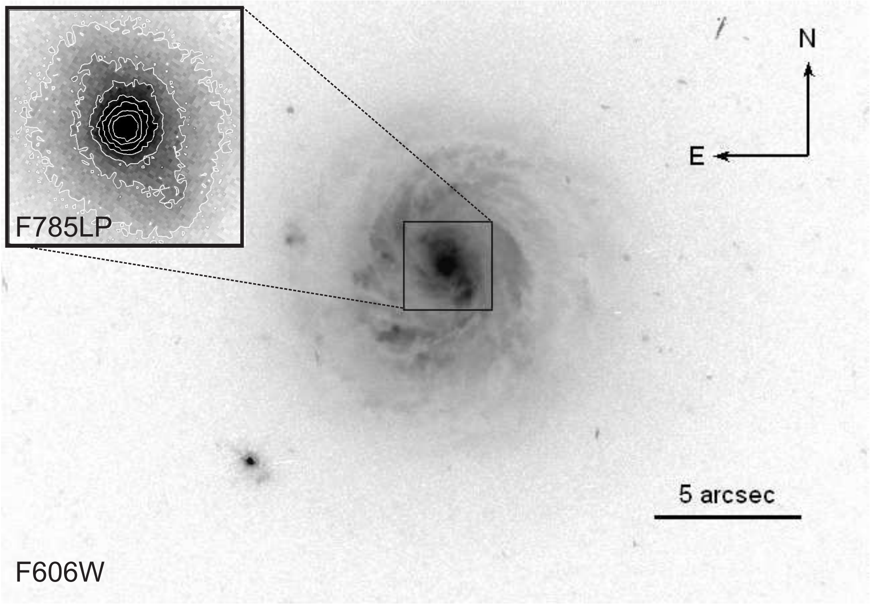

Figure 3.1: HST F606W (~0.6 μm) image of Mrk 609 (Malkan et al. 1998). The black box indicates the SINFONI field of view of 3 × 3 arcsec^2. The upper left inset is an HST F785LP (~0.9 μm) image of the nuclear 3 × 3 arcsec^2 (Nelson et al. 1996). Compare with Figs. 3.3 (d), 3.5 (a), and the structure image (Fig. 2) of Deo et al. (2006).

3.2 Mrk 609

Mrk 609 shows a mixture of nuclear star formation and Seyfert activity and appears to be a showcase for studying the nuclear activity with integral field spectroscopy (IFS) in order to probe the coeval existence of these phenomena.

There have been several observations of Mrk 609 (Figs. 3.1 and 3.17 for the SED). It is a member of the original sample of Osterbrock (1981), with which the role of reddening in Seyfert 1.8/1.9 galaxies was studied. These observations were followed up by X-ray, ultraviolet, optical, and infrared studies (Pappa et al. 2002; Rudy et al. 1988; Goodrich 1990; Rudy & Rodriguez-Espinosa 1985), refining the classification of Mrk 609 as a starburst/Seyfert composite. The UV/optical line ratios and the X-ray spectrum furthermore indicate a small extinction towards the nucleus. Rudy et al. (1988) and Goodrich (1990) suggest that smaller-than-normal optical depths and lower ionization are responsible for the large Balmer decrement found in the optical spectrum (Fig. 3.16).

Optical (~0.6 μm; Nelson et al. 1996) and NIR (~0.9 μm Crenshaw et al. 2003) imaging observations of Mrk 609 with the Hubble Space Telescope (HST) have been used to address questions regarding the extension of the scattering medium in Seyfert 2 galaxies and the dependence of AGN fueling on the host morphology (Fig. 3.1). Nelson et al. studied a sample of Seyfert and non-Seyfert Markarian galaxies and found that Seyfert 1.8 and 1.9 show extended nuclear light profiles similar to Seyfert 2 galaxies. The energetics of the (circum-) nuclear region of Seyfert 2s is strongly influenced by starburst activity. In combination with some scattering screen, this provides the extinction responsible for the observed shape of the light profiles. Seyfert 1.5 galaxies, on the other hand, have nuclear profiles typical of Seyfert 1 galaxies, which are unresolved and bright. Mrk 609 shows a strong Seyfert 1-like nucleus, but it appears to be slightly extended. Furthermore, weak broad H-recombination lines have been detected in optical spectra, which result in an intermediate Seyfert 1.5-1.8 classification (Goodrich 1990; Osterbrock 1981). This work supports the above findings.

Crenshaw et al. and Deo et al. (2006) find a larger bar fraction for narrow-line Seyfert 1 (NLS1) galaxies than for broad-line Seyferts (BLS1). NLS1 are believed to be systems accreting close-to or above the Eddington limit. The active state requires an efficient fuel supply, which can be supported by stellar bars. As a BLS1, the large-scale optical morphology of Mrk 609 appears flocculent and shows no signs of a bar (Crenshaw et al. 2003; Deo et al. 2006) (Fig. 3.1). The nuclear morphology, however, deviates from a circular symmetric appearance. The NIR image of Nelson et al. (see inset in Fig. 3.1), which is less influenced by dust extinction than the optical image, reflects this situation. Two spiral arms turn out to connect to an elongated nuclear structure (northeast-southwest direction), probably resembling a nuclear stellar bar. In a recent numerical study, Englmaier & Shlosman (2000) find that a grand-design nuclear two-arm spiral structure can be formed in the presence of a weak stellar bar. Only depending on the nuclear mass and the gas sound speed, such structures can allow for the inward mass transport beyond the inner Lindblad resonance towards radii of 50-100 pc. In respect thereof Deo et al. (2006) find that especially the class of flocculent spirals avoids the presence of large-scale bars, as appears to be the case for Mrk 609.

3.3 Observations and data reduction

3.3.1 Near-infrared data

The observations were carried out during the science verification phase[2] (October 2004) of SINFONI, the new AO-assisted integral field spectrometer (see Fig. 3.2) mounted at Yepun, Unit Telescope 4 of the ESO Very Large Telescope in Chile (Eisenhauer et al. 2003). The AO guiding was carried out on the nucleus of Mrk 609. The average seeing was around $0\farcs7$. The 100 mas pixel scale with a field-of-view (FOV) of $3'' \times 3''$ was used. The 2D image on the sky was sliced by small mirrors into 32 slitlets, which then were reimaged onto a pseudoslit and dispersed onto a 2k×2k detector (Fig. 3.2). The observations covered J and $H + K$ bands with integration times of 5 minutes and 30 minutes, respectively. Dispersion was achieved with the J and $H + K$ gratings at a spectral resolution of $R_J \sim 2000$ and $R_{H+K} \sim 1500$. Successive target (T) and sky (S) observations (...TSST...) were acquired to produce sky-subtracted frames.

The reduction and reconstruction of the 3D cubes were carried out using the MPE reduction software *spred 3.6* [3], IDL, and QFitsView[4]. Bad pixel, cosmic rays, and flat field corrections were applied to the 2D raw frames. The 3D cubes were reconstructed using calibration frames for the slitlet distances and the light dispersion.

Intermediate standard-star observations (near in both time and airmass

---

[2] `http://www.eso.org/science/vltsv/sinfonisv/xrayagn.html`

[3] Kindly provided by Matthew Horrobin (MPE, Garching).

[4] Written by Thomas Ott (MPE, Garching); `www.mpe.mpg.de/~ott/QFitsView`

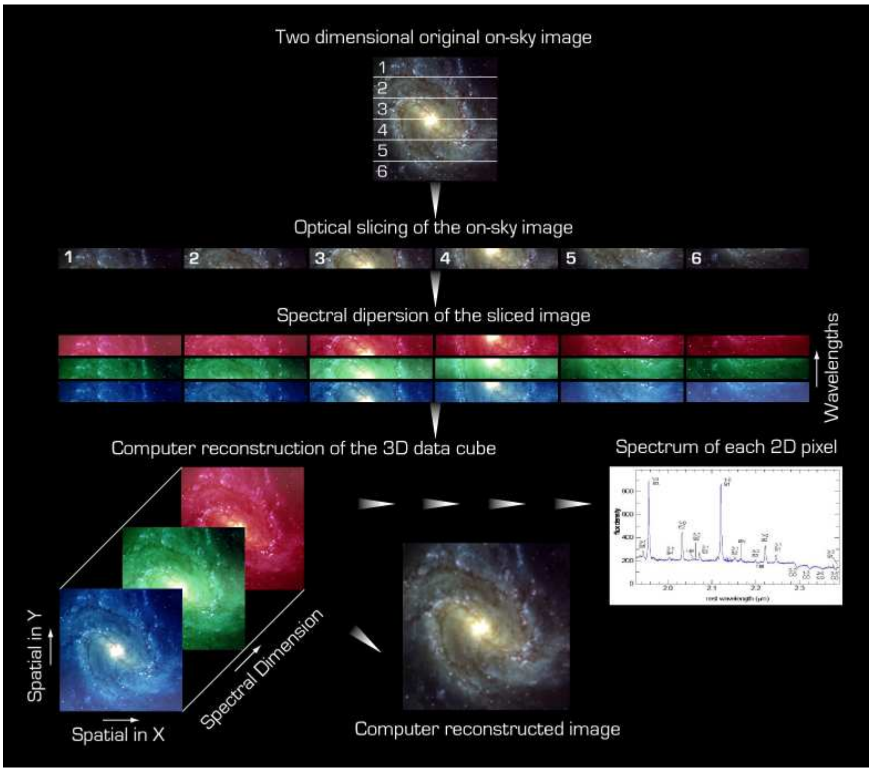

Figure 3.2: Principle of integral field spectroscopy. The 2D image on the sky is sliced into a number of small slitlets by small mirrors. These slitlets are rearanged along a pseudoslit and then dispersed onto the detector by a grating, resulting in a 3D datacube. Thus, each sky pixel is associated with a spectrum at this position. During post-observation analysis, the analysis software is able to reconstruct the 2D image from the 3D cube Courtesy of ESO.

to the target exposures) of the G2V star HIP-021070 were used to correct for strong atmospheric (telluric) absorptions. They can be minimized by dividing the science target spectrum by the standard star spectrum. This step introduces features into the resulting spectrum that are intrinsic to the standard star and that can be accounted for by multiplication by the atmospheric-transmission-corrected solar spectrum. Since the standard star was saturated on the detector (see below in the context of flux calibration), the spectrum with telluric absorptions was extracted from the wings of the 2D image. The G2V spectral characteristics were removed by multiplying by the well known, high signal-to-noise solar spectrum (as provided by Maiolino et al. 1996). In the range of reduced atmospheric transmission (as indicated in Fig. 3.6), which is not covered by the Maiolino et al. spectrum, the solar spectrum was interpolated with a blackbody, because the original solar atlas did not show any intrinsic features in that range (Wallace et al. 1996).

Flux calibration is problematic, since the calibration-star observations saturated the detector. In order to approach a flux calibration, ignoring the fact of variability (up to 30%) of Mrk 609 found by Rudy & Rodriguez-Espinosa (1985), the 2MASS J, H, and Ks fluxes were used. Fluxes were measured within a $3''$ diameter aperture in the 2MASS atlas images and were applied to the $3'' \times 3''$ SINFONI FOV. It has to be noted that this method has the drawback of ignoring the differences in spatial resolution. An accuracy of the absolute flux was estimated to be around 40%, but this is not of any significant importance, since the measurement of line ratios was the primary interest in this work. For these, in principle, an absolute flux calibration is not necessary. The magnitudes were converted to flux densities using the Spitzer space telescope magnitude to flux density converter[5]. For J a $J_{\mathrm{2MASS}} = 13.68$ was measured, which corresponds to $f_{J\mathrm{2MASS}} = 1.06 \times 10^{-14}$ W m$^{-2}\mu$m^{-1} at $\lambda_{\mathrm{eff}}(J_{\mathrm{2MASS}}) = 1.235$. For the $H + K$ band the flux density at the effective wavelength of the Ks band was used. The measured $Ks_{\mathrm{2MASS}} = 12.50$ corresponds to $f_{Ks\mathrm{2MASS}} = 4.29 \times 10^{-15}$ W m$^{-2}\mu$m^{-1} at $\lambda_{\mathrm{eff}}(Ks_{\mathrm{2MASS}}) = 2.159$. The total flux within the SINFONI FOV was scaled according to these values. Because of the low value of $E(B - V) = 0.056$ (Schlegel et al. 1998), no correction for Galactic extinction is applied.

From the final reconstructed 3D cube spectra and emission line maps were extracted. The emission line maps presented in Figs. 3.3, 3.4, and 3.5 were created by summing up the flux of the emission line and then subtracting the average flux density of the continuum left and right of the line. The features seen in the Paα map define the regions where spectra were extracted (Figs. 3.6, 3.7, 3.8, and 3.9). The radius of the extraction regions is 5 pixels ($0\farcs25$).

3.3.2 Millimeter data

Mrk 609 was additionally observed in ^{12}CO(1-0) during an observing campaign of cluster galaxies with the Nobeyama 45m telescope in March 2005. In this observation, the autocorrelator was used as backend and an integration time of 45 minutes was applied. The measured antenna temper-

---

[5] `http://ssc.spitzer.caltech.edu/tools/magtojy/`

atures were transformed to a main-beam temperature using a main-beam efficiency of 0.38. The baseline-subtracted CO(1-0) spectrum is presented in Fig. 3.14.

3.4 Results and discussion

In this section, the results of the spatially resolved spectroscopy of the circumnuclear environment of Mrk 609 and the CO(1-0) observation are presented.

3.4.1 Tracing the continuum and emission line gas

The SINFONI imaging spectroscopy allows us to study the inner 2 kpc of Mrk 609 at a spatial resolution of about 270 pc. Several emission and absorption features were identified in the individual J and $H+K$ spectra across the FOV (see Figs. 3.6 and 3.8). Among these are hydrogen recombination lines, rotational/vibrational lines of molecular hydrogen, forbidden transitions of [Fe II] and [Si VI], as well as stellar CO(6-3) and CO(2-0) absorption. From selected emission lines continuum-subtracted line maps were produced (Figs. 3.3, 3.4, and 3.5).

The nuclear Paα emission was used in order to assess the spatial resolution. Fitting a 2D Gaussian to the nuclear Paα gives a rough estimate for the spatial resolution, because no other point-source observations were available for these observations. An FWHM of about 8 pixel (~$0\farcs4$) was found for the minor axis, while the major axis is clearly extended. This is expected to be a reasonable measure of the point-spread function at all wavelengths. This size corresponds to a linear scale of about 270 pc ($1'' \approx 680$ pc) at the redshift of $z = 0.0345$.

The morphologies of the hydrogen recombination line maps cleary differ from the continuum maps. The Paα map reveals five emission peaks that are indicated in Fig. 3.3 (a). The continuum emission presented in panel (d) of Fig. 3.3 shows an elliptical structure extending in a northeast/southwest direction and connecting to the large-scale spiral arms visible in the HST image (Fig. 3.1). This morphology is similar to that of the nuclear stellar bars found in several other galaxies (e.g. Erwin & Sparke 2002; Martini et al. 2003). Results of N-body simulations carried out by Patsis (2005), in which stellar particles move on (quasi-) periodic orbits in a bar potential, also resemble the nuclear continuum morphology of Mrk 609.

The Paα peaks are apparently aligned with the barred continuum. One peak is centered on the nucleus. The four other peaks lie at the tip of the

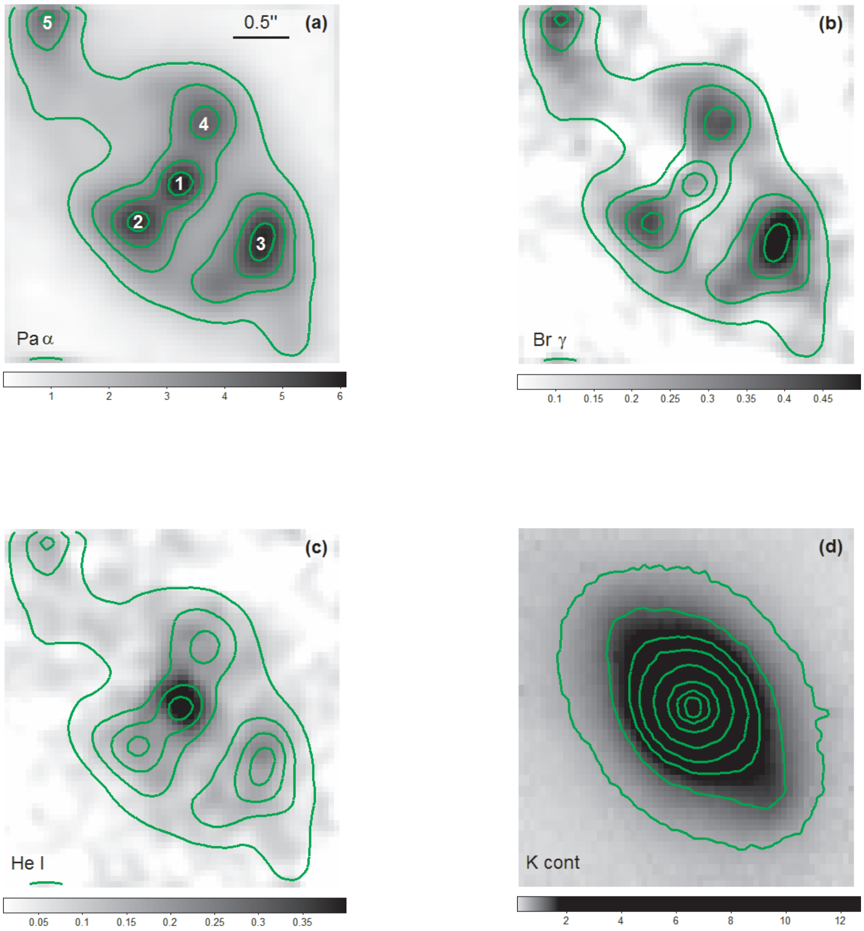

Figure 3.3: $H + K$ emission line maps of recombination lines. They were created with QFITSVIEW by summing the flux over the emission line and subtracting the median value of the neighboring continuum (a-c). All images were smoothed with a 3- pixel Gaussian. The values of the color bars are in units of 10^{-19} W m^{-2}. (a) Narrow Paα; contours are calculated relative to the peak flux (90, 70, 50, 30%). (b) Brγ overlayed with Paα contours. (c) He I 2.059 μm overlayed with Paα contours. (d) Continuum image in a region without emission lines around 2.2 μm. The panels are $3'' \times 3''$ each. North is up and east is left. Regions are indicated in panel (a) from which cummulative spectra were extracted. Regions 2 and 4 have a projected distance of about 420 pc, region 3 $\approx$ 630 pc, and region 5 $\approx$ 1.3 kpc to the center.

major axis where the bar connects to the spiral arms (regions 3 and 5) and on the minor axis (regions 2 and 4). In addition to the clumpy Paα emission

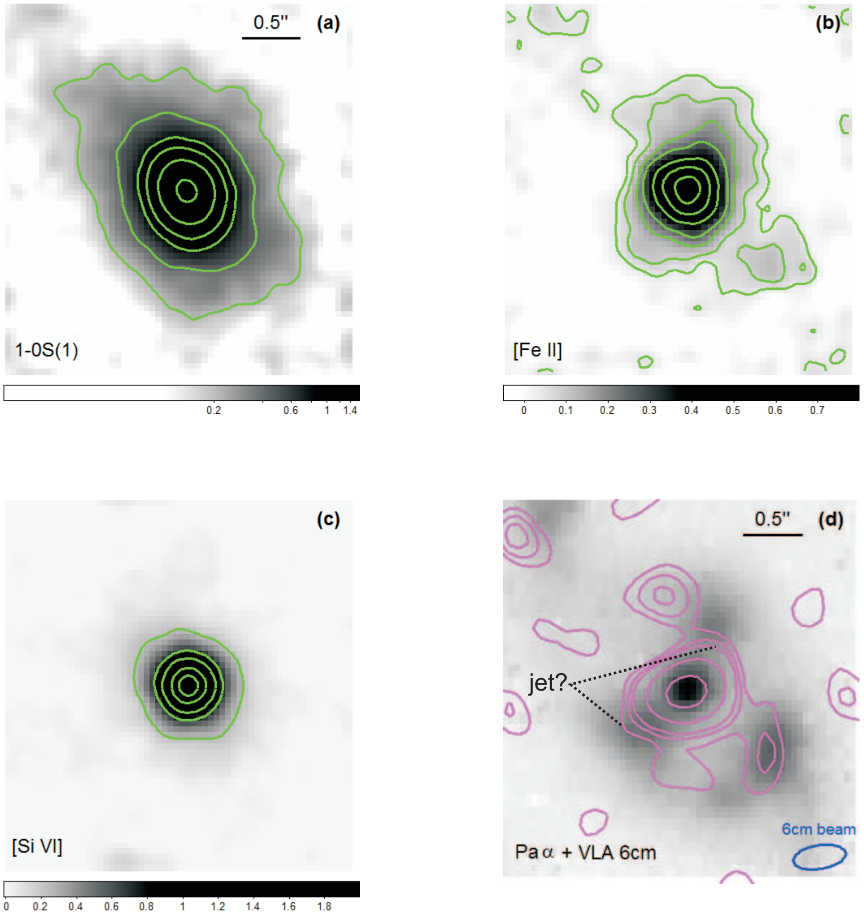

Figure 3.4: $H + K$ emission line maps (using the same procedure as for Fig. 3.3) of: (a) 1-0S(1) (contours: 90, 70, 50, 30, and 10% of peak flux), (b) [Fe II] 1.664 μm (contours: 90, 70, 50, 30, 20, 10, and 5% of peak flux), and (c) [Si VI] (contours: 90, 70, 50, 30, and 10% of peak flux). The colorbar values are in units of 10^{-19} W m^{-2}. Panel (d) displays an overlay of the Paα map from Fig. 3.3(a) with the 6 cm VLA map in (magenta) contours (from Ulvestad & Wilson 1984). The blue ellipse in the lower right corner indicates the 6 cm beam size. The panels are $3'' \times 3''$ each. North is up and east is left.

a fainter and smoother Paα component is visible, which extends between the distinct regions. There is a striking similarity between this configuration and the observation of Emsellem et al. (2003), who detected a nuclear two-arm gas spiral in the early type galaxy NGC 2974. This spiral structure (~200 pc radius) is embedded in a ~ 500 pc radius nuclear stellar bar. These

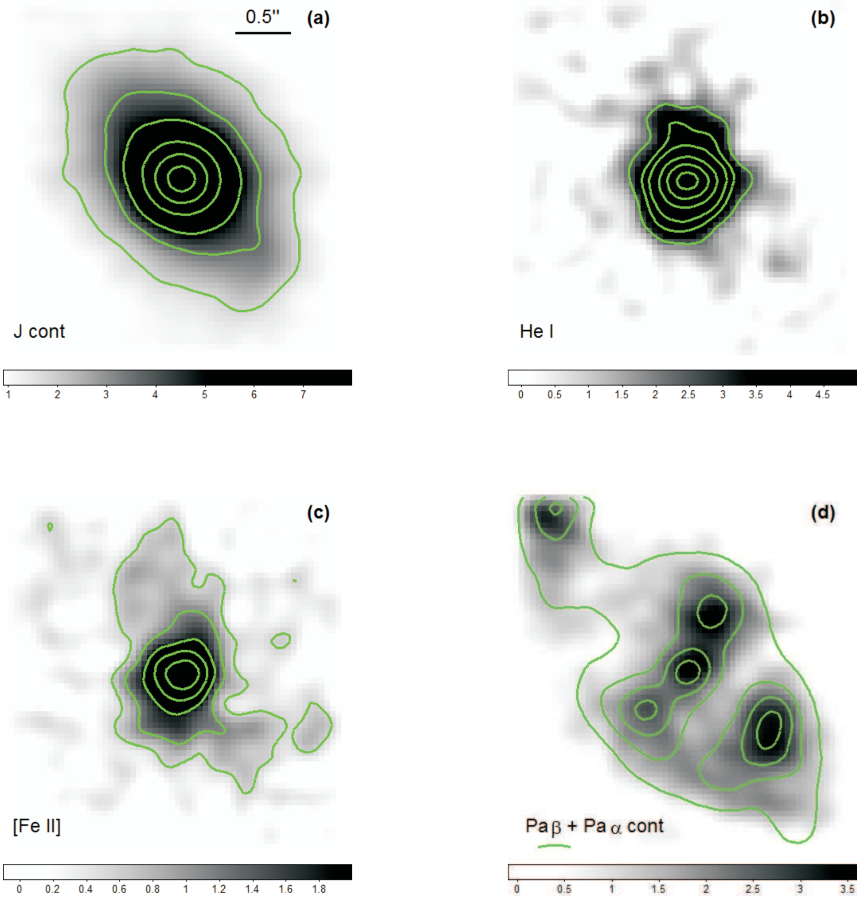

Figure 3.5: J-band continuum and emission line maps of: (a) 1.25 μm continuum (contours: 90, 70, 50, 30, 20, and 10% of peak flux), (b) He I 1.083 μm (contours: 90, 70, 50, 30, 20, and 10% of peak flux), (c) Fe II 1.257 μm (contours: 90, 70, 50, 30, and 15% of peak flux), and (d) Paβ overlayed with Paα in contours (see Fig. 3.3(a)). Color bar values are in units of 10^{-19} W m^{-2}. The panels are 3×3 arcsec^2 each. North is up and east is left.

dimensions are roughly the same (within a factor of 2) as for Mrk 609 (Fig. 3.3 (a) and (d)). Simulations show that gaseous material can be transported along these spiral arms towards the central region (Englmaier & Shlosman 2000). Mrk 609 has also been studied at 6 cm wavelengths (Ulvestad & Wilson 1984). Figure 3.4 (d) displays the Paα map overlayed with the radio contours. The radio emission appears to be slightly resolved and it also coincides with the recombination line emission. Accordingly, the 6 cm

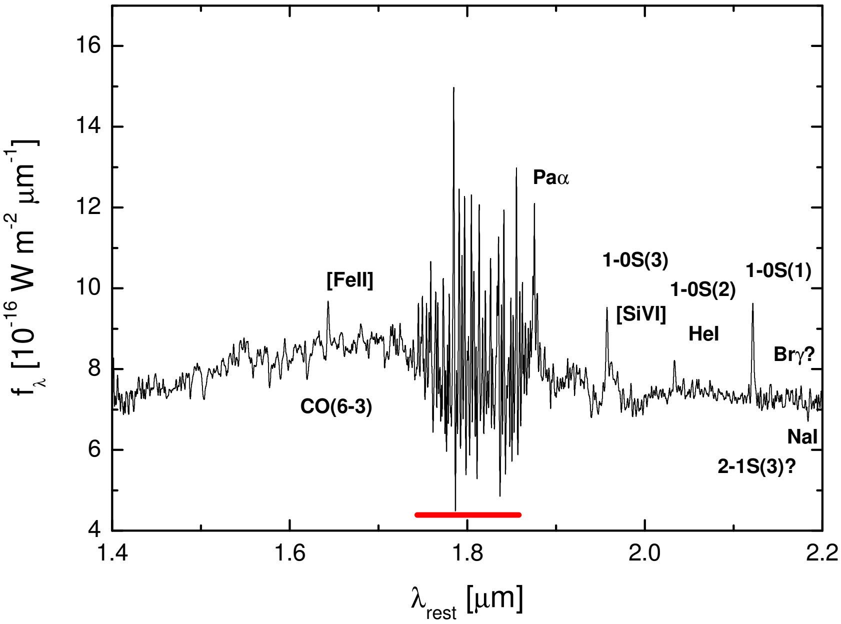

Figure 3.6: $H+K$ rest-frame spectrum extracted from a 5-pixel radius aperture centered on the nucleus (region 1 in Fig. 3.3 (a)). Prominent lines are indicated (cf Table 3.1). The high noise around 1.8 μm, indicated by the thick bar, is due to reduced atmospheric transmission between the H and the K bands.

radio continuum traces the zones of ongoing star formation. As indicated in Fig. 3.3 (d), there is an extension towards regions 2 and 4, which could also be interpreted as a jet component. Regions 2 and 4, therefore, might be excited by the radio jet impinging on the inter-stellar medium. In this case the nuclear spiral scenario has to be altered. See Sects. 3.4.2 and 3.4.5 for further discussion.

Next, 1D spectra were extracted from the $H+K$ and J bands for each of the five regions by summing up the individual spectra within apertures of 5 pixel radius, centered on the Paα emission peaks (see Figs. 3.6 and 3.8). The apertures sizes have been chosen to represent the angular resolution of the observation. Line fluxes for individual lines in the resulting spectra were measured by direct measurement. These fluxes and the FWHM of the line profiles are given in Tab. 3.1. The upper part of the table corresponds to the J part of the spectrum, the lower one to the H + K part. Fluxes are given in units of 10^{-19} W m^{-2} and observed line widths are given in km s^{-1}.

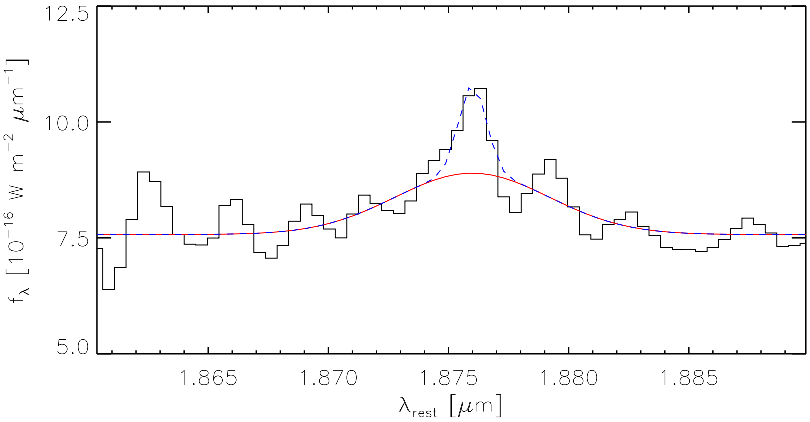

Figure 3.7: Rest-frame spectrum around Paα, extracted from the nuclear 5 pixel radius aperture. The spectrum has been smoothed with a 3-pixel boxcar. The blue dashed and red solid lines represent Gaussian fits to the narrow and broad components of Paα.

Errors of the line fluxes were estimated from the noise of the neighboring continuum alone. One has to keep in mind that errors introduced by the flux calibration become relevant when comparing line fluxes between bands (J and $H + K$) or when using absolute fluxes (see discussion about calibration in Sect. 3.3.1). The measurement of the FWHM depends on the shape of the continuum. Its error is estimated to be on the order of 30%. In the case of Paα and Paβ, a broad and narrow Gaussian component was fitted with a common line center (Figs. 3.7 and 3.9). The measurement of the broad components is quite intricate, since these lines are located in problematic regions of the spectrum. For example, Paα is located at the red end of the atmospheric transmission minimum ($\sim$ 1.8μm), and the spectrum is very noisy around this feature. As for Paβ and for He I, they are located at the beginning and at the end of the J-band spectrum and are also influenced by increased noise. For the nucelar 1-0S(3)/[Si VI] complex, two Gaussians and a telluric absorption component were fitted. A match without the telluric component recovers the 1-0S(3) flux and linewidth within the errors given in Table 3.1. In the case of the [Si VI], the flux and linewidth are considerably reduced (by about 60% and 30%, respectively). Thus, primarily the properties of [Si VI] and not of 1-0S(3) are influenced. Since the presence of the former is only used as an indicator of nuclear activity and is not consider any further, the telluric absorption for the 1-0S(3) measurement

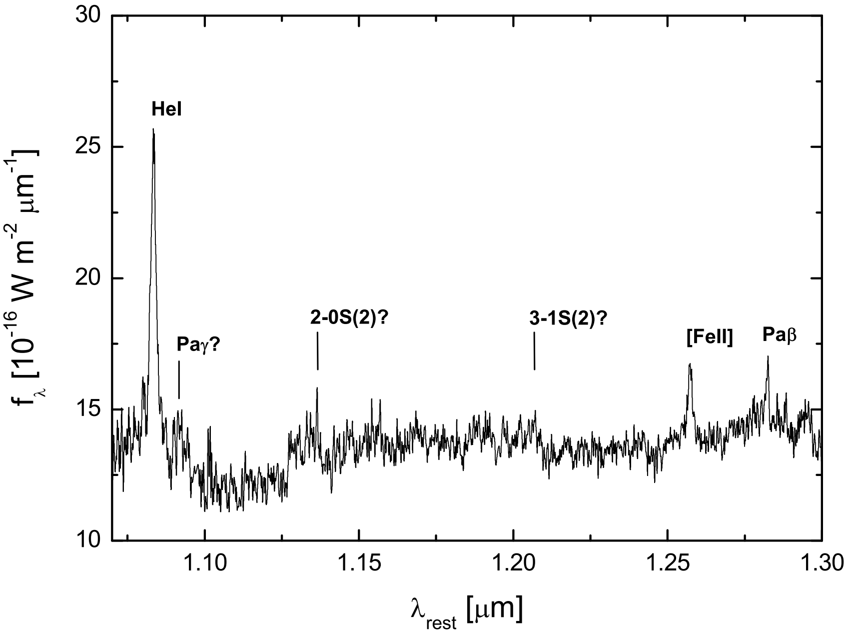

Figure 3.8: *J* rest-frame spectrum extracted from a 5 pixel radius aperture centered on the nucleus (region 1 in Fig. 3.3 (a)). Prominent lines are indicated (cf Table 3.1).

was neglected.

In contrast to Hα and Hβ at visible wavelengths (Fig.3.16), Paα (Fig. 3.7) and Paβ (Fig. 3.9) clearly show a broad component with an FWHM of about 3000 kms^{-1} (after correcting for the instrumental spectral resolution). This supports the Seyfert classification of Mrk 609 as deduced from the X-ray properties (Pappa et al. 2002). In the J-band spectrum, there is also evidence of a broad He I 1.083 μm component, but the low signal-to-noise ratio prevented the decomposition of broad and narrow components. Therefore, only the flux from direct measurement of the narrow component is stated in Table 3.1. The broad component also agrees with the line width of the broad Lyα ($\sim$ 3600 km s^{-1}, but blended with N V) found by Rudy et al. (1988), when taking the International Ultraviolet Explorer (IUE) spectral resolution of 7 Å into account. The coronal [Si VI] emission visible in the nuclear spectrum (Figs. 3.6 and 3.4(c) for the line map) is another common feature of the extreme energetics in AGN (Marconi et al. 1994; Prieto et al. 2005).

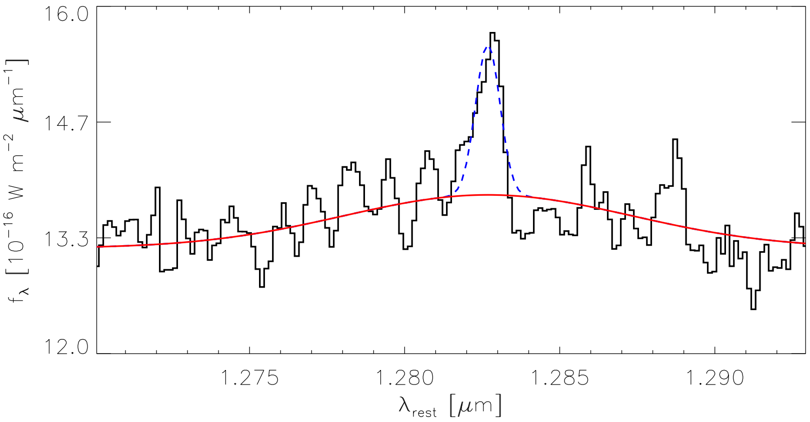

Figure 3.9: Rest frame spectrum around Paβ, extracted from the central 5 pixel radius aperture. The spectrum has been smoothed with a 3-pixel boxcar and the result of the fit of a narrow (blue dashed curve) and a broad (red solid curve) Gaussian component with a common line center is shown.

Using the unreddened case-B line ratio of Paα/Hβ = 0.332 (Osterbrock 1989), the broad component should be detectable in the visible; but as mentioned in the introduction, Mrk 609 exhibits unusual line ratios. Intrinsic extinction can be probed by comparing the ratios of hydrogen recombination lines with case-B values from Osterbrock (1989). For $T = 10^4$ K, $n_e = 10^4$ cm^{-3}, and no extinction, a ratio of Paα/Brγ = 12.4 is expected. Table 3.2 lists this ratio among others for the regions discussed here. Within the measurement uncertainties, the Paα/Brγ ratios are consistent with no intrinsic extinction. There is in fact a trend of the ratios being a bit larger then the case-B value. This is especially the case for the nuclear region, where the corresponding ratios of the broad components also show the same behavior. This result agrees with low H column densities derived from the X-ray spectra (Pappa et al. 2002) and the unusual line ratios found in the UV/optical by Rudy et al. (1988), who explained these ratios with low optical depths and low ionization parameters.

The 1.66 μm/2.16 μm continuum color map (Fig. 3.12) is sensitive to reddening caused by warm dust. The map shows reddening along the major bar axis, with peaks at the nucleus and at the tip of the bar, meeting the spiral arms. Previous studies of the NIR continuum of Seyfert galaxies concluded that their $J - H$ and $H - K$ nuclear colors can be explained by a mixture of a stellar component and a warm/hot dust component in emission (e.g. Hyland & Allen 1982; Glass & Moorwood 1985; Kotilainen et al. 1992; Alonso-Herrero et al. 1996). Using the H and K zero points from Table 3.4 in Glass (1999), the $H-K$ colors range from 0.6 in the outer regions up to 1.0 at the nucleus. These are compatible with warm ($\sim$ 500 K) dust emission and small extinction (cf Glass & Moorwood 1985). As Calzetti et al. (1996) and Fischera et al. (2003) furthermore show, the effects of dust in starbursts can often be fairly well modelled by a homogeneous or clumpy/turbulent foreground screen. Since the extinction curve is very flat in the NIR (Draine 1989) and since the wavelengths of the lines used in the present analysis have small separations, the differential reddening between these lines will be small. Therefore, the $H-K$ reddening will only have a neglegible influence on the measured line ratios.

Due to the uncertainties in the absolute calibration, i.e. ncomplete knowledge of the host galaxy and nuclear contribution in the measuring aperture, Paβ/Paβ ratio is not used as an indicator for extinction. Also the J-band spectrum shows no significant extinction. Assuming the same case-B conditions as above, the Paγ line (close to He I 1.0883 μm) would not have been detected. Figure 3.5, however, shows faint signs of Paγ, which point towards the same conclusion of small extinction around the nucleus.

Paβ, Brγ, and He I 2.058 μm exhibit the same spatial distribution (Fig 3.3 (b), (c), and Fig. 3.5 (d)), and their intrinsic line widths are comparable and are spectroscopically unresolved. This indicates that the lines arise in the same parcels of gas. Note that on the nucleus Brγ is only measured as an upper limit and He I 2.058 μm only has a narrow component. On the other hand He I 1.0883 μm is just concentrated on the nucleus (Fig. 3.5 (b)) and has both a broad component and a narrow one.

3.4.2 Molecular hydrogen and iron

The H_2 emission lines originate in surfaces of molecular clouds exposed to stellar or nuclear radiation. The observed line strengths and ratios strongly depend on the excitation mechanisms of H_2 discussed below.

[Fe II] emission is believed to originate in partially ionized zones, which occur around supernovae or the active nucleus. Such regions can be produced by the hard ionizing X-ray/UV continuum or by shocks in the circumnuclear gas or in supernova remnants (e.g. Alonso-Herrero et al. 1997).

Table 3.1: Emission line fluxes for the 5 regions identified in the Paα line map (Fig. 3.3 (a)). The upper part corresponds to the J part of the spectum, the lower to the $H + K$ part. Fluxes, measured in 10 pixel diameter apertures, are given in units of 10^{-19} W m^{-2}. Observed line widths are given in km s^{-1}.

Line	Region 1		Region 2		Region 3		Region 4		Region 5	
	Flux	FWHM	Flux	FWHM	Flux	FWHM	Flux	FWHM	Flux	FWHM
He I λ1.0833 narrow	31.8 ± 10.6	540	—	—	—	—	—	—	—	—
[Fe II] λ1.257	5.1 ± 1.0	439	1.3 ± 0.3	327	0.7 ± 0.1	160	1.3 ± 0.2	303	—	—
Paβ narrow[a]	1.9 ± 0.6	214	1.7 ± 0.1	150	2.2 ± 0.1	163	2.2 ± 0.2	183	—	—
Paβ broad[a]	15.0 ± 7.0	3400	—	—	—	—	—	—	—	—
[Fe II] λ1.644[c]	2.7 ± 0.2	410	0.6 ± 0.1	240	0.3 ± 0.1	200	0.5 ± 0.1	260	0.07 ± 0.01	200
Paα narrow	5.3 ± 0.6	300	7.9 ± 0.2	270	7.0 ± 0.1	200	5.4 ± 0.2	200	0.22 ± 0.01	210
Paα broad	16.4 ± 5.6	3000	—	—	—	—	—	—	—	—
1-0S(3)[b,c]	5.0 ± 0.8	317	1.1 ± 0.2	371	0.5 ± 0.1	345	0.6 ± 0.2	471	0.05 ± 0.02	230
[Si VI][b,c]	16.4 ± 4.2	2130	—	—	—	—	—	—	—	—
1-0S(2)	2.1 ± 0.4	308	0.6 ± 0.1	366	0.20 ± 0.06	321	0.4 ± 0.1	333	0.06 ± 0.02	450
He I λ2.058	0.3[d]	300	0.3 ± 0.1	338	0.20 ± 0.05	200	0.20 ± 0.05	200	0.07 ± 0.01	200
2-1S(3)[e]	0.2	317	0.1	322	0.1	312	0.1	316	0.02	300
1-0S(1)	6.4 ± 0.4	330	1.6 ± 0.1	375	0.6 ± 0.04	270	0.9 ± 0.1	300	0.10 ± 0.01	300
Brγ	0.37[d]	300	0.5 ± 0.1	267	0.6 ± 0.1	200	0.4 ± 0.1	200	0.18 ± 0.01	200

[a] Decomposition using two Gaussian components.

[b] 1-0S(3) and [Si VI] are decomposed using two Gaussian components.

[c] Result is strongly influenced by telluric absorption.

[d] Upper limit, assuming the FWHM of the narrow Paα component.

[e] Upper limit, assuming the average FWHM of the other molecular hydrogen lines.

Table 3.2: Ratios of prominent emission lines using the narrow components.

Region	$\frac{\mathrm{Pa}\alpha}{\mathrm{Br}\gamma}$	$\frac{\mathrm{H_2} 2.121\mu\mathrm{m}}{\mathrm{Br}\gamma}$	$\frac{\mathrm{[Fe\,II]} 1.257\mu\mathrm{m}}{\mathrm{Pa}\beta}$
1	> 14.3 (> 13.7)[a]	> 17.3	3 ± 1
2	15 ± 3	3.2 ± 0.7	0.8 ± 0.2
3	12 ± 2	1.0 ± 0.2	0.32 ± 0.04
4	14 ± 3	2.3 ± 0.6	0.5 ± 0.1
5	12.2 ± 0.1	0.6 ± 0.2	–

[a] Broad component in brackets.

Kinematics of the H_2 and [Fe II] lines

The $H + K$ spectra exhibit a couple of rotational/vibrational lines of molecular hydrogen (Fig. 3.6). The most prominent is the 1-0S(1) transition. Figure 3.4(b) shows the spatial distribution of H_2, which appears rather confined to the nucleus. Most of the 1-0S(1) emission is concentrated within 260 pc (30% peak contour in Fig. 3.4(a)) around the nucleus. The emission further shows a smooth decline towards the outer regions as it follows the continuum contours. This is in agreement with previous investigations of the molecular content of samples of Seyfert galaxies, which showed that the gas is concentrated in a disk around the centers of the galaxies (Reunanen et al. 2003; Rodríguez-Ardila et al. 2005). The [Fe II] emission is oriented almost perpendicular to the H_2 emission and follows the recombination line gas (Figs. 3.4 (b) and 3.3 (a)-(c)). Comparison of the line width of H_2 with the one of the narrow lines can thus yield constraints on the location of the molecular and narrow-line gas. Line widths are considered to be spectroscopically-resolved, if the FWHM is larger than 280 km s^{-1}, i.e. $\sqrt{2}$ times the spectral resolution of 200 km s^{-1}. From Table 3.1 can be found that the molecular hydrogen emission is slightly resolved spectroscopically and that the line widths are similar in all regions. The H_2 lines are also always broader than the narrow recombination lines. In contrast to this, [Fe II] 1.257 μm appears to be resolved spectroscopically only on the nucleus and in regions 2 and 4. In these three regions [Fe II] is also broader than the narrow recombination lines and even broader than molecular hydrogen. Apart from that its FHWM is similar to that of the narrow recombination lines. Off-nuclear [Fe II] follows the patchy Paα emission/Brγ/He I distribution, thereby tracing star formation. On the other hand, the unusual broadening of the iron emission in regions 1, 2, and 4 might also be related to a jet-like extension (southeast-northwest direction) in the 6 cm VLA continuum map of Ulvestad & Wilson (1984). Figure 3.4 (d) displays the Paα map overlayed with the radio map in contours. It is rather speculative but conceivable that a radio jet might alter the iron gas kinematics (cf discussion in Reunanen et al. 2003).

These observations seem to confirm previous results by Reunanen et al. (2003) and Rodríguez-Ardila et al. (2005) that the H_2 kinematics is decoupled from the [Fe II] and narrow recombination line kinematics.

However, because of the combination of low inclination and limited spectral resolution, no considerable dynamics from line shifts is evident.

H_2 excitation mechanism by line ratios.

Three distinct processes are commonly discussed: (1) UV fluorescence (non-thermal), (2) X-ray heating (thermal), and (3) shocks (thermal). The processes result in different H_2 responses and can thus helping distinguishing the dominant excitation process (e.g. Mouri 1994).

(1) ***Excitation via UV-fluorescence*** can occur via UV pumping and/or collision with H-atoms, which are controlled by temperature, density, and strength of the UV radiation field. Within a warm, high-density gas in a strong UV radiation field, thermal line ratios are found for the lower vibrational levels. In this case the lower levels are dominated by collisional excitation, whereas the higher levels are populated via UV pumping. To distinguish this scenario from pure shock excitation, observations of the high transitions are essential. In the UV excited gas, strong 2-1H_2 lines are expected, as well as strong lines in the *H* band, e.g. 6-4Q(1) 1.6 μm or 1-0S(7) 1.75 μm (cf Table 2 of Black & van Dishoeck 1987). The *H*-band lines only become weak relative to the *K*-band lines in the case of very high densities and high UV intensities. Since no H_2 lines are detected in the *H* band and the 2-1H_2 lines are only measured as upper limits, UV radiation as the main excitation mechanism seems unlikely.

(2) ***Excitation by X-rays or cosmic rays***. Tine et al. (1997), Draine & Woods (1990), as well as Maloney et al. (1996), analyzed the excitation of H_2 by X-rays and cosmic rays. Obvious non-thermal line spectra from these X-ray-dominated regions (XDRs) are only observable, if the temperature is well below 1000 K and the ionization-rate per H-atom is below 10^{-15}cm^{3}s^{-1}. At higher temperatures, the lower vibrational levels

will be populated mainly by collisions, whereas higher ionization-rates will destroy the H_2 molecules. Lepp & McCray (1983) derived the relation $L_{IR} \approx 10^{-3} L_X$ between the 1-10 keV X-ray luminosity and the 1-0S(1) line luminosity for isobaric models containing a compact X-ray source. The 2-10 keV X-ray flux of Mrk 609 (Pappa et al. 2002) is about 2.7×10^{-15} W m^{-2} and translates to a 1-0S(1) line flux of about $\sim 10^{-18}$ W m^{-2}. This is comparable in magnitude to the measured 1-0S(1) flux, if summing over all regions. The analysis of the line ratios, however, does not strongly support excitation via X-rays. a (3) ***Thermal excitation via shock fronts***. Thermal excitation occurs through collisions with H or H_2. The population of the electronic ground levels in the ro-vibrational transitions represents a Boltzmann distribution. Then the temperature of the gas represents a kinetic temperature that could be as high as 2000 K or more. See for example Draine & McKee (1993) for a review.

In order to test whether the [Fe II] and H_2 emission can be caused by X-ray heating, the models of Maloney et al. (1996) are used to estimate the emergent 1-0S(1) and [Fe II] fluxes of a gas cloud illuminated by a source of hard X-rays with an intrinsic luminosity L_X. The cloud is at a distance d from the X-ray source and has an electron density n_e. The cooling is then given by the effective ionization parameter ξ_{eff}:

$$\xi_{\text{eff}} = 1.26 \times 10^{-4} \frac{f_X}{n_5 N_{22}^{0.9}} \tag{3.1}$$

where f_X is the incident hard X-ray flux at the distance d [pc] from the X-ray source, n_5 [10^{-5}cm^{-3}] is the total hydrogen gas density, and N_{22} [10^{22} cm^{-2}] the AGN intrinsic attenuating column density. The value of f_X can be calculated via $L_X/4\pi d^2$. Maloney et al. (1996) calculate the emergent intensities for two gas densities, 10^5 cm^{-3} and 10^3 cm^{-3}, which can be directly read off their Fig. 6(a, b). Then, the flux can be calculated using the solid angle of the cloud region, i.e. the aperture of a 10-pixel diameter ($0\farcs5$ corresponding to 4.6×10^{-12} sr). The *BeppoSAX* 0.1-10 keV X-ray luminosity is 6.3×10^{42} erg s^{-1} (in the high state) and the absorbing column density is $N_H \leq 1.32 \times 10^{21}$ cm^{-2} for a single power-law model (Pappa et al. 2002). For the indicidual regions, Table 3.3 lists the H_2 and [FeII] fluxes in units of 10^{-20} W m^{-2} for the distances d in pc.

Taking the uncertainties in the flux calibration into account, the H_2 estimates show that X-ray heating can account for part of the observed 1-0S(1) flux (cf Table 3.1) in the nuclear region. The model also predicts the 2-1S(1) and the Brγ fluxes. The expected line ratios approximately resemble those of the observed 2-1S(1)/1-0S(1) and 1-0S(1)/Brγ ratios. On the other

Table 3.3: Emergent H_2 and [Fe II] fluxes using the models of Maloney et al. (1996).

	$n = 10^5$ cm^{-3}		$n = 10^3$ cm^{-3}	
d	1-0S(1)	[Fe II]	1-0S(1)	[Fe II]
50	1450.0	0.5	—	—
80	15.0	0.0	460.0	145.0
420	15.0	0.0	0.05	0.0
630	9.0	0.0	0.08	0.0
1300	3.0	0.0	0.15	0.0

hand, [Fe II] 1.644 μm appears not to be excited by X-ray heating, except for the nuclear region in case of the lower electron density environment. This indicates that other processes like shock heating or fluorescence have to be accounted for. In fact, the NIR diagnostic diagram (Fig. 3.15) points towards the importance of shock heating.

In summary, the observed line ratios displayed in Fig. 3.10 agree quite well with those of a shock model with 2000 K from Brand et al. (1989) for all regions. A scenario with mixed excitation is possible and more realistic as well. Fitting the 2-1 S(1)/1-0 S(1) ratio with the models 14 (UV excitation) and S2 (shock excitation) of Black & van Dishoeck (1987) for regions 1-4 about 96% of the line emission should be due to thermal excitation and about 4% due to UV pumping. For region 5 thermal excitation could account for up to 60% and UV pumping for up to 40%.

The H_2 population diagram.

Another approach to finding the relevant excitation mechanism is to assume thermal excitation. The ro-vibrational levels are then populated according to the Boltzmann equation. This can be illustrated by a population diagram showing the observed population density versus the energy of the upper level. If all values lie on a straight line, the gradient is proportional to the temperature of the molecular gas. The population density can be derived from the observed column density according to Lester et al. (1988):

$$N_{\mathrm{col}} = \frac{f}{A_{ul}} \frac{\lambda}{hc} \times \frac{4\pi}{\Omega_{\mathrm{aperture}}}, \qquad (3.2)$$

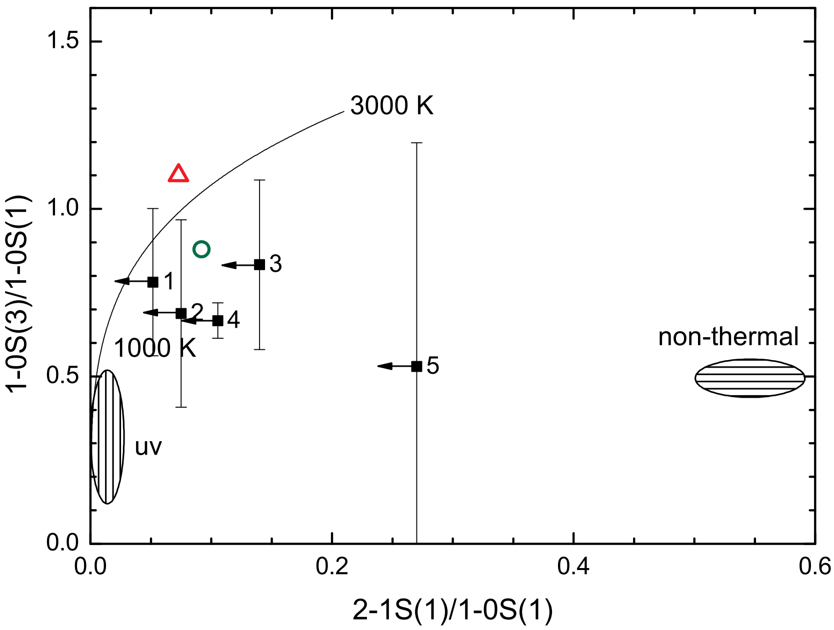

Figure 3.10: H_2 diagnostics diagram using the two line ratios 2-1S(1)/1-0S(1) vs. 1-0S(3)/1-0S(1). The region with the horizontal fill pattern covers the non-thermal models of Black & van Dishoeck (1987). The vertically patterned region are the thermally uv-excited models of Sternberg & Dalgarno (1989). The open triangle corresponds to the X-ray heating models of Draine & Woods (1990) and the open circle to the shock model of Brand et al. (1989). Filled squares are the measured line ratios with numbers indicating the extraction region (see Fig. 3.3 (a)).

where $[f] = \mathrm{W\,m^{-2}}$ is the observed line flux, A_{ul} the transition probability (taken from Wolniewicz et al. 1998), λ the rest frame line wavelength, h the Planck constant, and c the velocity of light. The additional factor $4\pi/\Omega_{\mathrm{aperture}}$ takes the spatial distribution into account. The Boltzmann distribution for thermal equilibrium can be written as

$$\frac{N'}{N''} = \frac{g'_J}{g''_J} e^{-\Delta E/kT}, \tag{3.3}$$

where N' and N'' denote the column densities at the corresponding levels, g'_J and g''_J are the statistical weights, and T the temperature of the thermal equilibrium. If the H_2 is non-thermally excited, only lines within one rotational level (e.g. $v = 1 - 0$) fall on a straight line.

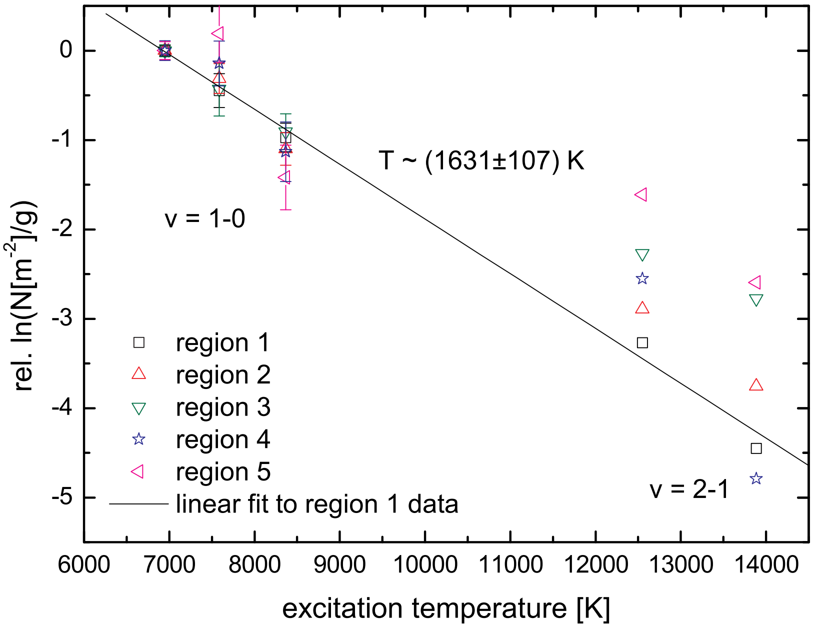

Figure 3.11: H_2 level population diagram relative to 1-0S(1) for the the five regions of Fig. 3.3 (a). All $v = 2 - 1$ fluxes are upper limits. A linear fit to the region 1 data is presented and yields an excitation temperature of about $T_{\rm ex} = (1631 \pm 107)$ K (cf Fig. 3.10).

The population diagram Fig. 3.11 for the H_2 lines of Mrk 609 shows that, within their errors, the different transitions fall on a straight line. From this a kinetic temperature for the nuclear region of about 1631 ± 107 K is estimated. It has to be noted that the $v = 2 - 1$ fluxes are upper limits. For region 1 these values are consistent with the $v = 1 - 0$ kinetic temperature. For regions 2, 3, and 4, the scatter with respect to a linear relationship is larger and the $v = 2 - 1$ values tend to show lower excitation temperatures. Nevertheless, the temperatures found in the population diagram agree with the temperatures indicated by the solid curve in Fig. 3.10. A stronger non-thermal contribution might be possible for region 5.

3.4.3 Stellar absorption features

The $H + K$ spectra of all five regions show stellar absorption features like the CO(6-3) 1.62 μm and CO(2-0) 2.29 μm, as well as Si I 1.59 μm, Mg I

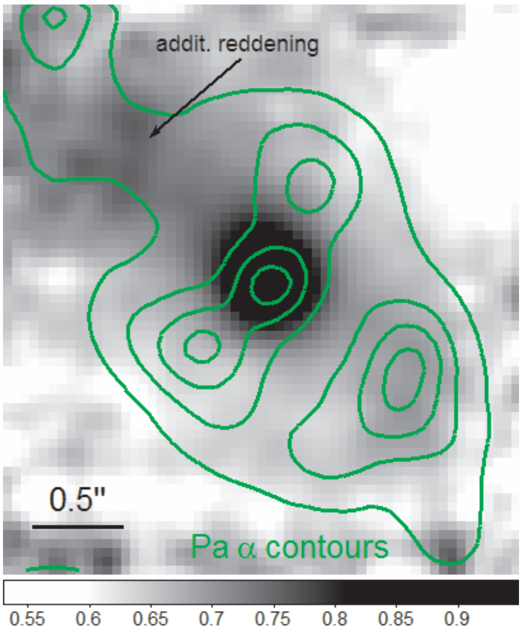

Figure 3.12: Color map derived from continuum fluxes measured at the 2MASS effective *H* and *Ks* band wavelengths and zero points. Darker greyscales indicate redder colors with $H - K$ ranging from 0.5 to 1. Contours correspond to Paα emission displayed in Fig. 3.3 (a).

1.5,1.71 μm, and Na I 2.206 μm (see Fig. 3.13). The details of the stellar content will be discussed in a subsequent paper, but one can get initial insight into the stellar populations by using the ratio of equivalent widths (EW) of CO(6-3) and Si I 1.59 μm to indicate the temperature of late-type stars (Origlia et al. 1993; Ivanov et al. 2004). CO(6-3) grows rapidly from early K to late M stars, while SiI varies only very slowly with temperature. Table 3.4 lists the ratio for all regions. The measured ratios correspond to M-type giants (see Fig. 5(b) in Origlia et al. 1993). One has to take into account that in active galaxies these stellar features can be substantially diluted by non-stellar nuclear emission. This effect can be recognized by comparing spectra of regions 1 and 2 of both panels in Fig. 3.13. While being very similar in the *H* band, the nuclear *K*-band spectrum is significantly reddened. However, this effect will not be considered further at this point.

The CO(2-0) index can be used to estimate the age of the stellar popu-

Table 3.4: Measurements of stellar absorption lines.

Region	EW(CO(6-3))/EW(SiI)	CO(2-0) index	EW(Na I) [Å]
1	0.31	0.09	2.5
2	0.28	0.19	2.8
3	0.26	0.14	3.0
4	0.31	0.13	3.0
5	0.24	0.17	3.8

lation (Origlia & Oliva 2000). As outlined in Ramos Almeida et al. (2006), the Ivanov CO index (Ivanov et al. 2004) is used, and converted to a photometric CO index, the approximate age can be read from Fig. 1 of Origlia & Oliva (2000). The photometric CO indices range from 0.1 to 0.15. For solar metallicity this corresponds to ages between 80 and 150 Myr for the Geneva tracks with the younger ages measured in regions 2 and 5. Such deep CO absorption is typically found in starburst galaxies (e.g. Fischer et al. 2006, and references therein). Note that the blue edge of the CO(2-0) bandhead is influenced by atmospheric OH emission, and the change in index is on the order of 20%. Thus, the stellar ages might become shorter by a few 10 Myr.

The Na I absorption is commonly found in late-type stars. Model calculations by Davies et al. (2005) show that the EW of Na I typically ranges between 2 and 3 Å. Their models include AGB phases that have a significant influence on the depth of the Na I feature (see Fig. 7 of Davies et al. 2005). Indeed, the EWs range between 2.5 (for region 1) and 3.8 (for region 5), which is consistent with the ages found from the CO(2-0) index. Both results agree with the young stars found by Rudy et al. (1988) from their UV/optical spectroscopy.

3.4.4 CO(1-0) observations

Another ingredient in the starburst/Seyfert picture is the presence of fuel in the form of molecular gas. Giant molecular clouds are the birthplaces of stars. The dense gas is dissipative and galaxy interaction is believed to channel huge amounts of molecular gas towards the nucleus of the interacting galaxies, providing fuel for the nuclear activity (e.g. Springel et al.

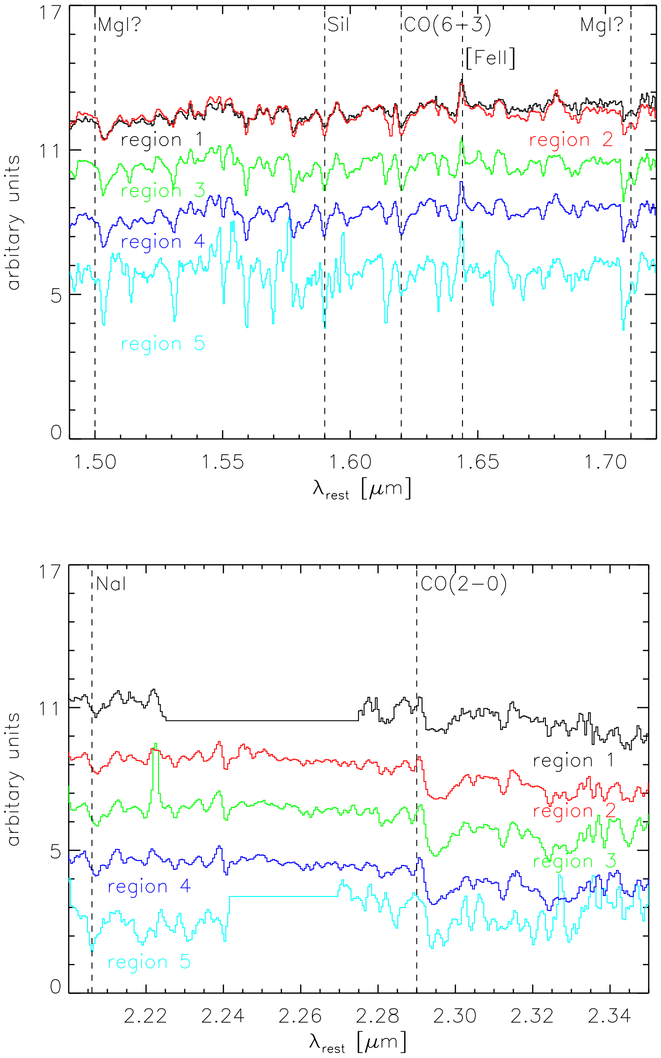

Figure 3.13: Stellar absorption features in the H-band (*upper panel*) and K-band (*lower panel*) parts of the spectra extracted from the five regions of Fig. 3.3 (a). The fluxes of the H and K spectra are scaled to the flux at 2.1 μm of region 1. Then the spectra were shifted by an arbitrary amount for better visibility. The K-band part of region 1 between 2.225 and 2.275 μm is not useable because of a detector defect and has been replaced by a flat line. The same situation applies for region 5 between 2.241 and 2.27 μm.

2005). Infrared luminous AGN ($L_{IR} > 10^{10}$ erg s^{-1}) are found to be rich in molecular gas (e.g. Evans et al. 2001, 2005, and references therein) with gas masses of up to $M_{\mathrm{H}_2} \sim 10^{10} M_{\odot}$. Maiolino et al. (1997) explain the more intense star formation found in Seyfert 2 galaxies with a significantly higher fraction of asymmetric morphologies than in Seyfert 1 and field galaxies. As discussed in Sect. 1.1, there is compelling observational and theoretical evidence that bars efficiently redistribute angular momentum in galaxies and cause gas to flow inwards into the circumnuclear region (inner 1-2 kpc), giving rise to starburst and nuclear activity (Kormendy & Kennicutt 2004; Jogee et al. 2005). A major result from the Nuclei of Galaxies (NUGA) project carried out at the Plateau de Bure interferometer is the wide variety of circumnuclear disk morphologies on the 100 pc scale associated with the AGN (García-Burillo et al. 2005 and also Schinnerer et al. 2000 for an integrated CO/NIR study of NGC 1068). It is believed that on these scales, secondary perturbations modes appear to take over and are responsible for channeling gas towards the center of the galaxy. Still the scales are large compared with nuclear scales. The actual fueling of the central engine is believed to be supported by viscous flow of the material delivered by the secondary perturbations (Duschl & Strittmatter 2004).

During an observing campaign of cluster galaxies with the Nobeyama 45m telescope in March 2005, T. Bertram also observed Mrk 609 in ^{12}CO(1-0). The baseline-subtracted, main-beam-efficiency corrected CO(1-0) spectrum is presented in Fig. 3.14. The beam with a size of about 15$''$ essentially covers the entire visual part of the galaxy (cf Fig. 3.1). The FWHM of the CO line is 51 ± 4 km s^{-1} and the line-integrated flux, corrected for main-beam efficiency, is $I_{\mathrm{CO}} = (14 \pm 1)$ K km s^{-1}. The narrow line width is reminiscent of the small inclination of Mrk 609. According to Eq. 2 in Solomon et al. (1992), the line luminosity results in $L'_{\mathrm{CO}} = (1.5 \pm 0.1) \times 10^9$ K km s^{-1} pc^2. Now one can estimate the H$_2$ mass, assuming optically thick and thermalized emission, originating from gravitationally bound molecular clouds (Evans et al. 2005):

$$\alpha = \frac{M(\mathrm{H}_2)}{L'_{\mathrm{CO}}} \, M_{\odot} \, (\mathrm{K\,km\,s^{-1}pc^2})^{-1}. \tag{3.4}$$

The conversion factor α lies between 2 and 5 (Radford et al. 1991). Here, $\alpha = 4$ is adopted, resulting in $M(\mathrm{H}_2) = (6.0 \pm 0.4) \times 10^9 M_{\odot}$, which is on the high end of the range of masses found in AGN (e.g. Rigopoulou et al. 1997).

The gas mass can be compared with the dust mass derived from the IRAS 60 μm and 100 μm fluxes ($f_{60} = 2550$ mJy, $f_{100} = 4760$ mJy; Rudy

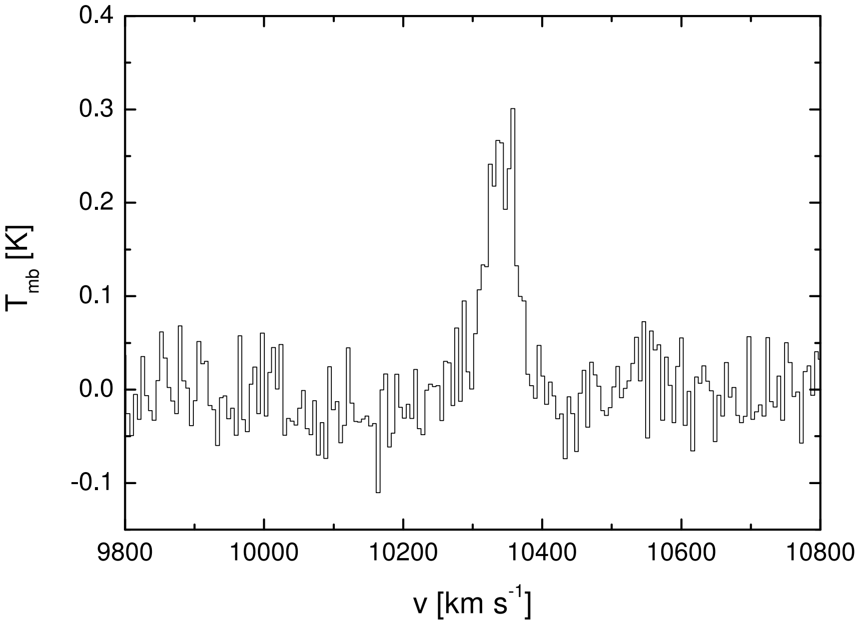

Figure 3.14: Observed-frame CO(1-0) spectrum of Mrk 609.

& Rodriguez-Espinosa 1985). The infrared emission originates from warm dust, heated either by star-formation or by the active nucleus. Following Evans et al. (2005), the dust temperature results in $T_{\text{dust}} \approx 47$ K, and the corresponding dust mass in $M_{\text{dust}} \approx 1.1 \times 10^7 M_\odot$. The gas-to-dust ratio, $\sim$ 545, is comparable to *IRAS*-detected spiral and luminous infrared galaxies (Young & Scoville 1991). Next, the infrared luminosity is calculated using the formula given in Solomon et al. (1997). Tutui et al. (2000) furthermore show that an IRAS K-correction for this type of galaxy is not necessary. The color correction, r, lies between 1.5 and 2.1 (Solomon et al. 1997). Assuming $r = 1.8$, the infrared luminosity calculates as $L_{FIR} \approx 10^{11} L_\odot$, which is typical for an infrared luminous galaxy.

The FIR luminosity of (inactive) galaxies is interpreted as a measure of the number of visible and UV photons, thus measuring the number of high-mass stars. This allows us to estimate the global star-formation rate (SFR) from the IRAS fluxes using Eqs. 7 and 8 in Hopkins et al. (2003). The global SFR of Mrk 609 amounts to $\sim 30 M_\odot$ yr^{-1}, on the other hand, CO(1-0) measures the cold molecular gas supplying the star formation. The ratio between FIR and CO luminosity, therefore, is a measure of the star-formation efficiency (SFE; cf Eckart et al. 1994). The global SFE is on the order $L_{\rm FIR}/M_{\rm H_2} \approx 17\ L_\odot\ M_\odot^{-1}$, which is again on the high end of the SFEs of non-interacting galaxies. Such SFRs and SFEs are also often found in interacting systems (Solomon & Sage 1988). Stars thus appear to be formed very efficiently in Mrk 609 and the gas depletion time is short ($\sim 3\times10^8$ yr).

One can also estimate an SFR using the 21 cm radio flux. For Mrk 609, the NRAO VLA Sky Survey (NVSS) 21 cm flux $f_{\rm 21cm} = 30$ mJy yields a luminosity of $L_{\rm 21cm} = 8.3 \times 10^{22}$ W Hz^{-1}. According to Eqs. 1 and 2 of Hopkins et al. (2003), the radio derived SFR amounts to $\sim 46 M_\odot$ yr^{-1}. This is somewhat higher than the FIR-derived SFR. Hopkins et al. (2003) find a tight correlation between radio and FIR flux. The differences in the derived SFRs could be caused by a stronger AGN contribution (e.g. jet) at the 21 cm wavelengths.

3.4.5 The starburst/AGN connection in Mrk 609

In contrast to previous data of Mrk 609, the present observations have now spatially resolved the inner circumnuclear environment on the 270 pc scale. This allows us to study the relative contributions and importance of nuclear and off-nuclear (H II regions, late-type stars) emission.

Analogously to the optical (e.g. Baldwin et al. 1981; Veilleux & Osterbrock 1987), Rodríguez-Ardila et al. (2004, 2005) emphasize the use of the line ratios [Fe II]/Paβ and 1-0S(1)/Brγ to distinguish between starbursts, AGN, and LINERs (low ionization nuclear emission-line region galaxy). They find that objects with either one of the ratios being lower than 2 were predominantly identified as Seyferts. Starburst galaxies, on the other hand, are located in a region where both ratios are lower then 0.4, while LINERs have both ratios higher than 2 (Fig. 3.15).

In this context, the ratios describe the transition from pure shock excitation driven by supernova remnants (upper right corner of the diagram) to purely ionizing radiation powered by star formation (lower left corner). For illustration purposes the data from Rodríguez-Ardila et al. (2005) are plotted as open symbols in Fig. 3.15. Starbursts from Dale et al. (2004) populate the lower left region of the diagram. Seyfert 1 and 2 galaxies from Rodríguez-Ardila et al. (2005) populate the middle part, whereas LINERs (Larkin et al. 1998) can be found in the upper right corner. The emission of the supernova IC 443, on the other hand, is believed to be driven by shocks (Graham et al. 1987). The location of AGN (powered by X-ray heating) between these two extremes has not been fully understood yet. But most

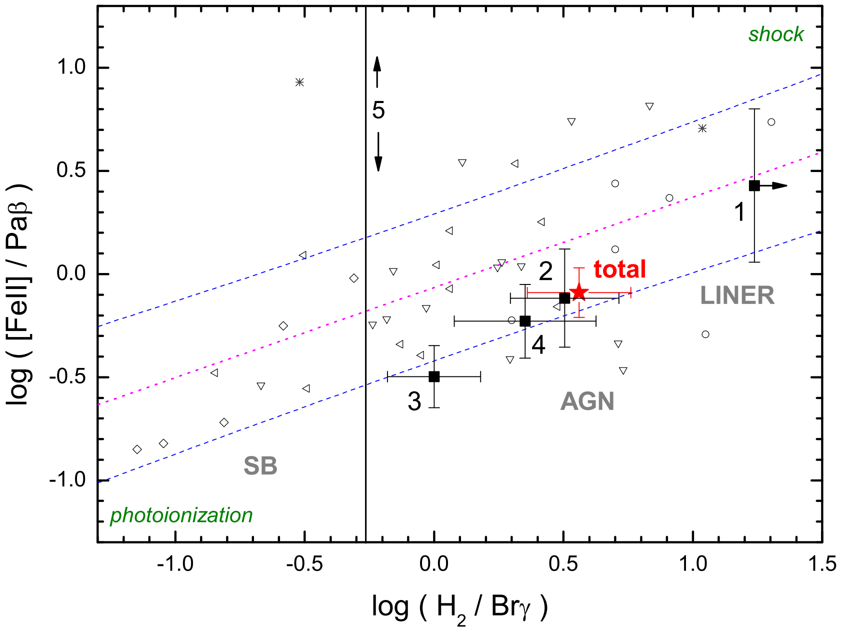

Figure 3.15: Line ratios of [Fe II] 1.257μm/Paβ and 1-0S(1) 2.121μm/Brγ. Activity types (starburst, AGN, LINER) are indicated. Filled symbols represent the measurements of the five regions of Mrk 609, as well as for the total FOV (red star). Because of missing J-band data, region 5 is only accurately located along H_2/Brγ. Open symbols correspond to literature values: rhombs represent starburst galaxies from Dale et al. (2004), left triangles Seyfert 1 galaxies from Rodríguez-Ardila et al. (2004), headlong triangles Seyfert 2s from Rodríguez-Ardila et al. (2005), circles LINERs from Larkin et al. (1998), and asteriks supernovae also from Larkin et al. (1998). The diagram is interpreted as displaying the transition from pure photoionization (lower left corner) to pure shock driven (upper right) emission (Rodríguez-Ardila et al. 2005). Assuming a linear relationship between the two line ratios, the dotted magenta line represents a linear fit to the literature data points. The blue dashed lines represent the 1σ prediction band of the fit.

probably it is the result of a power-law continuum illuminating a slab of gas (see below and Rodríguez-Ardila et al. 2005).

It can be seen from Figs. 3.3 (b) and 3.5 (c) that the [Fe II] emission is extended towards regions 2, 3, and 4. This extent is about perpendicular to the H_2 one. Moreover, the radio contours are approximately congruent with the [Fe II] distribution. The NIR line-ratios measured in the five regions fall into different parts of the NIR diagnostics diagram (Fig. 3.15). The calibration uncertainties discussed above play no role at this point, since the line ratios are calculated within a spectral band. The data points clearly follow a trend from a LINER-like value at the nucleus to a starburst-like value at the most distant region 5. The circumnuclear regions 2, 3, and 4 fall in the domain of potentially mixed excitation. This situation will be discussed below for the individual regions. Under the assumption that the literature values follow a linear relationship between the line ratios (from photoionization- to shock-driven excitation, see Larkin et al. 1998), a linear regression was carried out and is shown in Fig. 3.15 (correlation coefficient $R \sim 0.6$ and a probability of $R = 0$ of about 10^{-4}) with its 1σ prediction band. This fit, however, is only intended to guide the eye. A firm correlation has not been established yet. Notice that the data fall somewhat below the linear relation, but still within the prediction band. Incorrect estimations of the continuum levels during the measurement of emission line fluxes might in part be responsible for this trend. On the other hand, M-type giants are the dominating population in the NIR (Sect. 3.4.3), and stellar absorption can therefore influence the flux measurement of emission lines (e.g. Harrison et al. 1998, who found that stellar absorption plays an important role in their observation). The study of Larkin et al. (1998) used larger apertures compared to this work from which they extracted spectra. In this case a considerable part of the host galaxy emission can modify the emission-line measurements. On the other hand, Rodríguez-Ardila et al. (2005, 2004) use nuclear apertures of sizes comparable to this work. The latter study, however, does not consider circumnuclear stellar absorption features at the position of the emission lines, which can influence the results.

Visual inspection of the spectra of late-type stars (Wallace et al. 2000; Ivanov et al. 2004, in J and H, K, respectively) shows that there is no significant stellar absorption at the position of the emission lines. Atmospheric residuals might account for an uncertainty in flux on the order of 20%, as discussed in Sect. 3.4.3.

The nuclear region interestingly falls into the LINER regime. This contrasts with the optical classification as Sy1.8 by Osterbrock (1981) or from analysis of the SDSS spectrum (Fig. 3.16). This discrepancy may be due to aperture effects, since the SDSS spectrum has been measured in a $3''$ diameter fiber covering the total FOV of the NIR observations. The total narrow-line flux of the H-recombination lines is dominated by the extra-nuclear regions. The LINER character might therefore be hidden in the large-aperture optical spectrum. Such effects are also discussed by Kauffmann et al. (2003). This can be tested in the present case by computing the flux ratio of the line fluxes integrated over the SINFONI FOV

(~ 1.3kpc × 1.3kpc). Indeed, the position in the diagnostics diagram is shifted towards values typically found for Seyfert galaxies (Fig. 3.15). This demonstrates the importance of high angular resolution in studying the nature of activity in galaxies. It is furthermore interesting that the off-nuclear emission regions populate a region in the diagnostic diagram where AGN are usually found. This indicates that in these regions both shock and photoionization are important.

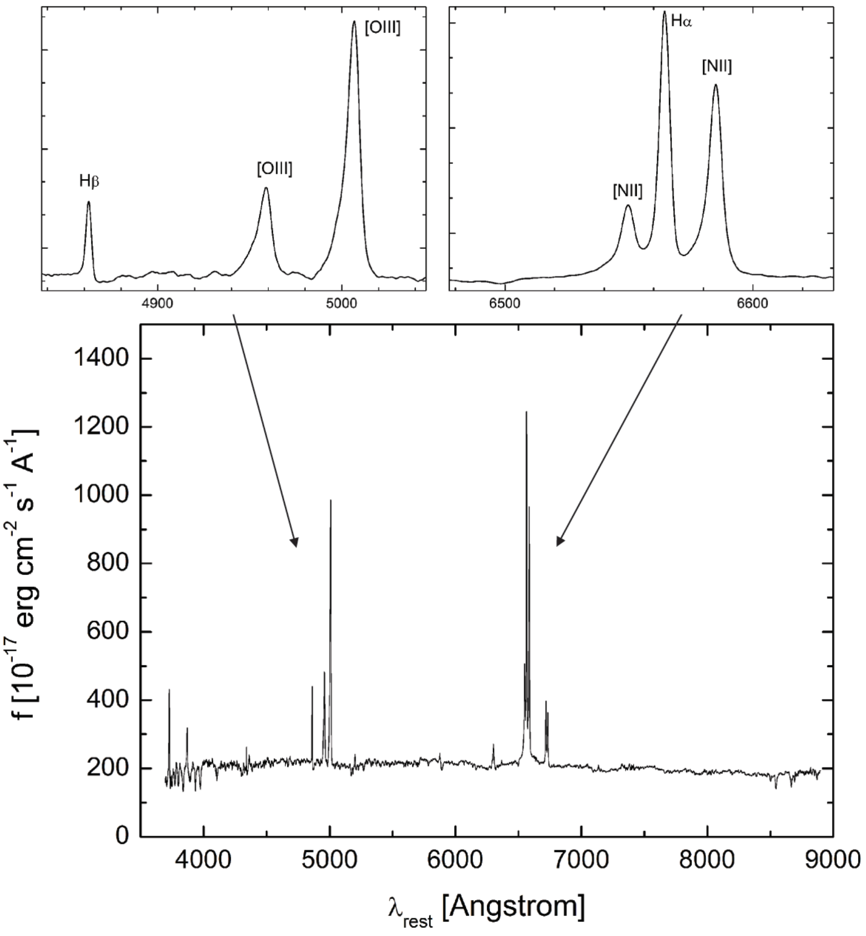

Figure 3.16: Rest frame SDSS spectrum (from SDSS DR4 Adelman-McCarthy et al. 2006). The upper insets are close-ups of the Hβ and Hα lines. The spectra are measured through a 3″ diameter fiber.

Regions 2, 3, and 4 have line ratios typical of AGN, although the ra-

Table 3.5: Emission line fluxes from SDSS spectrum (Fig. 3.16).

Line	flux $[10^{-17}\ \mathrm{Wm}^{-2}]$	FWHM $[\mathrm{km\ s}^{-1}]$
[O II] 3727Å	1.9 ± 0.1	480
Hβ narrow	0.80 ± 0.02	190
[O III] 5007Å	7.7 ± 0.1	400
[O I] 6300Å	0.71 ± 0.04	365
Hα narrow	4.9 ± 0.3	220
Hα broad	8.1 ± 0.4	3170
[N II] 6585Å	4.5 ± 0.3	300

tio of [Fe II]/Paβ is close to starburst values. Region 5 has a 1-0S(1)/Brγ ratio among those of starbursts, although the [Fe II]/Paβ ratio is unconstrained because of the lack of *J* band spectral information. The overlay of the Paα with the 6 cm radio map (Fig. 3.4 (d)) from Ulvestad & Wilson (1984) shows radio emission in all five regions. The two-point spectral index $\alpha_{6\mathrm{cm}/21\mathrm{cm}} \approx 1.3$, assuming a power-law of the form $F_\nu \propto \nu^{-\alpha}$, is on the high end of values observed for synchrotron radiation (Ulvestad & Wilson 1984; Filho et al. 2000). Such a steep spectral index is commonly found in star-forming late-type galaxies (Condon 1992). Together with the 1-0S(1)/Brγ value, this indicates the starburst nature of the emission region 5. As mentioned above, the three other off-nuclear ratios populate the transition region from starburst to AGN in the diagram. At a projected distance of about 420 pc, regions 2 and 4 still show the strong influence of the (LINER) active nucleus. The jet-like extension of the 6 cm emission towards regions 2 and 4 might also suggest the importance of outflows and associated shocks that are able to excite [Fe II] and/or H_2. Region 3 at a projected distance of about 630 pc lies even closer to the starburtst regime. This is expected, since the nuclear influence should decrease at larger separations.

In their study of LINERs, Larkin et al. (1998) investigated several multi-wavelength correlations. They found that LINERs and Seyferts do not follow the correlations between the IRAS 25 μm to 60 μm index and H_2/Brγ and [O I]/Hα found by Mouri & Taniguchi (1992) for starburst galaxies. The IRAS 25 μm and 60 μm fluxes are sensitive to warm (30-50 K) and hot (100-150 K) dust. Seyfert galaxies typically show a shallow index. Therefore this index can be used as a Seyfert identifier (de Grijp et al. 1992). LINERs show a wide spread in the IRAS index, whereas they only show little variation in the H_2/Brγ and [O I]/Hα ratios (Larkin et al. 1998). The values for Mrk 609 ($\alpha(25:60) = -1.9$; [O I]/H$\alpha \approx 0.15$; H_2/Br$\gamma \approx 0.55$ for the total FOV or H_2/Br$\gamma \approx 1.23$ for the nuclear region) fall between the starburst correlation and the region occupied by LINERs. Note that the optical line-ratio is derived from the $3''$ diameter aperture SDSS spectrum, whereas the NIR line-ratio is calculated for region 1 and for the total FOV. Nevertheless, a trend towards LINER values can be recognized at both wavelengths. Besides the aperture effects mentioned above, considerable variability in the emission has been detected (Rudy et al. 1988; Pappa et al. 2002), which can be combined with the *duty cycle hypothesis* of Eracleous et al. (1995). The authors propose recurring accretion events that enhance the non-stellar continuum and generate Seyfert characteristics like broad emission lines. After the accretion event, the ionizing flux drops and the high-ionization states weaken, whereas the lower-ionization lines persist much longer, because of longer decay and light crossing times compared to the broad-line region. In this respect, Mrk 609 might approach a quiescent activity state in which the relative contribution of lower-ionization and shock-driven emission is enhanced with respect to photoionization. The starburst, since farther away from the nucleus, remains constant. Unfortunately, no multi-epoch/multi-wavelength observations of Mrk 609 exist that could substantiate this scenario; and due to the calibration problems one cannot compare the line fluxes with the NIR measurements of Goodrich (1990) and Rix et al. (1990).

The panchromatic properties of Mrk 609 reveal its composite nature. In Fig. 3.17 the spectral energy distribution (SED) is plotted and compared to average SEDs of starburst, LINER, and spiral galaxies (taken from Schmitt et al. 1997). Also shown is the average SED of radio-quiet quasars from Elvis et al. (1994). It can be seen that the X-ray flux is nicely represented by an AGN-like contribution. Pappa et al. (2002) estimate from the FIR luminosity that a starburst can only contribute up to 50% of the X-ray luminosity. But the AGN itself cannot explain the longer wavelength fluxes, which appear to be a combination of the three other contributions. Only starbursts can produce the strong FIR fluxes. The LINER SED also fits nicely into this picture. Note that Mrk 609 is missing a significant big blue bump, which is also absent in low-luminosity AGN and might be explained by low accretion-rate models (Ho 1999). Furthermore, Ward et al. (1988) found a strong correlation between the broad Hα and the 2-10 keV X-ray lu-

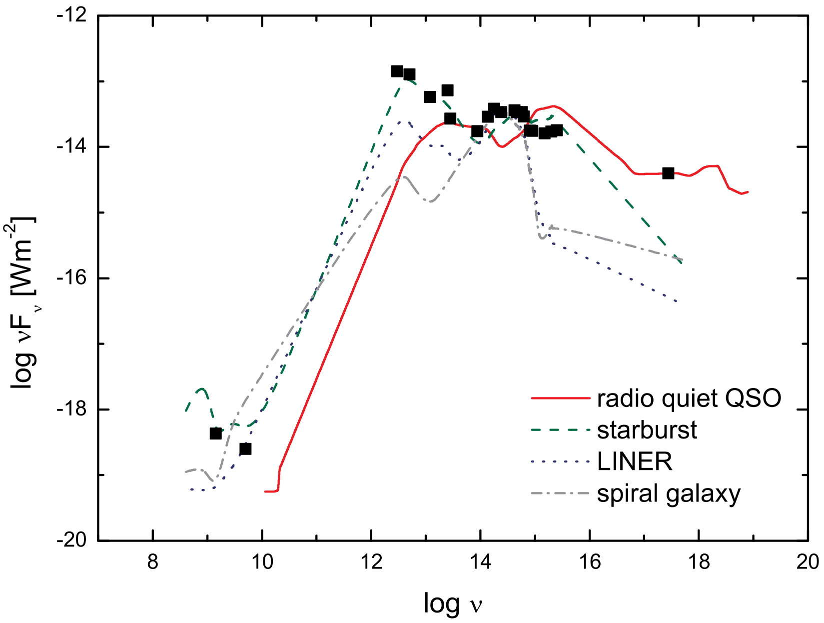

Figure 3.17: Spectral energy distribution of Mrk 609 constructed from literature values (Rudy et al. 1988; Polletta et al. 1996). The values are compared with average SEDs from normal galaxies, starbursts, LINERs (Schmitt et al. 1997), and radio-quiet QSOs (Elvis et al. 1994).

minosity as a measure for the ionizing strength of the active nucleus. Pappa et al. (2002) find, that the Hα emission from the large aperture spectrum is underluminous by a factor of about 40 and suggest a deficit of ionizing photons. This is agrees with the missing UV-bump in the SED. Another possibility is the variability of the nonstellar continuum over the 15 years between optical and X-ray emission.

The nuclear continuum and emission-line morphology is not symmetric and possibly resembles that of a weak nuclear bar (Fig. 3.3(d), 3.5(a)). The emission peaks of the Paα map are aligned with the major and minor axes of the bar. In addition, the slight elongation of the 6 cm radio emission towards regions 2 and 4 (Fig. 3.4(d)) could be interpreted as a jet, which might in part be responsible for the heating of regions 2 and 4 (e.g. van Breugel & Dey 1993). The interpretation is still not clear from the current data. On the other hand, the clumpy structure of the ISM seen in the recombination line maps might also resemble a ring-like structure or parts of a nuclear spiral.

Such structures have been uncovered in both the observation (e.g. Erwin & Sparke 2002; Martini et al. 2003; Emsellem et al. 2003) and simulation (e.g. Englmaier & Shlosman 2000; Maciejewski 2004) of several quiescent and active galaxies. Torques associated with the gas response to the stellar-bar potential allow considerable amounts of gas to flow closer to nuclear regions ($\sim 1\ M_\odot\ \mathrm{yr}^{-1}$ on time scales of $\sim 10^8$ yr; Englmaier & Shlosman 2004) where viscous processes take over the dissipation of angular momentum (Duschl & Strittmatter 2004). From the symmetrical appearance with respect to the bar's minor axis, one might expect a northeastern counterpart for region 3, which is missing, however, in the hydrogen emission-line maps. Nevertheless, the reddening map exhibits some additional reddening at the position of the proposed counterpart. The velocity maps of the hydrogen recombination line do not show any dynamical behavior, which is expected due to the face on view of the galaxy and the limited spectral resolution. Therefore, currently none of the above models can be favored with respect to the other.

3.5 Summary and conclusions

Mrk 609 was chosen from a sample of AO-suitable optical counterparts of luminous ROSAT X-ray AGN at low to intermediate redshifts (Zuther et al. 2004b, 2005b). It is one of the lowest redshift objects in the sample and is therefore best-suited for initial integral field observations.

In this chapter, first results on the circumnuclear structure of the starburst/Seyfert composite Mrk 609 in the NIR using imaging spectroscopy with SINFONI were presented. The morphology is complex, and the continuum images reveal a bar-like structure. The distribution of hydrogen recombination emission (Paα, Paβ, Brγ) is clumpy and peaks at the tip where the potential bar meets the spiral arms and in regions along the minor axis. Bars can account for the angular momentum transfer necessary for fueling nuclear activity. The 6 cm VLA emission is also extended in the latter direction. Whether this emission is associated with a jet or with resonances in the bar potential, is unclear. The presence of nuclear broad Paα and [Si VI] are clear indicators of the accretion of matter onto a nuclear super-massive black hole.

The analysis of molecular hydrogen and [Fe II] emission indicates the importance of shock heating, although X-ray heating by the nucleus and non-thermal contributions is possible. The distribution of molecular hydrogen follows the continuum shape, while that of [Fe II] is aligned with the minor axis of the continuum and with the radio contours, as well as with the H-recombination line peaks. The nucleus itself shows signs of LINER activity, which can be recognized by its high [Fe II]/Paβ and H_2/Brγ values. The integral-field data clearly resolve the nuclear and starburst activity in the central kilo parsec. Extinction appears to play no crucial role in this region, since the H-recombination line ratios are consistent with unreddened case-B values. This is supported further by the strong Lyα emission. However, already small amounts of extinction have considerable effects at visible wavelengths, as can be seen in the flocculent morphology of Fig. 3.1. Continuum reddening in the NIR, on the other hand, can already be caused by small amounts of warm/hot dust. The reddening of the continuum found toward the nucleus and the other regions is typical of AGN and star-forming regions where the dust reprocesses UV radiation from hot stars or the active nucleus.

Large amounts of cold molecular gas are found, which provide the fuel for the star-forming activity. M-type giants are the dominating stellar population in the NIR, which indicates starburst ages of about 100 Myr (for a single burst). The nuclear stellar absorption features are considerably diluted by the non-stellar continuum.

The proposed LINER classification, together with the published variability of the non-stellar NIR emission, might be explained by the duty-cycle hypothesis in which short-lived accretion events occur periodically and lead to the appearance of Seyfert features in the high state and of low-ionization (shock driven) emission features in the low state.

The X-ray emission can account for some of the H_2 excitation. This might also explain the higher H_2/Brγ ratios for the off-nuclear regions than expected for starbursts. The [Fe II] emission, however, does not seem to be excited by X-rays. Shock excitation along the southeast/northwest axis might be caused partly by a radio jet impinging into the ISM. The main driver for both species therefore appears to be shock excitation.

The results presented in this chapter show that high spatial resolution is vital for dissecting the nuclear and starburst activity in AGN. Morphological peculiarities, such as nuclear bars and nuclear starburst rings, are best detected at NIR wavelength, since the mass dominating stellar populations have their emission maximum in the NIR, and dust extinction is smaller than at visible wavelengths. In conjunction with high spectral resolution, it is possible to trace the stellar and gaseous nuclear kinematics in order to find important constraints for dynamical models describing the infall of matter into the nuclear regions (e.g. Fathi et al. 2005). This is a prerequisite for the study of composite systems in which nuclear star formation and Seyfert activity occur at similar levels of intensity.

CHAPTER 4

Broad absorption line quasars: Young AGN at high redshifts?

Based on work published in Zuther & Eckart (2005).

This chapter will proceed to even higher redshifts and the detection of the host galaxy of a $z \sim 2$ broad absorption line quasar (BALQ) in the field of the late-stage merger QSO 3C 48 (Zuther et al. 2004a) will be discussed. BALQs are important but rare probes of the mass assembly in galaxies in an evolutionary context. The few low-redshift examples of this QSO class are all associated with disturbed host galaxies, which apparently have undergone a merger event with another galaxy. In the ULIRG-to-QSO evolutionary scenario, as discussed by Canalizo & Stockton (2001), BALQs might represent an early AGN phase, in which outflows and radiation pressure from the accretion process drive away the gas and dust cocoon accumulated during the galaxy interaction in the central region of the merger remnant.

Host galaxies of high redshift QSOs are hard to detect, because of the high contrast between the faint host galaxy and the up to 100 times brighter QSO nucleus. The cosmological surface-brightness dimming further complicates matters. Using large telescopes (like the 8.4 m VLT), we are now able to overcome some of these limitations. State-of-the-art instrumentation allows us to separate the AGN from the underlying stellar component and to detect even faint, extended host galaxy structures at high redshifts. There is, however, only a handful of host detections of BALQs at high redshift and the detection presented here adds to this important class of objects.

The ensuing sections will briefly introduce the topic; then the ISAAC observations, and finally the results of this study will be discusses. As a reminder, unless noted, a cosmology with $H_0 = 70$ km s^{-1} Mpc^{-1}, $\Omega_m = 0.3$, and $\Omega_\Lambda = 0.7$ (Spergel et al. 2003) will be used throughout this chapter.

4.1 BALQs: a brief overview

As discussed in Chapter 1, there is evidence for an intimate link between the growth of massive black holes and the galaxy bulges they reside in (e.g. Page et al. 2001). This implies the existence of physical feedback mechanisms to regulate their coeval evolution. In the quasar phase, i.e. during the bulk of the accretion of matter onto the central massive black hole, winds/outflows from the innermost region of the quasar can be an important source of such a feedback (e.g. Gallagher et al. 2004).

BALQs form a rare class, comprising about 20% of the QSO population at moderate to high redshifts (Hewett & Foltz 2003). The BAL phenomenon is related to outflows in quasars (e.g. Hamann & Sabra 2004). Such outflows constitute metal absorption systems with large blueshifted velocities (several thousand km s^{-1}; see Fig. 4.1). Prominent P Cygny-type features are found at UV resonance transitions like C IV λ1548Å, Lyα λ1215Å, or Mg II $\lambda\lambda$2796 & 2803Å. ROSAT and *Chandra* observations revealed that BALQs are underluminous in X-rays as compared to non-BALQs, which indicates large H I absorbing column densities of $10^{22} - 10^{24}$ cm^{-2} (e.g., Green et al. 1995, 2001; Gallagher et al. 2002). There are currently two standard interpretations of these phenomena.

(1) Unified scheme: Under the assumption of the unified scheme for active galaxies (Antonucci 1993), the absorbing clouds have a small covering factor as seen from the QSO nucleus (Morris 1988; Weymann et al. 1991). Thus, the frequency of detection just translates to the rate at which our line of site intercepts the outflow (Figs. 4.2 and 4.3). Figure 4.4 demonstrates how an absorption trough can be generated by an opaque, line driven wind with a small covering fraction. The accretion disk material is accelerated radially outwards by the line radiation pressure of the UV photons of the hot accretion disk. In this configuration the presence of gas, shielding the soft X-ray emission from the very center of the accretion disk, is important in order to avoid the full ionization of the illuminated gas and therefore the loss of the line-driving mechanisms (e.g., Murray et al. 1995). In the geometrical scheme, BALQs are either viewed at large inclination angles close to the equatorial plane (Fig. 4.2; e.g., Weymann et al. 1991) or close to the polar direction (Fig. 4.3; Zhou et al. 2006; Ghosh & Punsly 2007).

(2) Evolutionary scheme: A different interpretation is that these objects are very young and are ejecting their dusty, gaseous envelopes at very high velocities following the initial turn-on of the active galactic nucleus (Voit et al. 1993; Hazard et al. 1984; Briggs et al. 1984; Lipari 1994; Canalizo & Stockton 2001; Lípari & Terlevich 2006).

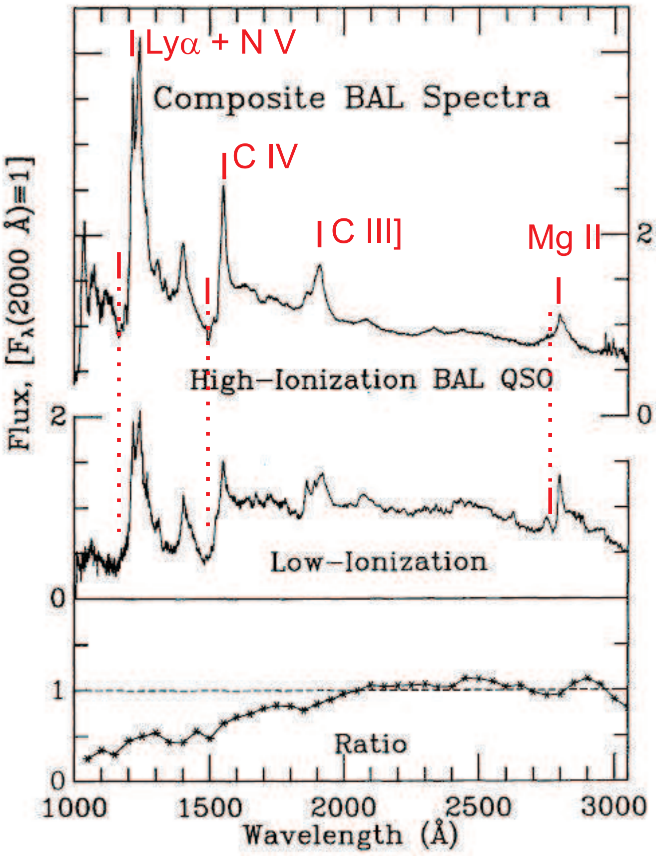

Figure 4.1: Composite rest-frame UV spectra of high (upper panel) and low (middle panel) -ionization BALQs (adapted from Sprayberry & Foltz 1992). Prominent emission lines and their associated broad absorption troughs are indicated. The lower panel shows the ratio between the two types of BALQs indicating that the low-ionization species is considerably reddened with respect to the high-ionization one.

The unified scheme would imply that all radio-quiet QSOs should be classified as BALQs if observed from the proper angle. This was supported until recently by the work of Stocke et al. (1992). However, in a spectroscopic follow-up of radio selected BALQs, Becker et al. (2000) found a population of FIRST[1] BALQs being rather radio-intermediate, indicating that the radio properties do not support the "simple" scenario stated above.

---

[1] VLA Faint Images of the Radio Sky at Twenty-centimeters

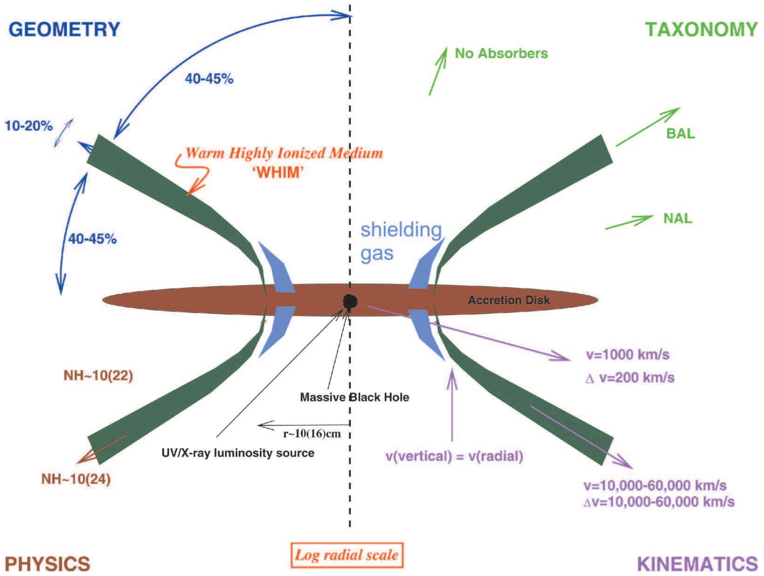

Figure 4.2: Interpretation of the broad absorption troughs in the context of the unified scheme. In this figure the covering factor of the outflow, causing the absorption, is small. The diagram shows the vertical structure of the central engine and the angular distribution of components. The right part of the figure give kinematic information on the outflow velocities. Adapted from Elvis (2000).

On the other hand, in case of the evolutionary scenario an enhanced sub-mm radiation would be expected, because the BALQs still possess a lot of molecular gas and dust while actively forming stars (Hall et al. 1997; Reichard et al. 2003; Richards et al. 2003) and the host galaxies would appear to be at early stages in their evolution. There seems to be a subclass of BALQs with enhanced far-IR emission (Low et al. 1989) for which this could be the case. The large number of low-ionization BALQs (LoBALQs)[2] in IRAS-selected luminous QSOs, along with the reddening from dust in these objects, suggests that this subclass may represent an evolutionary transition between ultraluminous IR galaxies and the classical QSO population in the early universe (Lipari 1994; Voit et al. 1993; Egami et al. 1996). Recent studies of BALQs by Lewis et al. (2003) and Willott et al. (2003), however, show no differences in the sub-mm properties between BALQs and non-BALQs which supports a small BAL covering factor.

---

[2] About 15% of the BALQ population show low-ionization-level systems in which, e.g., Mg II $\lambda\lambda 2796$, 2803, Al II $\lambda 1671$ are also prominent. LoBALQs are often associated with large amounts of dust.

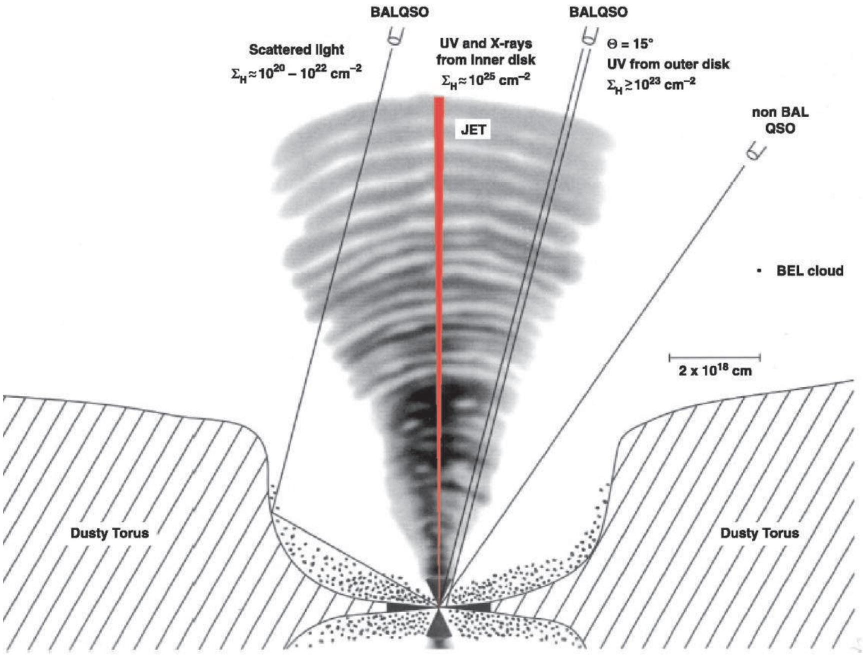

Figure 4.3: The gray cloud of the BAL wind has an opening angle of about 30°. Nested inside is a relativistic jet (in red). The highest BAL wind densities are near the polar axis. Thus, lines of sight near the polar axis have the maximum attenuation of X-ray and ionizing UV radiation from the accretion flow. This implies that lines of sight close to the polar axis are more likely to represent LoBALQs. Courtesy of Ghosh & Punsly (2007).

In addition Archibald et al. (2002) show that the star forming phase of the host and the dust/gas rich BAL wind do not need to coincide in time, thus providing constraints on alternative evolutionary models.

As the detailed nature of these objects is still under debate, the study of their host galaxies could provide important complementary information.

4.2 BALQ 0134+3253

One recent example of a detected extended emission around a BAL QSO is the object 0134+3253. Canalizo et al. (1998) (hereafter CS98) present in their work a rest frame UV spectrum as well as Hubble Space Telescope (HST) rest frame UV/optical images of the $z = 2.169$ BALQ 0134+3253 (Fig. 4.1). The authors find a deep absorption trough blueward of the C IV line which is composed of three elements and wind velocities of up to -

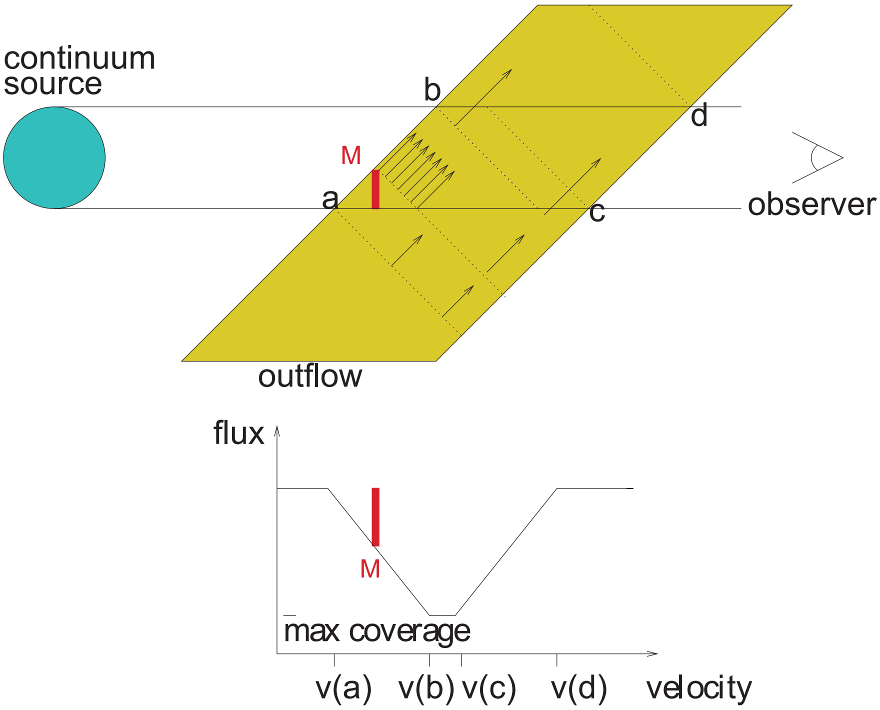

Figure 4.4: Generation of an absorption trough in an accretion disk wind. A fully opaque outflow produces an absorption trough purely from a velocity dependent covering factor. The wind accelerates across the 'cylinder of sight', but the velocity in an orthogonal cross-section (as defined by the dotted lines – base of the arrows – in the figure) is constant. Prior to the point a the radiation experiences no absorption ($v < v_a$). As the flow continues to accelerate, it gradually covers a larger fraction of the cylinder of sight. At point M the flow covers about one third of the cylinder of sight with material moving at v_M. The covering fraction $C(v)$ gradually increases until v_b, at which point a maximum coverage has been reached. At v_c the flow reaches the last point of maximum coverage and thereafter the coverage decreases. Adapted from Arav (2004).

12,000 km s^{-1}. The red edge is about +1000 km s^{-1} (their Fig. 2). There is no more spectroscopic information available to further classify this QSO as an high- or low-ionization BALQ. From their optical spectrum an intermediate absorption system at $z \approx 1.667$ is evident, probably being a damped Lyα absorber (CS98). In this context it is not clear whether the redness, with respect to the average HST quasar spectrum (Zheng et al. 1997), is due to the absorption system or intrinsic to the quasar host galaxy. Photometric data are summarized in Tab. 4.1. The HST F555W and F814W filters approximately correspond to V and I band, respectively, whereas g lies between B and V.

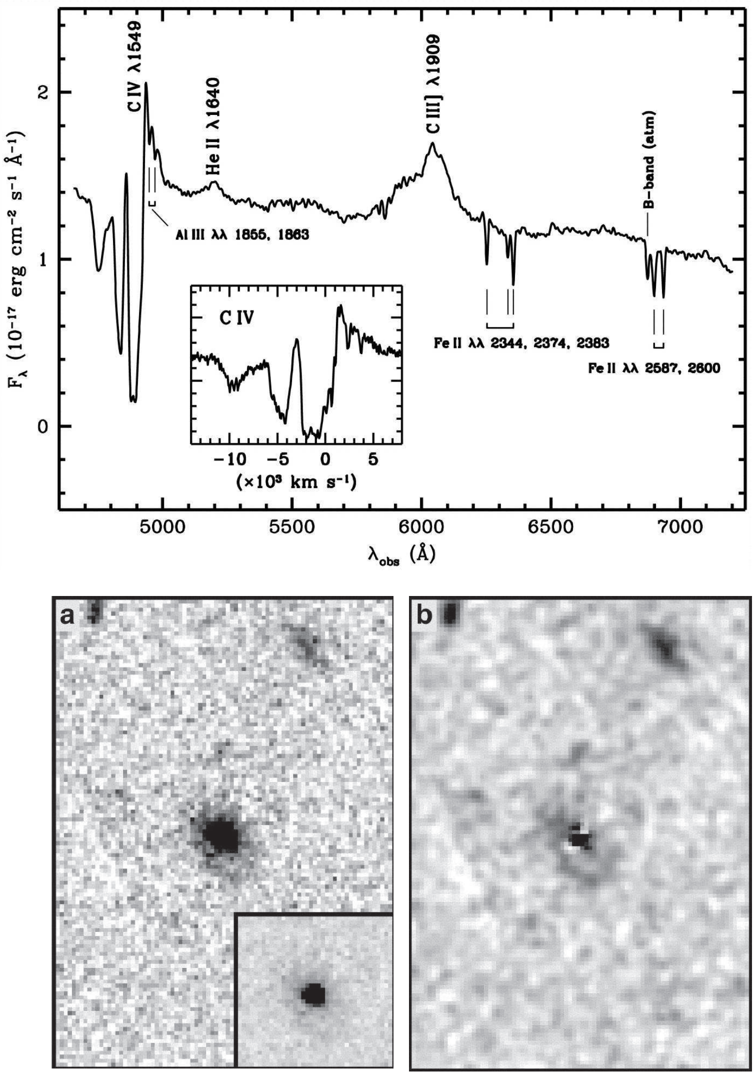

Figure 4.5: *Upper panel:* Rest-frame UV spectrum of BALQ 0134+3253. *Lower left panel:* HST WFPC2 F555W image of the BALQ with lower contrast inset. *Lower right panel:* Smoothed and PSF-subtracted version of left panel. Adapted from CS98.

4.3 Observation and Data Reduction

The data were acquired with the Infrared Spectrometer and Array Camera (ISAAC, Moorwood 1995) mounted at the Nasmyth B focus of Unit Tele-

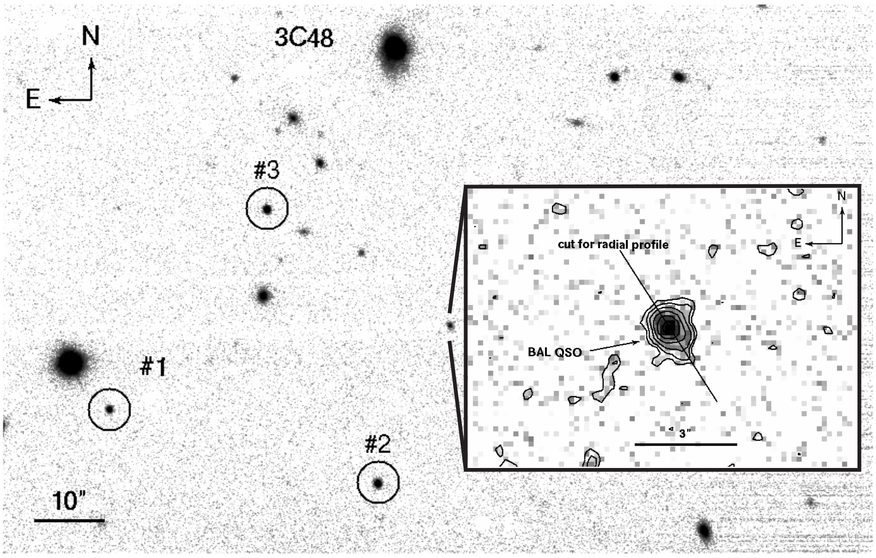

Figure 4.6: *H* band ISAAC image of the field of 3C 48 (Zuther et al. 2004a).The inset shows the *H* band close up of the broad absorption line quasar. The lowest contour is at the level of sky noise. Also indicated is the primary cut used for the radial profiles. The stars used for PSF estimation are marked with (#1, #2, and #3). See text for details.

scope 1 (UT1, Antu) of the Very Large Telescope (VLT; ESO, Chile).

Imaging was performed in the broad bands J, H and Ks (1.2 - 2.2 μm). The 1024×1024 pixel Hawaii Rockwell array detector provides a pixel scale of $0\farcs1484$/pixel with a field of view of 152×152 arcsec^2. On source integration time was 2880 s, 2160 s, and 1080 s in J, H, and Ks respectively. The data were reduced with IRAF using standard procedures. In all bands the images seem to be adequately flat with a variation smaller than 3% over the area of interest. Additionally, the science object was moved across the array, so that these variations are reduced due to the averaging of the individual exposures. Successive object and sky observations were subtracted and shifted to produce sky subtracted and averaged (median) images. Fig. 4.6 shows the H-band image including the quasar 3C 48. The average seeing was about FWHM $\approx 0\farcs4$ in H and about $0\farcs5$ in J and Ks. The calibration of the data relies on the observation of standard stars (Hawarden et al. 2001; Persson et al. 1998). More details on the data reduction can be found in Zuther et al. (2004a).

Table 4.1: Previous measurements of the BALQ and the extended emission.

Filter (1)	Total (2)	Host (3)
g	21.2 [a]	–
F555W = V	21.14 [b]	23.8 ± 0.1 [b]
F814W = I	21.28 [b]	24.1 ± 0.1 [b]
$H + K$	–	5×10^{-20} erg s^{-1}cm^{-2}Å^{-1}arcsec^{-2} [b,c]

[a] Kirhakos et al. (1994); listed as a star

[b] CS98; measured in a 2.6 arcsec diameter aperture

[c] CS98; 1σ detection threshold

Table 4.2: Photometry of the BALQ and the extended emission. The first part lists J, H, and Ks magnitudes measured from the radial profiles and in a $1\farcs5$ diameter aperture. The second part lists the deduced colors. Total fluxes and colors are listed in columns (2) and (3). Columns (4) and (5) give the host magnitudes and colors, and (6) and (7) correspondingly for the subtracted nucleus.

Filter	Total [mag]		Host [mag]		Nucleus [mag]	
(1)	rad. prof. (2)	$1\farcs5$ ap. (3)	rad. prof. (4)	$1\farcs5$ ap. (5)	rad. prof. (6)	$1\farcs5$ ap. (7)
J	19.9 ± 0.1	20.2 ± 0.1	23.5 ± 0.2	22.6 ± 0.1	22.1 ± 0.2	20.3 ± 0.1
H	19.1 ± 0.1	19.4 ± 0.1	22.4 ± 0.1	21.4 ± 0.1	21.2 ± 0.1	19.5 ± 0.1
Ks	18.5 ± 0.1	18.9 ± 0.1	21.8 ± 0.2	20.7 ± 0.1	20.6 ± 0.2	19.1 ± 0.1
Colors						
$J - H$	0.8 ± 0.1	0.8 ± 0.1	1.1 ± 0.2	1.2 ± 0.1	0.9 ± 0.2	0.8 ± 0.1
$H - Ks$	0.6 ± 0.1	0.5 ± 0.1	0.6 ± 0.2	0.7 ± 0.1	0.6 ± 0.2	0.4 ± 0.1
$B - Ks$	3.2	–	–	–	–	–

4.4 Results and discussion

While the connection between the super massive black holes (SMBH) and their host galaxies is still not clearly understood, the host galaxies are ex-

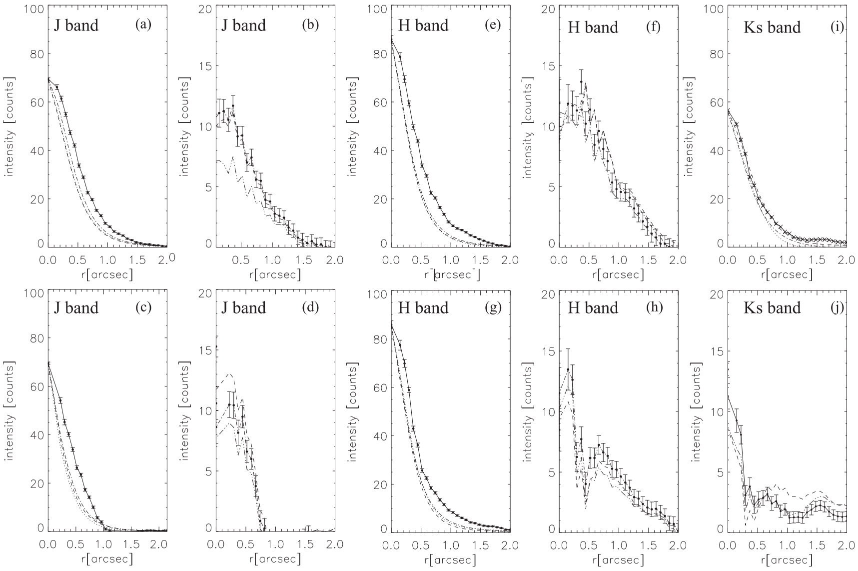

Figure 4.7: (a) *J* band radial profile of the BALQ (solid line) and three nearby stars (dotted, dashed, dash-dot; see Fig. 4.6). The peak flux of each star is scaled to the peak flux of the BALQ. (b) The residual radial host galaxy profile after subtracting the stellar profile, scaled such that the residual emission is approximately flat close to the center. (c) and (d) correspond to (a) and (b) but for a cut along a position angle of 132°. (e, f) and (g, h) same as (a, b) and (c, d) but for *H* band. (i) is the *Ks* band radial profile for the position angle of 132° and (j) is the residual after subtraction of the stellar profile. The profile of the BALQ along the PA of 45° shows only a marginal extent with respect to the stellar profile. See text for details.

tremely difficult to observe at redshifts $z > 1$, because of the high contrast between nucleus and host galaxy and the surface brightness dimming. The high sensitivity of the VLT and its instrumentation as well as the good seeing conditions (FWHM < $0\farcs5$) enabled me to investigate the extended rest-frame optical emission around the BALQ 0134+3252, providing a view on the unobscured star formation in these galaxies.

Fluxes in J, H, and Ks of the BALQ, the potential host galaxy, and the nucleus are measured. Galactic extinction is no corrected for, because its values are smaller than the photometric error. The results are listed Table 4.2. Previous measurements by Kirhakos et al. (1994) and CS98 are given in Table 4.1.

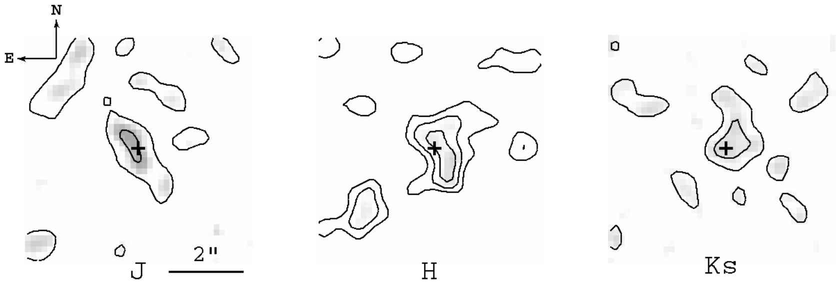

Figure 4.8: PSF-subtracted J, H, and Ks images. After subtraction the images have been smoothed with a three pixel Gaussian. The contour levels correspond to $(1,\ 4) \times \sigma$ in J, $(1.5,\ 3,\ 4) \times \sigma$ in H, and $(2,\ 3) \times \sigma$ in Ks of the sky noise. The crosses shows the position of the nucleus from which the PSF is subtracted.

4.4.1 Overall properties

Measuring the fluxes in a 2.″6 diameter aperture centered on the quasar nucleus (as done by CS98), The overall colors of the BALQ are $J - H = 0.8 \pm 0.1$ and $H - K = 0.5 \pm 0.1$ (cf Fig. 4.10). Using the F555W and the g magnitude together with the transformation from g to B magnitudes ($g = V - 0.19 + 0.41[B - V]$) stated in Kirhakos et al. (1994), on gets an observed $B - K \approx 3.3$. This is only slightly reddened compared to a typical $B - K = 3$ for unreddened $z > 1$ quasars (Hall et al. 1997, and references therein). CS98 found a small reddening of the rest-frame UV spectrum of the BALQ compared to the HST composite quasar spectrum (Zheng et al. 1997). Estimating this reddening to be about a factor of 1.3 and following the UV-optical extinction law (e.g. Sofia et al. 2005), the small UV-reddening contributes only little to the rest-frame optical, resulting in the slightly reddened observed $B - K$ color.

In the untreated H-band image (Fig. 4.6) a non stellar-like shape of the BALQ can already be emphasized, which will be discussed next.

4.4.2 Radial profiles and 2-dimensional images

In order to get an improved impression of the faint host galaxy emission, two radial profiles orthogonal to each other in each band are extracted, with one along the primary extended component at a position angle (PA) of about 45°. The profiles are measured over cone-like sections with a cone angle of 60° along this extension (apparent major axis) and along the orthogonal axis at PA= 132° (cf Fig. 4.6).

The radial profiles of the BALQ are compared with the profiles of three nearby unsaturated stars, circular in appearance (#1, #2, and #3 in Fig. 4.6), where the stellar profiles are scaled to the QSO peak flux (Figs. 4.7 (a, c), (e, g), and (i, j)). It is evident from the radial profiles that the intensity distribution in J and H is extended compared to the stellar radial profiles. Next, a Moffat function, which well represents the ISAAC seeing-limited PSF, is fitted to each stellar profile. After subtracting the three functions from the galaxy profile individually, a residual emission is clearly visible in the J and H band (Figs. 4.7 (b, d) and (f, h)), whereas in Ks there is only a faint and noisy residual profile (Fig. 4.7 (j)) visible. The low signal-to-noise ratio (SNR) in the Ks-band residual (especially in the PA= 45° cone section (cf Fig. 4.8)) can be accounted for by the facts, that young stellar populations are fading towards longer rest-frame optical wavelengths (e.g. Fig. 8 of Jahnke et al. 2004a) and that the sky background increases towards the observed Ks. In favor of clarity for the reader only the error bars of the 'middle' profile (star #3) are shown, which are also used to estimate the flux. The stellar flux was scaled such that its subtraction results in a smooth and flat central part of the profile (cf discussion in McLeod & McLeod 2001). This presents a conservative lower limit for the potential emission of a host galaxy. A subtraction of a larger point-like contribution resulting in a decrease of the intensity towards the center is likely to be not physical, and would yield colors not consistent with those of normal galaxies.

The fluxes are measured within the two perpendicular cone-sections by summing over the profiles. Then the mean flux is calculated as the geometric mean of the two measurements. Assuming an elliptical morphology would overestimate the flux when using the major axis alone, and underestimate the flux when only considering the minor axis. The integrated fluxes in the H and Ks measurements are consistent with the limits given by CS98. From the residual fluxes one can estimate colors of the extended emission around the BALQ.

Similarly, the same star (#3) is used and scaled for the subtraction of the nucleus in the 2-dimensional (2D) images. The results are smoothed with a 3 pixel FWHM Gaussian in order to reduce the noise. Nevertheless, the images show quite strong fluctuation, whereas the H band image has the best signal-to-noise ratio. The fluxes are measured in $1\overset{''}{.}5$ diameter apertures, because up to this size the fluctuations are not significant. The given errors only include measurement uncertainties. The host contribution to the total light in the NIR is of the order of 10%. The PSF subtracted images presented in Fig. 4.8 show an overall elliptical morphology. The

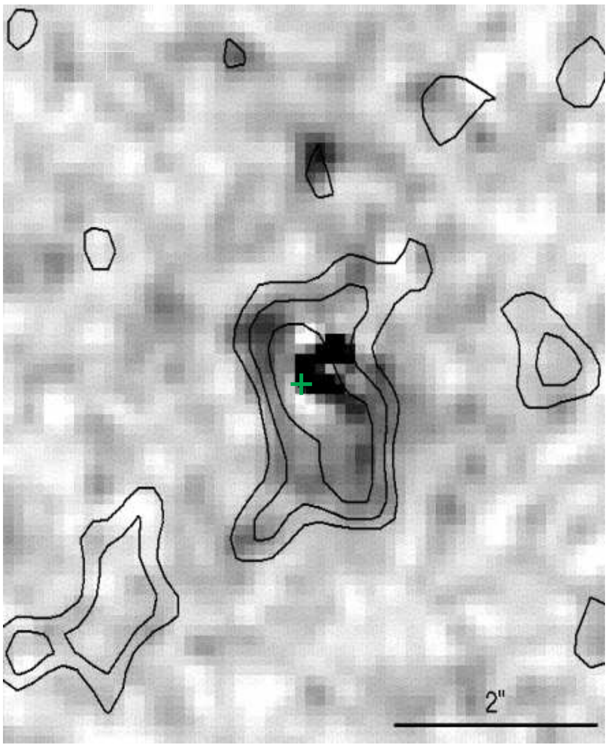

Figure 4.9: PSF-subtracted HST F814W image from Canalizo et al. (1998) overlaid with contours of the three-pixel-smoothed, PSF-subtracted *H* band image. The lowest contour level corresponds to $1.5 \times \sigma$ of the sky noise. The green cross shows the position of the nucleus in the *H* band image. North is up and east is to the right. Note that the PSF-subtracted HST images is extracted from Canalizo et al. (1998). Despite the values given in Table 4.2 no further photometric information is available.

lowest contours correspond to $\sim 2\sigma$ of the sky noise. The structures at distances larger than $3''$ from the nucleus are most probably due to noise. The feature about $2''$ southeast of the nucleus (*H* and *Ks*) is also visible in the untreated image (inset in Fig. 4.6) although it is not clear whether it is connected to the BALQ at all. Figure 4.4.2 shows the PSF-subtracted *H* band image in contours overlaid on the PSF-subtracted HST *V*-band image extracted from CS98. Although the exact position of the nucleus in the HST image is not known to us, the overall size and orientation is similar to what is reported on the optical by CS98.

The colors of the BALQ, its host, and its nucleus together with colors of starbursts of different ages at $z = 2$ and $z = 1.7$ are presented in Fig.

4.10. For comparison colors of other BALQs listed in Hall et al. (1997) are displayed. Among them are Hawaii 167 (Cowie et al. 1994) and the radio-loud QSO 1556+3517 (Hall et al. 1997), two of the reddest ($B - K > 5$) quasars known. Within the errors the colors of the two methods (radial profiles and 2D photometry) are consistent with each other.

Combining the available photometric data, one can use the four colors ($F555W - F814W$), ($F814W - J$), ($J - H$), and ($H - Ks$) to get a first impression of the stellar content of the extended emission by comparison with colors of simple stellar populations (Figs. 4.10 and 4.11). Colors of a 1 Gyr starburst followed by passive evolution are calculated at redshifts of $z = 2$ and $z = 1.7$, using the population synthesis code of Bruzual & Charlot (2003), and utilizing the Padova1994 initial spectral energy distributions of solar metallicity with a Chabrier initial mass function (Chabrier 2003).

The host colors from Fig. 4.10 infer a stellar population of about 2 Gyr dominating the emission at the redshifts of the BALQ. At the redshift of the intermediate absorber, the ages are somewhat older. Thus, the stellar populations in the rest-frame optical appear to be older than the ones found by CS98 in the rest-frame UV only, which is typically dominated by young and hot stars. The view on the unobscured star formation can be seen in Fig. 4.11. The rest-frame UV/optical host colors lie well below the color track of the 1 Gyr starburst. The mixing curve is calculated for a composite color made up of a 0.1 or 0.5 Gyr and a 2 Gyr population (the two thick dotted curves in Fig. 4.11). It is evident that a young population dominates the rest-frame UV/optical emission, accounting for about 80% of the colors. Correspondingly, the dominating population would be somewhat younger at $z = 1.667$. Similar results are found by Jahnke et al. (2004b, their Fig. 6) in their study of likewise luminous $z \sim 2 - 3$ GEMS quasar hosts.

Further details on the stellar populations are difficult to obtain, because of the possible degeneracies of colors related to dust and metallicity (cf Jahnke et al. 2004b). Moreover, the noisy residual after subtraction of the QSO nucleus can influence the resulting colors.

Assuming that the extended emission originates at the redshift of the BALQ, $z = 2.169$, $1''$ corresponds to a linear scale of 8.3 kpc. In the unified scheme BALQs should be common QSOs at the respective redshift, viewed such that our line of sight intercepts the QSO wind. Thus, one can compare the results with hosts of present-day and $z \sim 2 - 3$ radio-loud and radio-quiet QSOs. For this purpose two model-independent measures of the host galaxy size are used (Table 4.3). First the mean half width at half maximum (HWHM) of the radial profile is measured, because there is some degree of

Table 4.3: Physical scales of the residual emission determined from the *H*-band radial profile.

$\mathrm{HWHM}_{\mathrm{major}}$ [″] (1)	$\mathrm{HWHM}_{\mathrm{minor}}$ [″] (2)	$r_{1/2}$ [″] (3)	[kpc/arcsec] ($z = 2$) (4)	[kpc/arcsec] ($z = 1.7$) (5)
0.9 ± 0.1	0.5 ± 0.3	0.4 ± 0.1	8.3	8.5

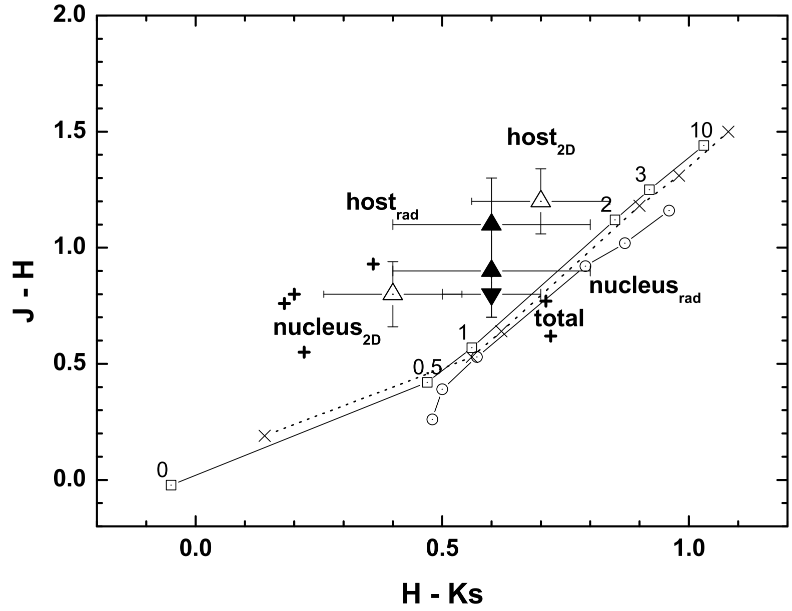

Figure 4.10: Two-color diagram presenting the $(J - H)$ vs. $(H - Ks)$ observed colors of the BALQ (upside-down triangle), the host, and the nucleus (filled triangles) as discussed in the text. The hollow triangles represent the host and nuclear colors measured in a 1.5″ diameter aperture from the 2D PSF-subtracted images. Also shown are colors of BALQs (crosses) from Hall et al. (1997). For comparison colors of a 1 Gyr starburst followed by passive evolution for ages of 0, 0.5, 1, 2, 3, and 10 Gyr at redshifts $z = 2$ (open rectangles) and $z = 1.7$ (open circles) are displayed (using Bruzual & Charlot 2003). The dotted line shows the effect of reddening of the $z = 2$ track following the model of Charlot & Fall (2000) with $\tau_V = 1.5$ and $\mu = 0.3$.

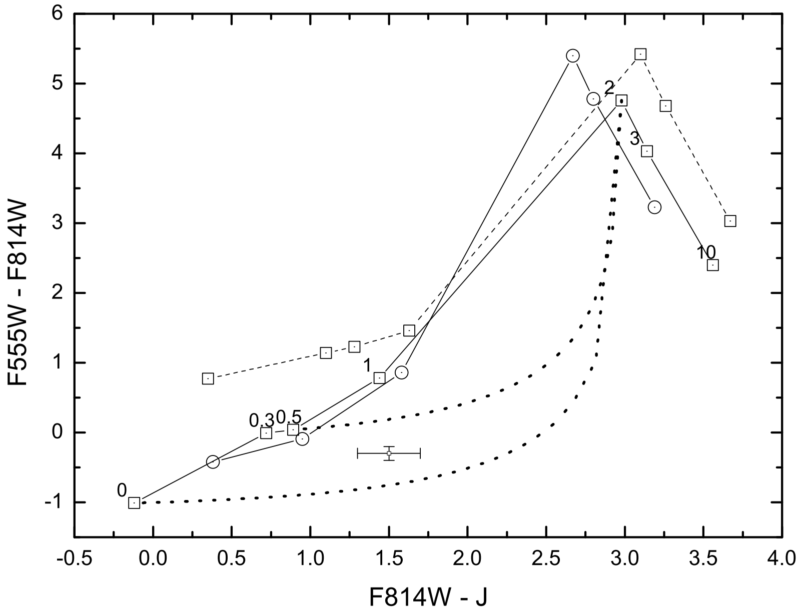

Figure 4.11: Two-color diagram presenting the $(F555W - F814W)$ vs. $(F814W - J)$ observed colors of the BALQ host galaxy (cf Fig. 4.10). Also shown are the colors of 1 Gyr single starbursts followed by passive evolution at $z = 2$ (open squares; numbers indicate the age in Gyr) and $z = 1.7$ (open circles). The effect of reddening of the $z = 2$ track, with $\tau_V = 1.5$ and $\mu = 0.3$ according to the model of Charlot & Fall (2000), is shown as open squares joined by a dashed line. Furthermore two curves displaying the effect of mixing of a 0.1 Gyr and 2 Gyr old (lower dotted line) and of a 0.5 Gyr and 2 Gyr old (upper dotted line) population are shown.

degeneracy in the radial profiles (cf Fig. 4.7 (h)). The H band profile shows an HWHM radius of $r = 0\farcs9 \pm 0\farcs1$, i.e. a physical scale of (7.5 ± 0.8) kpc, along the major axis. For the minor axis, $r = 0\farcs5 \pm 0\farcs3$, corresponding to (4.2 ± 2.5) kpc along the minor axis. In case of an elliptical galaxy this would give a Hubble type E4. For a spiral galaxy this would imply an inclination of about (60 ± 10)°. The axis ratio is also in agreement with the 2D PSF-subtracted H band image (Fig. 4.4.2). As a second measure, the half-light radius derived from the H band radial profile is about $r_{1/2} = 0\farcs4 \pm 0\farcs1$, corresponding to (3.3 ± 0.8) kpc. Ridgway et al. (2001) find a similar physical scale (2.3 kpc) in their sample of radio quiet QSOs at comparable redshift. These quite compact sizes seem to be more typical for Lyman break galaxies at $z \sim 2 - 3$ (Giavalisco et al. 1996; Dickinson 2000) than

Table 4.4: Estimated absolute *B*-band magnitude from 1.″5 aperture measurement. Given are the values for the redshift of the BALQ ($z = 2.169$) and the redshift of the intermediate absorber ($z = 1.667$). See text for details.

M_B Host		M_B Nucleus	
($z = 2.169$) (1)	($z = 1.667$) (2)	($z = 2.169$) (3)	($z = 1.667$) (4)
-22.5 ± 0.2	-21.9 ± 0.2	-24.9 ± 0.2	-24.2 ± 0.2

for present day QSOs hosts (McLure et al. 1999; Bahcall et al. 1997). This could imply that the compact systems are still in the process of forming. Note that because of the low SNR of the data the results can be biased towards more compact emission. Furthermore, use of the method described in Jahnke et al. (2004b) yields an estimate of the absolute *B* band magnitude (Table 4.4). Assuming an optical power law, $f_\lambda \propto \lambda^\beta$, the index β can be found from the NIR colors and then calculate the apparent *B* magnitude. The absolute magnitude turns out to be $M_B \approx -22.6 \pm 0.2$, which is also comparable to the results of Ridgway et al. (2001). The possible host would correspond to a $\sim 4 \times L_B^*$ galaxy using the luminosity function of local galaxies from Loveday et al. (1992)[3]. This is at the upper end of the range of luminosities ($0.2 - 4L_B^*$) found by Ridgway et al. (2001).

At the redshift of the absorber, $z = 1.667$, $1''$ corresponds to 8.5 kpc. Thus, the physical scales would be correspond to $\mathrm{HWHM}_{\mathrm{major}} \approx 7.7$ kpc and $\mathrm{HWHM}_{\mathrm{minor}} \approx 4.3$ kpc. The half-light radius would be $r_{1/2} \approx 3.4$ kpc. The absolute *B* magnitude of $M_B \approx -21.9$ would correspond to a $2.5 \times L_B^*$ host galaxy. Together with the colors this is still consistent with a relatively young stellar population at moderate extinction and with the host sizes at these redshifts. Therefore, one cannot pinpoint, whether the emission is coming from the BALQ host or from the intermediate absorber.

4.5 Summary

In this chapter the detection of rest-frame optical extended emission around the BALQ 0134+3252 was presented, complementing previous results on

---

[3] Their $M_B^* = -19.5$ for $h = 1$ has been adapted to the cosmology used here, i.e. $M_B^* \approx -21$.

the rest-frame UV extended emission (CS98). The UV/optical colors indicate a mixture of a young $\leq$ 500 Myr and a further evolved $\sim$ 2 Gyr old stellar population. As the broadband data are affected by various degeneracies related to dust and metallicity, a reliable age dating is still difficult to accomplish. This is even complicated due to the QSO subtraction in the noisy data. The rest-frame optical morphology is similar to the UV morphology. If associated with the BALQ, the host galaxy would correspond to a present day $4L_B^*$ host. Its compact size, $r_{1/2} = 3.2$ kpc, is comparable to radio quiet QSOs and Lyman break galaxies at $z \sim 2-3$, but smaller than present day QSO hosts. The small size, the influence of a young stellar population, and the high luminosity fit well into the framework of hierarchical galaxy formation (see Sect. 1.2). At the redshift of the potential Lyα absorber, the sizes are somewhat larger and the luminosity would correspond to a present day $2.5L_B^*$ host. Also the rest-frame optical stellar populations would be evolved slightly more than at the BALQ redshift. The data are still comparable to results found for RQQs and LBGs. However, it cannot be distinguish between the BALQ or Lyα absorber origin of the extended continuum emission.

A more detailed stellar population analysis awaits higher SNR and further spectroscopic observations. These can also help uncovering the yet unclear source of the UV/optical emission.

APPENDIX A

Notes on the implementation of the AO sample

A.1 General formulae

Angular distances in spherical geometry are calculated via *Haversine* formula (Zwillinger 2003):

$$Hav[\mathrm{rad}] = 2\sin^{-1}\left\{\sqrt{\sin^2\left(\frac{\delta_a-\delta_t}{2}\right)+\cos(\delta_a)\cos(\delta_t)\sin^2\left(\frac{\alpha_a-\alpha_t}{2}\right)}\right\} \tag{A.1}$$

Databases and programming languages do not always provide the inverse sinh function. An equivalent form is (Zwillinger 2003):

$$\sinh^{-1}(x) = \ln(\sqrt{1+x^2}+x) \tag{A.2}$$

A.2 SDSS related calculations

A.2.1 SDSS Photometric System

As described in several works, the SDSS uses a modified magnitude system to provide well-behaved magnitudes, colors and errors even for low S/N measurements.

$$\mathrm{mag} = -\left(\frac{2.5}{\ln 10}\right)\times\left[\sinh^{-1}\left(\frac{f/f_0}{2b}\right)+\ln b\right] \tag{A.3}$$

where b is the *softening parameter* for the photometric band in question (see Table A.1).

The values for b are approx. set to 1-sigma of the sky noise. The difference between Pogson and asinh magnitudes is less than 1% for objects brighter than $f/f_0 = 10b$.

Maggies are a linearized version of AB magnitudes – i.e. they are $10^{-0.4\mathrm{mag}}$.

Table A.1: Softening -b- parameter

Band	b	Zero-Flux Mag	$m(f/f_0 = 10b)$
u	1.4×10^{-10}	24.63	22.12
g	0.9×10^{-10}	25.11	22.60
r	1.2×10^{-10}	24.80	22.29
i	1.8×10^{-10}	24.36	21.85
z	7.4×10^{-10}	22.83	20.32

A.2.2 Conversion from SDSS *ugriz* magnitudes to physical fluxes

To get physical fluxes one has to invert Eq. (A.3):

$$f\left[\mathrm{erg\ cm^{-2} s^{-1} Hz^{-1}}\right] = -2bf_0 \sinh\left(\frac{\mathrm{mag}\ \ln 10}{2.5} + \ln b\right) \tag{A.4}$$

To obtain a flux density from SDSS data, you need to work out f/f_0. This number is then also the object's flux density expressed as fraction of the AB zeropoint flux density. Therefore, the conversion to flux density is

$$S = 3631\ \mathrm{Jy} \times f/f_0 \tag{A.5}$$

A.2.3 Petrosian magnitudes

The angular Petrosian radius θ_P of a galaxy is the radius at which the local surface brightness (SB) in an annulus about θ_P is one fifth of the mean SB within θ_P. The r-band Petrosian magnitude r_P is based on the flux within a circular aperture of radius $2\theta_P$. The half-light SB μ_{50} is the mean SB within a circular aperture containing half of the Petrosian flux. The data are also corrected for galactic extinction.

The Petrosian properties are based on the Petrosian ratio $\mathcal{R}$

$$\mathcal{R}(\theta) = \frac{2\pi \int_{0.8\theta}^{1.25\theta} I(\theta')\mathrm{d}\theta' / \{\pi[(1.25\theta)^2 - (0.8\theta)^2]\}}{2\pi \int_0^{\theta} I(\theta')\theta'\mathrm{d}\theta' / \pi\theta^2} \tag{A.6}$$

A fairly thick annulus is used to reduce the sensitivity of $\mathcal{R}(\theta)$ to noise and small-scale fluctuations in $I(\theta)$, which is the azimuthally averaged SB profile.

The Petrosian radius θ_P then is given by the implicit equation

$$\mathcal{R}(\theta_P) = f_1 \tag{A.7}$$

where $f_1 = 0.2$. It can have more than one solution. In this case, the outermost solution is taken.

The Petrosian flux within a circular aperture of radius $f_2\theta_P$ (Petrosian aperture) is given by

$$F_P = 2\pi \int_0^{f_2\theta_P} I(\theta')\theta' \mathrm{d}\theta' \tag{A.8}$$

with $f_2 = 2$.

The mean SB within the half-light radius, for which $\int_0^{\theta_{50}} I(\theta')\theta' \mathrm{d}\theta' = 0.5 \int_0^{f_2\theta_P} I(\theta')\theta' \mathrm{d}\theta'$, is

$$\mu_{50} = r_P + 2.5 \log(2\pi\theta_{50}^2) \tag{A.9}$$

The $2\theta_P$ Petrosian aperture contains 99% and 82% of the galaxy's light in the two cases of an exponential, $I(\theta) = I_0 \exp(-1.68\, \theta/\theta_e)$, and de Vaucouleurs, $I(\theta) = I_0 \exp\left[-7.67(\theta/\theta_e)^{1/4}\right]$, profile. Because the Petrosian aperture is always large enough to contain most of a galaxy's light, the ratio of the Petrosian to the total flux is insensitive to inclination.

In the absence of noise, the Petrosian aperture is also unaffected by foreground extinction or by cosmological dimming of the SB. Thus, identical galaxies seen at two different distances have fluxes related exactly as the inverse square of distance (in the absence of K-corrections). One can therefore determine the maximum distance at which a galaxy would enter a flux-limited sample without knowing the galaxy's SB profile. Thus, there is no bias against the selection of low SB galaxies of sufficiently bright Petrosian magnitude. These measures are independent of sky brightness and seeing for large galaxies.

For a poorly resolved galaxy, the SB profile approaches that of a PSF, and the ratio of Petrosian flux to total flux approaches 0.95, the value for a PSF. As the seeing radius approaches the half-light radius, the Petrosian flux of an exponential galaxy is biased downward, and the Petrosian flux of a de Vaucouleurs galaxy is biased upward. In practice, a galaxy with $\theta_{50} = 2''$ and $1.5''$ seeing will have its Petrosian magnitude biased by 1-3% depending on the profile and axis ratio, and the effects are much smaller for larger galaxies.

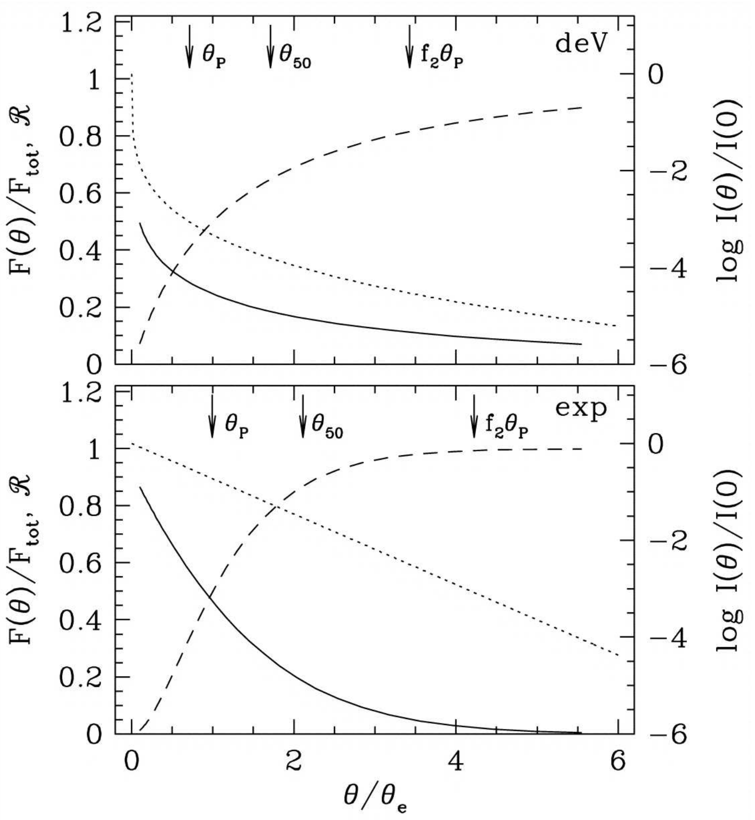

Figure A.1: Petrosian aperture procedure for a de Vaucouleurs profile (*top*) and an exponential profile (*bottom*). The dashed curves show the curve of growth, and the solid curves show the Petrosian ratio. The dotted curves show the logarithmic SB profile. Adapted from Strauss et al. (2002).

A.3 X-ray related calculations

A.3.1 Simulated grid of hardness ratios

A grid of hardness ratios HR1, HR2 can be simulated with PIMMS, assuming an initial number of photons to be distributed according to an absorbed power-law of the form

$$f(E, A, \Gamma, E_0, n_H)\,\mathrm{d}E = A e^{-n_H X(E)} \left(\frac{E}{E_0}\right)^{-\Gamma} \mathrm{d}E, \qquad \text{(A.10)}$$

where

A is the flux amplitude at reference energy E_0 in photons cm^{-2} s^{-1} keV^{-1},

Γ is the photon index,

E_0 is the refernce energy in keV,

n_H is the absorbing column density in cm^{-2}, and

$X(E)$ is the photoelectric absorption cross-section.

This distribution is subsequently folded with the ROSAT PSPC response matrix, to provide the fluxes within the energy bands A, B, C, and D. From these the values of HR1 and HR2 can be calculated for a set of Γ and n_H values, according to Eq. 2.28.

A.4 Cosmological measures

For details on cosmology, please refer to summary papers like that by (Hogg 1999). Throughout this work, the concordance cosmology is used. The current accepted cosmological parameters are a Hubble constant H_0 = 70 km s^{-1} Mpc^{-1}, a matter density $\Omega_m = 0.3$, and a cosmological constant $\Omega_\Lambda = 0.7$ (Spergel et al. 2003).

The *Hubble flow* is the general outward movement of galaxies and clusters of galaxies, resulting from the expansion of the Universe. It occurs radially away from the observer and obeys the Hubble law. Galaxies can overcome this expansion on scales smaller than that of clusters of galaxies. The clusters, however, are being forever driven apart by the Hubble flow.

For calculations of the luminosities and linear sizes of distant objects one has to use the *luminosity distance* and *angular diameter distance*, respectively. They take the accellerated expansion of the Universe into account. In terms of the concordance cosmological parameters, there is no simple solution to the Einstein field equations. In this case, the cosmological distances Web service at `http://voservices.net/Cosmology/ws_v1_0/Distance.asmx` has been utilized. Then, one can use the usual formulae to calculate luminosities and linear sizes.

A.4.1 *K* correction

Virtually all observations of galaxies are made through broadband filters. Therefore special care has to be taken to recover knowledge of galaxy spectral energy distributions (SEDs) from these observations. Sources observed through one filter at different redshifts are at different rest-frame wavelengths. The photon of a source at redshift z measured to have a frequency ν_o was emitted by the source at frequency ν_e:

$$\nu_e = (1+z)\nu_o \tag{A.11}$$

In addition to the change of the emitting frequency, the width of the passband changes as well. Therefore, calculating the appropriate K correction is not an easy task.

For a thorough discussion see e.g. Hogg et al. (2002). The K correction for a power-law flux distribution is particularly simple (Peterson 1997). The K-correction, $K(z)$, is defined as

$$m_{\text{intrinsic}} = m_{\text{observed}} - K(z) \tag{A.12}$$

or

$$F_{\text{intrinsic}} = F_{\text{observed}} 10^{0.4K(z)} \tag{A.13}$$

In general $K > 0$, since the SEDs of most objects decrease at shorter wavelength, so a Doppler shift decreases the apparent brightness of a receding source. The K-correction is formally defined as

$$K(z) = K_1 + K_2 \tag{A.14}$$

where the two terms are

$$K_1 = 2.5\log(1+z) \tag{A.15}$$

and

$$K_2 = 2.5\log\left[\int_0^\infty F(\lambda)S(\lambda)\mathrm{d}\lambda / \int_0^\infty F(\lambda/[1+z])S(\lambda)\mathrm{d}\lambda\right] \tag{A.16}$$

Here $F(\lambda)$ is the SED of the object observed and $S(\lambda)$ is the filter response function. The first term K_1 in the K-correction is due to the narrower width of the filter in the observer's frame; a spectral region of width $\delta\lambda_0$ is stretched to width $\delta\lambda_0(1+z)$ in the observer's frame, which is equivalent to apparent contraction of the observer's filter by the same factor. The integrals in the second term are the convolution of the spectrum with the filter response in the observer's frame, normalized by the value at rest.

Now consider a power-law SED of the form $F_\nu = C\nu^{-\alpha}$ as a good low-order approximation to a real AGN continuum. In λ-units: $F_\lambda = C'\lambda^{\alpha-2}$. Thus

$$F_\lambda\left(\frac{\lambda}{1+z}\right) = C'\left(\frac{\lambda}{1+z}\right)^{\alpha-2} = F_\lambda(\lambda)(1+z)^{2-\alpha} \tag{A.17}$$

K_2 then becomes

$$\begin{aligned} K_2 &= 2.5\log(1+z)^{\alpha-2} \\ &= 2.5(\alpha-2)\log(1+z) \end{aligned} \tag{A.18}$$

Equation (A.14) thus becomes

$$K(z) = 2.5(\alpha-1)\log(1+z) \tag{A.19}$$

so

$$m_{\text{intrinsic}} = m_{\text{observed}} - 2.5(\alpha-1)\log(1+z) \tag{A.20}$$

or

$$F_{\text{intrinsic}} = F_{\text{observed}}(1+z)^{\alpha-1} \tag{A.21}$$

For $\alpha \approx 1$ the K-correction vanishes. For flatter spectra ($\alpha < 1$), the K-correction is *negative*, as such objects are quite blue (compared to stars), and the Doppler shift brings a brighter part of the spectrum into the observed waveband.

APPENDIX B

Acronyms & abbreviations

2MASS: 2 Micron All Sky Survey
AGN: Active galactic nucleus
AO: Adaptive optics
BALQ: Broad absorption line QSO
BLAGN: Broad line AGN
BPT: Baldwin-Phillips-Terlevich diagram
BSC: Bright source catalog (RASS)
CDM: Cold dark matter
(C)XRB: (Cosmic) X-ray background
DM: Deformable mirror; Dark matter
DR5: 5th data release of the SDSS
ESO: European Southern Observatories. `www.eso.org`
EXO: Extreme X-ray/optical ratio object
FIRST: Faint Images of the Radio Sky at Twenty-cm
FSC: Faint source catalog (RASS)
FWHM: full width at half maximum
GAVO: German Astrophysical Virtual Observatory, `http://www.g-vo.org`
GOODS: The Great Observatories Origins Deep Survey unites extremely deep observations from NASA's Great Observatories, the Spitzer Space Telescope, Hubble, and Chandra, ESA's XMM-Newton, and from the most powerful ground-based facilities, to survey the distant universe to the faintest flux limits across the broadest range of wavelengths. `www.stsci.edu/science/goods`
GS: guide star
HWHM: mean half width at half maximum
IUE: The International Ultraviolet Explorer performed spectrophotometry at high (0.1-0.3 Å) and low (6-7 Å) resolution between 1150 Å and 3200 Å.
IVOA: International Virtual Observatory Alliance
LBG: Lyman-break galaxy

LDDE: Luminosity dependent density evolution
LF: Luminosity function
LGS: Laser guide star
LIRG: Luminous infrared galaxy, $10^{10}L_{\odot} < L_{IR} < 10^{11}L_{\odot}$
NACO: NAOS/CONICA: The Nasmyth Adaptive Optics System/Coude Near Infrared Camera and Spectrograph at the ESO VLT
NED: NASA/IPAC extragalactic database, `http://nedwww.ipac.caltech.edu`
NGS: Natural guide star
NIR: Near-infrared
NLAGN: Narrow line AGN
OSSE: Oriented Scintillation Spectrometer Experiment on board of the Compton Gamma Ray Observatory (CGRO). `http://cossc.gsfc.nasa.gov/docs/cgro/index.html`
QSO: Quasi-stellar object
Quasar: quasi-stellar radio source
PDE: Pure density evolution
PLE: Pure luminosity evolution
PSF: Point spread function
RASS: ROSAT All Sky Survey
RLQ: Radio-loud QSO
RQQ: Radio-quiet QSO
RTC: Real-time computer
SAM: Semi-analytical model
SB: Surface brightness
SDSS: Sloan Digital Sky Survey. www.sdss.org
SED: Spectral energy distribution
SFR: Star formation rate
SINFONI: Spectrograph for Integral Field Observations in the Near Infrared at the ESO VLT, Chile
SMBH: Supermassive black hole
ULIRG: Ultraluminous infrared galaxy
WFS: Wave-front sensor
WS: Web service
XBONG: X-ray bright optically normal galaxy

Bibliography

Adelman-McCarthy, J. K., Agüeros, M. A., Allam, S. S., et al. 2007, ApJS, 172, 634

—. 2006, ApJS, 162, 38

Adelman-McCarthy, J. K. & the SDSS Collaboration. 2007, submitted to ApJS, astro-ph/0707.3413

Adorf, H.-M., Lemson, G., & Voges, W. 2006, in Astronomical Society of the Pacific Conference Series, Vol. 351, Astronomical Data Analysis Software and Systems XV, ed. C. Gabriel, C. Arviset, D. Ponz, & S. Enrique, 695

Alexander, D. M., Aussel, H., Bauer, F. E., et al. 2002, ApJ, 568, L85

Alexander, D. M., Smail, I., Bauer, F. E., et al. 2005, Nature, 434, 738

Almaini, O. 2006, in Lecture Notes in Physics, Berlin Springer Verlag, Vol. 693, Physics of Active Galactic Nuclei at all Scales, ed. D. Alloin, 211

Almaini, O., Shanks, T., Boyle, B. J., et al. 1996, MNRAS, 282, 295

Alonso-Herrero, A., Rieke, M. J., Rieke, G. H., & Ruiz, M. 1997, ApJ, 482, 747

Alonso-Herrero, A., Ward, M. J., & Kotilainen, J. K. 1996, MNRAS, 278, 902

Anderson, S. F., Margon, B., Voges, W., et al. 2007, AJ, 133, 313

Anderson, S. F., Voges, W., Margon, B., et al. 2003, AJ, 126, 2209

Antonucci, R. 1993, ARA&A, 31, 473

Arav, N. 2004, in Astronomical Society of the Pacific Conference Series, Vol. 311, AGN Physics with the Sloan Digital Sky Survey, ed. G. T. Richards & P. B. Hall, 213

Archibald, E. N., Dunlop, J. S., Jimenez, R., et al. 2002, MNRAS, 336, 353

Babcock, H. W. 1953, PASP, 65, 229

Bade, N., Fink, H. H., Engels, D., et al. 1995, A&AS, 110, 469

Bahcall, J. N., Kirhakos, S., Saxe, D. H., & Schneider, D. P. 1997, ApJ, 479, 642

Balbus, S. A. & Hawley, J. F. 1998, Reviews of Modern Physics, 70, 1

Baldwin, J. A., Phillips, M. M., & Terlevich, R. 1981, PASP, 93, 5

Barger, A. J., Cowie, L. L., Capak, P., et al. 2003, AJ, 126, 632

Barger, A. J., Cowie, L. L., Mushotzky, R. F., et al. 2005, AJ, 129, 578

Barger, A. J., Cowie, L. L., & Richards, E. A. 2000, AJ, 119, 2092

Bauer, F. E., Alexander, D. M., Brandt, W. N., et al. 2002, AJ, 124, 2351

—. 2004, AJ, 128, 2048

Bazell, D., Miller, D. J., & SubbaRao, M. 2006, ApJ, 649, 678

Becker, R. H., White, R. L., Gregg, M. D., et al. 2000, ApJ, 538, 72

Beckers, J. M. 1993, ARA&A, 31, 13

Begelman, M. C. 1985, ApJ, 297, 492

Begelman, M. C. 2004, in Coevolution of Black Holes and Galaxies, ed. L. C. Ho, 374

Black, J. H. & van Dishoeck, E. F. 1987, ApJ, 322, 412

Blumenthal, G. R., Faber, S. M., Primack, J. R., & Rees, M. J. 1984, Nature, 311, 517

Bower, R. G., Benson, A. J., Malbon, R., et al. 2006, MNRAS, 370, 645

Boyle, B. J., McMahon, R. G., Wilkes, B. J., & Elvis, M. 1995, MNRAS, 276, 315

Brand, P. W. J. L., Toner, M. P., Geballe, T. R., et al. 1989, MNRAS, 236, 929

Brandner, W. & Kasper, M. E., eds. 2005, Science with Adaptive Optics

Brandt, W. N. & Hasinger, G. 2005, ARA&A, 43, 827

Bridge, C. R., Appleton, P. N., Conselice, C. J., et al. 2007, ApJ, 659, 931

Briggs, F. H., Turnshek, D. A., & Wolfe, A. M. 1984, ApJ, 287, 549

Brinkmann, W., Laurent-Muehleisen, S. A., Voges, W., et al. 2000, A&A, 356, 445

Brunner, R. J., Djorgovski, S. G., & Szalay, A. S., eds. 2001, Astronomical Society of the Pacific Conference Series, Vol. 225, Virtual Observatories of the Future

Brusa, M., Comastri, A., Mignoli, M., et al. 2003, A&A, 409, 65

Bruzual, G. & Charlot, S. 2003, MNRAS, 344, 1000

Bruzual A., G. & Charlot, S. 1993, ApJ, 405, 538

Budavári, T., Szalay, A. S., Gray, J., et al. 2004, in ASP Conf. Ser. 314: Astronomical Data Analysis Software and Systems (ADASS) XIII, 177

Calzetti, D., Kinney, A. L., & Storchi-Bergmann, T. 1996, ApJ, 458, 132

Canalizo, G. & Stockton, A. 2001, ApJ, 555, 719

Canalizo, G., Stockton, A., & Roth, K. C. 1998, AJ, 115, 890 (CS98)

Cardelli, J. A., Clayton, G. C., & Mathis, J. S. 1989, ApJ, 345, 245

Carr, M. J., Meurs, E. J. A., & Cunniffe, J. 2004, in Astronomical Data Analysis III, ed. F. Murtagh, G. Longo, S. J.-L., & V. Di Gesù, Electronic Workshops in Computing

Carroll, B. W. & Ostlie, D. A. 2006, An introduction to modern astrophysics (Addison-Wesley Longman Publishing Co., Inc.)

Chabrier, G. 2003, PASP, 115, 763

Chapman, S. C., Blain, A. W., Ivison, R. J., & Smail, I. R. 2003, Nature, 422, 695

Charlot, S. & Fall, S. M. 2000, ApJ, 539, 718

Cimatti, A., Daddi, E., Renzini, A., et al. 2004, Nature, 430, 184

Comastri, A., Brusa, M., Ciliegi, P., et al. 2002, ArXiv Astrophysics e-prints

Combes, F. 1996, in IAU Symp. 169: Unsolved Problems of the Milky Way, ed. L. Blitz & P. J. Teuben, 133

Condon, J. J. 1992, ARA&A, 30, 575

Connolly, A. J., Szalay, A. S., Dickinson, M., Subbarao, M. U., & Brunner, R. J. 1997, ApJ, 486, L11

Conselice, C. J. 2007, in IAU Symposium, Vol. 235, IAU Symposium, ed. F. Combes & J. Palous, 381

Conselice, C. J., Bershady, M. A., Dickinson, M., & Papovich, C. 2003, AJ, 126, 1183

Cowie, L. L., Songaila, A., Hu, E. M., & Cohen, J. G. 1996, AJ, 112, 839

Cowie, L. L., Songaila, A., Hu, E. M., et al. 1994, ApJ, 432, L83

Crenshaw, D. M., Kraemer, S. B., & Gabel, J. R. 2003, AJ, 126, 1690

Croom, S. M., Smith, R. J., Boyle, B. J., et al. 2004, MNRAS, 349, 1397

Dale, D. A., Roussel, H., Contursi, A., et al. 2004, ApJ, 601, 813

Davies, R. I., Sternberg, A., Lehnert, M. D., & Tacconi-Garman, L. E. 2005, ApJ, 633, 105

Davies, R. I., Thomas, J., Genzel, R., et al. 2006, ApJ, 646, 754

de Grijp, M. H. K., Keel, W. C., Miley, G. K., Goudfrooij, P., & Lub, J. 1992, A&AS, 96, 389

Deo, R. P., Crenshaw, D. M., & Kraemer, S. B. 2006, AJ, 132, 321

Dickey, J. M. & Lockman, F. J. 1990, ARA&A, 28, 215

Dickinson, M. 2000, in Astronomy, physics and chemistry of H_3^+, 2001

Dijkstra, M., Haiman, Z., & Loeb, A. 2004, ApJ, 613, 646

Draine, B. T. 1989, Interstellar extinction in the infrared (Infrared Spectroscopy in Astronomy, Proceedings of the 22nd Eslab Symposium held in Salamanca, Spain, 7-9 December, 1988. Edited by B.H. Kaldeich. ESA SP-290. European Space Agency, 1989., p.93), 93

Draine, B. T. & McKee, C. F. 1993, ARA&A, 31, 373

Draine, B. T. & Woods, D. T. 1990, ApJ, 363, 464

Dunlop, J. S., McLure, R. J., Kukula, M. J., et al. 2003, MNRAS, 340, 1095

Duschl, W. J. & Strittmatter, P. A. 2004, in Studies of Galaxies in the Young Universe with New Generation Telescope, ed. N. Arimoto & W. J. Duschl, 205

Eckart, A., van der Werf, P. P., Hofmann, R., & Harris, A. I. 1994, ApJ, 424, 627

Egami, E., Iwamuro, F., Maihara, T., Oya, S., & Cowie, L. L. 1996, AJ, 112, 73

Eggen, O. J., Lynden-Bell, D., & Sandage, A. R. 1962, ApJ, 136, 748

Eisenhauer, F., Abuter, R., Bickert, K., et al. 2003, in Instrument Design and Performance for Optical/Infrared Ground-based Telescopes. Edited by Iye, Masanori; Moorwood, Alan F. M. Proceedings of the SPIE, Volume 4841, pp. 1548-1561 (2003)., 1548

Elitzur, M. & Shlosman, I. 2006, ApJ, 648, L101

Ellis, R. S., Abraham, R. G., Brinchmann, J., & Menanteau, F. 2000, Astronomy and Geophysics, 41, 10

Elvis, M. 2000, ApJ, 545, 63

Elvis, M., Wilkes, B. J., McDowell, J. C., et al. 1994, ApJS, 95, 1

Emsellem, E., Goudfrooij, P., & Ferruit, P. 2003, MNRAS, 345, 1297

Englmaier, P. & Shlosman, I. 2000, ApJ, 528, 677

—. 2004, ApJ, 617, L115

Eracleous, M., Livio, M., & Binette, L. 1995, ApJ, 445, L1

Erwin, P. & Sparke, L. S. 2002, AJ, 124, 65

Evans, A. S., Frayer, D. T., Surace, J. A., & Sanders, D. B. 2001, AJ, 121, 3285

Evans, A. S., Mazzarella, J. M., Surace, J. A., et al. 2005, ApJS, 159, 197

Faber, S. M. & Gallagher, J. S. 1979, ARA&A, 17, 135

Fabian, A. C. 1999, MNRAS, 308, L39

Fan, X., Strauss, M. A., Schneider, D. P., et al. 2001, AJ, 121, 54

Fathi, K., van de Ven, G., Peletier, R. F., et al. 2005, MNRAS, 364, 773

Filho, M. E., Barthel, P. D., & Ho, L. C. 2000, ApJS, 129, 93

Fischer, S., Iserlohe, C., Zuther, J., et al. 2006, A&A, 452, 827

Fischera, J., Dopita, M. A., & Sutherland, R. S. 2003, ApJ, 599, L21

Freedman, W. L. & Turner, M. S. 2003, Reviews of Modern Physics, 75, 1433

Fried, D. L. 1965, Optical Society of America Journal, 55, 1427

Fukugita, M., Ichikawa, T., Gunn, J. E., et al. 1996, AJ, 111, 1748+

Gallagher, S. C., Brandt, W. N., Chartas, G., & Garmire, G. P. 2002, ApJ, 567, 37

Gallagher, S. C., Brandt, W. N., Chartas, G., Garmire, G. P., & Sambruna, R. M. 2004, Advances in Space Research, 34, 2594

García-Burillo, S., Combes, F., Schinnerer, E., Boone, F., & Hunt, L. K. 2005, A&A, 441, 1011

Gebhardt, K., Bender, R., Bower, G., et al. 2000, ApJ, 539, L13

Georgantopoulos, I. & Georgakakis, A. 2005, MNRAS, 358, 131

George, I. M. & Fabian, A. C. 1991, MNRAS, 249, 352

Ghosh, K. K. & Punsly, B. 2007, ApJ, 661, L139

Giacconi, R., Gursky, H., Paolini, F. R., & Rossi, B. B. 1962, Physical Review Letters, 9, 439

Giacconi, R., Rosati, P., Tozzi, P., et al. 2001, ApJ, 551, 624

Giavalisco, M. 2002, ARA&A, 40, 579

Giavalisco, M., Dickinson, M., Ferguson, H. C., et al. 2004, ApJ, 600, L103

Giavalisco, M., Steidel, C. C., & Macchetto, F. D. 1996, ApJ, 470, 189

Gilli, R., Comastri, A., & Hasinger, G. 2007, A&A, 463, 79

Glass, I. S. 1999, Handbook of infrared astronomy (Cambridge University Press)

Glass, I. S. & Moorwood, A. F. M. 1985, MNRAS, 214, 429

Glazebrook, K., Abraham, R. G., McCarthy, P. J., et al. 2004, Nature, 430, 181

Gondhalekar, P. M., Rouillon-Foley, C., & Kellett, B. J. 1996, MNRAS, 282, 117

—. 1997, MNRAS, 288, 260

Goodrich, R. W. 1990, ApJ, 355, 88

Graham, J. R., Wright, G. S., & Longmore, A. J. 1987, ApJ, 313, 847

Green, P. J., Aldcroft, T. L., Mathur, S., Wilkes, B. J., & Elvis, M. 2001, ApJ, 558, 109

Green, P. J., Schartel, N., Anderson, S. F., et al. 1995, ApJ, 450, 51

Griffiths, R. E., della Ceca, R., Georgantopoulos, I., et al. 1996, MNRAS, 281, 71

Grogin, N. A., Conselice, C. J., Chatzichristou, E., et al. 2005, ApJ, 627, L97

Haardt, F., Maraschi, L., & Ghisellini, G. 1994, ApJ, 432, L95

Hall, P. B., Martini, P., Depoy, D. L., & Gatley, I. 1997, ApJ, 484, L17

Hamann, F. & Sabra, B. 2004, in Astronomical Society of the Pacific Conference Series, 203

Harrison, A., Puxley, P., Russell, A., & Brand, P. 1998, MNRAS, 297, 624

Hasinger, G. 1998, Astronomische Nachrichten, 319, 37

Hasinger, G., Altieri, B., Arnaud, M., et al. 2001, A&A, 365, L45

Hasinger, G., Miyaji, T., & Schmidt, M. 2005, A&A, 441, 417

Hawarden, T. G., Leggett, S. K., Letawsky, M. B., Ballantyne, D. R., & Casali, M. M. 2001, MNRAS, 325, 563

Hazard, C., Morton, D. C., Terlevich, R., & McMahon, R. 1984, ApJ, 282, 33

Heavens, A., Panter, B., Jimenez, R., & Dunlop, J. 2004, Nature, 428, 625

Heckman, T. M., Kauffmann, G., Brinchmann, J., et al. 2004, ApJ, 613, 109

Hewett, P. C. & Foltz, C. B. 2003, AJ, 125, 1784

Hill, T. L., Heisler, C. A., Sutherland, R., & Hunstead, R. W. 1999, AJ, 117, 111

Ho, L. C. 1999, ApJ, 516, 672

Ho, L. C., Filippenko, A. V., & Sargent, W. L. W. 1997, ApJ, 487, 568

Hogg, D. W. 1999, astro-ph/9905116

Hogg, D. W., Baldry, I. K., Blanton, M. R., & Eisenstein, D. J. 2002, astro-ph/0210394

Hong, J., Schlegel, E. M., & Grindlay, J. E. 2004, ApJ, 614, 508

Hopkins, A. M., Miller, C. J., Nichol, R. C., et al. 2003, ApJ, 599, 971

Hopkins, P. F., Somerville, R. S., Hernquist, L., et al. 2006, ApJ, 652, 864

Hubble, E. P. 1926, ApJ, 64, 321

Hunt, L. K. & Malkan, M. A. 1999, ApJ, 516, 660

Hyland, A. R. & Allen, D. A. 1982, MNRAS, 199, 943

Ivanov, V. D., Rieke, M. J., Engelbracht, C. W., et al. 2004, ApJS, 151, 387

Ivezić, Ž., Becker, R. H., Blanton, M., et al. 2002a, in Astronomical Society of the Pacific Conference Series, Vol. 284, IAU Colloq. 184: AGN Surveys, ed. R. F. Green, E. Y. Khachikian, & D. B. Sanders, 137

Ivezić, Ž., Menou, K., Knapp, G. R., et al. 2002b, AJ, 124, 2364

Jahnke, K., Kuhlbrodt, B., & Wisotzki, L. 2004a, MNRAS, 352, 399

Jahnke, K., Sánchez, S. F., Wisotzki, L., et al. 2004b, ApJ, 614, 568

Jogee, S., Scoville, N., & Kenney, J. D. P. 2005, ApJ, 630, 837

Kamionkowski, M. 2007, astro-ph/0706.2986

Kauffmann, G., Heckman, T. M., Tremonti, C., et al. 2003, MNRAS, 346, 1055

Kauffmann, G., White, S. D. M., & Guiderdoni, B. 1993, MNRAS, 264, 201

Kaviraj, S., Devriendt, J. E. G., Ferreras, I., & Yi, S. K. 2005, MNRAS, 360, 60

Kewley, L. J., Dopita, M. A., Sutherland, R. S., Heisler, C. A., & Trevena, J. 2001, ApJ, 556, 121

Kewley, L. J., Jansen, R. A., & Geller, M. J. 2005, PASP, 117, 227

Kirhakos, S., Sargent, W. L. W., Schneider, D. P., et al. 1994, PASP, 106, 646

Knapen, J. H. 2005, Ap&SS, 295, 85

Koekemoer, A. M., Alexander, D. M., Bauer, F. E., et al. 2004, ApJ, 600, L123

Kormendy, J. & Djorgovski, S. 1989, ARA&A, 27, 235

Kormendy, J. & Kennicutt, R. C. 2004, ARA&A, 42, 603

Kormendy, J. & Richstone, D. 1995, ARA&A, 33, 581

Kotilainen, J. K., Ward, M. J., Boisson, C., Depoy, D. L., & Smith, M. G. 1992, MNRAS, 256, 149

Krolik, J. H. & Kriss, G. A. 2001, ApJ, 561, 684

Kronberger, T., Kapferer, W., Schindler, S., & Ziegler, B. L. 2007, A&A in press, astro-ph/0707.2301

Ku, W. H.-M., Helfand, D. J., & Lucy, L. B. 1980, Nature, 288, 323

Laine, S., Shlosman, I., Knapen, J. H., & Peletier, R. F. 2002, ApJ, 567, 97

Larkin, J. E., Armus, L., Knop, R. A., Soifer, B. T., & Matthews, K. 1998, ApJS, 114, 59

Lehmer, B. D., Brandt, W. N., Alexander, D. M., et al. 2005, AJ, 129, 1

Lemson, G. & Virgo Consortium. 2006, astro-ph/0608019

Lepp, S. & McCray, R. 1983, ApJ, 269, 560

Lester, D. F., Harvey, P. M., & Carr, J. 1988, ApJ, 329, 641

Lewis, G. F., Chapman, S. C., & Kuncic, Z. 2003, ApJ, 596, L35

Lilly, S. J., Le Fevre, O., Hammer, F., & Crampton, D. 1996, ApJ, 460, L1

Lipari, S. 1994, ApJ, 436, 102

Lípari, S. L. & Terlevich, R. J. 2006, MNRAS, 368, 1001

Loveday, J., Peterson, B. A., Efstathiou, G., & Maddox, S. J. 1992, ApJ, 390, 338

Low, F. J., Cutri, R. M., Kleinmann, S. G., & Huchra, J. P. 1989, ApJ, 340, L1

Lynden-Bell, D. 1969, Nature, 223, 690

Maccacaro, T., Gioia, I. M., Wolter, A., Zamorani, G., & Stocke, J. T. 1988, ApJ, 326, 680

Maciejewski, W. 2004, MNRAS, 354, 892

Magdziarz, P., Blaes, O. M., Zdziarski, A. A., Johnson, W. N., & Smith, D. A. 1998, MNRAS, 301, 179

Magorrian, J., Tremaine, S., Richstone, D., et al. 1998, AJ, 115, 2285

Mainieri, V., Rosati, P., Tozzi, P., et al. 2005, A&A, 437, 805

Maiolino, R., Rieke, G. H., & Rieke, M. J. 1996, AJ, 111, 537

Maiolino, R., Ruiz, M., Rieke, G. H., & Papadopoulos, P. 1997, ApJ, 485, 552

Malkan, M. A., Gorjian, V., & Tam, R. 1998, ApJS, 117, 25

Maloney, P. R., Hollenbach, D. J., & Tielens, A. G. G. M. 1996, ApJ, 466, 561

Marchesini, D. & van Dokkum, P. G. 2007, ApJ, 663, L89

Marconi, A., Moorwood, A. F. M., Salvati, M., & Oliva, E. 1994, A&A, 291, 18

Marconi, A., Risaliti, G., Gilli, R., et al. 2004, MNRAS, 351, 169

Martini, P. 2004, in Coevolution of Black Holes and Galaxies, ed. L. C. Ho, 169

Martini, P., Regan, M. W., Mulchaey, J. S., & Pogge, R. W. 2003, ApJ, 589, 774

Matt, G. 2002, Royal Society of London Philosophical Transactions Series A, 360, 2045

McGlynn, T. A., Suchkov, A. A., Winter, E. L., et al. 2004, ApJ, 616, 1284

McKernan, B., Yaqoob, T., & Reynolds, C. S. 2007, MNRAS, 625

McLeod, K. K. & McLeod, B. A. 2001, ApJ, 546, 782

McLure, R. J., Kukula, M. J., Dunlop, J. S., et al. 1999, MNRAS, 308, 377

Mickaelian, A. M., Hovhannisyan, L. R., Engels, D., Hagen, H.-J., & Voges, W. 2006, A&A, 449, 425

Mitsuda, K., Kunieda, H., Inoue, H., & Kelley, R. 2004, in Presented at the Society of Photo-Optical Instrumentation Engineers (SPIE) Conference, Vol. 5488, UV and Gamma-Ray Space Telescope Systems. Edited by Hasinger, Günther; Turner, Martin J. L. Proceedings of the SPIE, Volume 5488, pp. (2004)., ed. G. Hasinger & M. J. L. Turner, 177

Miyaji, T. & Griffiths, R. E. 2002, ApJ, 564, L5

Monson-Haefel, R. 2003, J2EE Web Services (Boston, MA, USA: Addison-Wesley Longman Publishing Co., Inc.)

Moorwood, A. F. 1995, in Proc. SPIE Vol. 2475, p. 262-267, Infrared Detectors and Instrumentation for Astronomy, Albert M. Fowler; Ed., Vol. 2475, 262–267

Moran, E. C., Filippenko, A. V., & Chornock, R. 2002, ApJ, 579, L71

Moran, E. C., Halpern, J. P., & Helfand, D. J. 1996, ApJS, 106, 341

Morris, S. L. 1988, ApJ, 330, L83

Mouri, H. 1994, ApJ, 427, 777

Mouri, H. & Taniguchi, Y. 1992, ApJ, 386, 68

Murray, N., Chiang, J., Grossman, S. A., & Voit, G. M. 1995, ApJ, 451, 498

Mushotzky, R. F. 1997, in Astronomical Society of the Pacific Conference Series, Vol. 128, Mass Ejection from Active Galactic Nuclei, ed. N. Arav, I. Shlosman, & R. J. Weymann, 141

Mushotzky, R. F., Cowie, L. L., Barger, A. J., & Arnaud, K. A. 2000, Nature, 404, 459

Mushotzky, R. F., Done, C., & Pounds, K. A. 1993, ARA&A, 31, 717

Mushotzky, R. F., Fabian, A. C., Iwasawa, K., et al. 1995, MNRAS, 272, L9

Nandra, K. & Pounds, K. A. 1994, MNRAS, 268, 405

Neistein, E., van den Bosch, F. C., & Dekel, A. 2006, MNRAS, 372, 933

Nelson, C. H., MacKenty, J. W., Simkin, S. M., & Griffiths, R. E. 1996, ApJ, 466, 713

Nieto-Santisteban, M. A., Szalay, A. S., Thakar, A. R., et al. 2005, cs/0502018

Origlia, L., Moorwood, A. F. M., & Oliva, E. 1993, A&A, 280, 536

Origlia, L. & Oliva, E. 2000, A&A, 357, 61

Osterbrock, D. E. 1981, ApJ, 249, 462

—. 1989, Astrophysics of gaseous nebulae and active galactic nuclei (Research supported by the University of California, John Simon Guggenheim Memorial Foundation, University of Minnesota, et al. Mill Valley, CA, University Science Books, 1989, 422 p.)

Padovani, P., Allen, M. G., Rosati, P., & Walton, N. A. 2004, A&A, 424, 545

Page, M. J., Stevens, J. A., Mittaz, J. P. D., & Carrera, F. J. 2001, Science, 294, 2516

Panessa, F., Barcons, X., Bassani, L., et al. 2007, A&A, 467, 519

Panessa, F., Wolter, A., Pellegrini, S., et al. 2005, ApJ, 631, 707

Papovich, C., Dickinson, M., & Ferguson, H. C. 2001, ApJ, 559, 620

Pappa, A., Georgantopoulos, I., Ward, M., & Zezas, A. L. 2002, MNRAS, 336, 714

Patsis, P. A. 2005, MNRAS, 358, 305

Peebles, P. J. E. & Ratra, B. 2003, Rev. Mod. Phys., 75, 559

Pei, Y. C., Fall, S. M., & Hauser, M. G. 1999, ApJ, 522, 604

Perola, G. C., Matt, G., Cappi, M., et al. 2002, A&A, 389, 802

Persson, S. E., Murphy, D. C., Krzeminski, W., Roth, M., & Rieke, M. J. 1998, AJ, 116, 2475

Peterson, B. M., ed. 1997, An introduction to active galactic nuclei

Petrosian, V. 1976, ApJ, 209, L1

Piccinotti, G., Mushotzky, R. F., Boldt, E. A., et al. 1982, ApJ, 253, 485

Pierce, C. M., Lotz, J. M., Laird, E. S., et al. 2007, ApJ, 660, L19

Polletta, M., Bassani, L., Malaguti, G., Palumbo, G. G. C., & Caroli, E. 1996, ApJS, 106, 399

Pounds, K. & Reeves, J. 2002, ArXiv Astrophysics e-prints

Prieto, M. A., Marco, O., & Gallimore, J. 2005, MNRAS, 364, L28

Radford, S. J. E., Downes, D., & Solomon, P. M. 1991, ApJ, 368, L15

Raichoudhuri, A. 1998, The Physics of Fluids and Plasmas (Cambridge University Press)

Ramos Almeida, C., Pérez García, A. M., Acosta-Pulido, J. A., et al. 2006, ApJ, 645, 148

Reichard, T. A., Richards, G. T., Hall, P. B., et al. 2003, AJ, 126, 2594

Reunanen, J., Kotilainen, J. K., & Prieto, M. A. 2003, MNRAS, 343, 192

Richards, G. T., Fan, X., Newberg, H. J., et al. 2002, AJ, 123, 2945

Richards, G. T., Hall, P. B., Vanden Berk, D. E., et al. 2003, AJ, 126, 1131

Ridgway, S. E., Heckman, T. M., Calzetti, D., & Lehnert, M. 2001, ApJ, 550, 122

Rigby, J. R., Rieke, G. H., Donley, J. L., Alonso-Herrero, A., & Pérez-González, P. G. 2006, ApJ, 645, 115

Rigopoulou, D., Papadakis, I., Lawrence, A., & Ward, M. 1997, A&A, 327, 493

Rix, H.-W., Rieke, G., Rieke, M., & Carleton, N. P. 1990, ApJ, 363, 480

Roddier, F., ed. 1999, Adaptive optics in astronomy

Roddier, F. & Roddier, C. 1986, in Presented at the Society of Photo-Optical Instrumentation Engineers (SPIE) Conference, Vol. 628, Advanced technology optical telescopes III; Proceedings of the Meeting, Tucson, AZ, Mar. 3-6, 1986 (A87-35201 15-89). Bellingham, WA, Society of Photo-Optical Instrumentation Engineers, ed. L. D. Barr, 298

Rodríguez-Ardila, A., Pastoriza, M. G., Viegas, S., Sigut, T. A. A., & Pradhan, A. K. 2004, A&A, 425, 457

Rodríguez-Ardila, A., Riffel, R., & Pastoriza, M. G. 2005, MNRAS, 364, 1041

Roggemann, M. C., Welsh, B. M., & Fugate, R. Q. 1997, Reviews of Modern Physics, 69, 437

Rubin, V. C., Thonnard, N., & Ford, Jr., W. K. 1980, ApJ, 238, 471

Rudy, R. J., Cohen, R. D., & Ake, T. B. 1988, ApJ, 332, 172

Rudy, R. J. & Rodriguez-Espinosa, J. M. 1985, ApJ, 298, 614

Rybicki, G. B. & Lightman, A. P. 1986, Radiative Processes in Astrophysics (Radiative Processes in Astrophysics, by George B. Rybicki, Alan P. Lightman, pp. 400. ISBN 0-471-82759-2. Wiley-VCH , June 1986.)

Sanders, D. B., Soifer, B. T., Elias, J. H., et al. 1988, ApJ, 325, 74

Scannapieco, E., Silk, J., & Bouwens, R. 2005, ApJ, 635, L13

Schade, D. J., Boyle, B. J., & Letawsky, M. 2000, MNRAS, 315, 498

Schawinski, K., Khochfar, S., Kaviraj, S., et al. 2006, Nature, 442, 888

Schinnerer, E., Eckart, A., Tacconi, L. J., Genzel, R., & Downes, D. 2000, ApJ, 533, 850

Schlegel, D. J., Finkbeiner, D. P., & Davis, M. 1998, ApJ, 500, 525

Schmidt, M. & Green, R. F. 1983, ApJ, 269, 352

Schmitt, H. R., Kinney, A. L., Calzetti, D., & Storchi Bergmann, T. 1997, AJ, 114, 592

Schneider, D. P., Fan, X., Hall, P. B., et al. 2003, AJ, 126, 2579

Schneider, D. P., Hall, P. B., Richards, G. T., et al. 2007, AJ, 134, 102

Schuecker, P., Böhringer, H., & Voges, W. 2004, A&A, 420, 61

Severgnini, P., Caccianiga, A., Braito, V., et al. 2003, A&A, 406, 483

Shields, G. A. 1978, Nature, 272, 706

Shields, G. A., Gebhardt, K., Salviander, S., et al. 2003, ApJ, 583, 124

Shimasaku, K., Fukugita, M., Doi, M., et al. 2001, AJ, 122, 1238

Shlosman, I., Begelman, M. C., & Frank, J. 1990, Nature, 345, 679

Shlosman, I., Frank, J., & Begelman, M. C. 1989, Nature, 338, 45

Silk, J. & Rees, M. J. 1998, A&A, 331, L1

Silva, L., Maiolino, R., & Granato, G. L. 2004, MNRAS, 355, 973

Smith, J. A., Tucker, D. L., Kent, S., et al. 2002, AJ, 123, 2121

Sofia, U. J., Wolff, M. J., Rachford, B., et al. 2005, ApJ, 625, 167

Solomon, P. M., Downes, D., & Radford, S. J. E. 1992, ApJ, 398, L29

Solomon, P. M., Downes, D., Radford, S. J. E., & Barrett, J. W. 1997, ApJ, 478, 144

Solomon, P. M. & Sage, L. J. 1988, ApJ, 334, 613

Soltan, A. 1982, MNRAS, 200, 115

Somerville, R. S., Lemson, G., Sigad, Y., et al. 2001, MNRAS, 320, 289

Spergel, D. N., Verde, L., Peiris, H. V., et al. 2003, ApJS, 148, 175

Sprayberry, D. & Foltz, C. B. 1992, ApJ, 390, 39

Springel, V., Di Matteo, T., & Hernquist, L. 2005, MNRAS, 361, 776

Steffen, A. T., Barger, A. J., Cowie, L. L., Mushotzky, R. F., & Yang, Y. 2003, ApJ, 596, L23

Steidel, C. C., Adelberger, K. L., Giavalisco, M., Dickinson, M., & Pettini, M. 1999, ApJ, 519, 1

Stern, B. E., Poutanen, J., Svensson, R., Sikora, M., & Begelman, M. C. 1995, ApJ, 449, L13

Sternberg, A. & Dalgarno, A. 1989, ApJ, 338, 197

Stocke, J. T., Morris, S. L., Gioia, I. M., et al. 1991, ApJS, 76, 813

Stocke, J. T., Morris, S. L., Weymann, R. J., & Foltz, C. B. 1992, ApJ, 396, 487

Stoughton, C., Lupton, R. H., Bernardi, M., et al. 2002, AJ, 123, 485

Strateva, I., Ivezić, Ž., Knapp, G. R., et al. 2001, AJ, 122, 1861

Strateva, I. V., Brandt, W. N., Schneider, D. P., Vanden Berk, D. G., & Vignali, C. 2005, AJ, 130, 387

Strauss, M. A., Weinberg, D. H., Lupton, R. H., et al. 2002, AJ, 124, 1810

Suchkov, A. A., Hanisch, R. J., Voges, W., & Heckman, T. M. 2006, AJ, 132, 1475

Szalay, A. & Gray, J. 2001, Science, 293, 2037

Szalay, A. S. & Gray, J. 2004, in The Grid2: Blueprint for a New Computing Infrastructure (San Francisco, CA, USA: Morgan Kaufmann Publishers Inc.), 95–108

Szalay, A. S., Kunszt, P., Thakar, A., & Gray, J. 1999, ArXiv Computer Science e-prints

Szokoly, G. P., Bergeron, J., Hasinger, G., et al. 2004, ApJS, 155, 271

Tacconi, L. J., Genzel, R., Lutz, D., et al. 2002, ApJ, 580, 73

Tatarski, V. I. 1961, Wave Propagation in a Turbulent Medium (McGraw-Hill Book Co., Inc.)

Tine, S., Lepp, S., Gredel, R., & Dalgarno, A. 1997, ApJ, 481, 282

Treister, E., Urry, C. M., Chatzichristou, E., et al. 2004, ApJ, 616, 123

Tremaine, S., Gebhardt, K., Bender, R., et al. 2002, ApJ, 574, 740

Tutui, Y., Sofue, Y., Honma, M., Ichikawa, T., & Wakamatsu, K.-i. 2000, PASJ, 52, 803

Ueda, Y., Eguchi, S., Terashima, Y., et al. 2007, ApJ, 664, L79

Ulvestad, J. S. & Wilson, A. S. 1984, ApJ, 278, 544

van Breugel, W. J. M. & Dey, A. 1993, ApJ, 414, 563

van den Bergh, S. 1998, Galaxy morphology and classification (Galaxy morphology and classification / Sidney van den Bergh. Cambridge ; New York : Cambridge University Press)

—. 2007, Nature, 445, 265

Vanden Berk, D. E., Richards, G. T., Bauer, A., et al. 2001, AJ, 122, 549

Veilleux, S. & Osterbrock, D. E. 1987, ApJS, 63, 295

Vignali, C., Brandt, W. N., & Schneider, D. P. 2003, AJ, 125, 433

Voges, W., Aschenbach, B., Boller, T., et al. 1999, A&A, 349, 389

Voit, G. M., Weymann, R. J., & Korista, K. T. 1993, ApJ, 413, 95

Wallace, L., Livingston, W., Hinkle, K., & Bernath, P. 1996, ApJS, 106, 165

Wallace, L., Meyer, M. R., Hinkle, K., & Edwards, S. 2000, ApJ, 535, 325

Ward, M. J., Done, C., Fabian, A. C., Tennant, A. F., & Shafer, R. A. 1988, ApJ, 324, 767

Weinmann, S. M., van den Bosch, F. C., Yang, X., et al. 2006, MNRAS, 372, 1161

Weymann, R. J., Morris, S. L., Foltz, C. B., & Hewett, P. C. 1991, ApJ, 373, 23

Willott, C. J., Rawlings, S., & Grimes, J. A. 2003, ApJ, 598, 909

Wolf, C., Wisotzki, L., Borch, A., et al. 2003, A&A, 408, 499

Wolniewicz, L., Simbotin, I., & Dalgarno, A. 1998, ApJS, 115, 293

Worsley, M. A., Fabian, A. C., Barcons, X., et al. 2004, MNRAS, 352, L28

Wyse, R. F. G. 2004, ApJ, 612, L17

York, D. G., Adelman, J., Anderson, J. E., et al. 2000, AJ, 120, 1579

Young, J. S. & Scoville, N. Z. 1991, ARA&A, 29, 581

Yu, Q. & Tremaine, S. 2002, MNRAS, 335, 965

Yuan, F. & Narayan, R. 2004, ApJ, 612, 724

Zheng, W., Kriss, G. A., Telfer, R. C., Grimes, J. P., & Davidsen, A. F. 1997, ApJ, 475, 469

Zhou, H., Wang, T., Wang, H., et al. 2006, ApJ, 639, 716

Zuther, J. & Eckart, A. 2005, A&A, 443, 903

Zuther, J., Eckart, A., Scharwächter, J., Krips, M., & Straubmeier, C. 2004a, A&A, 414, 919

Zuther, J., Eckart, A., Straubmeier, C., & Voges, W. 2004b, in "AGN Physics with the Sloan Digital Sky Survey", ASP Conf. Ser. 311, 325

Zuther, J., Eckart, A., & Voges, W. 2005a, AN, 326, 573

Zuther, J., Eckart, A., Voges, W., Bertram, T., & Straubmeier, C. 2005b, in "Science with Adaptive Optics", Proceedings of the ESO Workshop Held at Garching, Germany, 16-19 September 2003, Brandner, W., Kasper, M. E., eds., Springer, 375

Zuther, J., Iserlohe, C., Pott, J.-U., et al. 2007, A&A, 466, 451

Zuther, J., Iserlohe, C., Pott, J.-U., Eckart, A., & Voges, W. 2006, New Astronomy Review, 49, 508

Zwicky, F. 1933, Helvetica Physica Acta, 6, 110

Zwillinger, D. 2003, CRC Standard Mathematical Tables and Formulae (Chapman & Hall/CRC Press)

List of Figures

List of Tables

Acknowledgments

Now it is the proper time and place to express my deepest gratitude to all the people involved in making this work become possible.

It has been a very interesting time and I learned a lot, not only about the astronomical subject, but also about working and researching within an international collaboration.

First of all, I have to thank Prof. Dr. Andreas Eckart for giving me the opportunity carrying out this research. Visits to his office were always inspiring. When leaving his office, not only the reason for the visit has been tackled, but a new bunch of ideas to follow on arose. He has always good advice at hand, providing directions, but he is permitting a lot of freedom to follow one's own ideas. It has been a great pleasure working with him and learning from his experience.

I have very much enjoyed the cordial and cooperative atmosphere in the group. My thanks go to all colleagues and to the secretaries who are involved in workaday life.

Next, I have to thank Dr. Wolfgang Voges at the Max-Planck Institute for Extraterrestrial Physics in Garching near Munich for his co-mentoring and sharing his expertise on the X-ray and ROSAT part in particular. Inviting me to contribute to the GAVO initiative affirmed my interest in the connection of astronomy and distributed computing. Dr. Gerard Lemson's excellent support of GAVO tools and his introduction into using Web services with Java are sincerely acknowledged.

Special thanks go to Dr. Günther Hasinger for supporting my research, in particular in the form of financial aid for traveling to the Keck telescope on Hawaii.

The "extragalactic guys" are at the heart of things: Thomas Bertram, with whom I spent endless hours, not only installing computers, but also working on hard astronomical problems and more. Working with Sebastian Fischer, and Dr. Jörg-Uwe Pott was always fun and, of course, fruitful. Many thanks

also go to Julia Scharwächter (now at ESO, Chile) for continuing exciting collaborations on interacting QSOs.

I am grateful to Dr. Jörg-Uwe Pott and Dr. Christof Iserlohe for their collaboration of the Mrk 609 paper and to Christof in particular for sharing his wisdom on SINFONI data reduction and analysis.

I have to cordially thank Dr. Christian Straubmeier for his support and cooperation, which has always been fundamental for my work.

Acknowledgments are also due for the colleagues carefully reading through parts of the manuscript. In particular, thanks go to Sebastian Fischer (giving good advice until the last minute), Sabine König, Christoph Olczak, Leo Meyer, and Dr. Rainer Schödel.

Bei meinen Eltern bedanke ich mich von ganzen Herzen für ihre unermüdliche und unschätzbare Unterstützung durch das gesamte Studium und die Doktorarbeit hindurch, ohne die diese Arbeit nicht möglich gewesen wäre.

Zu guter Letzt möchte ich mich von ganzem Herzen bei Susanne für ihre liebevolle Unterstützung und unendliche Geduld während der gesamten Zeit bedanken.

Funding for the SDSS and SDSS-II has been provided by the Alfred P. Sloan Foundation, the Participating Institutions, the National Science Foundation, the U.S. Department of Energy, the National Aeronautics and Space Administration, the Japanese Monbukagakusho, the Max Planck Society, and the Higher Education Funding Council for England. The SDSS Web Site is `http://www.sdss.org`.

The SDSS is managed by the Astrophysical Research Consortium for the Participating Institutions. The Participating Institutions are the American Museum of Natural History, Astrophysical Institute Potsdam, University of Basel, University of Cambridge, Case Western Reserve University, University of Chicago, Drexel University, Fermilab, the Institute for Advanced Study, the Japan Participation Group, Johns Hopkins University, the Joint Institute for Nuclear Astrophysics, the Kavli Institute for Particle Astrophysics and Cosmology, the Korean Scientist Group, the Chinese Academy of Sciences (LAMOST), Los Alamos National Laboratory, the Max-Planck-Institute for Astronomy (MPIA), the Max-Planck-Institute for Astrophysics (MPA), New Mexico State University, Ohio State University, University

of Pittsburgh, University of Portsmouth, Princeton University, the United States Naval Observatory, and the University of Washington.

I have made use of the ROSAT Data Archive of the Max-Planck-Institut für extraterrestrische Physik (MPE) at Garching, Germany.

This work is partly based on observations carried out at the Very Large Telescope of the European Southern Observatory in Chile under projects 60.A-9041 and 67.B-0019.

This work was supported in part by the Deutsche Forschungsgemeinschaft (DFG) via grant SFB 494.

Erklärung

Ich versichere, dass ich die von mir vorgelegte Dissertation selbständig angefertigt, die benutzten Quellen und Hilfsmittel vollständig angegeben und die Stellen der Arbeit – einschließlich Tabellen, Karten und Abbildungen –, die anderen Werken im Wortlaut oder dem Sinn nach entnommen sind, in jedem Einzelfall als Entlehnung kenntlich gemacht habe; dass diese Dissertation noch keiner anderen Fakultät oder Universität zur Prüfung vorgelegen hat; dass sie - abgesehen von unten angegebenen Teilpublikationen - noch nicht veröffentlicht worden ist sowie, dass ich eine solche Veröffentlichung vor Abschluss des Promotionsverfahrens nicht vornehmen werde. Die Bestimmungen dieser Promotionsordnung sind mir bekannt. Die von mir vorgelegte Dissertation ist von Herrn Prof. Dr. Andreas Eckart betreut worden.

Köln, den 28.8.2007

Teilpublikationen

J. Zuther, S. Fischer, J.-U. Pott, T. Bertram, A. Eckart, C. Straubmeier, C. Iserlohe, W. Voges, G. Hasinger, *Dissecting the nuclear environment of Mrk 609 with SINFONI - The starburst-AGN connection*, 2007, ESO Messenger, 128

J. Zuther, C. Iserlohe, J.-U. Pott, T. Bertram, S. Fischer, W. Voges, G. Hasinger, A. Eckart., *Mrk 609: resolving the circum-nuclear structure with near-infrared integral-field-spectroscopy*, 2007, A&A, 466, 451

J. Zuther, J.-U. Pott, C. Iserlohe, A. Eckart, W. Voges, *VLT-SINFONI observations of Mrk 609 - A showcase for X-ray active galaxies chosen from a sample of AGN suitable for adaptive optics observations with natural guide stars*, 2006, New Astr. Rev, 49, 508

J. Zuther & A. Eckart, *Near infrared imaging of the broad absorption line quasar BAL QSO 0134+3253*, 2005, A&A, 443, 903

J. Zuther, A. Eckart, W. Voges, T. Bertram, and C. Straubmeier, *Selection of extragalactic Targets for AO and VLTI Observations*, in "Science with Adaptive Optics", ed. W. Brandner and M. Kasper, Springer-Verlag, ESO Astrophysics Symposia, 2005, ISBN: 3-540-25034-4

J. Zuther, A. Eckart, J. Scharwächter, M. Krips and C.Straubmeier, *NIR Observations of the QSO 3C 48 Host Galaxy*, 2004, A&A, 414, 919

J. Zuther, A. Eckart, W. Voges, and Christian Straubmeier, *A Sample of X-Ray active extragalactic Sources suitable for NIR Adaptive Optics Observations*, in "AGN Physics with the Sloan Digital Sky Survey", ed. G. T. Richards and P. B. Hall (San Francisco: ASP) , 2004, Vol. CS-311, ISBN: 58381-164-8

Weitere Teilpublikationen

J. Scharwächter, A. Eckart, **J. Zuther**, S. Pfalzner, I. Savine, V. D. Ivanov, L. E. Tacconi-German, J. K. Kotilainen, J. Reunanen, R. Schödel, *Case studies of interacting QSO host galaxies*, 2007, to appear in "The Nuclear Region, Host Galaxy, and Environment of Active Galaxies", Huatulco (Mexico), RevMexAA

J. Zuther, A. Eckart, S. Fischer, S. König, J. Scharwc̆hter, *NIR observations of late-stage merger QSOs in the context of ULIRG-to QSO evolution*, 2007, The 10th Birmingham-Nottingham Extragalactic Workshop, "Galaxy Interactions and Mergers", online proceedings,
`http://www.nottingham.ac.uk/~ppzcc1/meeting/nir_merger_zuther.pdf`

T. Bertram, A. Eckart, S. Fischer, **J. Zuther**, C. Straubmeier, L. Wisotzki, and M. Krips, *Molecular gas in nearby low-luminosity QSO host galaxies*, 2007, A&A, 470, 571

J. Scharwächter, A. Eckart, S. Pfalzner, I. Saviane, **J. Zuther**, *The nearby QSO host I Zw 1: The stellar disk and adjacent objects*, 2007, A&A, 469, 913

S. Fischer, C. Iserlohe, **J. Zuther**, T. Bertram, C. Straubmeier, R. Schödel, and A. Eckart, *Nearby AGN and their hosts in the near infrared*, 2006, A&A, 452, 827

J. Zuther, M. Krips, J. Scharwächter, A. Eckart, *Merger driven ULIRG-QSO evolution: The case of 3C 48*, 2006, New Astr. Rev,50, 837

S. Fischer, C. Iserlohe, **J. Zuther**, T. Bertram, C. Straubmeier, A. Eckart, NIR imaging and spectroscopy of AGN hosts at z<0.06, 2006, New Astr. Rev, 50, 736

M. Krips, R. Neri, **J. Zuther**, D. Downes, and J. Scharwächter, *Molecular gas and continuum emission in 3C 48: Evidence for two merger nuclei?*, 2005, A&A, 439, 75

J. Zuther, A. Eckart, W. Voges, *Mining the sky: selection of extragalactic targets for interferometric observations*, 2005, AN, 326, 573Z

J. Zuther, A. Eckart, C. Iserlohe, J.-U. Pott, W. Voges, *A sample of X-ray luminous AGN and quiecent galaxies suitable for AO-assisted studies in the NIR*, 2005, Japanese-German Symposium, Regensburg, online proceedings,
`http://jgs05.ita.uni-heidelberg.de/Proceedings/Zuther.pdf`

M. Krips, A. Eckart, R. Neri, J.-U. Pott, **J. Zuther**, J. Scharwächter, T. Bertram, *Feeding Monsters - A Study of Active Galaxies*, 2005, Ap&SS, 295, 95K

J. Scharwächter, A. Eckart, S. Pfalzner, **J. Zuther**, M. Krips, E. Schinnerer, J. Staguhn, *The Qso Hosts I Zw 1 and 3C 48: Prototypes of a Merger-Driven Quasar Evolution?*, 2005, Ap&SS, 295, 101S

J. Scharwächter, A. Eckart, S. Pfalzner, **J. Zuther**, M. Krips, C. Straubmeier, *A multi-particle model of the 3C 48 host*, 2004, A&A, 414, 497

J. Zuther, A. Eckart, J. Scharwächter, M. Krips, S. Pfalzner, and C. Straubmeier, *The Merger QSO 3C 48 and its Host Galaxy in the Near Infrared*, in "Proceedings of the 4th Cologne-Bonn-Zermatt-Symposium", ed. S. Pfalzner, C. Kramer, C. Straubmeier, and A. Heithausen (Springer Verlag), 2004, ISBN: 3-540-21254-X

Eckart, **J. Zuther**, N. Mouawad, R. Schödel, C. Straubmeier, T. Bertram, J.-U. Pott, J. Scharwachter, T. M. Herbst, *Scientific potential for LINC NIRVANA observations of galactic nuclei*, 2004, SPIE, 5491, 106E

A. Eckart, T. Bertram, N. Mouawad, T. Viehmann, C. Straubmeier, **J. Zuther**, *Long Range Science Perspectives for the VLTI*, 2003, Astrophysics and Space Science, 286, 1, 269